The Structure-Property Relation in Nanocrystalline Materials: A Computational Study on Nanocrystalline Copper by Monte Carlo and Molecular Dynamics Simulations

A Dissertation
Presented to
The Academic Faculty

by

Tao Xu

In Partial Fulfillment
of the Requirements for the Degree
Doctor of Philosophy in the
School of Materials Science and Engineering

Georgia Institute of Technology
December, 2009

The Structure-Property Relation in Nanocrystalline Materials: A Computational Study on Nanocrystalline Copper by Monte Carlo and Molecular Dynamics Simulations

Approved by:

Dr. Mo Li, Advisor
School of Materials Science and Engineering
Georgia Institute of Technology

Dr. Naresh Tadhani
School of Materials Science and Engineering
Georgia Institute of Technology

Dr. Christopher J. Summers
School of Materials Science and Engineering
Georgia Institute of Technology

Dr. David C. Sherrill
School of Molecular Science and Engineering
Georgia Institute of Technology

Dr. Arash Yavari
School of Civil Engineering
Georgia Institute of Technology

Date Approved: October 23, 2009

ACKNOWLEDGEMENTS

Firstly and most importantly, I would like to thank my advisor, Dr. Mo Li, for his academic guidance and financial support during my entire Ph.D. study here in School of Materials Science and Engineering at Georgia Institute of Technology. Following him, I walked into this wonderful world of computational material science where the limit of science seems constantly expanding. Along the way, I have learned the basic steps to develop original and creative research interest. I also would like to thank my committee members, Dr. Tadhani, Dr. Summers, Dr. Sherrill and Dr. Yavari for their precious time.

Secondly, I would like to extend my appreciation to the current and former members of computational material science group, especially to Dr. Xianming Bai, Dr. Qikai Li, Dr. J. Payman and Dr. Guangping Zheng. Without their help, I would spend more time solving problems encountered in my research.

I am very grateful to my parents, Dr. Taixi Xu and Guizhen Wang, who have raised and supported me unconditionally. I would like to take this special moment to remember my mother and hope that she can receive this message in the heaven. I am also grateful to my dear relatives, especially my sister Lei Xu and my stepmother Dr. Yange Zhang.

Finally, I am very grateful to my wife, Dr. Shuli Mao, who has always been by my side during my Ph.D. study. Without her support, I will not be able to make to the finish line.

TABLE OF CONTENTS

Page

ACKNOWLEDGEMENTS iii

LIST OF TABLES viii

LIST OF FIGURES ix

SUMMARY xx

CHAPTER

1 Introduction 1

2 Properties of nanocrystalline materials 5

2.1 Characteristic properties of nano-crystalline materials 6

2.2 Difficulties in determining the mechanical properties of nano-crystalline materials 6

2.3 Deformation mechanism for nanocrystalline materials 9

2.4 Deformation mechanism maps 12

2.5 Current progress in molecular dynamic simulation on nc materials 13

3 Digital microstructure constructions 15

3.1 Potts model 16

3.2 Topological and statistical properties of a constrained Voronoi tessellation 21

3.2.1 Background 22

3.2.2 Methods 27

3.2.2.1 Poisson-Voronoi tessellation 27

3.2.2.2 Constrained Voronoi tessellation 28

3.2.3 Results: P(V) 31

3.2.3 Results: P(V) 31

3.2.3.1 Poisson-Voronoi distribution and delta-function distribution 32

3.2.3.2 Lognormal distributions 33

3.2.3.3 Bimodal distribution 47

3.2.3.4 Normal cell volume distributions 56

3.2.4 Minimize the number of small faces and short edges 59

3.2.4.1 Edge length distribution: P(l) 60

3.2.4.2 Face area distribution: P(a) 63

3.2.5 Discussion 67

3.2.5.1 The effects on the Lewis rule by various cell volume distributions 68

3.2.5.2 Cell shape anisotropy 70

3.2.5.3 Point vs. sphere PV process 72

3.2.5.4 Discrepancy between theoretical models and experimental observation 73

3.2.5.5 Application of the CVT in microstructure modeling 75

3.2.5.6 Summary 76

4 Sample preparation 78

4.1 Crystallographic orientation and misorientation distribution 78

4.2 Atomic structure of grains 82

4.3 Relaxation of thermal stability test of the atomic structures 85

4.3.1 Molecular dynamics method 86

4.3.2 Interatomic potential for copper 89

4.3.3 MD Relaxation and Thermal stability of EAM copper potential 91

4.4 Summary 93

5 Atomistic grain boundary characterization 94

5.1 Introduction 94

5.2 Structure analysis 98

5.2.1 Radial distribution function 98

5.2.2 Central-symmetry parameter 100

5.2.3 Common neighbor analysis 102

5.2.4 Potential Energy 103

5.2.5 Atomic Voronoi Volume 105

5.3 Atomic Scale Characterization of Grain Boundaries of Nanocrystalline Materials 105

5.3.1 Method to give each atom an accurate GI 106

5.3.2 Grain Boundary Characterization 112

5.3.3 Results 113

5.3.3.1 Classification of atoms into grain, grain boundary, triple junction, and vertex point 113

5.3.3.2 Grain boundary profile 115

5.3.3.3 Effects of misorientation 120

5.3.3.4 Effects of grain size 123

5.3.3.5 Effects of temperature 129

5.3.3.6 Pair Correlation Function of Grain Boundary Atoms 133

5.4 Conclusions 146

6 Topological properties of grain boundaries of nc-Cu materials 147

6.1 Introduction 147

6.2 Sample Preparation 150

6.3 Methods 152

6.3.1 Calculate the number of atoms in each GB entity 152

6.3.2 Calculate the interface area and triple junction length 153

6.4 Results 158

6.4.1 Number of atoms in each GB entity 158

6.4.2 Interface area and triple junction length 161

6.4.3 Advantages and Limitations 167

6.5 Summary 168

7 Grain boundary misorientation effects on mechanical properties of nanocrystalline copper 170

7.1 Introduction 170

7.2 Methods 174

7.2.1 Sample preparation 174

7.2.2 Deformation simulation 177

7.2.3 Grain boundary orientation and anisotropy 178

7.2.4 Misorientation 184

7.2.5 Structure and defect characterization 186

7.3 Results 186

7.3.1 Stress-strain relation and shear modulus 187

7.3.2 Defect process 189

7.3.3 Grain rotation 206

7.3.4 Grain size effects 210

7.4 Discussion 213

7.5 Conclusions 214

8 Conclusions 216

Appendix A 220

Appendix B 221

Appendix C 223

Appendix D 224

REFERENCES 225

LIST OF TABLES

Page

Table 3.1: The mean numbers of faces ($\langle F \rangle$), edges ($\langle E \rangle$), and vertices ($\langle V_C \rangle$) per cell, and the mean bond angle ($\langle \theta \rangle$) and mean dihedron angle ($\langle \alpha \rangle$). $\langle E_F \rangle$ is the mean number of edges per face. σ is the standard deviation in the cell volume distribution for samples with lognormal distribution with the mean at unity. Bimodal cases are labeled based on the separation between the two means: Bimodal 1, 2, and 3 are for v_b =1.2, 1.3 and 1.4, respectively. We also include the results from the PVT, Meijering's analytical estimates[93], and Potts model simulation[79]. The Euler's relation $\langle \mathrm{V_C} \rangle - \langle \mathrm{E} \rangle + \langle \mathrm{F} \rangle = 2$ and the relation $\langle \mathrm{V_C} \rangle = 2\langle \mathrm{F} \rangle - 4$ are obeyed within statistical error. 41

Table 3.2: The variance of the face number, $\mu_2 = \langle F^2 \rangle - \langle F \rangle^2$, and the constant in the Aboav-Weaire law, *a*, in the four samples with lognormal cell volume distribution and three samples with bimodal cell volume distribution. σ is the standard deviation of cell volume. 47

Table 5.1: The properties of atoms in different layers in a procedure using the *peeling-onion* method: the number fraction of atoms in each layer, fcc percentage (%) of the atoms, mean central symmetry parameter <CSP>, mean square displacement <MSD>, in the layers. 108

Table 5.2: The fitted parameters of the 3rd-order polynomials to $N_{pair}(r)$ for atoms in different slice position, *d*, where $N_{pair}(r) = a_0 + a_1 r + a_2 r^2 + a_3 r^3$. 142

Table 7.1: The average misorientation angle per grain, $\langle \theta \rangle$, Maximum shear stresses, $\tau_{\max}$, the shear strains at maximum shear stress, $\gamma_{\max}$, yield stress at 2% strain, and the shear modulus μ. 188

LIST OF FIGURES

Page

Figure 3.1: Grain structure from 256 by 256 Potts model lattice. 18

Figure 3.2: Edge length distribution of configuration 256 by256. 18

Figure 3.3: Angle distribution of configuration 256 by256. 19

Figure 3.4: Grain structure from 512 by 512 Potts model lattice and $Q = 48$. 19

Figure 3.5: Edge length distribution of configuration 512 by 512, $Q = 48$. 20

Figure 3.6: Angle distribution of configuration 512 by 512, $Q = 48$. 20

Figure 3.7: Area distribution of configuration 512 by 512, $Q = 48$ 21

Figure 3.8: The schematics of two neighboring Voronoi cells at the two points P_1 and P_2. The shaded area of the interface between the two cells is labeled as s, the edge as e, the vertex as v, the bond angle as θ, and the dihedral angle as α. 23

Figure 3.9: The PVT and fcc cell volume/grain size distributions $P(v)$ normalized by the mean volume $\langle \mathrm{V} \rangle$, $\mathrm{v} = \mathrm{V}/\langle \mathrm{V} \rangle$. (a) The random Poisson-Voronoi volume distribution marked by the filled squares in black; the solid line is the numerical fitting from the data, and (b) that of a randomly displaced fcc lattice shown in the inset. 32

Figure 3.10: The cell volume distributions $P(v)$ obtained using the CVT method: four target cell volume distributions with the standard deviation of 0.15, 0.2, 0.3 and 0.4 are presented by solid lines. The cell volume distribution of a PVT is also shown as the dashed line. The corresponding CVT results are plotted as scatted datum points using thesame gray-scale as the target function. 35

Figure 3.11: (a) The distributions of the cell surface area $P(S)$ for the four lognormal samples with the standard deviation at 0.15, 0.2, 0.3 and 0.4 respectively. (b) The distributions $P(L)$ of the cell perimeter for the four lognormal samples with the standard deviation at 0.15, 0.2, 0.3 and 0.4 respectively. Both $P(S)$ and $P(L)$ distributions of PVT are plotted as references. 36

Figure 3.12: (a) The face area distribution, $P(s)$, of the four lognormal samples with the standard deviation of 0.15, 0.2, 0.3, and 0.4 respectively. (b) The face area

distributions at small face areas; (c) The edge length distribution, $P(l)$, of four lognormal samples with the crossover point around 0.2. 38

Figure 3.13: The bond angle distributions, $P(\theta)$, and the dihedral angle distribution, $P(\alpha)$, of the four lognormal samples with the standard deviation of 0.15, 0.2, 0.3, and 0.4 respectively. The bond angle distribution for the PV cells is also shown as a reference. 39

Figure 3.14: a) The number of faces per cell/grain distributions, $P(F_C)$, of the four lognormal samples. The number of the faces for the PV cells is also shown. Note that the smallest number of the faces is 4, or a tetrahedron. b) The number of edges per face distributions, $P(E_F)$, of the four lognormal samples. The number of the edges for the PV cells is also shown. Note that the smallest number of the edges is 3, or a triangle. 40

Figure 3.15: (a) Lewis plots of the four lognormal samples and two special cases (the random Poisson-Voronoi and randomly displaced fcc lattice); (b) The slope of Lewis plots (fitted by Eq. 4a) increase with the standard deviation of the cell volume distributions. 42

Figure 3.16: The plots of Aboav-Weaire law of the three lognormal samples. The plot of $Fm(F)$ vs. F of the CVT ($\sigma = 0.4$, open square) is drawn first. Other plots are superimposed in the order of decreasing standard deviation, $\sigma = 0.3$ (open circle), $\sigma = 0.2$ (open triangle). For each curve, there are 5,000 data points represented by the same symbol. For each Aboav-Weaire plot, the best fitted result for $Fm(F) = aF + b$ is shown as a solid line. As the standard deviation (σ) increases, the domain of each curve shrinks. 46

Figure 3.17: The cell volume distributions of bimodal samples obtained using the CVT method in conjunction with non-uniform weights for the systems with 2,000 points. For comparison, the distribution for the PV cells with 2,000 points is also shown as the dashed line. The target bimodal distribution functions are shown as the solid line and the CVT results are shown as scattered data points labeled with "CVT". The first peak (v_a) is located at 0.8 and the second peaks (v_b) are located at 1.2, 1.3, and 1.4 for the three cases. 48

Figure 3.18: a) The number of faces per cell/grain distributions of the three bimodal samples with 2,000 points. The number of the faces distribution for the PV cells is also shown. Note that the smallest number of the faces is 4, or a tetrahedron. b) The number of edges per face distributions of the three bimodal samples with 2,000 points. The number of the edges for the PV cells is also shown. Note that the smallest number of the edges is 3, or a triangle. 50

Figure 3.19: a) The face area distribution of three bimodal samples with 2,000 points. b) The edge length distribution of the three bimodal samples with 2,000 points.

For comparison, the distribution for the PV cells from a sample with 2,000 points is also shown. 51

Figure 3.20: a) The distribution of the cell surface area of the three bimodal samples with 2,000 points. b) The distribution of the cell perimeter of the three bimodal samples with 2,000 points. For comparison, the distribution for the PV cells from a sample with 2,000 points is also shown. 52

Figure 3.21: The distributions of the dihedral and bond angles of the three bimodal samples with 2,000 points. For comparison, the distribution for the PV cells from a sample with 2,000 points is also shown. 53

Figure 3.22: The Lewis plots for the three bimodal samples with 2,000 points. The Lewis plot of the PV cells of 2,000 points is also shown as a reference. The data become noisy at the ends of the curves due to the limited number of faces available in the models. 54

Figure 3.23: The plots of Aboav-Weaire law for the two bimodal samples ($v_b = 1.2$ and $v_b = 1.4$) with 2,000 points. The plot of $Fm(F)$ vs. F of the PVT (open square) is drawn first. Other plots are superimposed in the order of decreasing standard deviation, $v_b = 1.4$ (open circle), $v_b = 1.2$ (open triangle). For each Aboav-Weaire plot, the best-fitted result for $Fm(F) = aF + b$ is shown as a solid line with the different gray-scale. 55

Figure 3.24: Cell volume distributions of Voronoi tessellations with normal cell volume distribution ($\sigma = 0.3$). 57

Figure 3.25: The Lewis plots for two Voronoi tessellations with the same standard deviation but different cell volume distributions: lognormal distributions (filled squares) and normal distributions (filled triangles). 58

Figure 3.26: The Aboav-Weaire plots for two Voronoi tessellations with the same standard deviation but different cell volume distributions: lognormal distributions (filled squares) and normal distributions (filled triangles). 59

Figure 3.27: Edge length distributions and cell volume distributions of a VT with reduced number of short edges ($l < l_{CUT}$) and the initial VT with a lognormal cell volume distribution ($\sigma = 0.3$). 61

Figure 3.28: a) Face area distributions of initial VT and VT with reduced number of short edges ($l < l_{CUT}$); b) Face number distributions; c) Lewis plots. 62

Figure 3.29: Face area distributions and cell volume distributions of a VT with reduced number of small areas ($s < s_{CUT}$) and the initial VT with a lognormal cell volume distribution ($\sigma = 0.3$). 64

Figure 3.30: a) Edge length distributions of initial VT and VT with reduced number of small faces ($s < s_{CUT}$); b) Face number distributions; c) Lewis plots. 65

Figure 3.31: a) $Fm(F)$ vs. F for three Voronoi samples: 1) VT of lognormal cell volume distribution ($\sigma = 0.3$); 2) VT of reduced short edges ($l < l_{CUT}$); 3) VT of reduced small faces ($s < s_{CUT}$). b) Fitted linear relation according to Eqn. 3.5. 66

Figure 3.32: Cell volume distributions of Voronoi tessellations with four different cell volume distributions: 1) lognormal ($\sigma = 0.3$); 2) normal ($\sigma = 0.3$); 3) PVT; 4) bimodal ($v_a = 1.2$, $v_b = 1.3$). 68

Figure 3.33: Lewis plots of four Voronoi tessellations with different cell volume distributions: 1) lognormal ($\sigma = 0.3$); 2) normal ($\sigma = 0.3$); 3) PVT; 4) bimodal ($v_a = 1.2$, $v_b = 1.3$). 69

Figure 3.34: The cell shape isotropy (CSI) of the PVT and the two lognormal samples with the standard deviations of 0.15 and 0.3. For each sample, there are 5,000 CSI data points. The CSI of PVT is drawn first followed by two lognormal samples in the order of decreasing standard deviations. For each sample, the relation between $\langle CSI \rangle_F$ and F is also shown as a solid line using the same color as that of CSI plot. 71

Figure 3.35: Cell shape isotropy of the PVT and three bimodal CVT samples with 2,000 points. For each sample, there are 2,000 CSI data points. The CSI of PVT is drawn first and that of three bimodal samples are superimposed according to the center of second peaks. The bimodal sample located at $v_b = 1.4$ is drawn first, followed by $v_b = 1.3$ and $v_b = 1.2$. 72

Figure 4.1: The distributions of misorientation angles for a sample with 50 grains. The black square represents the distribution with a minimized misorientation with the mean misorientation angle at 10.496°, the filled green triangle represents the distribution with a maximized misorientation with the mean misorientation angle at 46.705°, and the filled red circles represents an intermediate distribution. 82

Figure 4.2: Projection of 3D Voronoi structure and reference lattice onto a 2D plane. The box length of reference lattice must be larger than $\sqrt{3}L$ to cover the domain of Voronoi structure during rotation around the origin. 85

Figure 4.3: The projections of smallest grain in <111> before and after relaxation. The red atoms represent the initial atomic positions and the blue atoms represent the atomic positions after relaxation. 92

Figure 5.1: Temperature effects on radial distribution function of nc-Cu sample relaxed at different temperatures from 350K to 900K. 100

Figure 5.2: A nc-Cu sample of 50 grains is characterized by the CSP after MD relaxation at 300K. 101

Figure 5.3: The nc-Cu sample of 50 grains after MD relaxation is characterized by common neighbor analysis. The blue atoms are fcc atoms. Green atoms are hcp atoms and yellow atoms represent the rest. 102

Figure 5.4: A nc-Cu sample characterized by the potential energy. 103

Figure 5.5: A nc-Cu sample of 50 grains characterized by the atomic Voronoi volume. 104

Figure 5.6: a) Step 1 in the peeling-onion method during which the grain cores (red polygon) are identified. The dotted black line shows the positions of the grain boundaries from the constrained Voronoi construction; b) Step 2 during which additional layers of atoms are associated with the identified grain cores; 107

Figure 5.7: 2D section of the relaxed nc-Cu sample showing the layered structure identified by the peeling-onion method. The blue area is occupied by atoms in grain core. The green area is occupied by atoms in layer 1. The dark yellow area is occupied by atoms in layer 2. The yellow are is occupied by atoms in layer 3. The red area is occupied by atoms in layer 4. 107

Figure 5.8: The initial Voronoi cells for grain 07, 22 and 46. Red cell represents grain 07, green cell represents grain 22 and blue cell represents grain 46 109

Figure 5.9: Three neighboring grains 07, 22 and 46 characterized by the shell method. Blue atoms represent atoms in grain core. Green atoms are atoms in shell 1. Dark yellow atoms are in shell 2. Yellow atoms are in shell 3. Red atoms are in shell 4. 110

Figure 5.10: Three neighboring grains (07, 22, 46) without atoms in grain core. Blue atoms are in shell 1. Dark yellow atoms are in shell 2. Yellow atoms are in shell 3 and red atoms are in shell 4. 111

Figure 5.11: The characterized grain 7. Blue atoms represent atoms inside the grain. Green atoms represent grain boundary interface. Yellow atoms are triple junction atoms and red atoms are vertex atoms. 114

Figure 5.12: The fraction of the different types of atoms in the sample that is associated with different microstructure entities. 115

Figure 5.13: The projection of interface between two grains in two different directions, one parallel to the GB (a) and other perpendicular to it (b); (c) the grain boundary on a reference plane from the crystal structure inside the grain which

is perpendicular to the surface normal; (d) the cylinder cut along the direction of GB interface normal; (e) thin slices within the cylinder (2Å) cut parallel to the GB. 117

Figure 5.14: The potential energy and central symmetry parameter profiles across a grain boundary interface between two neighboring grains and definition of grain boundary width. 118

Figure 5.15: The distributions of H_{CSP} (a) and H_{pot} (b) with a mean grain size of $\langle D \rangle = 8.696nm$. 119

Figure 5.16: The average Voronoi volume profile for GB interface between grain 07 and 46. 119

Figure 5.17: The distribution of maximum Voronoi volume from the average Voronoi volume profile for each GB interface in nc-Cu sample of 50 grains. $\langle D \rangle = 8.696nm$. 120

Figure 5.18: GB width distributions for two samples with random and minimized misorientation distributions 122

Figure 5.19: The distributions of H_{CSP} for two samples with random and minimized misorientation distributions. 123

Figure 5.20: a) The grain size effects on the distribution of H_{CSP} obtained from GB CSP profiles; b) $\langle H_{CSP} \rangle$ increases with mean grain size. 124

Figure 5.21: a) Grain size effects on the distribution of GB width obtained from GB CSP profiles; b) The average GB width decreases as mean grain size increases. 125

Figure 5.22: a) The grain size effects on the distribution of H_{AVV} obtained from GB atomic Voronoi volume profiles; b) H_{AVV} fluctuates as $\langle D \rangle$ increase. 126

Figure 5.23: The normalized GB width distributions of two nc-Cu samples of $\langle D \rangle = 8.696nm$ (50 grains) and $\langle D \rangle = 16.52nm$ (20 grains). Both have the same topological structure. 127

Figure 5.24: Stress profile of the interface between two grains in the sample with the largest mean grain size ($\langle D \rangle = 10.145nm$) 128

Figure 5.25: Stress profile of the interface between two grains in the sample with the smallest mean grain size ($\langle D \rangle = 7.609nm$) 129

Figure 5.26: The effects of rising temperature on the mean potential energies of all grain atoms in the sample as well as that of grain boundary interface atoms, triple junction atoms and vertices atoms. 130

Figure 5.27: The effects of rising temperature on the number of atoms in the grains, grain boundaries, triple junctions and vertex points. 130

Figure 5.28: The effects of rising temperature on the distribution of mean potential energies of atoms on the same grain boundary interface. 131

Figure 5.29: The effects of rising temperature on the distribution of GB width. 132

Figure 5.30: The temperature effects on the distribution of maximum atomic Voronoi volumes. 132

Figure 5.31: The number of atom pairs increases as the distance to GB increases. 134

Figure 5.32: Pair correlation function (PCF) of atoms in slices with the same distance to the grain boundary interfaces. The PCF becomes more acute as the distance to GB interfaces decrease indicating that atoms are more ordered. 136

Figure 5.33: The temperature effects on the GB PCF profiles at different slice positions: a) d=1; b) d=3; c) d=5; d) d=7 angstroms. Only the first peaks are shown. 137

Figure 5.34: a) The accumulated pair distances for two nc-Cu samples of mean grain sizes of 8.696 (black) and 10.145nm (red); b) The normalized pair correlation functions of two samples by the fitting third-order polynomials. 139

Figure 5.35: The relations between N_{pair} and pair distance r_{ij} of a nc-Cu sample at 300K (black lines) and 1200K (red lines) are fitted by a 3rd-order polynomial. 140

Figure 5.36: The normalized pair correlation functions at two temperatures for the same 50-grain nc-Cu sample with a mean grain size of 8.696nm. A dotted line is plotted at $PCF(r) = 1.0$. 141

Figure 5.37: The relations between the number of atom pairs and pair distances are fitted by a 3rd-order polynomial for atoms in slices with a different distance, *d*, to grain boundaries (*d*=1, 3, 5, 7 and 17 Å). 142

Figure 5.38: The normalized pair correlation functions for atoms in slices with a distance, *d*, to the grain boundaries (*d*=1, 3, 5, 7 and 17Å). 143

Figure 5.39: The relations between the number of atom pairs and pair distances for three types of atoms are fitted using a 3rd-order polynomial: 1) Grain atoms (*d*=17Å, black lines); 2) GB atoms (*d*=1Å, red lines); and 3) TJ atoms (blue lines). 144

Figure 5.40: Normalized PCFs for three types of atoms: 1) Grain atoms; 2) GB atoms; 3) TJ atoms. 144

Figure 5.41: The relation between the number of atom pairs and the pair distance for vertex atoms in nc-Cu samples of different mean grain sizes: 1) 8.696nm (black line) and 2) 10.145nm (red line). 145

Figure 6.1: The nc-Cu sample of 50 grains after MD relaxation is characterized by common neighbor analysis. The blue atoms are fcc atoms. Green atoms are hcp atoms and yellow atoms represent the rest. 151

Figure 6.2: a) Schematic diagram of GB interface between Grain 06 and 07. b) The perfect closed loop linked by a common grain index, either $gid1$ or $gid2$. 154

Figure 6.3: Atomic configuration of the GB interface between 06 and 34. 155

Figure 6.4: The missing link identified in the open loop. 156

Figure 6.5: Atomic configuration of the GB interface between 06 and 46. The mass center of grain boundary atoms (pink atoms) is plotted as a gray atom. The mass centers of all vertices are plotted as atoms of different colors. 157

Figure 6.6: An additional vertex identified as (30,35). 157

Figure 6.7: GB interface (6, 46) and grain 35. The additional vertex is introduced by the neighboring grain 35. 158

Figure 6.8: a) Cell volume distribution of nc-Cu sample with $\langle D \rangle = 8.05nm$, number of grains is 100; b) the distribution of number of atoms in each grain core 159

Figure 6.9: a) Face area distribution of Voronoi structure with 100 cells; b) The distribution of the number of atoms per GB interface. 160

Figure 6.10: a) Triple junction length distribution of Voronoi structure with 100 cells; b) The distribution of number of atoms per triple junction. 160

Figure 6.11: The linear relation between the number of atoms per interface, n_f, and the calculated GB interface area is best fitted by $a = 1.9957 n_f - 382.37$, for a 50-grain sample of mean grain size of 12.17nm 162

Figure 6.12: The linear relation between the number of atoms per TJ, n_{tj}, and the calculated TJ length is best fitted by $l = 0.27416 n_{tj} + 1.01826$. Number of grains is 50 and average grain size is 12.17nm. The minimum number of atoms on a TJ is 18 163

Figure 6.13: The calculated GB interface areas for three samples with different mean grain sizes and grain numbers: a) <d>=12.17nm, Ng=50; b) <d>=10.15nm, Ng=50 and c) <d>=8.05nm, number of grains is 100 164

Figure 6.14: The calculated TJ lengths for three samples with different mean grain sizes and grain numbers: a) <d>=12.17nm, Ng=50; b) <d>=10.15nm, Ng=50 and c) <d>=8.05nm, number of grain is 100. 165

Figure 6.15: The temperature effects on the linear relation between interface area, a, and the number of atoms per interface, n_f, for the same 50-grain nc-Cu sample with a mean grain size of 12.17nm. The slope, a/n_f, decreases as the temperature increases from 100K to 500K 166

Figure 6.16: The temperature effects on the linear relation between TJ length, l, and the number of atoms per TJ, n_{tj}, for the same 50-grain nc-Cu sample with a mean grain size of 12.17nm. The slope, l/n_{tj}, does not change much as the temperature increases from 100K to 500K 167

Figure 7.1: Common neighbor analysis of nc-Cu sample before relaxation. Green atoms are fcc atoms, blue atoms are hcp atoms and red atoms are the rest of atoms. 176

Figure 7.2: Common neighbor analysis of nc-Cu sample after relaxation. Green atoms are fcc atoms, blue atoms are hcp atoms and red atoms are the rest of atoms. 177

Figure 7.3: Probability GB interfaces whose unit normal vectors are located in the range from θ_{xy} to $\theta_{xy}+\Delta\theta_{xy}$ is equivalent to the area of surface on the sphere between two planes normal to the z-axis, where $d_0=\cos\theta_{xy}$ and $d_1=\cos(\theta_{xy}+\Delta\theta_{xy})$. 180

Figure 7.4: The distributions of θ_{xy}, θ_{zx} and θ_{zy} *w.r.t* the probability of the ideal isotropic case calculated from 5,000 Voronoi cells. The total number of interfaces is 38494. 181

Figure 7.5: The distributions of θ_{xy}, θ_{zx} and θ_{zy} w.r.t the probability of the ideal isotropic case calculated from 200 Voronoi cells. The total number of interfaces is 1570. 181

Figure 7.6: The distributions of θ_{xy}, θ_{zx} and θ_{zy} w.r.t the probability of the ideal isotropic case calculated from 50 Voronoi cells. The total number of interfaces is 325. 182

Figure 7.7: The distributions of θ_{xy}, θ_{zx} and θ_{zy} with respect to the probability of the ideal isotropic case calculated from 20 Voronoi cells. The total number of interfaces is 134. 182

Figure 7.8: The deviation from ideal probability of angles between GB and shear planes increases as the number of Voronoi cells decreases. 183

Figure 7.9: The maximum difference among $P(\theta_{zx})$, $P(\theta_{yx})$ and $P(\theta_{zy})$ increases as the number of cells decreases. 184

Figure 7.10: Distributions of misorientation angle obtained through minimization and maximization using Monte Carlo technique. 185

Figure 7.11: Shear stress-strain curves show misorientation effects on the mechanical properties of nc-Cu. Number of grains = 100, L=30.125nm, <D>=8.05nm.187

Figure 7.12: The change in percentage of (1421) type with different misorientation distributions. 190

Figure 7.13: The relation between average misorientation angles, $\langle\theta\rangle$ and the percentage of (1421) type atoms. 190

Figure 7.14: The change in percentage of (1422) type with different misorientation distributions. 192

Figure 7.15: The change in percentage of (1311) type of atoms with different mirorientation distributions. 193

Figure 7.16: Characterization of grain boundary atoms in nc-Cu samples of different misorientation distributions. Number of grains = 100, L=30.125nm, <D>=8.05nm. 194

Figure 7.17: The distributions of average Central symmetry parameter of atoms on the each grain boundary are accumulated from all GB interfaces presented in eight misorientation samples: $\langle\theta\rangle = 10.46$, 15.36, 20.22, 25.08, 29.95, 34.81, 39.67, 46.71. 195

Figure 7.18: The distributions of average atomic Voronoi volume of atoms on the each grain boundary are accumulated from all GB interfaces presented in two misorientation samples: random and minimized misorientation distributions. 196

Figure 7.19: CN analysis of nc-Cu with <θ>=10.496 at 0% shear strain. Pink atoms are fcc atoms, green atoms are hcp atoms and silver atoms are the rest. 198

Figure 7.20: CN analysis of nc-Cu with <θ>=20.222 at 0% shear strain. 198

Figure 7.21: CN analysis of nc-Cu with <θ>=29.948 at 0% shear strain. 199

Figure 7.22: CN analysis of nc-Cu with <θ>=39.673 at 0% shear strain. 199

Figure 7.23: CN analysis of nc-Cu with <θ>=10.496 at 3.3% shear strain. 200

Figure 7.24: CN analysis of nc-Cu with <θ>=20.222 at 3.3% shear strain. 200

Figure 7.25: CN analysis of nc-Cu with <θ>=29.948 at 3.3% shear strain. 201

Figure 7.26: CN analysis of nc-Cu with <θ>=39.673 at 3.3% shear strain. 201

Figure 7.27: CN analysis of nc-Cu with <θ>=10.496 at 4.98% shear strain. 202

Figure 7.28: CN analysis of nc-Cu with <θ>=20.222 at 4.98% shear strain. 202

Figure 7.29: CN analysis of nc-Cu with <θ>=29.948 at 4.98% shear strain. 203

Figure 7.30: CN analysis of nc-Cu with <θ>=39.673 at 4.98% shear strain. 203

Figure 7.31: CN analysis of nc-Cu with <θ>=10.496 at 6.6% shear strain. 204

Figure 7.32: CN analysis of nc-Cu with <θ>=20.222 at 6.6% shear strain. 204

Figure 7.33: CN analysis of nc-Cu with <θ>=29.948 at 6.6% shear strain. 205

Figure 7.34: CN analysis of nc-Cu with <θ>=39.673 at 6.6% shear strain. 205

Figure 7.35: The core atoms of a grain in a 20-grain nc-Cu samples at zero shear strain and a finite shear strain. The rotation angle can be evaluated by Eqn. 7.4. 207

Figure 7.36: The rotation angles of grains in a 20-grain nc-Cu sample with an average misorientation angle of 10 at different timestep during shear deformation. 208

Figure 7.37: The rotation angles of grains in a 20-grain nc-Cu sample with an average misorientation angle of 25 at different timestep during shear deformation. 208

Figure 7.38: The rotation angles of grains in a 20-grain nc-Cu sample with an average misorientation angle of 40 at different timestep during shear deformation. 209

Figure 7.39: The average rotation angles of three 20-grain nc-Cu samples at different timestep during shear deformation. 209

Figure 7.40: The shear stress-strain curves for nc-Cu samples of the same box size but different number of grains and misorientation distributions. The box size is 30.125nm. The average grain sizes are 13.77nm (Ng=20), 10.145nm (Ng=50), 8.05nm (Ng=100) and 6.39nm (Ng=200). 211

Figure 7.41: The percentage change of (1422) type of atoms during shear deformation for nc-Cu samples of different misorientation distributions and different number of grains. The box sizes are kept the same at 30.125nm as the number of grains varies from 20 to 100. 212

SUMMARY

Nanocrystalline materials have been under extensive study in the past two decades. The reduction in grain size induces many abnormal behaviors in the properties of nanocrystalline materials, that have been investigated systematically and quantitatively. As one of the most fundamental relations in materials science, the structure-property relation should still apply on materials of nano-scale grain sizes. The characterization of grain boundaries (GBs) and related entities remains a big obstacle to understanding the structure-property relation in nanocrystalline materials. It is challenging experimentally to determine the topological properties of polycrystalline materials due to the complex and disordered grain boundary network presented in the nanocrystalline materials. The constantly improving computing power enables us to study the structure-property relation in nanocrystalline materials via Monte Carlo and molecular dynamic simulations.

In this study, we will first propose a geometrical construction method based on inverse Monte Carlo simulation to generate digital microstructures with desired topological properties such as grain size, interface area, triple junction length as well as their statistical distributions. The influences on the grain shapes by different topological properties are studied. Two empirical geometrical laws are examined including the Lewis rule and Aboav-Weaire law. Secondly, defect free nanocrystalline Copper (*nc*-Cu) samples are generated by filling atoms into the Voronoi structure and then relaxed by molecular dynamics simulations. Atoms in the relaxed *nc*-Cu samples are then characterized into grain atoms, GB interface atoms, GB triple junction atoms and vertex

atoms using a newly proposed method. Atoms in each GB entity can also be identified. Next, the topological properties of *nc*-Cu samples before and after relaxation are calculated and compared, indicating that there exists a physical limit in the number of atoms to form a stable grain boundary interface and triple junction in nanocrystalline materials. In addition, we are able to obtain the statistical averages of geometrical and thermal properties of atoms across each GB interfaces, the so-called GB profiles, and study the grain size, misorientation and temperature effects on the microstructures in nanocrystalline materials. Finally, nc-Cu samples with different topological properties are deformed under simple shear using MD simulation in an attempt to study the structure-property relation in nanocrystalline materials.

Chapter 1

Introduction

Over the past two decades, the mechanical behavior of nanocrystalline (*nc*) metals and alloys has been a subject of considerable interest, owing largely to the tremendous increase of the strength expected in the materials at nanometer scales. The classical Hall-Petch [1, 2] (H-P) relation based on dislocation pile-up at grain boundaries has been applied successfully to describe the strength dependence on grain sizes, $\sigma_y = \sigma_0 + kd^{-1/2}$, where σ_y is the yield strength, d is the average grain size, σ_0 and $k(>0)$ are material constants. However, the strength does not always increase monotonically with the decreasing grain size. Softening and inverse Hall-Patch relation ($k<0$) were also observed at smaller grain sizes experimentally [3-7] and theoretically [8, 9]. To rationalize this abnormality, many non-dislocation-centric models were proposed, including grain boundary sliding and grain rotation [10], Cobb creep or grain boundary diffusion [11], and grain boundary thickness change [12, 13]. Despite intensive research performed in the past two decades, a definitive and qualitative answer to the mechanical response in nanocrystalline materials is still not fully comprehended. The difficulty lies in the fact that both experimental characterization and atomistic modeling of microscopic mechanisms are severely limited by the small dimensions and a large number of grains that are present in the *nc*-materials. For example, TEM could handle only a limited number of grains while a reliable answer should be drawn from the ensemble average of a large number of grains and measurements. What is fundamentally short-handed in this endeavor comes from the lack of detailed account of microstructures that are as equally prevalent in the nanocrystalline materials as those in coarse-grained, or

polycrystalline materials since, after all, the former is also a kind of polycrystalline materials only with grain sizes in nanometer scales. The microstructure attributes include the geometric and structure properties: (a) grain size, (b) grain shape, (c) grain boundary type (or misorientation), (d) crystallographic orientation (or texture), (e) grain boundary disorder (or thickness), (f) triple junctions, and (g) vertices. Of course, there are also the statistical properties of these geometric attributes, including their means, variance, and higher order moments. These properties are known to contribute collectively to physical and mechanical properties of polycrystalline materials. Therefore, one should expect to see the same, if not larger, influence on the properties from the microstructures in the nanoscale.

Currently, the grain size is the focus of most research on the strength of nanocrystalline materials and other microstructure attributes have not been paid much attention. In this study, we will attempt to study the influence on the physical and mechanical properties by various geometrical properties such as grain size, grain shape, GB misorientation, GB disorder or thickness, etc. In Chapter 2, we will go through the properties of nanocrystalline materials. In Chapter 3, we will study the advantages and disadvantages of several methods to generate 2D or 3D digital microstructures, mainly the Potts model and Voronoi model, and propose a new method called the constrained Voronoi Tessellation [14] (CVT), which is based on the inverse Monte Carlo method [15] (IMC). Using this method, we are able to generate Voronoi structures with desired topological properties, such as cell volume distribution, face area distribution, triple junction length distribution, and then study the effects on several empirical laws including Lewis rule, Aboav-Weaire law and cell shape isotropy (CSI). Once we obtain the desired Voronoi structure, a Monte Carlo procedure is performed to obtain different misorientation distributions based on the same grain structure.

In Chapter 4, we fill copper atoms with *fcc* lattice into the dimensionless Voronoi structures generated from Chapter 3. *nc*-Cu samples are generated by assigning random

orientation to each grain and need to be further relaxed by molecular dynamics simulations. Here, we will introduce the Embedded-Atom method (EAM) as the potential during MD relaxations. In Chapter 5, the relaxed samples are then characterized using different methods including central symmetry parameter (CSP), common neighbor analysis (CNA), mean square displacement (MSD), potential energy (PE), atomic stress, atomic Voronoi volume (AVV). However, we still need another method to accurately identify each grain boundary entities in the relaxed samples such as grain boundary interfaces, triple junctions and vertices. A new method, called "peeling-onion" method, is proposed to give a unique identification number (ID) to each atom in the relaxed samples. Based on the new IDs, we are able to identify atoms in each GB entities by examining each atom's neighbors within $1.5R_{1NN}$ (First nearest neighbor distance). Next, the surface normal of each grain boundary interface is calculated and thin slices (2Å in thickness) are cut parallel to the GB interface. The averages of CSP, PE and AVV can then be calculated for atoms in each slice, which give us the profiles of all grain boundary interfaces and their statistical mean and distributions. The temperature effects on these distributions are also studied. In Chapter 6, we calculate the topological properties of grain boundary structures in the relaxed samples using the identified vertices and obtain the distributions of GB interface area and triple junction length. This newly developed grain boundary characterization (GBC) technique gives us another powerful tool to study the properties of nanocrystalline materials.

In Chapter 7, we will perform mechanical deformation on the relaxed *nc*-Cu samples of different grain sizes and misorientation distributions. Simple shear deformation is performed using two different loading conditions: one is the method proposed by Wolf et al [16], where a velocity scheme is applied with non-periodic boundary condition only in one direction; another is an in-house developed Rahman-Parrinello [17, 18] MD program where periodic boundary condition is preserved in all three directions. Results using both methods are compared and similar results are found.

Firstly, we will inspect the relationship between the number of cells and the anisotropy in shear stress induced by shearing the samples in three different directions: -*zx*, -*zy* and –*yx*. The GBC technique is applied onto the deformed samples at different stage during shear deformation using the LAMMPS program. The detailed atomic information enables us to compare the deformation processes of samples with different grain sizes and misorientation distributions. The result confirms our belief that the complexity and the degree of disorder in grain boundary region induced by different grain size and misorientation distributions are the most critical parameters controlling the strength of nanocrystalline materials.

Chapter 2

Properties of nanocrystalline materials

Nanocrystalline (*nc*) materials have been extensively investigated during the past two decades as metallurgists and materials scientists looking for a material that is stronger, stiffer and lighter. A wide range of novel properties including magnetic, superconducting, magetoresistive, mechanical, tribological, optical and chemical properties, that are not unattainable in materials with a conventional grain size, are now being achieved through the use of nanostructures. Activities on the synthesis of *nc* materials has increased in recent years since H. Gleiter [19] synthesized ultra-fine nanometer sized metallic particles using an inert gas condensation technique [20]. Since then a number of techniques have been developed including mechanical alloying [21], spray conversion processing [22], sputtering [23], physical vapor deposition (PVD) [24], chemical vapour processing [25], electro-deposition [26], plasma processing [27], laser ablation [28], equal channel extrusion [29] and shock loading [30]. Although the mechanical properties of *nc* materials have been under extensive investigation, the fundamental structure-property relationship has not been understood due to difficulties in determining the properties of *nc* materials experimentally. The challenging task of making high-quality bulk *nc* metals has long been the bottleneck in this field. In this study, we will make an attempt to understand the structure-properties relationship of nano-crystalline materials using molecular dynamic simulation, especially the plastic deformation mechanisms.

2.1 Characteristic properties of nano-crystalline materials

The most significant property of nano-crystalline materials is the small grain size usually in the range of 1-100nm and large volume fraction of grain boundaries. According to the Hall-Petch relation, the yield strength of *nc* materials will increase significantly as the grain size decreases. Hardness should increase tremendously at the expense of brittleness. Fracture toughness should improve greatly as the number of grains increases. Low temperature superplasticity was found in nanostructured nickel and metal alloys [31].

However, a number of adversary effects also appear. For example, accompanying the high strength is a diminishing plastic strain, the toughness is traded with brittleness, and the materials as a whole show extreme sensitivity to localized strain or shear banding, a precursor for material failure or fracture [32]. Another puzzling issue is the so-called inverse Hall-Petch relation, where the decreasing grain size enhanced strengthening diminishes and is replaced sometimes by softening at smaller grain size [4, 8]. The underlying physical deformation mechanisms of the above phenomena have not been fully understood. The difficulties in determining the microstructures experimentally greatly hindered further investigation.

2.2 Difficulties in determining the mechanical properties of nano-crystalline materials

The mechanical behavior of *nc* metals and alloys has been a subject of considerable interest for over a decade. Among the large number of *nc* materials investigated so far, copper is arguably the most widely used model metal [33]. The mechanical properties of *nc*-Cu reported in the literature vary over a wide range. For example, for grain sizes of order of 30nm, the yield strength observed varies as much as from 400 to 850 MPa [33]. The great spread in the experimental results available makes

it impossible to check the accuracy of model calculations against the properties actually measured.

The inconsistent experimental findings for the *nc*-Cu arise largely from the difficulties in preparing flaw-free *nc*-Cu (or any other nc material) samples for reliable mechanical property evaluations. Porosity, flaws, and recrystallized grains have been found in most *nc* materials [34]. To obtain true nanoscale grain sizes (<100nm), the *nc*-metals are often obtained in powder form. A consolidation step is then needed to obtain bulk compacts for mechanical testing. Due to the residual porosities, the intrinsic tensile behavior of *nc*-metals is often overshadowed by responses from the flaws and artifacts. Similar porosity and particle bonding problems exist in samples consolidated from mechanically milled powers [35].

To date, most of the mechanical testing of nanocrystalline materials has been carried out through the use of indentation techniques [36] for thin films and micro-sample tensile testing [37] for bulk *nc* materials. Hardness enhancements of a factor of over four resulting from grain refinement have been reported for nanocrystalline materials and alloys [38]. Historically, uni-axial loading has proven to be the most direct way of characterizing the mechanical strength and ductility of a material, and the scarcity of tensile data on well characterized, high-density and high-purity nanocrystalline samples has hindered the development of a fundamental understanding of their mechanical behavior. The development of a 'microsample' tensile-testing machine by Shapre *et al*. [39], has greatly facilitated the mechanical testing of specimens on the strength of several pure metals with nanocrystalline grain sizes. Tremendous strength enhancements have been measured in the ultrafine-grained and nanocrystalline materials using this technique. However, brittle behavior or strain to failure of not more than few percent is found during studies of the deformation of *nc* materials, using micro tensile tests [37].

Recent advance in synthesis and testing on well-controlled quality samples sheds tremendous light on the relation, although more quantitative information is still waiting to be determined. For example, Champion *et al.* [40] reported a nearly six-fold increase in yield strength for *nc*-Cu in a quasistatic tensile test. An elastic-perfect plastic behavior was observed for this material. Although no quantitative measurements are given, it appears that the co-existence of both ordered and disordered grain boundaries on different length scales are responsible for the observed mechanical property, which was also suggested by Weertman [37] and Estrin [41].

Youssef *et al* [42] also succeeded in developing an *in-situ* consolidation method to produce porosity-free *nc*-Cu spheres 5-7 mm in diameter. They used combinations of ball milling runs at liquid nitrogen temperature and room temperature to create the *nc*-grain structure and consolidate (cold weld) the powders to full density. The resultant *nc*-Cu had very small grain sizes (all grains are below 50 nm) and a narrow grain size distribution. Youssef *et al* evaluated the mechanical properties of this *nc*-Cu using miniaturized disk bend tests (MDBT). The *nc*-Cu showed a very high strength of 770 MPa and at the same time appeared to have good ductility and possibly strong strain hardening capability. They also obtained statistical distribution of grain size from multiple dark-field TEM images of the same sample. In another experiment done by Wang Y. *et al* [43], a *nc*-Cu sample with bimodal grain size distribution is achieved after a thermo-mechanical treatment of Cu. As nanocrystalline materials often exhibit low tensile ductility at room temperature with elongation to failure typically less than a few per cent, this *nc*-Cu sample with micro-metre-sized grains embedded inside a matrix of nanocrystalline and ultra-fine (<300nm) grains exhibit a high tensile ductility-65% elongation to failure, and 30% uniform elongation. The bimodal grain size distribution may have played an important role.

2.3 Deformation mechanism for nanocrystalline materials

Nanostructured metals and alloys have demonstrated superior mechanical properties, such as excellent super plasticity, high strength, and in a few cases, the combination of very high yield strengths and high ductility. The unique deformation mechanisms in nanostructured materials are believed responsible for the superior mechanical properties of the materials. Recently, tremendous effort has been made to understand the deformation mechanisms in nanostructured materials. For example, molecular dynamic simulations suggested that grain-boundary (GB) sliding [44] plays a significant role at very fine grain sizes (e.g., 3-10nm), while partial dislocations emitted from GBs dominate the deformation at the grain sizes of several tens of nanometers. Recent experimental observations on nanocrystalline Al and Cu have provided strong evidence of partial dislocation emission from GBs, which subsequently form deformation twins and stacking faults [45].

Zhu B. *et al* [46] estimates the shear stress required to generate and move dislocation segments as $\tau \geq (3-4)G(b/d)$, where b is the magnitude of the Burger's vector, and d is the grain diameter. For pure Ni with $d \approx 1\mu m$, $\tau \geq 82MPa$, which is reasonable. However, if $d \approx 30nm$, then $\tau \geq 3280MPa$, which is too large. Experimental evidence shows that, at grain sizes in this nanocrystalline range, grains seem free of dislocations in the their interior.

Grain boundaries and triple junctions as obstacles for dislocation motion may play an important role during plastic deformation since grains in *nc* materials are free of dislocations. When the grain size of a metal reduces into nano-scale, dislocation activity should become comparatively less important. Alternative mechanisms, which involve transport at grain boundaries, most notably diffusion creep, grain boundary sliding and grain boundary rotation. Materials that are brittle, in the coarse-grained state, are brittle due to a lack of active slip systems, might become ductile when in the nanocrystalline

form. Diffusion creep has been ruled out as a practicable deformation pathway at room temperature since an unphysical high stress of order of 10^{10} MPa would be required to achieve the strain rates of order of 10^{-1}/s needed in industrial forming processes.

How does dislocation contribute to the plasticity? Due to the unreasonably large stress involved in a Frank-Read type source in nanocrystalline materials, full dislocation is unlikely to form inside nano-grains. In spite of the observation of dislocations in nano-grains, there is so far no reported observation of a Frank-Read source in a nanocrystalline solid. Even MD simulation at very high stress and strain rate doesn't show any dislocation emission from Frank-Read sources. Instead the simulations indicate that a fundamentally different mechanism is active: new dislocations, often partials, nucleate at grain boundaries, transverse the grain, and are then absorbed by the grain boundary on the opposite side of the grain. Thus, the dislocation density does not increase as the deformation progresses. In agreement with this notion, nanocrystalline *fcc* metals exhibit unusually low work hardening [45].

It is well established that grain boundary sliding plays an important role in the super-plastic deformation of conventional coarse-grained materials. Since the number of grain boundaries per volume increases as the grain size is reduced, it can be expected that sliding is a relatively more important process at smaller grain size. Intricately linked to this issue is that of grain rotation. Dislocation glide on preferred slip systems gives rise to rotation and to crystallographic texture. On the other hand, grain rotation via grain boundary sliding alone may randomize the grain orientation distribution. Experiments on *nc*-Pd deformed to a large true strain, 0.6, by rolling at room temperature show that the random grain orientation distribution of the starting material is maintained, whereas coarse-grained Pd deformed under identical conditions develops a pronounced rolling texture [11]. This provides strong evidence for a significant role of grain rotation in the deformation of the nanocrystalline metal, similar to the grain rotation during superplastic

deformation of coarse-grained materials at elevated temperature. In fact, individual rotation events have recently been observed by *in-situ* transmission electron microscopy (TEM) [47].

In several reports, twinning is observed in nanocrystalline materials, implying that the grain size effect on deformation twinning in coarse-grained copper (i.e., smaller grains are less likely to win) does not apply to nanocrystalline copper. Detailed analysis of the twinning morphology in nanocrystalline copper grains has suggested that these twins were formed via partial dislocation emission from grain boundaries [48]. Twinning has also been found prevalent in cryogenically ball-milled Al-Mg nanocrystalline grains when the grain sizes were reduced to smaller than 10 nm [49]. In fact, twinning in nanocrystalline grains through partial dislocation emission from GBs has been predicted by molecular dynamic simulations [50-52] and has been confirmed by TEM observation of nanocrystalline Al [53, 54].

In another experiment by Rosner *et al* [55], they found abundant faulting in Pd deformed by rolling at strain rates near 0.08 s^{-1}, but no twinning. By contrast, when the strain rate was raised to 0.3 s^{-1}, abundant twinning was observed. In other words, the generation of partial dislocations is only a necessary condition to form twinning. There appears to be a barrier to twinning which is only overcome at the higher strain rate. The nature of this barrier is not understood so far. Rosner *et al* also pointed out that the twinning selects exclusively parallel planes in deformed *nc*-Pd, which implies that only one glide system is active within each grain. They suggested that grain rotation might provide the requested degree of freedom. Grain rotation allows each nano-grain to adjust its orientation in such a way that, throughout all stages of the deformation, the active glide plane remains aligned in parallel with the local shear direction.

2.4 Deformation mechanism maps

The deformation mechanism maps can be drawn in various representations depending on the grain size, temperature, and stress or strain rate. Based on recent experimental and simulation results, a tentative map was plotted by Weissmuller *et al* [56].

The map shows Coble creep at very small strain rate, followed by the combination of partial dislocation activity with grain rotation and grain boundary sliding as discussed above, including the transition from faulting to twinning. At the highest rate, the map lists the formation of twin networks as indicated by MD simulation [57]. As a result, MD works is the transition to a dominantly sliding-controlled deformation at the very smallest grain size and high strain rate, represented by the top left region of the map. It is emphasized that the regime of strain rates covered by the combined experimental and simulation studies extends over 17 orders of magnitude; in view of the few available results it appears highly likely that processes not so far identified are active in regions of the deformation map which have not yet been exploded. Another deformation mechanism map was proposed by Yamakov V. et al for nanocrystalline metals by molecular dynamics simulation [58]. Molecular dynamic simulations were used to elucidate the transition with decreasing grain size from a dislocation-based to a grain-boundary-based deformation mechanism in nanocrystalline *fcc* metals. This transition in the deformation mechanism results in a maximum yield strength at a grain size that depends strongly on the stacking-fault energy, the elastic properties of the metal and the magnitude of the applied stress. By exploring the role of the stacking-fault energy in this crossover, they demonstrated how the size of the extended dislocations nucleated from the grain boundaries affects the mechanical behavior. Based on the simulation results, a two-dimensional stress-grain size deformation-mechanism map is proposed for the *nc*-*fcc*-metals at low temperature. The map captures this transition in both the deformation

mechanism and the related mechanical behavior with decreasing grain size as well as its dependence on the stacking-fault energy, the elastic properties of the material and the applied stress level.

2.5 Current progress in molecular dynamic simulation on nc materials

Computer simulation and modeling have been applied to nanocrystalline material research since the inception of this field [59-62]. These early efforts, however, were largely influenced by Gleiter's suggestion [63] that the nanocrystalline materials are composed of single crystallites and separated by severely disordered or amorphous grain boundaries. Less attention has been paid to other microstructure properties. For example, Wolf and his colleagues investigated various properties in nanocrystalline materials. The sample used in their simulations is composed of simple geometric objects such as cubes. The grain boundaries are made of a thin layer with either amorphous structure or high-angle grain boundaries. The quadruple junctions instead of triple junctions are present. Furthermore, the grain size distribution in their approach is simply a delta function, i.e. there is only one size for all grains [63, 64].

In another work by Shimokawa *et al* [65], they used the same delta function grain size distribution to study the grain boundary structures of nanocrystalline materials with different grain sizes. The relative proportion of the grain boundary region in simulated nanocrystalline metals versus grain size d. Nanocrystalline models consisting of hexagonal grains with grain size d between 5nm and 80nm are deformed by the application of tension. A transition from grain-size hardening region to grain-size softening was reported in the region where d =30 nm, which is the optimum grain size for strength. In the grain-size hardening region, nanocrystalline models primarily deform by intra-granular deformation. Consequently, a pile-up of dislocation was observed. When the grain size becomes less than 30 nm, where the thickness of the grain boundaries cannot be neglected in comparison to the grain sizes, the dominant

deformation mechanism of nanocrystalline metals is inter-granular deformation by grain boundary sliding.

However, experimental results suggest that the grain size distributions found in various *nc* samples are not a simple delta function. Instead, lognormal function is usually found in *nc* samples. Potts model has been applied to generate digital microstructures with a lognormal size distribution. Although this method produces a realistic grain boundary structure, small vanishing grains are frequently seen due to the nature of grain growth. Another geometric model, Voronoi construction, is widely used for initial microstructure. In a large number of recent studies, Voronoi polyhedron is used to represent microstructures. As compared with the model made of cubes of the same size and shape [66, 67], this model is obviously much improved. The grains and boundaries generated from Voronoi tessellation have the visual appeals that resemble real experimentally observed microstructures. As a result, a growing number of molecular dynamics simulation works have employed this model [8, 51, 52, 67-76]. However, the quantitative microstructures of the Voronoi grains are quite different from those with lognormal grain size distributions including those obtained from Potts model. Both methods are lack of the flexibility to produce microstructures of desired topological properties. Without an improved digital microstructure sample, it is difficult to study the structure-property relationship of nanocrystalline materials systemically.

Chapter 3

Digital microstructure constructions

In order to simulate nanocrystalline materials using atomistic or continuum methods, an initial input of model structure is a pre-requisite that should have the reliability and flexibility in dealing with various microstructures. This is not an issue at all in modeling homogeneous materials such as single crystals, liquids and amorphous materials. Even for materials with limited amount of defects (vacancies, grain boundaries and free surfaces), initial structure can be easily treated [77]. Nanocrystalline materials are intrinsically inhomogeneous. Both their structures and properties have more attributes.

In this Chapter, we will make comparative study on the existing digital microstructure models and develop systematic methods to construct accurate digital microstructures as input to molecular dynamic simulations. This is a necessary step for performing meaningful numerical studies of atomic structures as well as continuum modeling of nanocrystalline materials. The microstructures include the following attributes:

1) Topological properties: grain shape, grain size, grain boundary interface area, triple junction length, bond angle, dihedral angle, number of faces per grain, number of edges per grain, number of vertices per grain, number of edges per face, etc.
2) Statistical properties: mean and variance of the topological properties, e.g. grain size or volume distribution, GB interface area distributions, etc.
3) Structural properties: detailed atomic structural information about crystallite grains, grain boundary interfaces, triple junction, etc.

3.1 Potts model

Potts model has been employed in studies of grain growth and microstructure evolution of polycrystals [78, 79]. The microstructure is mapped onto a 3D simple-cubic lattice. Each lattice site is assigned a spin number, $S_i: 1 \le S_i \le Q$, which corresponds to the orientation of the grain volume element. Grain boundary segment is defined to lie between sites of unlike orientations.

The grain boundary energy is defined in terms of lattice site energy:

$$E_i(k) = j\sum_{j=1}^{N(k)}\left(1-\delta_{S_iS_j}\right), \qquad (3.1)$$

where, S_i corresponds to the orientation of site i $(1 \le S_i \le Q)$, δ_{ab} is the Kronecker delta function, and the summation is over all sites j within the neighbor shell k of site i [80].

The kinetics of boundary motion is simulated by a Monte Carlo technique in which a site is selected at random and reoriented to a randomly chosen orientation between 1 and Q. If the change in energy ΔE is less than or equal to 0, the move is accepted. However, if the reorientation may also be accepted with a probability of $\exp(-\Delta E/kT)$, where kT is the thermal energy. For the present study, kT was effectively restricted to low temperature such that only $\Delta E \le 0$ reorientations were accepted.

Using this model, the grains can grow into equilibrium (or metastable) configuration driven naturally by interface/grain boundary energies. The experimentally observed lognormal grain size distribution can be obtained naturally. This model uses the discrete spins to represent different orientations of crystalline grains. A region with the same spin orientation is defined as a "grain". As suggested by Glazier [81], grains growth in three dimensions depends on grain topology. Using a three-dimensional Q-state Potts model simulation, they find that the average canonical growth rate of a grain

depends linearly on its number of faces and is independent of its volume, a surprisingly simple and unexplained result. Therefore, a new procedure is needed to study the topological properties of Potts model grains in details.

Despite its ability to model polycrystal grains, there has little attempt to use this approach to atomistic modeling for nanocrystalline materials. Zheng and Li [82] employed this technique to produce microstructures for nanolycrystalline materials. The grains are found to obey lognormal distribution in size. The grain cells are obtained from the regions of differently oriented spins. Once the grain cells are obtained, we fill them with atoms of specific lattice structure. The density of the sample, after relaxation using molecular dynamics, could reach 99% of that of the single crystal. Since there is no natural length scale associated with Potts spins, any desired length scale can be chosen. For atomistic modeling, lattice parameter and the mean grain size are used as the guide. However, this method lacks the flexibility to produce equilibrium, grain size distributions.

In the present study, a procedure is developed to study the topological properties of grains generated using Potts model. Firstly, the vertices representing triple junction points are identified and indexed. The grain size distribution, grain boundary length (edge) distribution, and angle distribution are then calculated using the index information obtained in the previous step. Following are the results from Potts model for two configurations with different number of lattice sites and spins.

The first configuration is a 256 by 256 lattice with 36 different spins ($Q = 36$) shown in Figure 3.1. The small red circle represents a vertex and the edges are represented using green lines connecting two adjacent vertices. Each grain is draw once based on periodic boundary condition. The grain size distribution, edge length distribution and angle distribution are also calculated and shown in Figure 3.2 and 3.3.

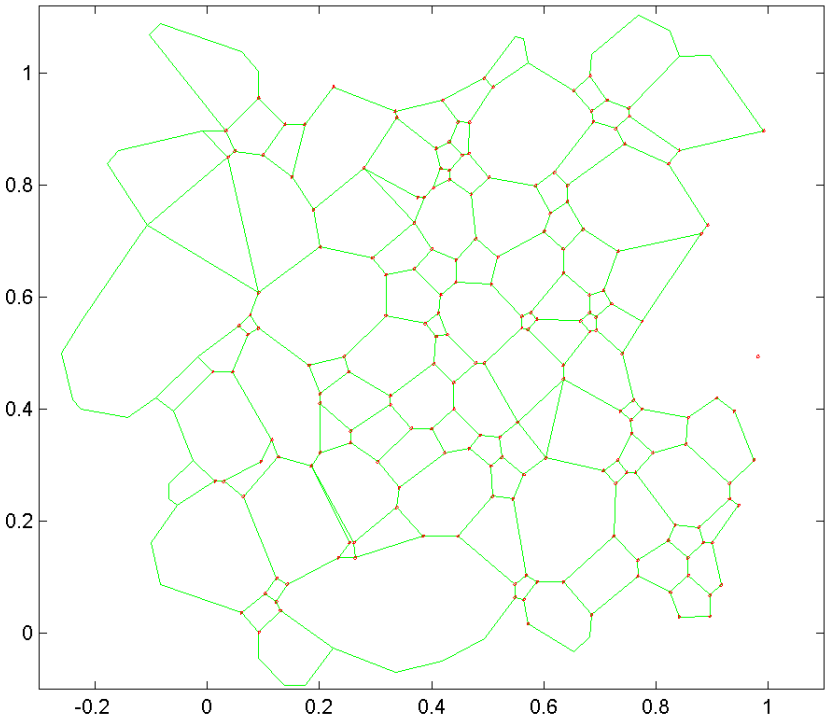

Figure 3.1.Grain structure from 256 by 256 Potts model lattice.

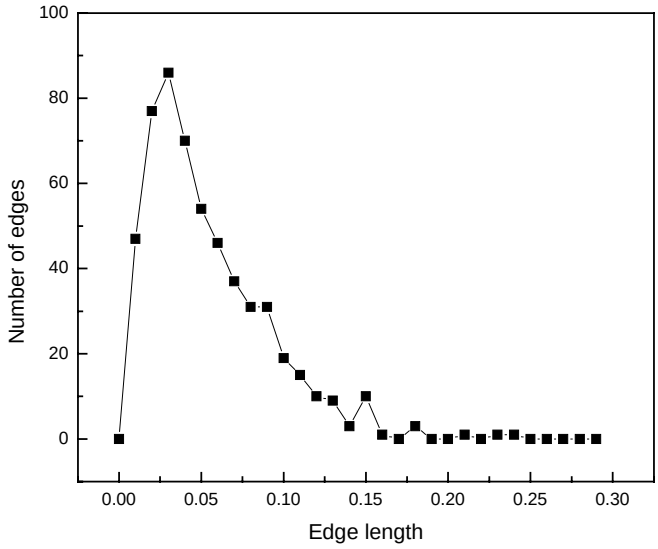

Figure 3.2. Edge length distribution of configuration 256 by256.

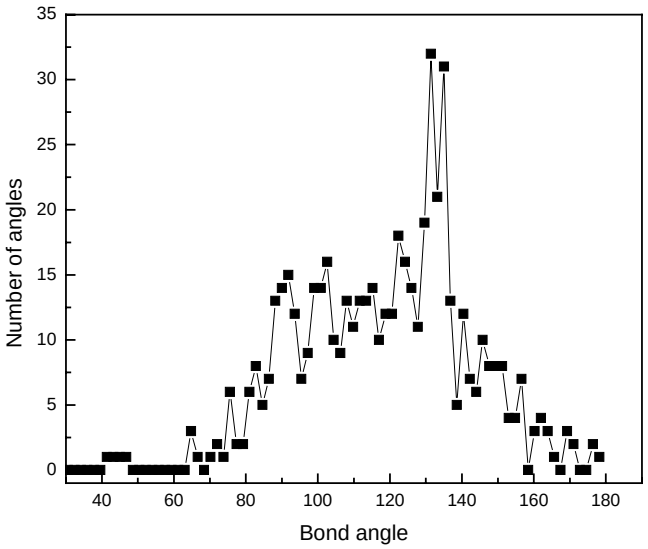

Figure 3.3. Angle distribution of configuration 256 by256.

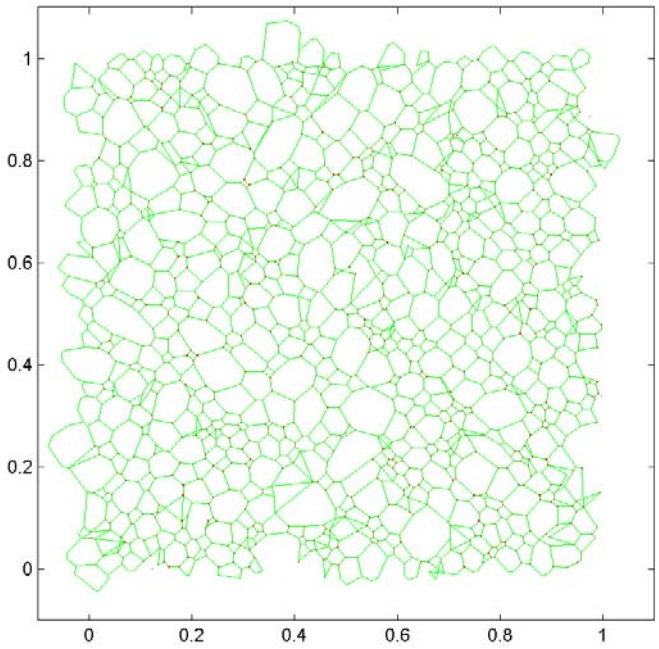

Figure 3.4. Grain structure from 512 by 512 Potts model lattice and $Q = 48$.

The second configuration is a 512 by 512 lattice with 48 different spins ($Q = 48$) shown in Figure 3.4. Distributions of grain sizes, edge lengths, angles are shown in figure 3.5, 3.6 and 3.7.

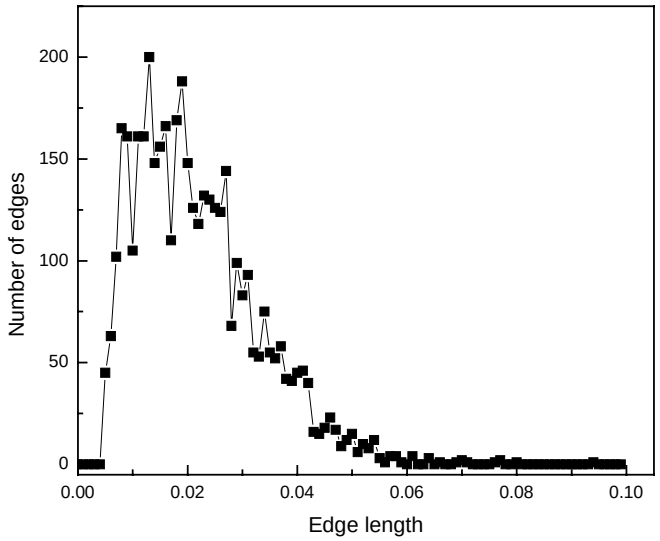

Figure 3.5. Edge length distribution of configuration 512 by 512, $Q = 48$.

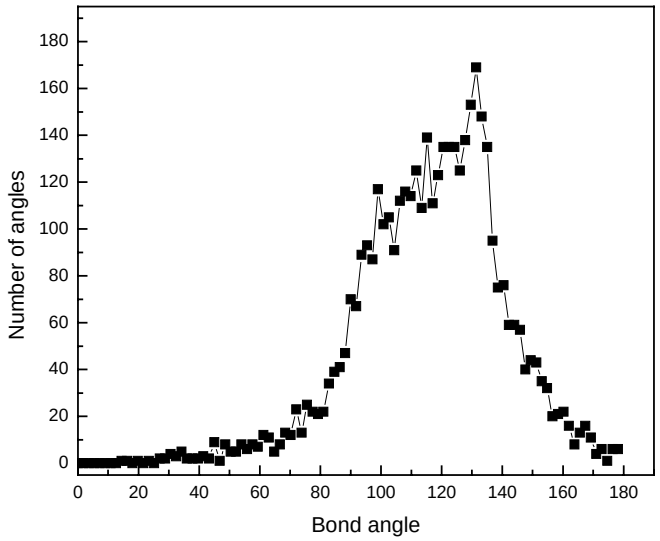

Figure 3.6. Angle distribution of configuration 512 by 512, $Q = 48$.

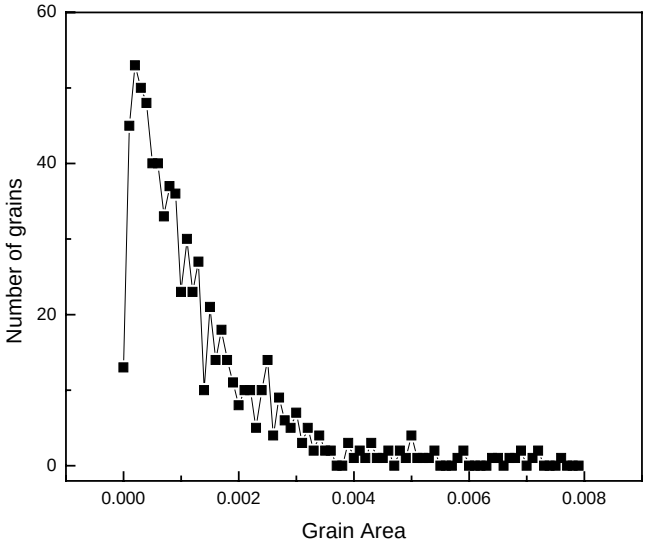

Figure 3.7. Area distribution of configuration 512 by 512, $Q = 48$.

One of the disadvantages of Potts model is the existence of vanishing grains, especially at the beginning of the simulation. It is difficult to control the number of remaining grains as well as other topological properties such as the distributions of faces area, edge length, etc. Another drawback is that it usually takes a long time to obtain a stable grain structure. Thus, we need to find another model that provides the flexibility to easily control the evolution of topological properties.

3.2 Topological and statistical properties of a constrained Voronoi tessellation

Voronoi tessellation has been used widely to approximate and model various cellular structures and stochastic patterns appearing in nature as well as grain structures in metallurgy. However, the classical Poisson Voronoi tessellation (PVT) gives a fixed cell volume distribution and does not offer the flexibility to approximate various grain structures found in experiments. In this section, we present an extended version of the Voronoi tessellation method that partitions the space with certain constraints commonly

encountered in either experimental measurements or theoretical models, such as the cell volume or size distribution, face area distribution and edge length distribution. The new tessellation method is implemented using inverse Monte Carlo method. We calculate the topological and statistical properties of the tessellated Voronoi cells in several model systems with the cell volumes obeying lognormal and bimodal distributions; we also compare the results with those obtained by using the conventional Poisson-Voronoi method. We observed systematic changes in the topological properties as well as deviations from some established topological relations as we vary the parameters in the constraint. The application of this constrained Voronoi method in microstructure modeling and characterization in poly- and nano-crystalline materials is also discussed.

This chapter is organized as follows. In section 3.2.1, we give a brief introduction of Voronoi tessellation and define the primitive geometric entities identified in a typical Voronoi cell. In section 3.2.2, we present the algorithms and methods for the CVT with a particular attention paid to the inverse Monte Carlo method. In section 3.2.3, we present the results of the topological properties and their statistical properties. We shall organize our results according to the input cell volume distributions used. In section 3.2.4, we discuss the results and some new findings and clarify some discrepancies in light of the results from this work; we also discuss briefly the potential applications of this method in modeling of the properties in nanocrystalline materials. Finally, we draw conclusions and comments from the results.

3.2.1 Background

Voronoi tessellation (VT) is a geometric method that partitions a space of dimension d into space-filling, convex polyhedron, or cells [83]. The polyhedron are constructed by first placing N random points in the space and then partitioning the space into N numbers of polyhedron formed by the planes bisecting the bonds connecting each

point and its nearest neighbors. The bisecting planes of the nearest neighbor bonds of each point intercept to form the so-called Poisson-Voronoi (PV) polyhedron with edges (e), vertices ($vert$), face areas (s), and cell volume (v), which give rise to the unique geometric properties for the polyhedron (Figure 3.8).

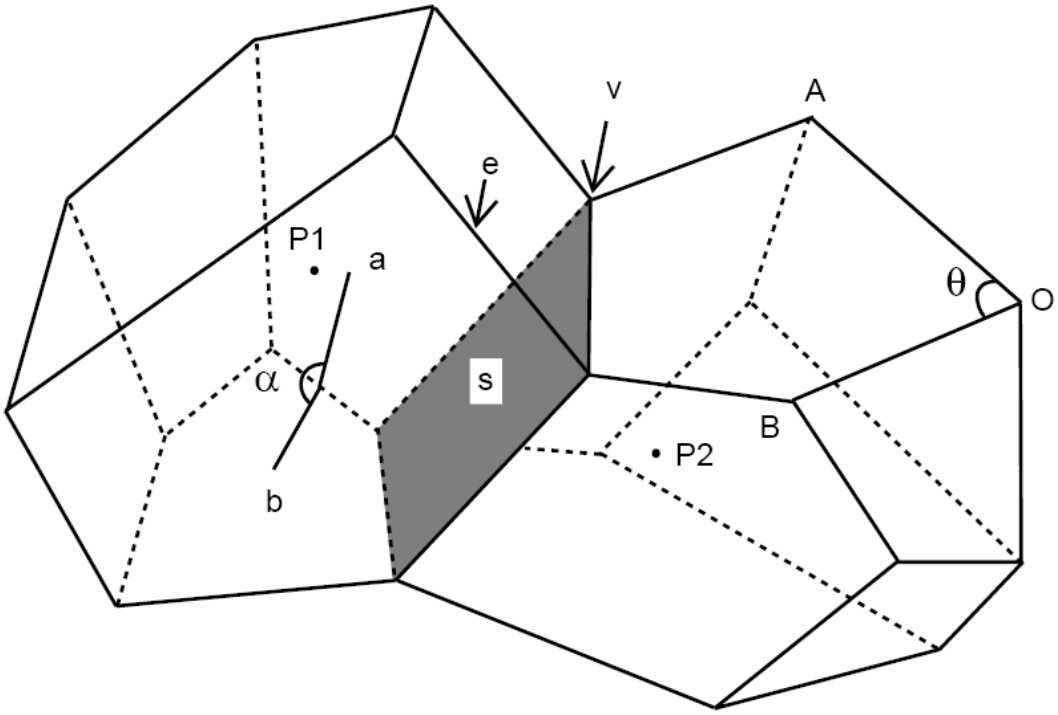

Figure 3.8. The schematics of two neighboring Voronoi cells at the two points P_1 and P_2. The shaded area of the interface between the two cells is labeled as s, the edge as e, the vertex as v, the bond angle as θ, and the dihedral angle as α.

The collection of polyhedron forms a statistical ensemble with a range of the geometric properties described by their statistical distributions. The connectivity of these geometric entities forms the topological properties of the Voronoi cells. This simple geometric construction has found many applications in the past hundred years in a wide range of fields [84], including biology [85], astrophysics [86], botany [87], zoology [88], metallurgy or crystallography [89], forestry [90], and numerical methods [91] and communication networks [92]. An example of the direct connections between the Voronoi cells and physical objects is the crystal grains in polycrystalline materials

formed through nucleation and growth [93]. As demonstrated by Meijering, when crystal nucleation starts from N numbers of randomly placed seeds which grow subsequently with the same growth rate until impinging on each other, the grains formed can be described by the Meijering's crystals, or Voronoi cells. In general, the PV cells follow specific statistical distributions in their geometric properties with certain means and variances (see Table 3.1). For example, the Voronoi cell volume distribution, although still not known yet analytically, is found through numerical fitting to follow a Gamma, or lognormal distribution with the mean at unity and variance of 0.424 [94].

Owing to the resemblance, in the geometric and statistical *appearance*, to many of the cellular structures and stochastic patterns appearing in nature, Voronoi tessellation has been widely used to represent or approximate them [83-89]. In computational physics and materials science, the PV cells are used routinely for simulations of polycrystalline and cellular structures [9, 82, 95]. However, in many cases obvious deviations are found in both topological and statistical properties. For example, the mean number of faces per grain in many polycrystalline materials is found less than 15.535 as predicted in Voronoi tessellations [96]; the variance of the grain volumes is not a constant but spans a wide range [97]. The grain volume distribution follows either lognormal or Gamma distributions with varying means and variances [98]; and often much complex grain size distributions such as bimodal or multi-modal are observed which have little resemblance to that of Poisson-Voronoi cells [99]. These discrepancies or departure from those in the PV tessellated patterns inevitably lead us to the following questions: First, are there changes for other geometric and statistical properties, such as the cell volumes, edges, vertices, and face areas in the systems that do not resemble Voronoi tessellation? As known, the geometric properties such as the cell volume, the cell areas, and cell edges are intimately connected. The change in one of the geometric entities, such as the cell volume, would certainly lead to changes in the other properties. So far, however, the quantitative measurement of the changes remains largely unknown. Second, to what

extent do these changes lead to the change in physical properties in the cellular structures? The Poisson-Voronoi tessellation is used widely to date to not only mimic the cellular patterns in nature but also represent the so-called microstructures from which various physical properties are derived [100, 101]. However, often it is the default version of the PV method that is used to generate the microstructures. Therefore, having a reliable and flexible method to produce as well as to reproduce correct space tessellation in order to obtain accurate microstructure-property relations in such properties as diffusion, mechanical strength, and diffraction patterns becomes highly relevant in materials science and physics [101].

To date, however, these questions have not been given sufficient attentions although tremendous efforts have been made in the past to analyze and characterize the VT cells[83-93] and some *ad hoc* modifications were made to the VT method to explain the different cellular patterns observed in experiments. One is the Johnson-Mehl method, which was developed to mimic the asynchronous nucleation process. Others used weighted VT method or Laguerre-weighted VT method where finite size spheres or disks are used to replace the points. Clearly, a systematic and quantitative investigation of these questions should be performed in order to extend the VT method to a more general setting.

In the next section, we present an extended version of the Voronoi tessellation method to address the first question. To be specific, we shall focus exclusively on the point Poisson-Voronoi process, which is different from the so-called Laguerre-Voronoi process where instead of points, spheres of certain finite size are used to generate the PV cells. The chief difference between this constrained Voronoi tessellation (CVT) and the conventional Poisson-Voronoi tessellation (PVT) method is that the former is subject to certain constraints. The constraints are various statistical distribution functions for the

geometric properties. These properties are normally the output from experimental measurements, or other theoretical or numerical models. In this work, however, we use them as input for the CVT. Since the most commonly accessible microstructure property is the cell or grain volume/size distribution, we shall use it as our first input or constraint. The constrained Voronoi tessellation is conducted in conjunction with an inverse Monte Carlo method. To test the versatility of the method, we use different cell volume distributions, lognormal, and bimodal in particular, which are commonly seen from various patterns in nature and offer enough complexity to challenge the new method.

Armed with this new method, we can compute the topological properties for each case systematically as we vary the parameters in the constraints. The properties include

(1) the mean values and distributions for cell volume, face area, edge length, and vertices;

(2) the number of faces, edges, and vertices per cell and their sample means;

(3) the Aboav-Weaire law and Lewis's rule that connect the neighboring cell information on volumes and the number of faces.

To make a comparison, we also computed the geometric and statistical properties of the system tessellated with the PVT method using the Poisson random point process, which is known to have a fixed cell volume distribution. The second system used for comparison is the system with a delta-function cell volume distribution. These models together provide a systematic case study for the topological properties. We found systematic changes in the topological and their statistical properties as we vary the parameters in the cell volume distributions. Moreover, we observed deviations in one of the well-established topological laws in cellular patterns, i.e., Lewis's rule, and their systematic variations with the cell volume parameters.

These changes in topological properties are expected to lead to changes in the physical properties. Since one of the important applications of the Voronoi construction is to modeling polycrystalline or cellular structures, in order to predict physical properties reliably, an accurate method to represent the microstructures such as the CVT is necessary. This new method is a first step toward a systematic approach for quantifiable representation of the microstructures. We shall present our results in modeling of nanoscale polycrystalline materials in a separate publication.

3.2.2 Methods

3.2.2.1 Poisson-Voronoi tessellation

As mentioned in the introduction, in this work we shall focus on *point* Poisson-Voronoi method only, The Voronoi tessellation in the three-dimensional dimensional Euclidean space consists of two steps: (1) Distributing N numbers of points according to Poisson point process in the space, $x \in R^3$; $P = \{p_1, p_2, ..., p_N\}$ is the set of the points; and (2) for each point p_i, finding the closest neighboring points p_j ($j \neq i$), such that the Voronoi region $V(p_i)$ partitioned to p_i is defined by

$$V(p_i) = \{x : |p_i - x| \leq |p_j - x| \forall j \neq i\}. \qquad (3.2)$$

The polyhedron, or Voronoi cells formed, are convex and space-filling. Each of the Voronoi cells, $V(p_i)$, possesses a set of specific geometric attributes (Figure 3.8: edges (e_i), vertices ($vert_i$), face areas (s_i), and cell volume (v_i). Statistical properties of these geometric attributes can be obtained for the collection of all Voronoi cells, including the distribution functions, means and standard deviation (or variances), or higher moments, which provide a complete description of the topological properties of the Voronoi tessellations.

3.2.2.2 Constrained Voronoi tessellation

As known, the Poisson-Voronoi tessellation gives a specific set of topological properties. But it was realized long time ago that in nature many cellular patterns and structures show different set of properties that can not be described by the properties from straightforward application of the PVT method [94]. To overcome this difficulty, a number of attempts have been made. One of the attempts is the weighted VT in which either a finite size or exclusive radius is assigned to p_i, which leads to the so-called Laguerre-Voronoi tessellation (LVT) [102]. Another example is to let the random point process not be contemporaneous, such as in the actual nucleation and growth process of many materials, which leads to the Johnson-Mehl (JM) model [103]. In the following, we present a general model that utilizes the constraints from either experiments or theoretical models known *posterior*. As will become clear, this new method bears the spirit of the Johnson-Mehl model, but with the flexibility and generality beyond those of the JM model, or other modified PV methods.

One of such constraints used is the cell volume, or its equivalent diameter distribution, $P(v)$. The cell volume, or area in two dimensions, is among the easiest to measure experimentally and therefore widely used to rationalize material properties [104]. For example, in crystallography, the grain sizes are shown often to follow lognormal distribution. In many occasions, other types of distributions, such as bimodal and multi-modal, are also found. Clearly, the PVT method and the weighted VT methods do not provide the flexibility to produce the microstructures with these cell volume distributions. However, by including these distributions and through a series of optimization process, we expect to obtain the Voronoi cells that are closer to the real systems in their topological properties and other statistical properties. (Certainly, we will first obtain the desired cell volume distribution.) A key step in this approach is to use the inverse Monte Carlo (IMC) approach proposed earlier by Gross and Li [15] which was

proposed to generate digital microstructures with desired topological properties. Inverse Monte Carlo (IMC) method is a general method for optimization under certain constraints, such as $P(v)$. It has been widely used in atomic structure modeling based on experimental data from x-ray, neutron, and electron diffractions [105].

Let the cell volume distribution function be $P_{input}(v)$, which is supposedly known already. There are two different ways to represent the cell volume. One is to use the cell volume v directly, and the other is the equivalent sphere diameter d of the volume $v = 4\pi/3(d/2)^3$. The later can be determined directly using stereological methods [106] and has been used widely in materials science and biology. We shall use the cell volume here while the diameter can be employed easily also through a straightforward transformation between the two [107]. Therefore, the CVT method and the results should remain the same if we chose to use the equivalent cell diameter. We formulate the algorithm to include the constraint $P_{input}(v)$ in our CVT method by using inverse Monte Carlo method as follows:

(a) Take N numbers of points and distribute them randomly in a space of volume V;

(b) Construct Voronoi polyhedron cells around each of the points and compute the cell sizes or volumes v_i, or the equivalent diameters d_i of these polyhedron cells;

(c) Compute the cell volume distribution function $P(v)$ from the Voronoi cells and the penalty function,

$$\chi^2 = \sum_k^M w_k [P_{input}(v_k) - P(v_k)]^2 , \qquad (3.3)$$

where the input distribution function $P_{input}(v_k)$ can be taken from experiments, or theoretical models; k here stands for the k_{th} bin of the discritized cell volume in the distribution functions; w_k is the weight imposed onto the bins to accelerate

the convergence, or to take into consideration the uncertainties in the input data; and M is the total number of the bins used in the distribution functions.

(d) Move the center of a randomly chosen point with a small random displacement; then calculate the new penalty function, χ';

(e) If $\chi' \leq \chi$, keep the move; if χ' is larger, but $e^{-\Delta\chi/\alpha} \geq \rho$, where ρ is a random number and α is another parameter used in controlling the acceptance rate in the Monte Carlo run, keep the move; Otherwise do not move the grain center.

The entire process repeats many times until the system reaches a steady state, or χ approaches a preset number, say, $\chi_{final} = 10^{-3}$.

The CVT method described above consists of two parts, the conventional VT method to compute the Voronoi cells, or polyhedra and their geometric properties, and the inverse Monte Carlo method. The VT part is straightforward to implement. The inverse Monte Carlo part is a randomized optimization process dictated by χ, the goodness of fit between the constraint, or input cell volume distribution function $P_{input}(v)$ and the instantaneous or transient cell volume distribution function, $P(v)$. As a general approach, we can also include other constraints in Eqn. 3.2, such as the cell surface area or cell perimeter distribution if they are known. Since the random point process performed in the IMC part remains uniform, the displacements made for the points during the optimization process is homogeneous and local; no clustering or some correlations occur for the points and subsequently in the topological properties. This may exclude some interesting cases with inhomogeneous distributions of the cells. (Operationally, however, we could also include the correlations by using the IMC method, if they are known.) We should mention that in the IMC part one can also move the vertices simultaneously, which can improve the efficiency if the face area or edge length

distributions are used. (It is not the case if $P_{input}(v)$ is used only, due to the duality between the points and the vertices.)

Note that the purpose of the modification made to the Voronoi cells using the CVT is to make the cells confirm to the constraint cell distribution by moving the locations of the points, p_i. For a lognormal cell volume distribution, this leads to the results similar to those in the Johnson-Mehl model. However, as shown below, we can treat much complicated cases using the CVT.

3.2.3 Results: P(V)

Our motivation for the development of the CVT is to improve the VT to make it more flexible as a computational geometry method such that the complex geometric and statistical properties produced are quantitatively more close to those found in nature or experiments. For these properties used as the constraint, such as the cell volume, the best optimization is achieved of course. Other topological properties that are not part of the input or constraint, less confidence should be expected. Nevertheless, we will see systematic changes in these properties as we vary the cell volume. In the following, we shall present the results of the topological and statistical properties from the CVT. To test its versatility, we used several different cell volume distribution functions, including lognormal, bimodal, normal and gamma distributions as the target functions.

The properties calculated include (1) the geometric attributes of *each cell*: vertices, edges, areas, and volumes, (2) statistical properties of the *collection of cells* in the sample: the distributions of the number of vertices, edge length, cell areas, cell volumes, and their moments, and (3) topological properties of *neighboring cells*: the Aboav-Weaire law and Lewis's rule. In this section, we will focus on the results from CVT by applying constrains on cell volume distribution. In section 3.2.4, we will focus on the results by applying constrains on face area and edge length distribution.

3.2.3.1 Poisson-Voronoi distribution and delta-function distribution

Two special cases are considered first as our base models so comparison can be made with the results from the CVT method. The first is the random PVT cells generated using the Poisson-Voronoi method by placing 5,000 points randomly in the unit volume. To get better statistics, 200 random configurations were generated and the data were collected for analysis. The PVT cell distribution is shown in Figure 3.9.

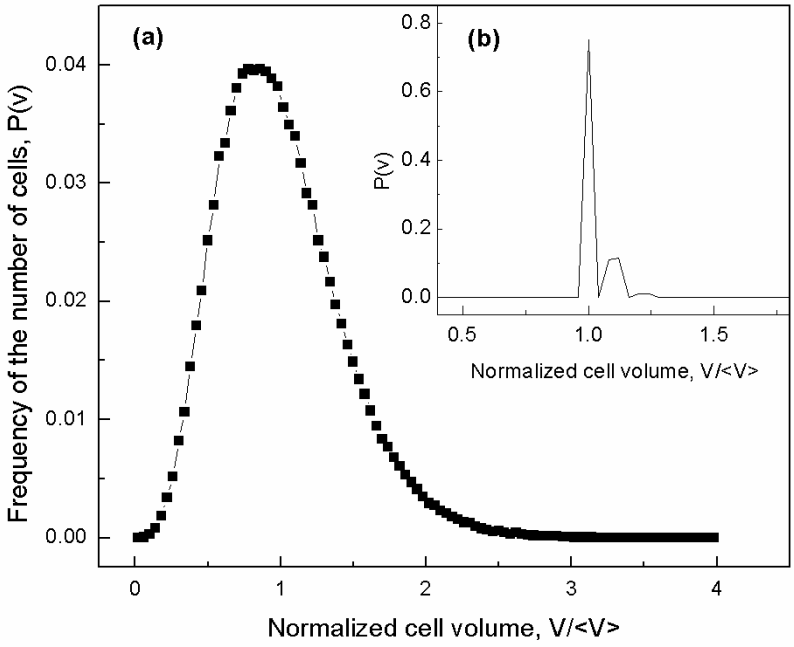

Figure 3.9. The PVT and fcc cell volume/grain size distributions $P(v)$ normalized by the mean volume $\langle \mathrm{V} \rangle$, $\mathrm{v} = \mathrm{V}/\langle \mathrm{V} \rangle$. (a) The random Poisson-Voronoi volume distribution marked by the filled squares in black; the solid line is the numerical fitting from the data, and (b) that of a randomly displaced fcc lattice shown in the inset.

Contrast to the complete random points used in the PV tessellation, we also used a system with a delta-function cell volume distribution, which has complete "ordered" points [108]. We used 5,324 points assigned on to the face-centered-cubic (fcc) lattice

sites; we then displace the points randomly by a small distance to avoid degeneracy. Same as in the Poisson Voronoi case, we also generated 200 configurations for this model. We used this special model for two purposes: (1) as an initial configuration for generating the VT cells using the CVT method, and (2) also as a special case with a set of geometric properties that we can compare with those from PVT and CVT space tessellations where random point distributions are used. The cell volume distribution of the ordered lattice points forms almost a delta-function cell volume distribution. The maximum frequency of the PVT is about 0.04, but that of perturbed *fcc* lattice is about 0.75. As known, the majority of the cells are dodecahedron cells that are much regular than those generated from the PV process [108]. In contrast, the complete random PVT gives the well-known PV distribution in the cell size distribution with specific mean at unity and the standard deviation of 0.4454 fitting with lognormal distribution. (For comparison, we also fit the volume distribution of the PV cells using a 2-parameter Gamma distribution with $\alpha = 5.42556,\ \beta = 0.18528$ and variance of 0.429.)

3.2.3.2 Lognormal distributions

Many of the cellular structures and stochastic structures appeared in nature have cell volume distributions different from that of the PVT. For example, many of the cell size observed in biology [85] and the grain size found in metallurgy and materials science follow lognormal distributions (or Gamma) [104, 109, 110] which can be described as

$$f(x) = \frac{1}{x\sigma\sqrt{2\pi}} \exp\left[-\frac{(\ln(x) - \mu)^2}{2\sigma^2} \right], \qquad (3.4)$$

where x stands for cell/grain volume; σ and μ are the standard deviation and (log) mean of $\ln x$ respectively. The standard deviation of the cell/grain volume, σ, spans from 0.1 to 0.445, whereas it is approximately a constant in the VT cells (i.e., it depends slightly on the sample size used [99]). As noted by many [46, 109, 111], the means and variances

in the cell volume, plus other geometric attributes such as the cell shape, constitute the co-called statistical properties of the microstructures in materials science or metallurgy that have direct influence on the mechanical and transport properties. Despite these differences, the PVT method is still widely used in characterization and modeling of microstructures [95].

In the CVT we shall use the cell/grain volume distribution as an input, or constraint in obtaining the VT cells. Since the cell volume distribution is the attribute commonly seen in nature and easier to measure, we began our first case study with it. Specifically, we shall use Eqn. 3.4 as the input constraint, or target cell volume distributions $P_{input}(v)$ in Equation (3.3). As we use the normalized cell volume in the distribution with the mean at unity, we chose to have different standard deviations to represent different distributions. Figure 3.10 shows four lognormal cell volume distributions with σ ranging from 0.15 to 0.4 (solid lines). Each target cell volume distribution is then discretized with an internal of 0.04. To avoid unphysical results or large cell volume dispersity, we chose a cut-off of normalized cell volume at 3.0. For the initial configuration, we use either the randomly distributed points as in the Poisson-Voronoi process or the ordered *fcc* configuration with a delta-function cell size distribution. Then we optimize the initial configurations through the IMC algorithm presented in section 3.2.2.2 to obtain the desired cell volume distribution. For lognormal case, it is straightforward to implement the algorithm and easy to reach the desired convergence using the CVT. We used $\alpha = 0.001$ to achieve 50% acceptance rate in the Monte Carlo runs and $w = 1/N$ for the weights.

Figure 3.10 shows the results for the cell volume/size distribution obtained using the CVT method for the four target cell volume distributions with the standard deviations at 0.15, 0.2, 0.3 and 0.4 respectively. The cell volume distribution of the random PVT cells with 5,000 points/grains is also shown, which is best fitted by a lognormal

distribution with $\sigma =$ 0.4454 and $\mu =$ -0.03916. As shown in the following, the PVT cells and their topological and statistical properties are very close to the CVT cells with the lognormal cell volume distribution with $\sigma > 0.4$.

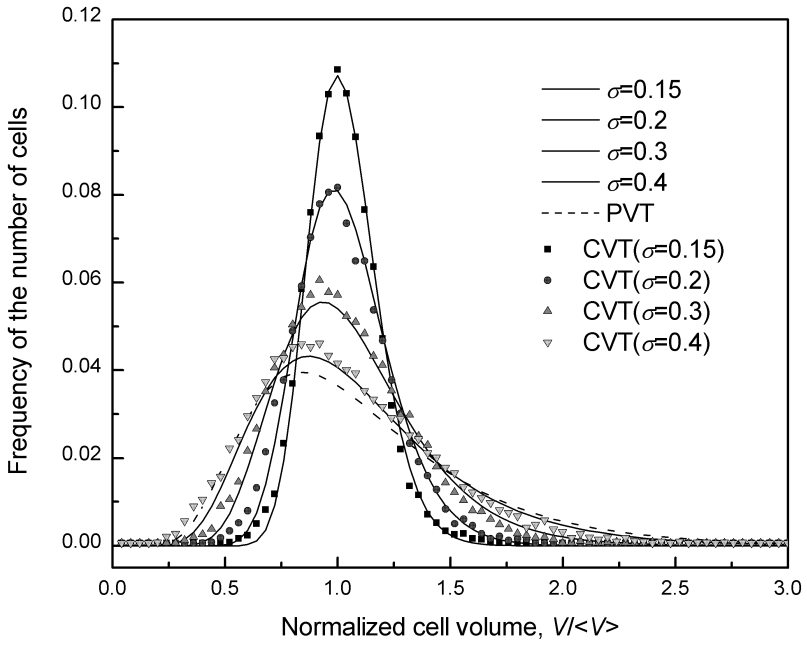

Figure 3.10. The cell volume distributions $P(v)$ obtained using the CVT method: four target cell volume distributions with the standard deviation of 0.15, 0.2, 0.3 and 0.4 are presented by solid lines. The cell volume distribution of a PVT is also shown as the dashed line. The corresponding CVT results are plotted as scatted datum points using the same gray-scale as the target function.

Once we obtain the CVT cells with the specific cell volume distributions, we can compute other geometric properties, such as the edge or triple junction length, (l), face area or grain boundary area, (s), and bond angle, (θ), and dihedral angle, (α). We can also calculate the cell perimeter (L) (the total length of the edges of each cell), cell face area (S) for each cell, the number of faces (F) and the number of edges per cell (E), etc (see Figure 3.1 for detailed definition of these quantities). Figure 3.11(a) shows the cell

surface area (S) distribution for the four samples. The cell surface area distribution for the Poisson-Voronoi cells is also shown in this figure as a comparison. Figure 3.11(b) shows the cell perimeter (L) distributions for the same four samples. We noticed that as the cell surface area and the cell perimeter distributions are far less skewed as compared with that of the cell volume distribution; and as the standard deviations of cell volume distributions increases, the standard deviations of the cell surface area and the cell perimeter distributions also increase, almost in a linear fashion. The relations among the standard deviations for the faces and the cell volumes appear to be linear.

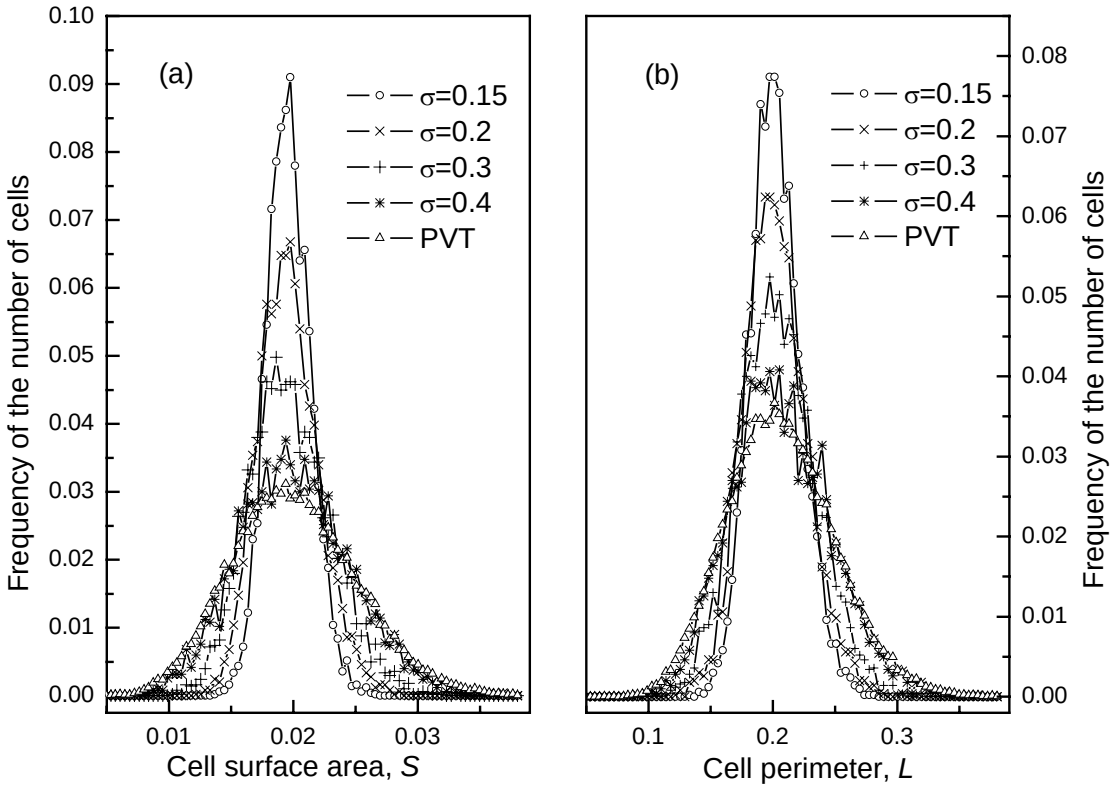

Figure 3.11. (a) The distributions of the cell surface area $P(S)$ for the four lognormal samples with the standard deviation at 0.15, 0.2, 0.3 and 0.4 respectively. (b) The distributions $P(L)$ of the cell perimeter for the four lognormal samples with the standard deviation at 0.15, 0.2, 0.3 and 0.4 respectively. Both $P(S)$ and $P(L)$ distributions of PVT are plotted as references.

Figure 3.12 show the face area (s) distribution and the edge length (l) distribution of all faces and edges in the entire sample (with no distinction made for which cell they belong to). The most noticeable features are (1) the distributions show a systematic shift with the standard deviation of the cell volumes. We noticed that for the face area distribution (Figure 3.12(a)), there exists two crossover points. The first point is located around 0.001 and the second point is located around 0.0034; (2) there are more small face areas for VT cells of the samples with large σ in the lognormal case (Figure 3.12(b)). These are two key findings that we will come back to explain in detail. The same trend seen in the face area distribution is also shown in the edge length distribution. Namely, there are more short edges as σ increases (Figure 3.12(c)). In addition, the number of the edge lengths begins to decrease with σ in the region with small length (<0.175) when σ is less than 0.4. A crossover point for the edge length distributions is observed at the edge length around 0.2. The second crossover is observed at the edge length around 0.055.

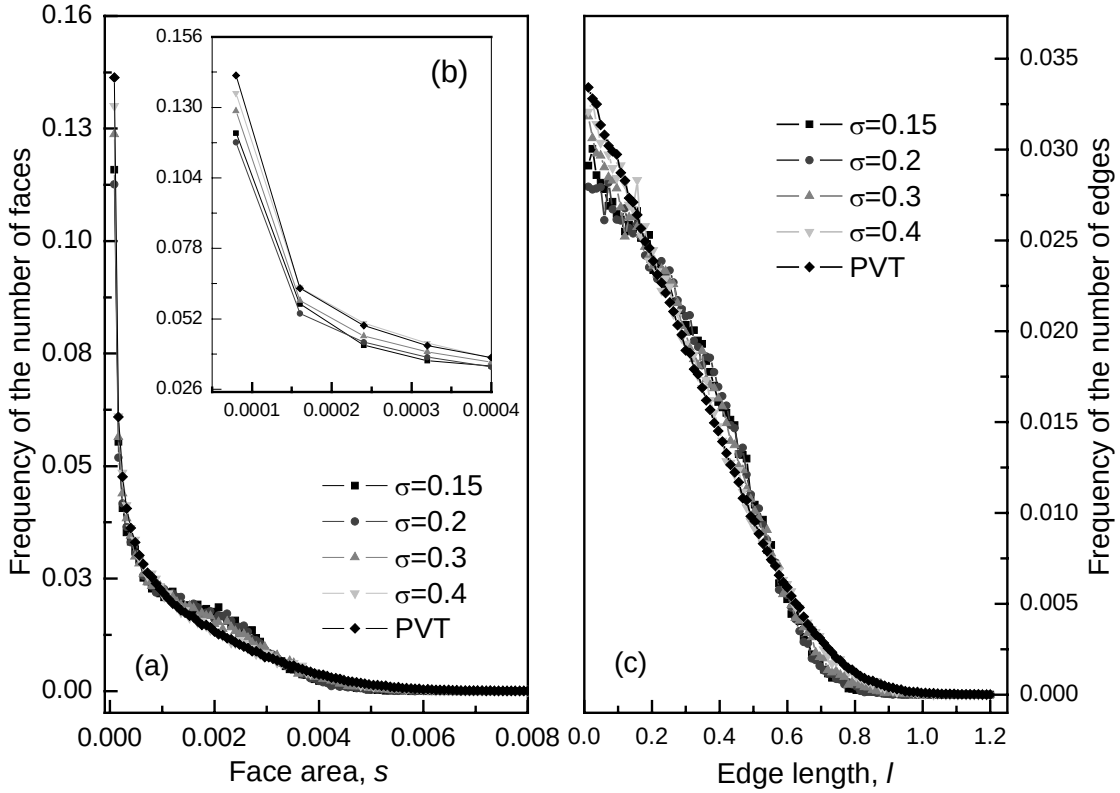

Figure 3.12. (a) The face area distribution, $P(s)$, of the four lognormal samples with the standard deviation of 0.15, 0.2, 0.3, and 0.4 respectively. (b) The face area distributions at small face areas; (c) The edge length distribution, $P(l)$, of four lognormal samples with the crossover point around 0.2.

Figure 3.13 shows the bond angle (θ) distribution and the dihedral angle (α) distribution for the four lognormal samples. As shown in Figure 3.8, the bond angle is defined as the angle between two neighboring edges (denoted as OA and OB) emerging from the same vertex (O). The dihedron angle is defined as the angle between two planes (denoted as a and b) intersecting at the same edge. Both bond angle and dihedral angle distributions show systematic narrowing as the standard deviation of the cell volume σ becomes small. Once again, we see that there are more small and large angles present when σ becomes larger. As a result, the mean bond angle increases with increasing σ.

They are 109.6637, 111.8237, 111.9275, and 112.0213; and the mean dihedral angles are 120.5218, 120.5041, 120.4277, and 120.3123 for σ =0.15, 0.20, 0.30, 0.40, respectively. As a comparison, the bond angle and dihedral angles are 112.05 and 120.2730 for the PVT cells, which are often interpreted based on the argument of the grain growth driven by the interfacial (or capillary) energy [112].

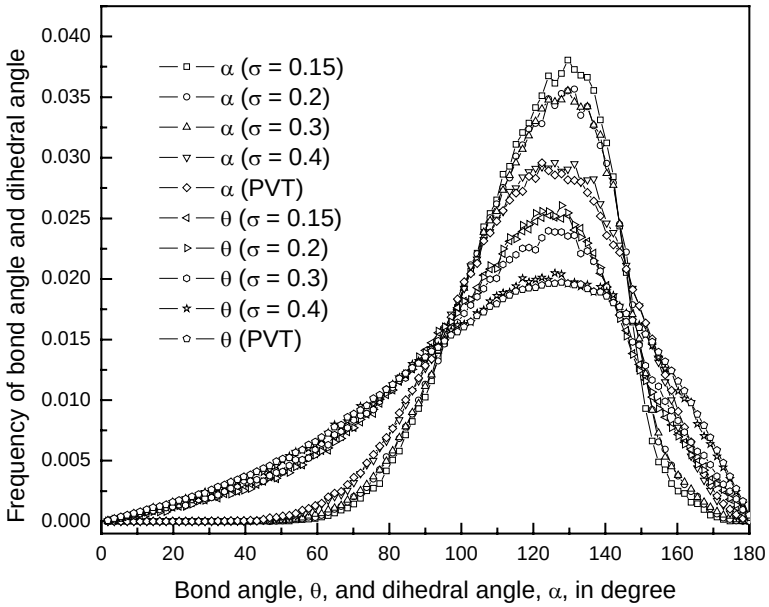

Figure 3.13. The bond angle distributions, $P(\theta)$, and the dihedral angle distribution, $P(\alpha)$, of the four lognormal samples with the standard deviation of 0.15, 0.2, 0.3, and 0.4 respectively. The bond angle distribution for the PV cells is also shown as a reference.

In Figure 3.14, we give the calculated distributions for the number of faces per cell, F_C, and the number of edges per face, E_F, of the four samples obtained using CVT method. The number of vertices per cell, V_C, can be obtained by using the relation, $V_C = 2F_C - 4$ for each cell. From Figure 3.14, we found the same systematic narrowing in the distributions of the number of faces per cell and the number of edges per face as the standard deviation of cell volume becomes smaller while the change in the edge

number distribution remains relatively small (Figure 3.14(b)). The distribution of the number of faces is also less skewed than that of the cell volumes (Figure 3.10). This finding is key to the explanations of many geometric properties.

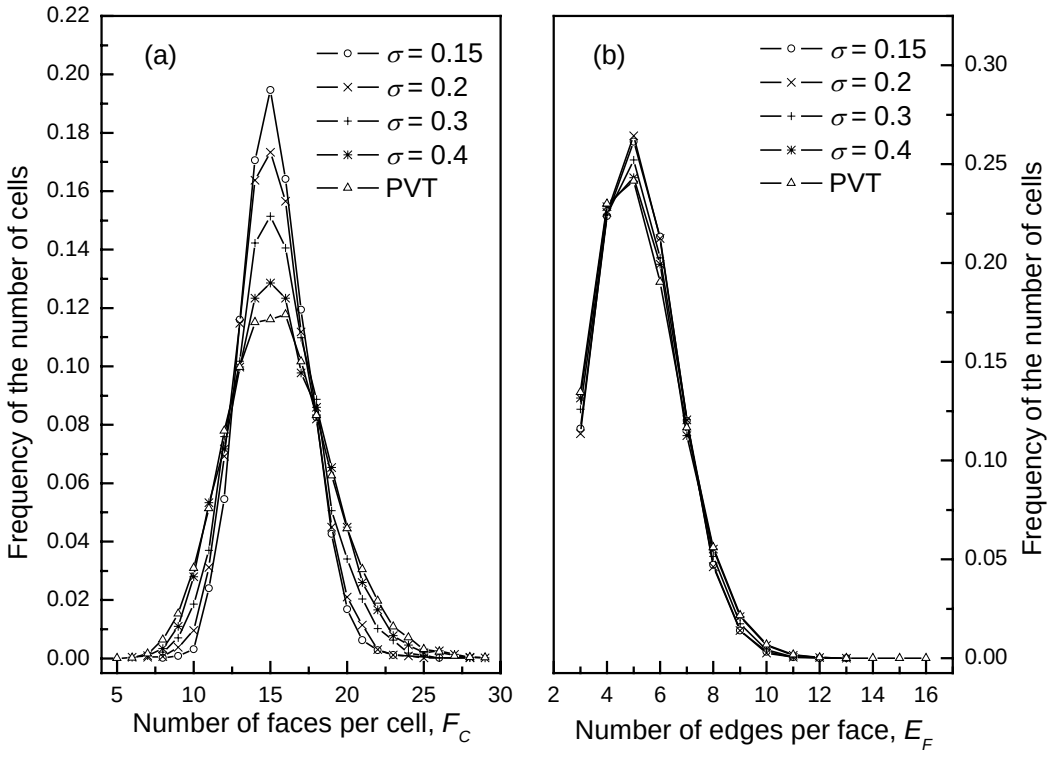

Figure 3.14. a) The number of faces per cell/grain distributions, $P(F_C)$, of the four lognormal samples. The number of the faces for the PV cells is also shown. Note that the smallest number of the faces is 4, or a tetrahedron. b) The number of edges per face distributions, $P(E_F)$, of the four lognormal samples. The number of the edges for the PV cells is also shown. Note that the smallest number of the edges is 3, or a triangle.

Table 3.1 summarizes the results for the mean number of faces per cell, $\langle F \rangle$, the mean number of edges per cell, $\langle E \rangle$, and the mean number of vertices per cell, $\langle V_C \rangle$. We also include in the table the mean number of the edges per face, $\langle E_F \rangle$, the mean dihedron angles, $\langle \theta \rangle$, and the mean bond angle, $\langle \alpha \rangle$. We see that all these quantities decrease with

the decrease in σ. The geometric properties of the random PVT cells with $\sigma = 0.445$ are found to follow Meijering's [93] estimates very well.

Table 3.1. The mean numbers of faces ($\langle F \rangle$), edges ($\langle E \rangle$), and vertices ($\langle V_C \rangle$) per cell, and the mean bond angle ($\langle \theta \rangle$) and mean dihedron angle ($\langle \alpha \rangle$). $\langle E_F \rangle$ is the mean number of edges per face. σ is the standard deviation in the cell volume distribution for samples with lognormal distribution with the mean at unity. Bimodal cases are labeled based on the separation between the two means: Bimodal 1, 2, and 3 are for v_b=1.2, 1.3 and 1.4, respectively. We also include the results from the PVT, Meijering's analytical estimates [93], and Potts model simulation [79]. The Euler's relation $\langle \mathrm{V_C} \rangle - \langle \mathrm{E} \rangle + \langle \mathrm{F} \rangle = 2$ and the relation $\langle \mathrm{V_C} \rangle = 2\langle \mathrm{F} \rangle - 4$ are obeyed within statistical error.

σ	$\langle E \rangle$	$\langle F \rangle$	$\langle V_C \rangle$	$\langle E_F \rangle$	$\langle \theta \rangle$	$\langle \alpha \rangle$
fcc	36.1003	14.0332	24.0684	5.1449	109.081	—
0.15	39.8676	15.2892	26.578	5.2151	109.6637	120.5218
0.2	40.1940	15.398	26.796	5.22068	111.8237	120.5041
0.3	40.2036	15.4012	26.8024	5.22084	111.9275	120.4277
0.4	40.5588	15.5196	27.039	5.22675	112.0213	120.3123
PVT	40.6046	15.5299	27.0544	5.22918	112.05	120.2730
Meijering[a]	40.61	15.54	27.07	—	—	—
Potts Model[b]	40.606	15.535	27.071	5.228	—	—
Bimodal 1	40.602	15.534	27.068	5.2275	111.13344	120.4258
Bimodal 2	40.41	15.47	26.94	5.2243	111.09132	120.4177
Bimodal 3	40.482	15.494	26.988	5.2255	111.10716	120.4170

[a]Reference: [93]
[b]Reference: [79]

Other topological properties can also be obtained for the cells generated using CVT methods. The relationship between the average cell volume $\langle V \rangle_F$ of a polyhedron cell with F faces and the number of faces F in that cell, or its neighbor cell number is specified by the so-called Lewis's rule [113],

$$\langle V \rangle_F = a_L (F - F_0), \tag{3.4a}$$

in a linear fashion, where F_0 is a constant and a_L is the Lewis coefficient.

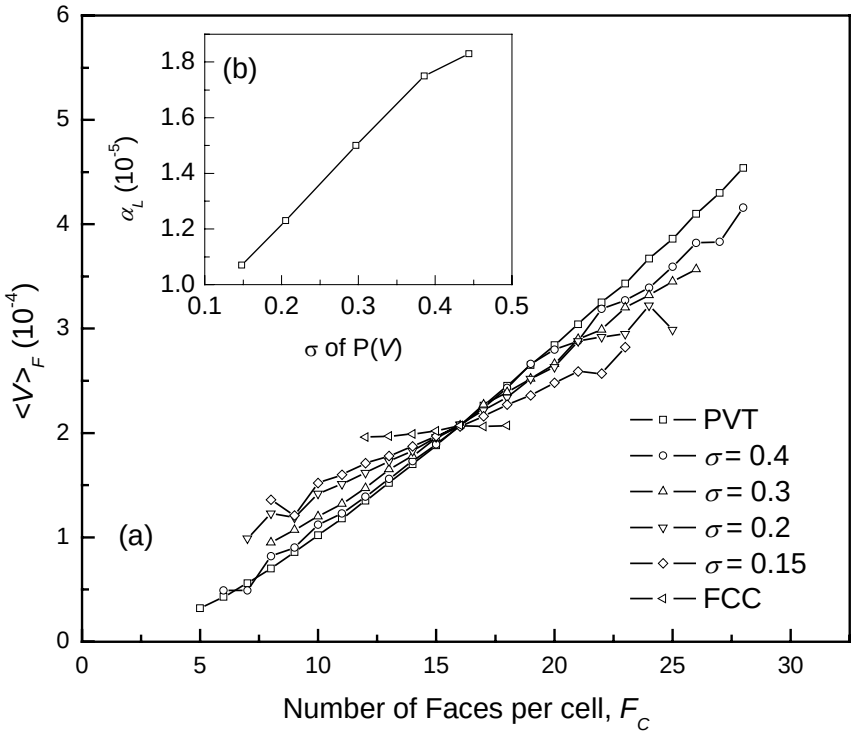

Figure 3.15. (a) Lewis plots of the four lognormal samples and two special cases (the random Poisson-Voronoi and randomly displaced *fcc* lattice); (b) The slope of Lewis plots (fitted by Eq. 4a) increase with the standard deviation of the cell volume distributions.

As shown in Figure 3.15, the linear relation in Lewis's rule does not hold for all four samples with the lognormal cell volume distributions as well as the PVT. The

deviations occur most obviously at the datum points corresponding to the large and small number of faces. However, the Lewis rule still holds in the range of F around the mean number of faces, $\langle F \rangle = 15.5335$ (Meijering's analytical result). For the perturbed *fcc* lattice, the Lewis' rule fits perfectly because of the narrow distribution of the number of faces per cell, as shown in Figure 3.15(a). For the PV cells, Lewis' rule fits well while using the datum points close to the 15.5335, e.g. $12 \le F \le 20$. As the standard deviation of cell volume increases, the deviation is more obvious. The deviation from Lewis linear relation happens around the upper and lower limit of the number of faces per cell. The largest deviation appears in the PVT where the Lewis' rule fits poorly. First, the convexity is observed for the supposedly straight lines. The upswing of $\langle V \rangle_F$ becomes obvious at both ends of each curve, or at the small and large face numbers. The larger the span in the number of the faces, the more non-linear the Lewis's rule becomes. The largest span in the number of faces is for the PV cells and the lognormal distribution with σ=0.4, which as shown in Figure 3.14(a) have large distributions in the number of faces. In addition, the deviation of $\langle V \rangle_F$ is smaller for the larger F values than that for the small faces. In these two cases, the non-linear relation between $\langle V \rangle_F$ and F can be best fitted by a polynomial of the third order,

$$\langle V \rangle_F = a_L (F - F_0) + \beta (F - \langle F \rangle)^2 + \gamma (F - \langle F \rangle)^3, \qquad (3.4b)$$

where β and γ are the two new coefficients, and $\langle F \rangle$ is the mean number of faces. For the PV cells, the best fit from the least square fitting gives $\alpha_L = 1.86041 \times 10^{-5}$, $F_0 = 4.88094$, $\beta = 1.82512 \times 10^{-7}$, and $\gamma = -4.68096 \times 10^{-9}$.

This non-linear behavior, or violation of the Lewis's rule has been reported in a number of experiments on polycrystalline samples [114, 115]. The most noticeable is the condition under which the violation is found: a majority of the grain cells are distorted either through annealing or plastic deformation [114]. The same non-linear behavior was

also reported in a numerical simulation of *hard sphere particle* packing [116]: The more loose the particle packing density is, the larger the deviation from the Lewis's rule. As shown in Figure 3.15, the non-linear behavior becomes less pronounced when the standard deviation of the cell volume becomes smaller. Obviously, one can see that this is related to the range of the number of faces available to the systems (Figure 3.14a). The smaller the standard deviation of the cell volume is, the narrow the distribution of the number of faces per cell is, or the smaller the range of the number of the faces per cell becomes smaller, then the more linear the $\langle V \rangle_F$ vs. F looks. The *fcc* ordered lattice has the smallest range in F and thus fits to Lewis's rule perfectly, while in the particle packing, there is a larger range of F for the loosely packed particles [116]. It is interesting to note that the range of the number of faces in the 2D sections that Lewis observed and used to obtain the relation (Eqn. 3.4a) is quite small [87]. Drouffe and Itzykson already reported that Lewis's rule does not apply when $F > 12$ in 2D VT [117].

The slope of Lewis plots, or the coefficient, a_L, fitted using Equation 3.4(a), increases as the standard deviation increases in a linear fashion (Figure 3.15(b)). As a comparison, the Lewis plot for the ordered *fcc* lattice with a slight displacement in the initial lattice points is also shown in Figure 3.15. The slope of the *fcc* lattice with a delta-function cell volume distribution represents the lowest limit of Lewis plots since the standard deviation of cell volume is among the smallest. On the other hand, the slope of the PVT represents an upper limit. This trend is understandable as we saw earlier that the mean number of faces per cell increases with the standard deviation of the cell volume. This increase in the number of faces per cell is amount to a larger coefficient a_L for a nearly invariant $\langle V \rangle$. As pointed out by Rivier [113], a_L should change for different systems with more diversity in the grain sizes and isotropy of the grain shapes. Our result (see Inset in Figure 3.15) confirms this claim. In addition, as the slopes of the Lewis plots for different samples change, we observed that the Lewis's plots intercept each

other at approximately the same value of the number of faces (~15.5), including the ordered fcc lattice which has a much small mean number of faces per cell (~14).

Another topological relation between the number of faces, F, in a (central) cell and the average number of the faces in all its neighboring cells, $M(F)$, is specified by the Aboav-Weaire law [118, 119],

$$FM(F) = [\langle F \rangle - a]F + \langle F \rangle a + \mu_2, \tag{3.5a}$$

or

$$M(F) = [\langle F \rangle - a] + \frac{\langle F \rangle a + \mu_2}{F}, \tag{3.5b}$$

where a is a constant, $\mu_2 = \langle F^2 \rangle - \langle F \rangle^2$ is the variance of the face number. Figure 3.16 plots $FM(F)$ vs. F for the lognormal samples. We plotted both the raw data for $M(F)$ corresponding to each F and the mean value of $M(F)$. The results show agreement with the Aboav-Weaire law (i.e., the linear dependence on F). As the standard deviation of the cell volume distribution decreases, the domain of the datum points for $FM(F)$ vs. F shrinks. The best fitted result for Eqn. 3.5(a) is also shown in Figure 3.16. Table 3.2 lists the values of a and μ_2 for the samples with lognormal cell/grain volume distributions as well as for the PV cells. In general, we see that μ_2 increases (which can also be seen in Figure 3.14(a)) and a decreases with the increase of the standard deviation of the cell volume, σ. The Aboav-Weaire law indicates that the "equal" partitioning of the number of the neighbors (i.e., the number of faces) neighboring to each other still holds in the random VT as well as CVT cells that follow different cell volume distributions.

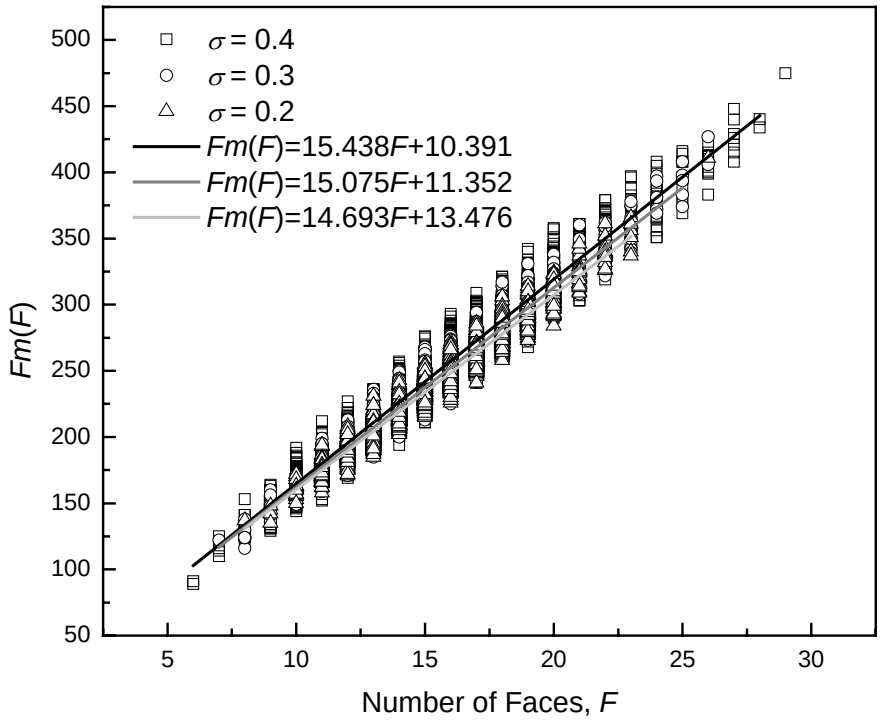

Figure 3.16. The plots of Aboav-Weaire law of the three lognormal samples. The plot of $Fm(F)$ vs. F of the CVT ($\sigma = 0.4$, open square) is drawn first. Other plots are superimposed in the order of decreasing standard deviation, $\sigma = 0.3$ (open circle), $\sigma = 0.2$ (open triangle). For each curve, there are 5,000 data points represented by the same symbol. For each Aboav-Weaire plot, the best fitted result for $Fm(F) = aF + b$ is shown as a solid line. As the standard deviation (σ) increases, the domain of each curve shrinks.

Table 3.2. The variance of the face number, $\mu_2 = \langle F^2 \rangle - \langle F \rangle^2$, and the constant in the Aboav-Weaire law, *a*, in the four samples with lognormal cell volume distribution and three samples with bimodal cell volume distribution. σ is the standard deviation of cell volume.

Lognormal σ		μ_2	a
0.15		4.493163	0.589549
0.2		5.468876	0.370536
0.3		7.065216	0.202516
0.4		10.01642	-0.049441
Bimodal v_a	v_b	μ_2	a
0.8	1.2	6.3908	0.634938
0.8	1.3	7.0511	0.257293
0.8	1.4	7.5330	0.169353
Random VT		11.1337	-0.095505

3.2.3.3 Bimodal distribution

Bimodal grain/cell volume distribution represents an obvious departure from the cell volume distribution as seen in the random PVT and lognormal cases where the means and variances are well defined for the former but not for the later. Moreover, many stochastic structures and cellular patterns follow multi-modal distribution in its size, in particular in materials and natural phenomena where non-equilibrium and non-uniform condition are dominant in the formation process of the patterns. For example, in nanocrystalline copper materials [43], Al-Li alloy [120, 121], ball-milled α-Al_2O_3 [122] and ceramics [123], and aerosol growth [124], bimodal grain size is widely observed.

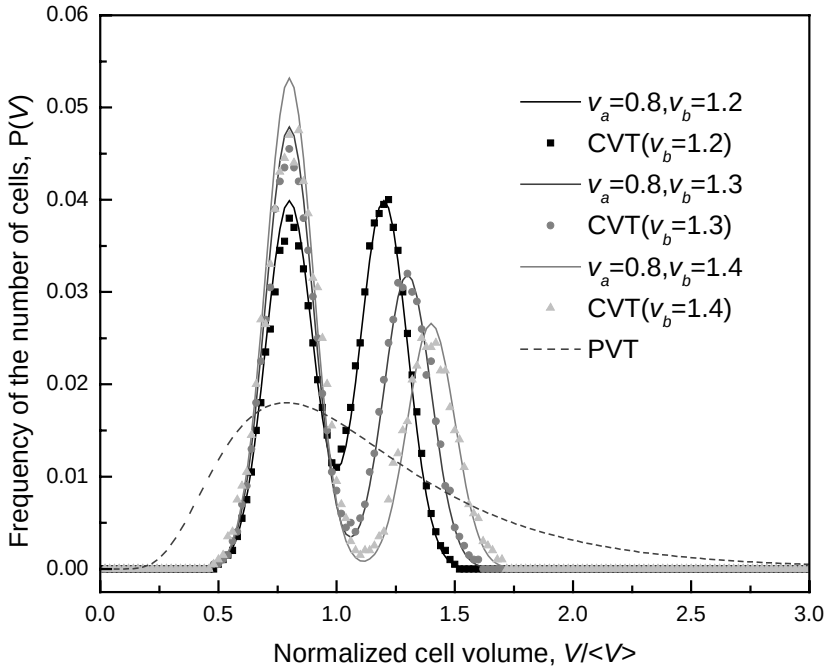

Figure 3.17. The cell volume distributions of bimodal samples obtained using the CVT method in conjunction with non-uniform weights for the systems with 2,000 points. For comparison, the distribution for the PV cells with 2,000 points is also shown as the dashed line. The target bimodal distribution functions are shown as the solid line and the CVT results are shown as scattered data points labeled with "CVT". The first peak (v_a) is located at 0.8 and the second peaks (v_b) are located at 1.2, 1.3, and 1.4 for the three cases.

For simplicity, we take two normal distributions as the target bimodal distribution function for cell volume. The first peak is located at v_a and the second peak is located at v_b. The mean cell volume of the sample is fixed at 1. Both normal distributions have the same standard deviation (0.1). In this study, we select three bimodal distributions with the same first peak position at 0.8. The positions of second peaks are at 1.2, 1.3 and 1.4 respectively. Note that all target bimodal distributions are normalized (Figure 3.17).

As shown earlier, the lognormal cell size distribution can be obtained from the homogeneously distributed random points or PVT through the IMC optimization. To

achieve a bimodal distribution from the random point process or PV tessellation, extra efforts are needed. Specifically, we divide the target bimodal distribution into four cell volume regions and apply a series of weights to accelerate the convergence (see Eqn. 3.2). We take the following steps in applying the weights to the different regions: (1) Large weight is applied in regions I ($V/\langle V\rangle < 0.48$) and II ($V/\langle V\rangle > 1.6$) to prevent the system from producing cell volumes that exceed the lower and upper cell volume limits; (2) We shift the weight toward the valley between two normal distributions (region IV) to accelerate the separation of the cells into two modes; (3) We shift the weights toward two peaks (region III) in the distribution to achieve the target cell volume distribution. As the second peaks moves further away from the first one, or the separation between the two peaks becomes larger and the valley between them becomes deeper, it is more time-consuming to achieve the best fit. The final results for the three samples with different bimodal cell size distributions with 2,000 points are shown in Figure 3.17. The separations between two peaks are achieved, but the best fitting for the first peak is sacrificed slightly.

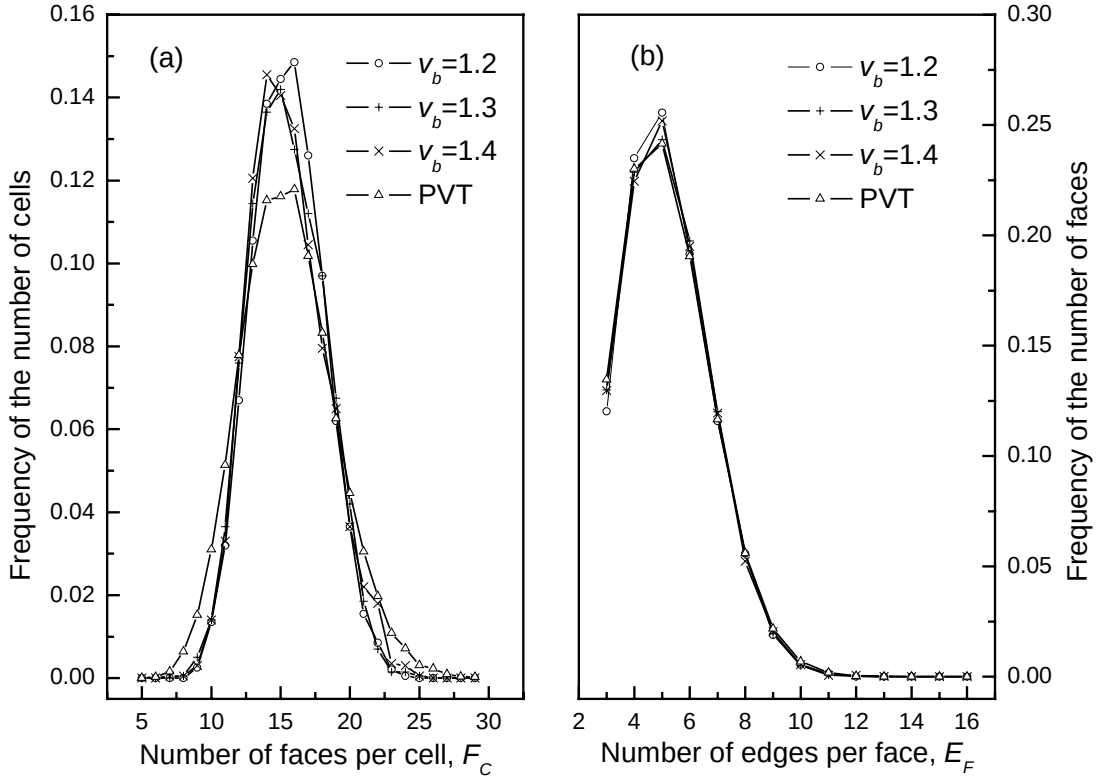

Figure 3.18. a) The number of faces per cell/grain distributions of the three bimodal samples with 2,000 points. The number of the faces distribution for the PV cells is also shown. Note that the smallest number of the faces is 4, or a tetrahedron. b) The number of edges per face distributions of the three bimodal samples with 2,000 points. The number of the edges for the PV cells is also shown. Note that the smallest number of the edges is 3, or a triangle.

The statistical accounts of the geometric properties in the bimodal samples are computed from the final optimized samples. The distributions of the number of faces per cell and the number of edges per face are shown in Figure 3.18, along with those of PV cells as a reference. We see that the mean face number remains relatively invariant while the variance increases (slightly) with the separation between the two modes (Figure 3.18(a)). For the number of edges per face, very small changes are observed (Figure 3.18(b)). The mean values for the number of face, edge, and vertex per cell, along with other geometric properties are listed in Table 3.1. Interestingly, we observe that the

statistical distributions of these sets of geometric properties in the bimodal samples are very close to those from the PV tessellations. This is due mainly to the spread in the cell volume distribution from the two modes. The face area and edge length distributions for the entire sample are shown in Figure 3.19, along with those from the PVT as a reference. We see little difference among the three samples as well as the PVT.

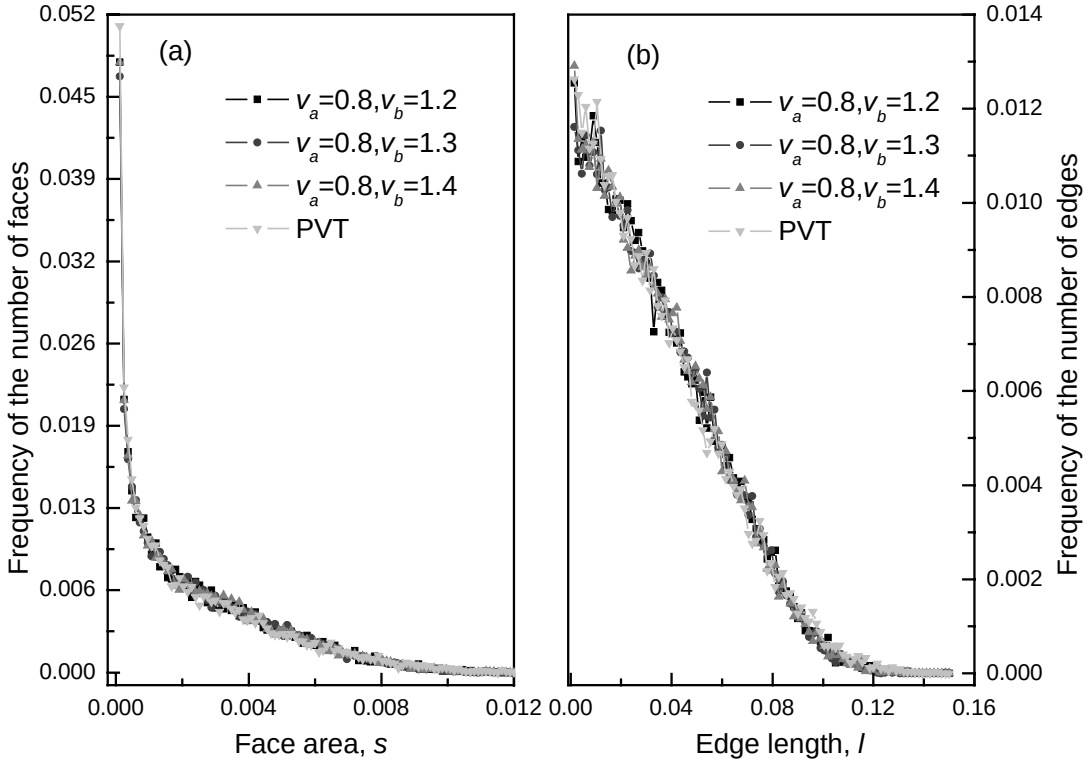

Figure 3.19. a) The face area distribution of three bimodal samples with 2,000 points. b) The edge length distribution of the three bimodal samples with 2,000 points. For comparison, the distribution for the PV cells from a sample with 2,000 points is also shown.

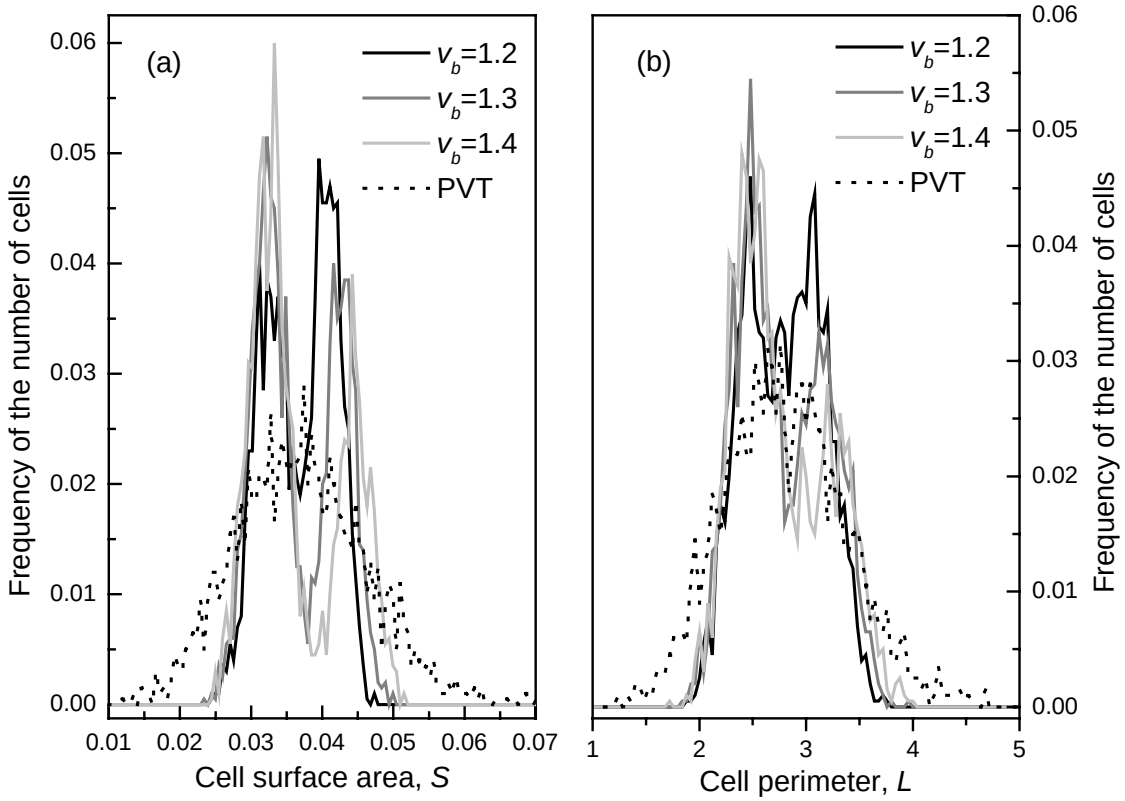

Figure 3.20. a) The distribution of the cell surface area of the three bimodal samples with 2,000 points. b) The distribution of the cell perimeter of the three bimodal samples with 2,000 points. For comparison, the distribution for the PV cells from a sample with 2,000 points is also shown.

The distributions of the cell surface area and cell perimeter per cell are shown in Figure 3.20. Here we start to see very different characteristics. Namely, both the cell face area and cell perimeter obtained follow the similar bimodal distributions as in the cell volume distributions. The bond angle and dihedral angle distributions for the entire sample are shown in Figure 3.21, along with those from the PVT. The mean values of the bond angle and dihedral angle are listed in Table 3.1. Again, we see that both distributions show little difference from each other.

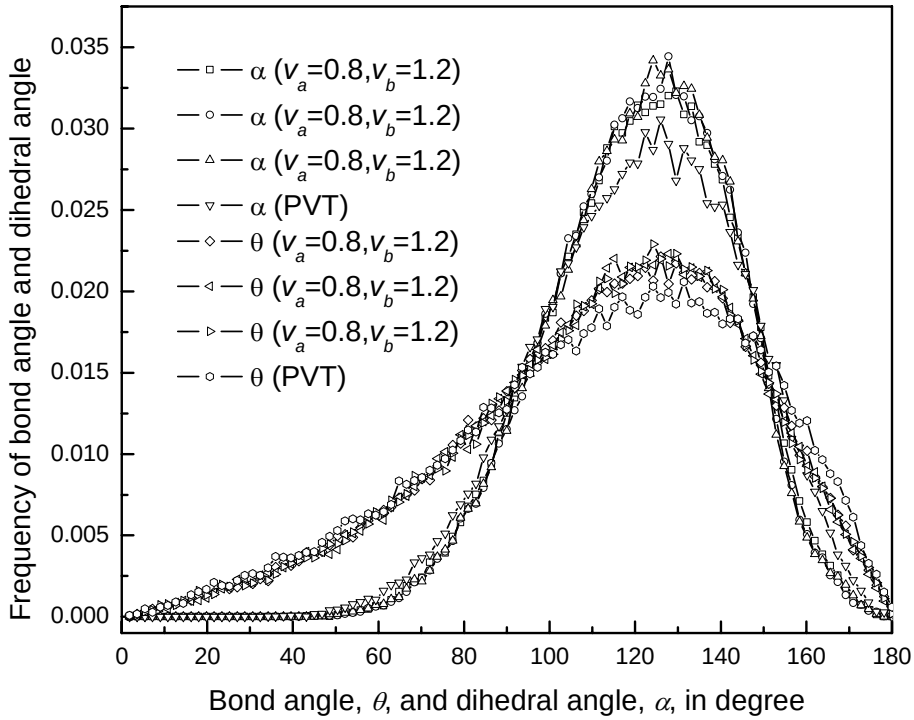

Figure 3.21. The distributions of the dihedral and bond angles of the three bimodal samples with 2,000 points. For comparison, the distribution for the PV cells from a sample with 2,000 points is also shown.

For the bimodal cell size distributions, Lewis's rule does not hold at all as the relation between $\langle V \rangle_F$ and F becomes obviously nonlinear (Figure 3.22). This should be anticipated as the cell volume is divided into two modes while the mean number of faces per cell still remains in single mode (Figure 3.18(a)). In fact, the agreement with the Lewis rule was reported for each type of hard spheres in the Voronoi cells in the binary hard sphere system while the Lewis' rule doesn't hold for the entire system [125]. In the point PV process as used in this work, we cannot distinguish which point belonging to which mode in the cell volume distribution. Therefore, we can only measure the relation for the entire sample.

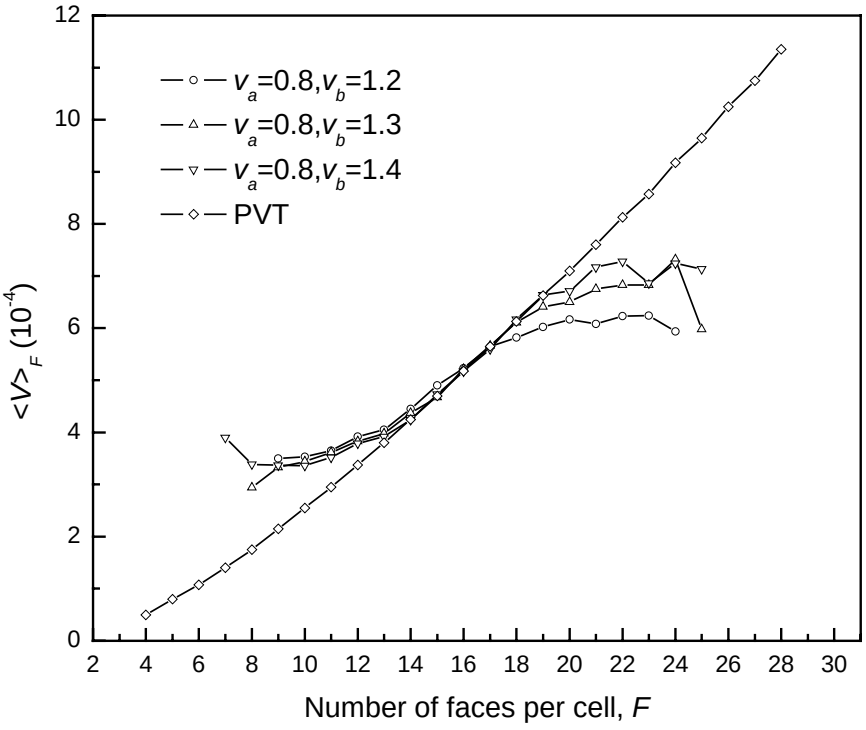

Figure 3.22. The Lewis plots for the three bimodal samples with 2,000 points. The Lewis plot of the PV cells of 2,000 points is also shown as a reference. The data become noisy at the ends of the curves due to the limited number of faces available in the models.

Moreover, we see that the Lewis rule still holds linearly around the average number of faces per cell, $\langle F \rangle = 15.5335$ (Figure 3.22). There is a turnover point from the linear relation in Lewis plot around the mean number of faces per cell $\langle F \rangle$ since $\langle F \rangle$ remains almost invariance for the three bimodal cases (Figure 3.18(a) and Table 3.1). In addition, we found that the deviations from the linear relation are asymmetry in Lewis plots in. The deviation is smaller in region with F smaller than $\langle F \rangle$ and becomes much larger in region with F larger than $\langle F \rangle$. This is because we increase effectively the cell volume by varying v_b while keeping v_a fixed. This causes a larger deviation from the

linear relation in Lewis plots in the region with F larger than $\langle F \rangle$. As illustrated in the lognormal case, standard deviation of cell volume distribution does affect the slope of Lewis' plot. While increasing v_b, the variance of the second peak increases and causes the deviation from Lewis' relation. The difference between normal distribution and lognormal distribution maybe another possible reason for the deviation. In contrast to Lewis's rule, Aboav-Weaire law is obeyed quite well in the bimodal cases. As shown in Figure 3.23, a linear relation between $FM(F)$ and F is observed for the three bimodal samples.

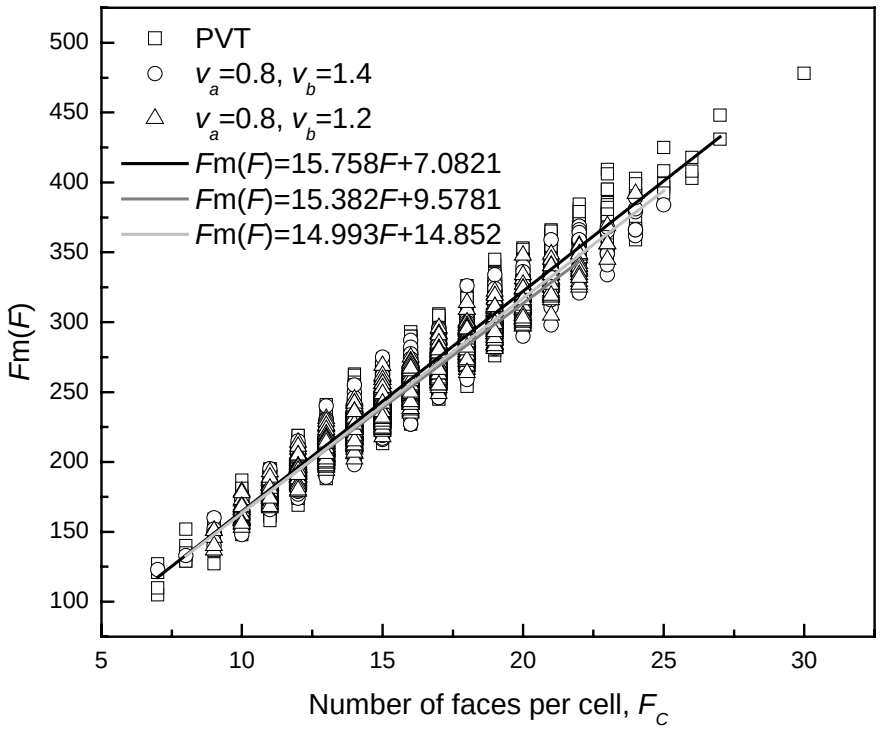

Figure 3.23. The plots of Aboav-Weaire law for the two bimodal samples ($v_b = 1.2$ and $v_b = 1.4$) with 2,000 points. The plot of $Fm(F)$ vs. F of the PVT (open square) is drawn first. Other plots are superimposed in the order of decreasing standard deviation, $v_b = 1.4$ (open circle), $v_b = 1.2$ (open triangle). For each Aboav-Weaire plot, the best-fitted result for $Fm(F) = aF + b$ is shown as a solid line with the different gray-scale.

3.2.3.4 Normal cell volume distributions

In the previous two sections, the CVT method is tested against two types of cell volume distributions commonly observed in experiments. Here, we will make additional test on a hypothetical cell volume distributions, namely the normal distributions. In the bimodal cases, the Lewis rule is no longer followed linearly. As pointed out earlier, the Lewis rule is still obeyed for cells in the same mode. This prompts us to study how the Lewis's rule is affected by a normal cell volume distribution.

The standard deviation of the target normal cell volume distribution is 0.3. The target function is plotted in Figure 3.24 as the solid line. Using the same procedure as the lognormal case (section 3.2.3.2), we obtain the best-approximated Voronoi tessellation with a cell volume distribution close to the target function, which is plotted in Figure 3.24 as the filled squares. For comparison, we also plot the lognormal distribution with the same standard deviation as the dotted line. The Lewis plots of Voronoi tessellations with normal and lognormal distributions are shown in Figure 3.25.

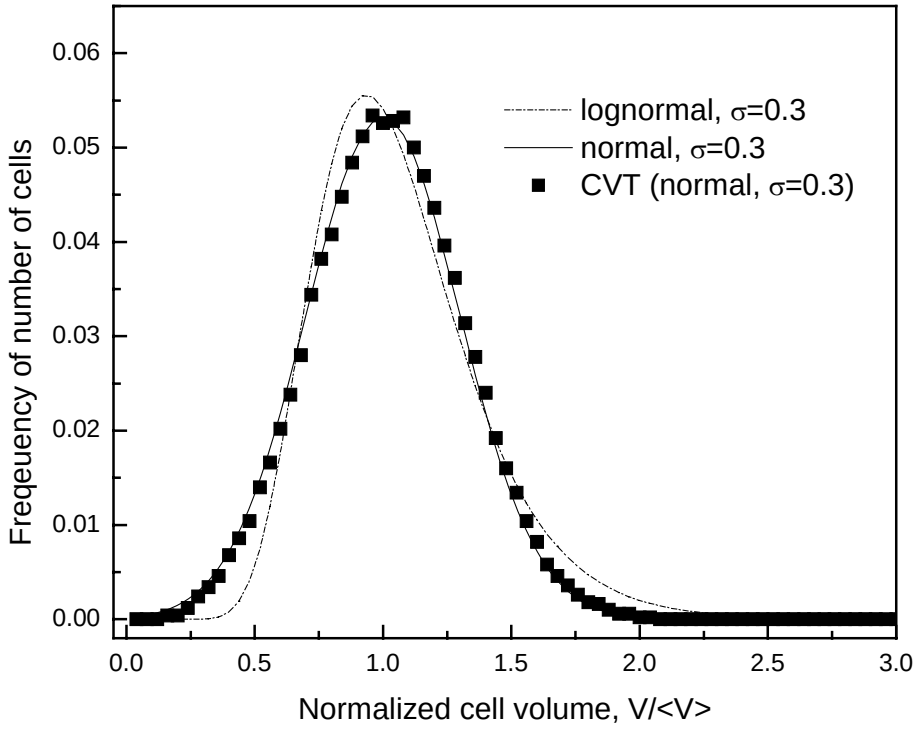

Figure 3.24. Cell volume distributions of Voronoi tessellations with normal cell volume distribution ($\sigma = 0.3$).

The Lewis plot of VT with normal cell volume distribution is best-fitted by a polynomial of the second order:

$$\langle V \rangle_F = \alpha_L (F - F_0) + \beta (F - \langle F \rangle)^2 \tag{3.6}$$

where $\alpha_L = 1.55368 \times 10^{-5}$, $F_0 = 2.41255$, $\beta = -3.40861 \times 10^{-7}$, and $\langle F \rangle$ is the mean number of faces per cell. Similarly, the Lewis plot of VT with lognormal cell volume distribution is also fitted by Eqn. 3.6 where $\alpha_L = 1.48965 \times 10^{-5}$, $F_0 = 1.97126$ and $\beta = 3.16969 \times 10^{-8}$. Comparing results of two samples, it is clear that the shape of the cell volume distribution greatly influence the shape of the Lewis plot. Although the Lewis law still holds in the domain of F close to Meijering's analytical value, the Lewis

plot of normal distribution clearly has a convex shape and is sitting below that of lognormal distribution at both ends of the plot.

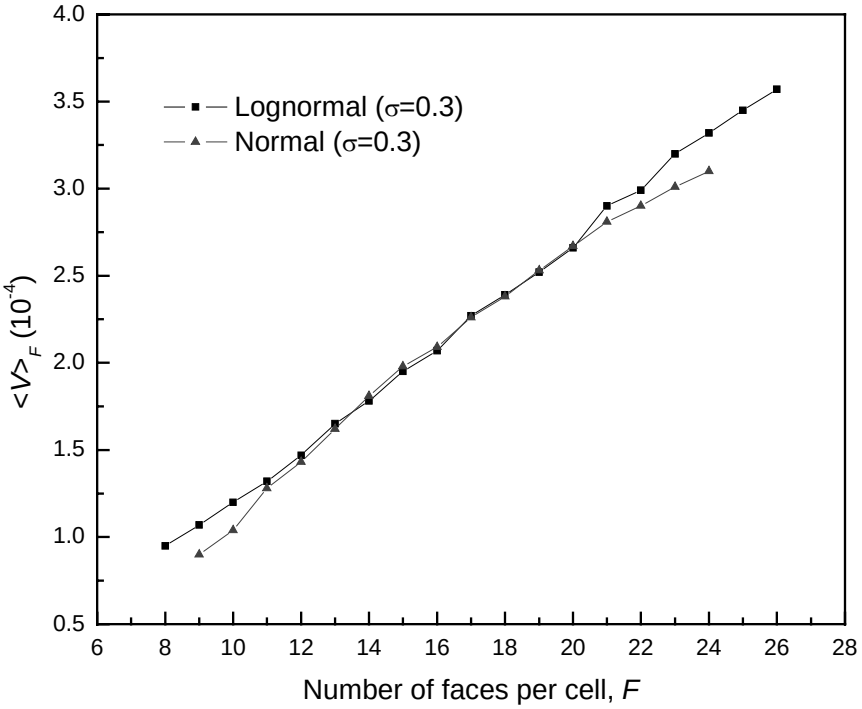

Figure 3.25. The Lewis plots for two Voronoi tessellations with the same standard deviation but different cell volume distributions: lognormal distributions (filled squares) and normal distributions (filled triangles).

Another topological linear relation between the number of faces, F, in a cell and the average number of faces in all its neighboring cells, $M(F)$, is specified by the Aboav-Weaire law, equation (2). Figure 3.26 plots $FM(F)$ against F for Voronoi tessellations of lognormal and normal cell volume distributions. The linear dependence on F is clearly presented in both cases. Each data series in Figure 3.26 has 5,000 points.

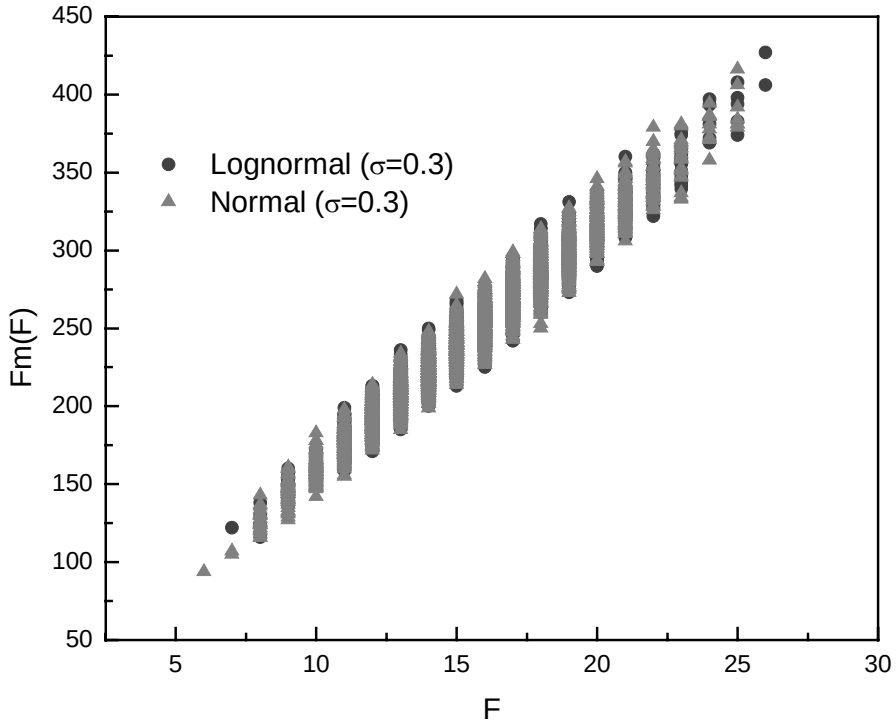

Figure 3.26. The Aboav-Weaire plots for two Voronoi tessellations with the same standard deviation but different cell volume distributions: lognormal distributions (filled squares) and normal distributions (filled triangles).

3.2.4 Minimize the number of small faces and short edges

Voronoi tessellations have been used widely to generate nanocrystalline samples by filling atoms into the dimensionless Voronoi structure. These digital nanocrystalline samples often undergo molecular dynamic (MD) relaxation and plastic deformation. However, there are large amount of small faces and short edges in typical Voronoi tessellations. Due to the finite size of atoms, those small grain boundary (GB) interfaces and triple junctions tend to vanish during atomistic relaxation and the GB. The grain structure of relaxed *nc* samples is no longer the same as the original Voronoi structure. Therefore, it is critical to reduce the number of small faces and edges presented in the Voronoi structures and study the effects on other topological properties.

In section 3.2.4.1, we use a Monte Carlo (MC) minimization procedure to generate Voronoi structures with face area distributions best fitted to a two-parameter gamma distribution by reducing the amount of short edges. In the section 3.2.4.2, a similar Monte Carlo (MC) procedure is then used to minimize the amount of small faces by simply moving the points around according to the Metropolis algorithm.

3.2.4.1 Edge length distribution: P(l)

Our goal is try to reduce the number of small faces and short edge that are usually presented in VT. We cannot use the CVT method here because we do not know the exact target functions. Instead, a Monte Carlo minimization procedure is utilized. The cost function, χ_0, of each configuration is the number of edges with a length less than a cutoff length, l_{CUT}. In the case of 5,000 cells, the cutoff length is set at 0.0012. The algorithm of each Monte Carlo step is summarized as follows:

1) For each Voronoi cell, calculate the minimum length among all edges in that cell and record it into an array;
2) Sort the array into ascending order;
3) Select cells with their minimum cell lengths in the top 4% and then randomly choose one of them;
4) Randomly move the center of the selected cell, recalculate the number of short edges, χ', and decide whether or not to keep the move according to the metropolis algorithm.

The initial configuration is the same as the VT of lognormal cell volume distribution ($\sigma = 0.3$). The number of edges with length less than the cutoff length is reduced close to zero after long MC simulation. Due to the low convergence, the MC minimization is terminated after 10,000 MC steps and the Voronoi tessellation of the

final configuration is calculated. The edge length distribution of the initial VT and that of the final configuration of MC minimization are shown as Figure (3.27(a)).

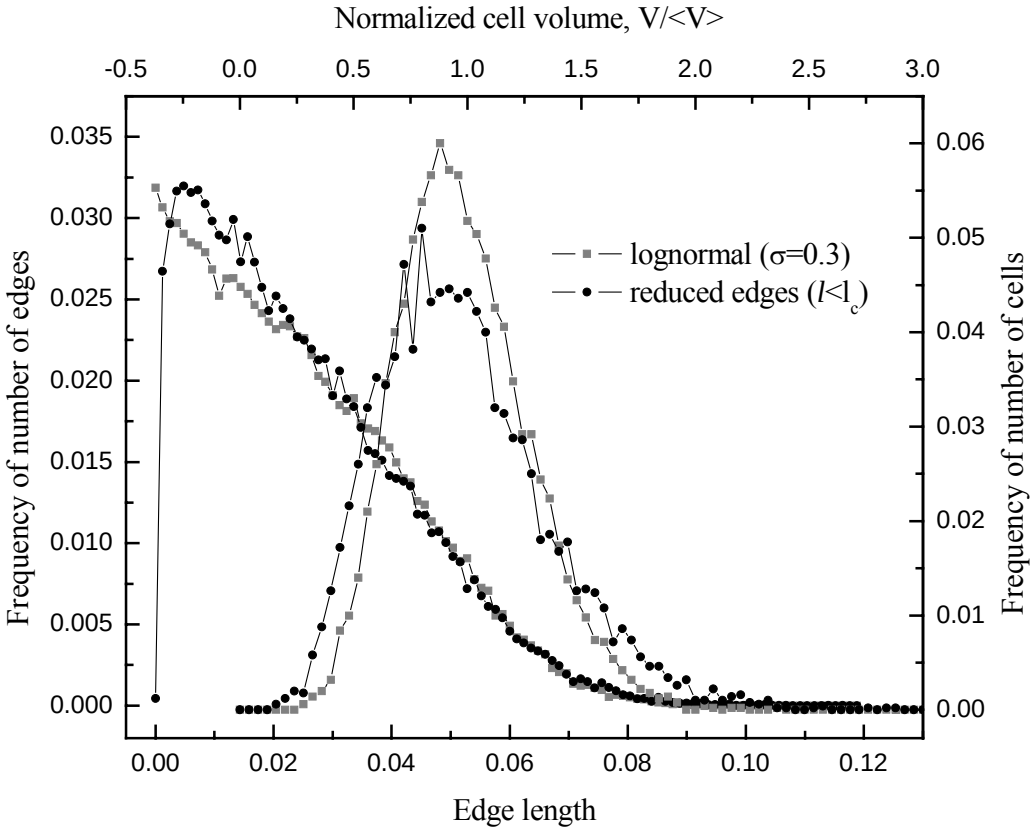

Figure 3.27. Edge length distributions and cell volume distributions of a VT with reduced number of short edges ($l < l_{CUT}$) and the initial VT with a lognormal cell volume distribution ($\sigma = 0.3$).

The edge length distribution of the final configuration can be fitted using a two parameter gamma function:

$$f(x) = \frac{1}{\beta \Gamma(\alpha)} \left(\frac{x}{\beta} \right)^{\alpha - 1} \exp\left(-\frac{x}{\beta} \right) \tag{3.7}$$

where $\alpha = 1.36739$ and $\beta = 0.812196$. The average edge length, $\langle l \rangle$, is 0.024782 and the interval in edge length distribution, Δl, is 0.048421339. Also shown in Figure 3.27 is the cell volume distribution of the initial and final configurations. As the number of

short edges, χ, decreases, the variance in cell volume increases as the peak density decreases and the spread increases.

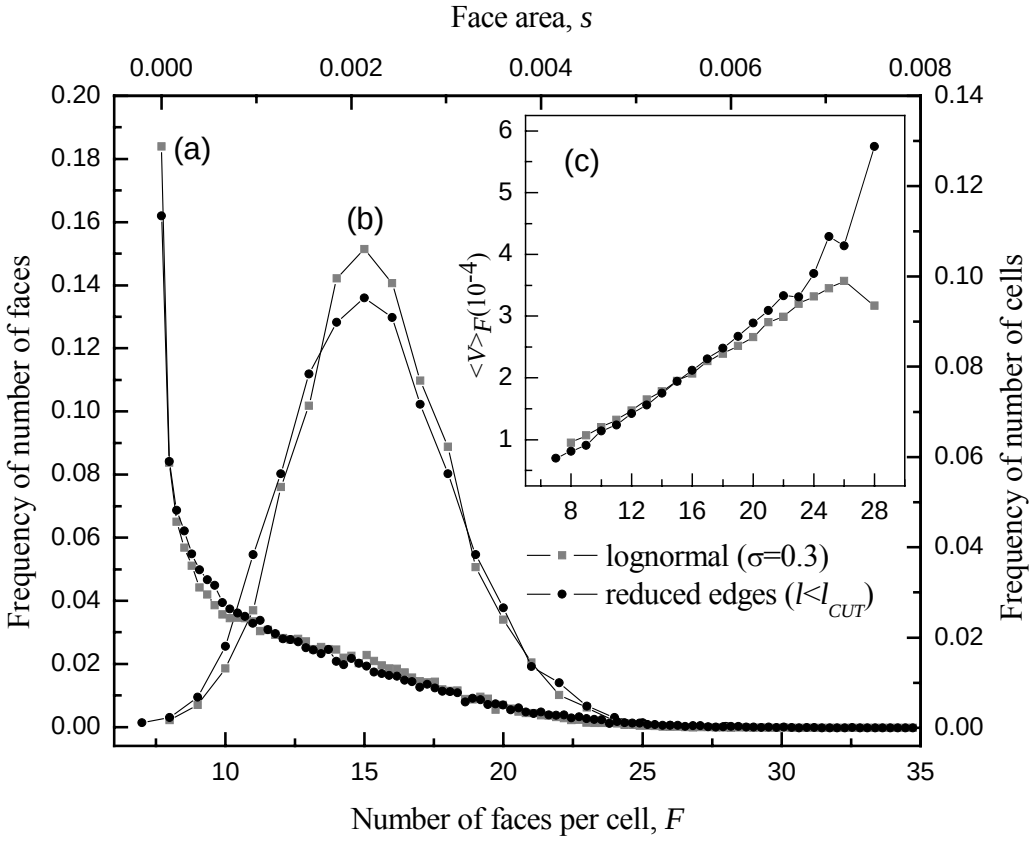

Figure 3.28. a) Face area distributions of initial VT and VT with reduced number of short edges ($l < l_{CUT}$); b) Face number distributions; c) Lewis plots.

The face area distributions of initial and final configurations are shown in Figure 3.28(a). There is a slight drop in the number of small faces and the face area distributions intercept twice. The distribution of number of faces per cell (Figure 3.28(b)) shifts slightly to the left as the peak density decreases. The average number of faces, $\langle F \rangle$, decreases from 15.4012 to 15.2728. The Lewis relations of initial and final configurations are plotted as Figure (3.28(c)). Because of the limited number of data in the face number distribution outside of the range of $7 \le F \le 21$, the Lewis plot is

scattered when the number of faces per cell, F, is outside of this range. The intercept is found at 15.04548 when the data in the range of $7 \le F \le 21$ are fitted using Eqn. 3.4(a).

3.2.4.2 Face area distribution: P(a)

Similar to the minimization of short edges, another MC minimization is carried out using a similar procedure described earlier. The cost function in this case is the number of faces, ξ, with an area less than a cutoff area, s_{CUT}. The MC procedure is summarized as follows:

1) For the initial configuration, calculate the number of faces with an area less than the cutoff area, ξ;
2) For each Voronoi cell, calculate the minimum area among all faces in that cell and record it into an array; Sort the array into ascending order;
3) Select cells with their minimum face area in the top 4% and then randomly choose one of them. Randomly move the center of the selected cell and recalculate the number of small faces, ξ'.
4) If $\xi' < \xi$, keeps the move. If $\xi' \ge \xi$, but satisfies the condition of $\exp\left(-\frac{\Delta\xi}{kT}\right) < \rho$, where ρ is another random number between 0 and 1, still keeps the move. Otherwise, reject the move.

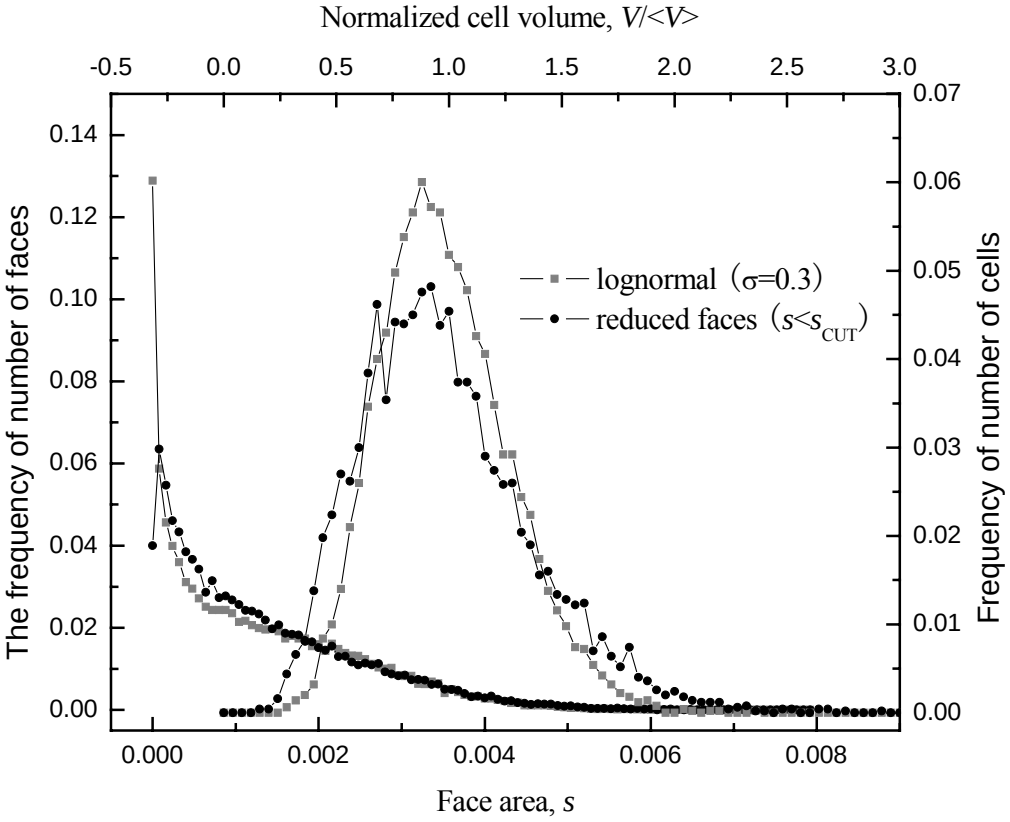

Figure 3.29. Face area distributions and cell volume distributions of a VT with reduced number of small areas ($s < s_{CUT}$) and the initial VT with a lognormal cell volume distribution ($\sigma = 0.3$).

The face area distributions of the initial and final configurations are plotted in Figure 3.29 as well as the normalized cell volume distributions. The convergence of the MC simulation becomes extremely slow after the fraction of small areas ($s < s_{CUT}$) reduces to 0.04 and the simulation is stopped after a long time of simulations. In the case of trying to reduce the number of short edges, it is relatively easier to reduce to cost function close to zero because we only need to move the center of one Voronoi cell in order to remove a short length. However, the task becomes more challenging when we are trying to remove a small face. As a 2D object, it often requires moving the centers of at least two neighboring cells to remove a small face. Different methods to improve the

convergence are tried without much success. Another possibility is that the simulation has reached a limit imposed by the geometrical laws associated with Voronoi tessellations.

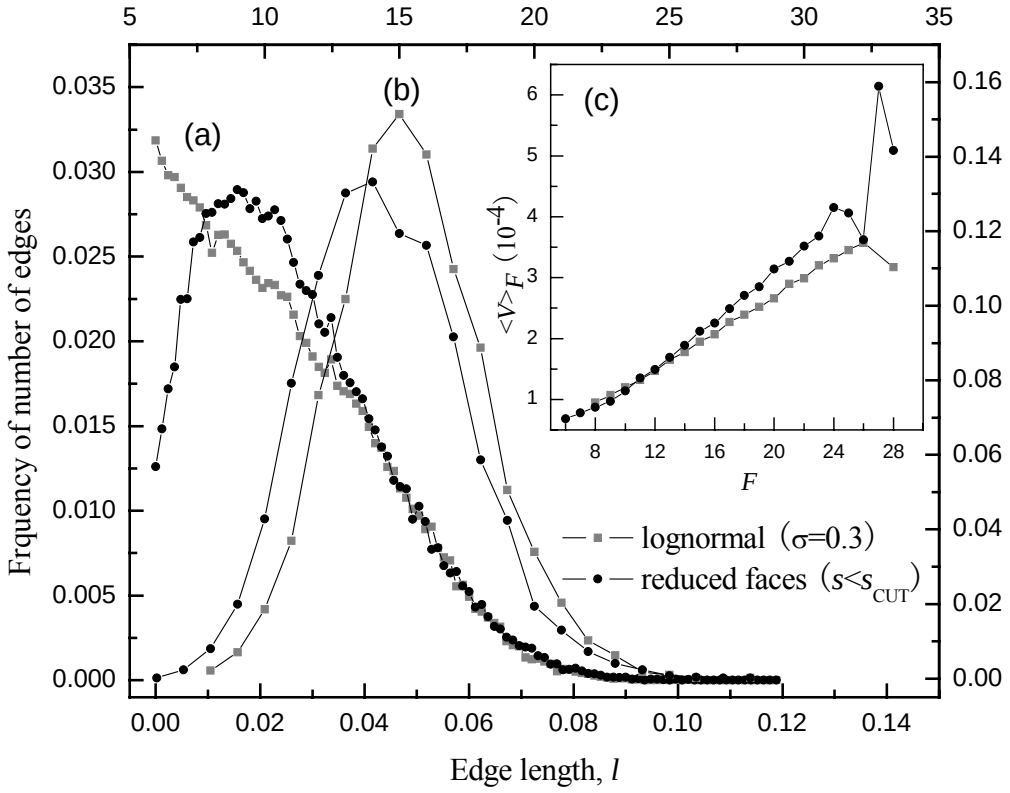

Figure 3.30. a) Edge length distributions of initial VT and VT with reduced number of small faces ($s < s_{CUT}$); b) Face number distributions; c) Lewis plots.

Figure 3.30 shows the edge length distributions, face number distributions and the Lewis plots of initial VT and VT with reduced number of small faces ($s < s_{CUT}$). During the minimization of number of small faces, the number of short edges also decreases and the average number of faces per cell increases. The slopes of Lewis plots increase as the number of small faces decreases as their intersections with that of initial VT of lognormal distribution keep decreasing to a small number of faces per cell. As mentioned earlier,

the Voronoi tessellation of randomly perturbed *fcc* lattice possess the smallest variance in cell volume. The geometrical averages of VT of randomly perturbed *fcc* lattice is very close to that of Tetrakaidecahedra including: $\langle F \rangle = 14$, $\langle E \rangle = 36$, $\langle V \rangle = 24$. The geometrical averages of the VT of reduced number of small faces are: $\langle F \rangle = 14.9904$, $\langle E \rangle = 37.4856$ and $\langle V \rangle = 24.9904$, which are approaching the geometrical averages of Tetrakaidecahedra. Additionally, the Euler relation that regulate the geometry properties of a Voronoi cell, $V - E + F = 2$, is another constrain that cause the slow convergence during the minimization of number of small faces.

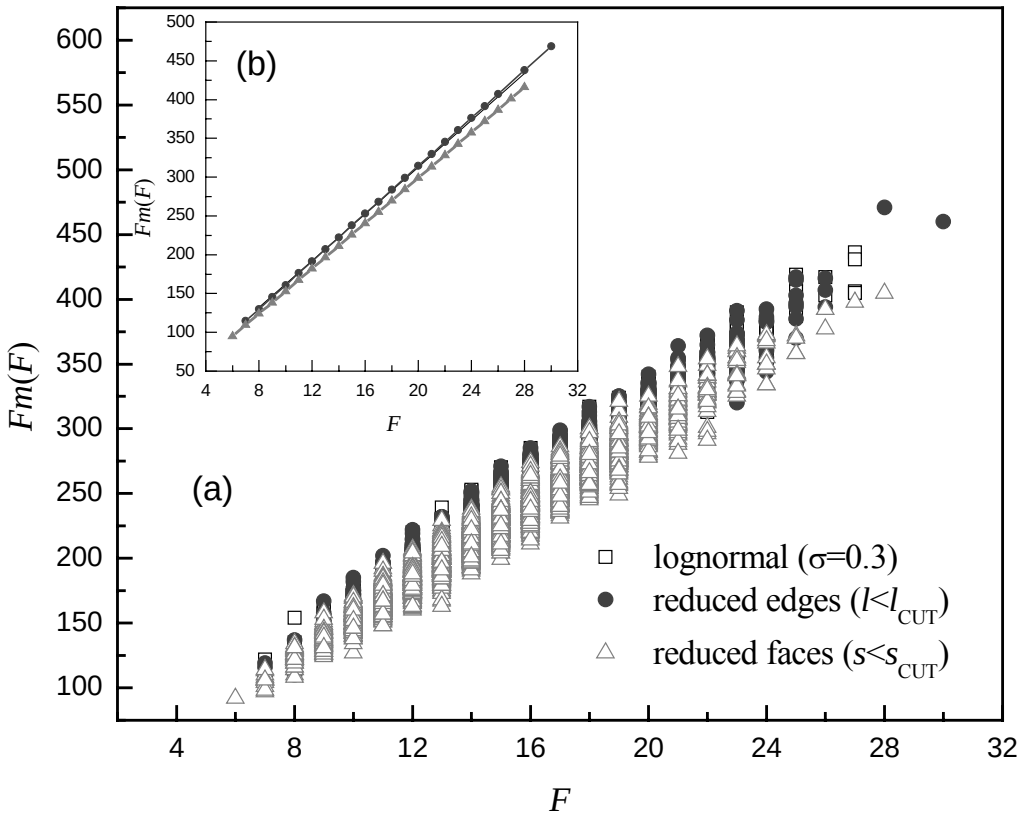

Figure 3.31. a) $Fm(F)$ vs. F for three Voronoi samples: 1) VT of lognormal cell volume distribution ($\sigma = 0.3$); 2) VT of reduced short edges ($l < l_{CUT}$); 3) VT of reduced small faces ($s < s_{CUT}$). b) Fitted linear relation according to Eqn. 3.5.

From previous results, we know that the Aboav-Weaire law is obeyed quite well in earlier case studies including the VT of reduced number of short edges. Here, the linear relation is again observed in the Aboav-Weaire plots of the VT of reduced number of small faces (Figure 3.31). However, there exists a significant shift in the domain of the Aboav-Weaire plot (Figure 3.31(a)). The Aboav-Weaire plots of both initial VT and the VT of reduced number of short edges almost overlap with each other. The plot of VT of reduced number of small area is clearly away from those two as shown in the inset of Figure 3.31. This behaviour indicates that there exists a significant structure change in during the MC simulation to reduce the number of small faces.

3.2.5 Discussion

Up to now, we have carried out a systematic calculation of the topological properties of several 3D systems with different cell volume distributions using the CVT method. By doing so, we show that the statistical properties of the systems with lognormal, bimodal and normal distributions as well as the two special cases, the PV cells and the nearly perfectly ordered *fcc* cells indeed show systematic changes or trends in the topological properties. The most noticeable one is the (almost linear) decrease in the variances of all topological properties with the decrease in the cell size variance. The second is the violation of the Lewis's rule in all cases studied with an exception of the *fcc* ordered sample. In the following, we shall show that the systematic changes in the properties are also closely related to the cell shape *uniformity* or *anisotropy*.

3.2.5.1 The effects on the Lewis rule by various cell volume distributions

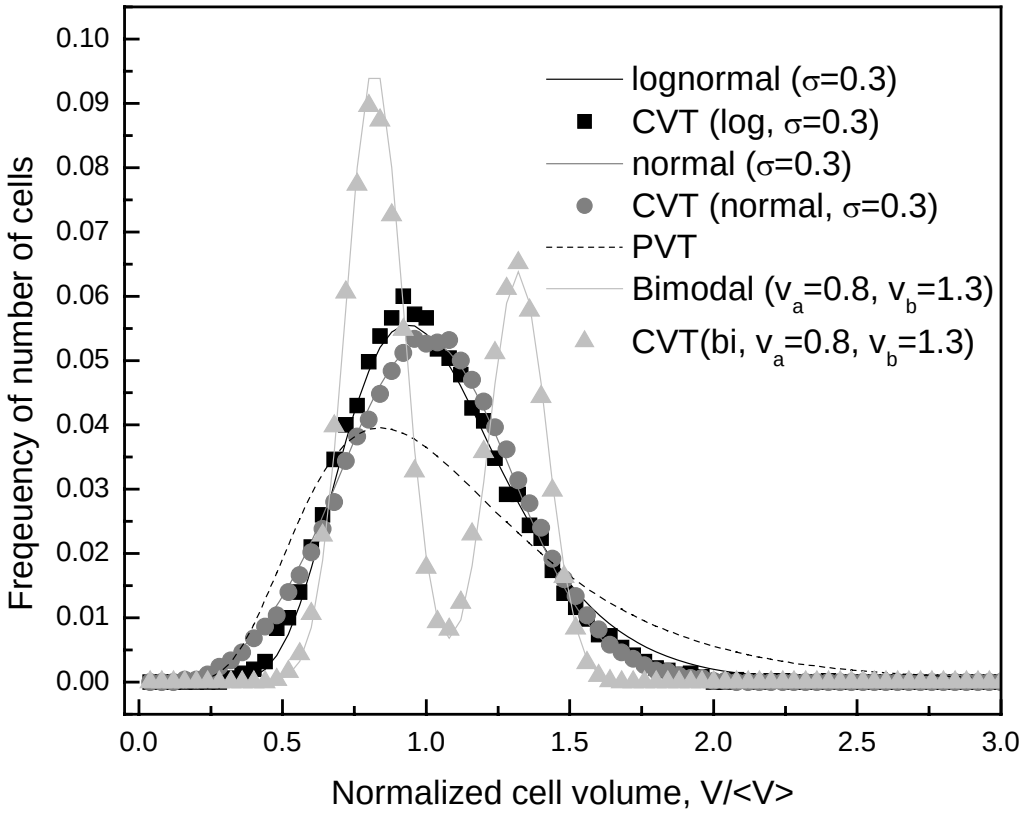

Figure 3.32. Cell volume distributions of Voronoi tessellations with four different cell volume distributions: 1) lognormal ($\sigma = 0.3$); 2) normal ($\sigma = 0.3$); 3) PVT; 4) bimodal ($v_a = 1.2$, $v_b = 1.3$).

Let us first examine the effect on the Lewis rule by various cell volume distributions. Here we select four typical distributions: 1) PVT; 2) lognormal distribution ($\sigma = 0.3$); 3) normal distribution ($\sigma = 0.3$) and 4) bimodal distribution ($v_a = 1.2$, $v_b = 1.3$). Results obtained from CVT method for these four distributions are plotted together in Figure 3.32 and the corresponding Lewis relations are plotted in Figure 3.33.

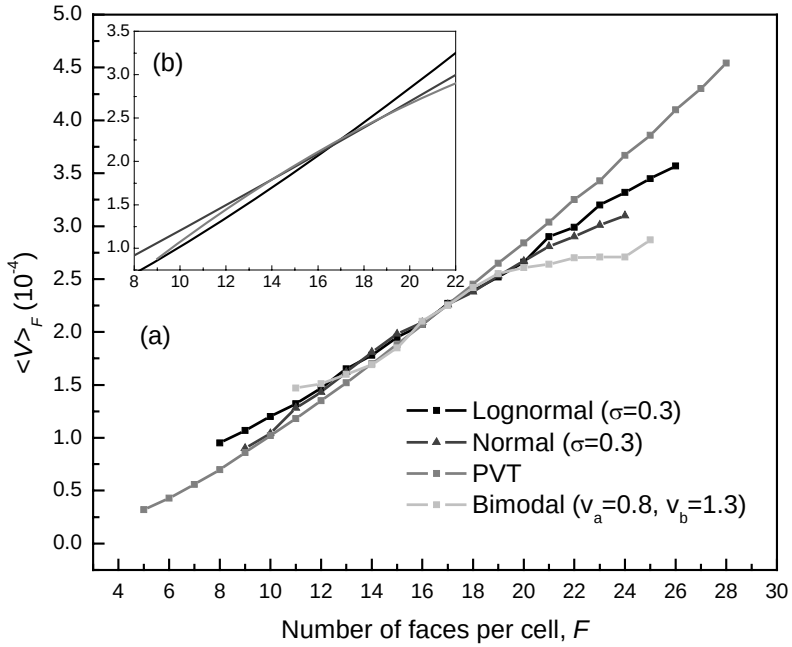

Figure 3.33. Lewis plots of four Voronoi tessellations with different cell volume distributions: 1) lognormal ($\sigma = 0.3$); 2) normal ($\sigma = 0.3$); 3) PVT; 4) bimodal ($v_a = 1.2$, $v_b = 1.3$).

The Lewis plots always intersect each other around $\langle F \rangle = 15.5335$ (Meijering's analytical result) and the linear relation is obeyed in the range close to $\langle F \rangle = 15.5335$. However, deviation from the linear relation starts to appear as the number of face per cell moving away from the intersection. In four cases, the lognormal distribution shows the most linear behavior in the whole range of face number. The PVT case comes in second where the relation between $\langle V \rangle_F$ and the number of faces per cell is best-fitted by a third order polynomial. Eqn 3.4(b) is fitted using one million data points in the case of PVT and a concave shape is observed especially around the lower limit in the face number. On the other hand, the VT with a normal cell volume distribution shows a convex shape. The VT with a bimodal cell volume distribution shows the most deviation from the linear relation where a concave shape is observed around the lower limit and a convex shape

around the upper limit. These results indicate that the Lewis relation is strongly affected by the cell volume distribution and violations are frequently found in the lower and upper limits of the face number.

3.2.5.2 Cell shape anisotropy

The increase in the cell volume variance in the lognormal case and the separation of the two modes in the bimodal case both lead to increase in cell shape anisotropy. To evaluate the cell shape anisotropy, we use the ratio between the actual cell surface area (S) [126] and the equivalent area of a sphere with the same cell volume. The ratio approaches unity if the cells are less distorted in shape (i.e., the three principal axis of the cell have equal length). Otherwise, it will be larger than unity (i.e., there will be more cell surface area for the cells with the same volume). We found that as the standard deviation of cell volume decreases, the ratio approaches closer to unity, or the Voronoi cells become more isotropic (Figure 3.34).

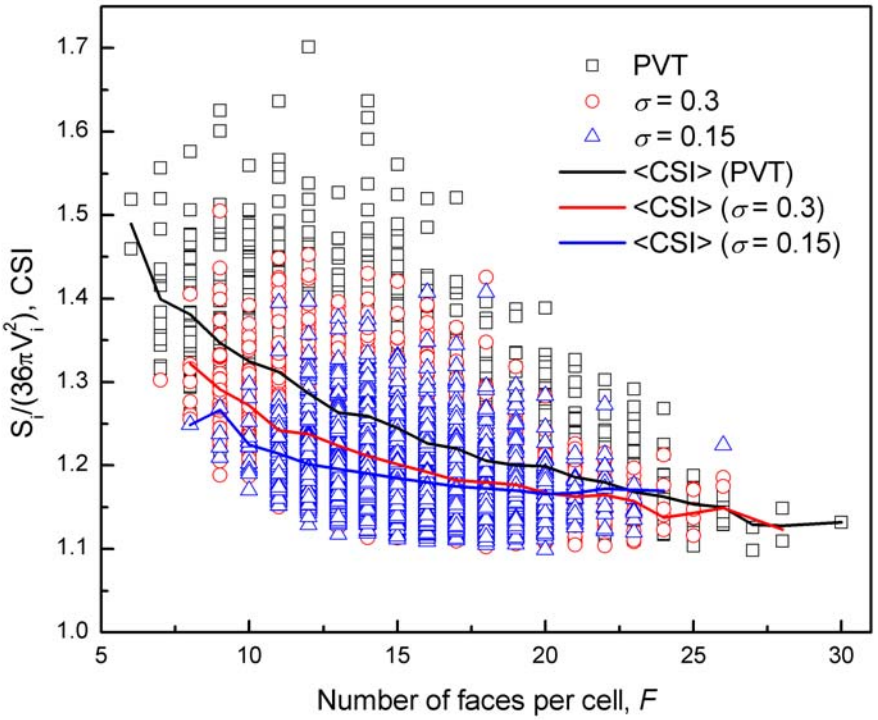

Figure 3.34. The cell shape isotropy (CSI) of the PVT and the two lognormal samples with the standard deviations of 0.15 and 0.3. For each sample, there are 5,000 CSI data points. The CSI of PVT is drawn first followed by two lognormal samples in the order of decreasing standard deviations. For each sample, the relation between $\langle CSI \rangle_F$ and F is also shown as a solid line using the same color as that of CSI plot.

The same happens in bimodal case (Figure 3.35). The cell shapes are less distorted, or more isotropic as the second peak moves further to the left, or closer to each other. The PV cells, which have the larger standard deviation in the cell volume, exhibit the largest anisotropy so far. Our results also indicate that the cell anisotropy becomes smaller for cells with a large number of faces. As we show below, this relation leads to some interesting consequences in the other topological properties.

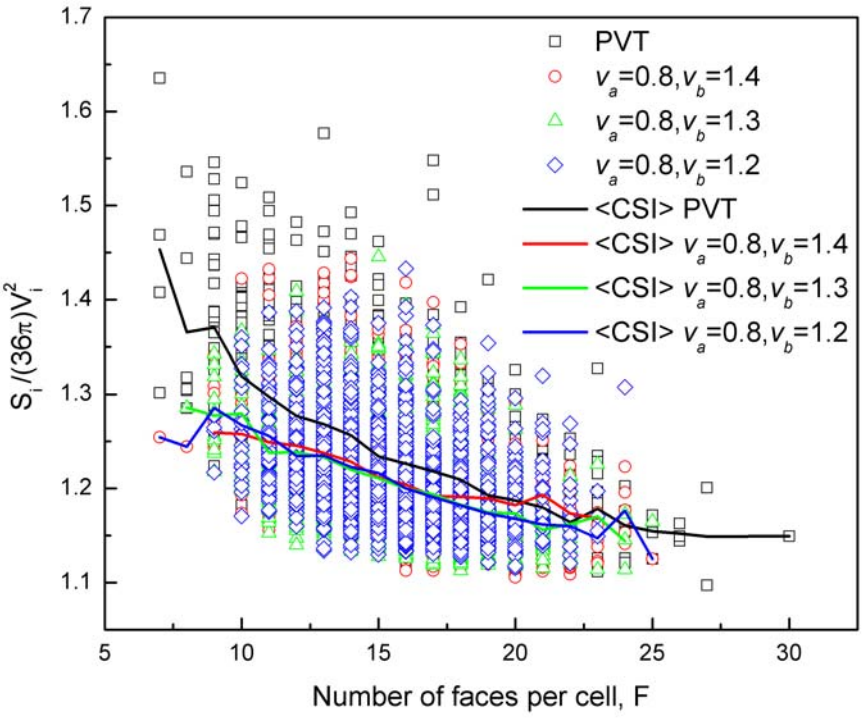

Figure 3.35. Cell shape isotropy of the PVT and three bimodal CVT samples with 2,000 points. For each sample, there are 2,000 CSI data points. The CSI of PVT is drawn first and that of three bimodal samples are superimposed according to the center of second peaks. The bimodal sample located at $v_b = 1.4$ is drawn first, followed by $v_b = 1.3$ and $v_b = 1.2$.

3.2.5.3 Point vs. sphere PV process

As we mentioned in the Introduction, rather than using the points to obtain PVT cells, one can use spheres of a finite radius. By setting finite radii for the particles, one imposes a region of inaccessibility for the neighbor cells, which automatically results in the cell shapes that are more isotropic than those in the point PV process. This sphere PV process is suitable naturally for cases such as Voronoi volume estimation for atoms with different sizes, or particles as in powder metallurgy [127-130], where the exclusive region around the atoms or spheres are present. Nevertheless, the general procedure of

generating desired cell volume distributions described for the point PV process could be used for general cases including the hard spheres.

However, there is a fundamental difference between point process and sphere process during VT. The shape of Voronoi cells generated by Laguerre-weighted method is more isotropic due to the disappearance of the short bond lengths and surface areas. It is reasonable to use Laguerre method on the application of VT on atomic configurations and hard sphere systems where the geometric limitation (sizes) comes into play due to the finite sizes of atoms and hard spheres. When it comes to study the microstructures in metallurgy, the Laguerre method is no longer applicable considering the fact that the volume of critical nuclei is usually small compared to the grain volumes.

3.2.5.4 Discrepancy between theoretical models and experimental observation

Poisson-Voronoi tessellation has been used widely for modeling microstructures in polycrystalline materials [100, 101]. The earlier work by Meijering [93] and others, and recent numerical simulation using Monte Carlo method for a Potts model [79] show close agreement with each other in the topological properties (See Table 3.1). However, some experimental measurements show obvious deviations from these results. For example, the average number of faces per cell ranges from 12.5 ~ 13.7 while $\langle F \rangle = 15.5335$, for Poisson-Voronoi tessellation. The same trend was found for the average number of edges per cell. This discrepancy is often considered as a sign of inadequacy for the PVT method in general for microstructure modeling. In the following, we will explain that the discrepancy may be caused by the nature of the PVT method and the VT cell anisotropy.

We examined the distribution of the face area (s) and edge length (l) carefully in our calculations for both PVT and CVT cells and found that there are many small faces and small edges (Figure 3.12). In addition, the larger the cell volume variance is, the

larger the numbers of these geometric entities. As the PV cells have the largest cell volume variance, they have the largest number of small areas and edges. In light of the discussion in the previous section, we also see that the less isotropic the cells are, the more small areas and edge lengths the cells have.

Besides the cell shape anisotropy, the lack of a natural length scale in the PVT and CVT method as well also contributes to the abovementioned results. For example, the smallest area and edge length in the PVT are on the order of 10^{-12} to 10^{-6}. Since the PV cells have no natural length scale, even the smallest area or edge, as long as they are within the computing machine accuracy, they are admissible as the right area and lengths. In both experiments and atomistic modeling of cellular structures as well, the length scales are determined by the size of the atoms or thermodynamic and kinetic parameters. As a result, some of the small faces and edges are no longer allowed (in Chapter 6). Therefore, the mean number of faces and edges in the PV cells can be overestimated as compared with the experimental results. To test this argument, we selected different cutoffs for the smallest admissible values in the area and edge calculations and then compute the average numbers of the remaining faces and edge lengths. Tests are performed on the same Voronoi cells. We start from no cutoff and then gradually increase the values of cutoff area and cutoff edge length. For each cutoff area, only faces with area larger than the cutoff area are counted. For each cutoff edge length, only edges with length larger than the cutoff edge length are counted. We found that $\langle F \rangle$ decreases dramatically initially when the cutoff for area increases while $\langle E \rangle$ decreases linearly with increasing cutoff for edge length. The relation between $\langle F \rangle$ and $s_{CUT} / \langle s \rangle \equiv x$ can be best-fitted by six-order polynomial:

$$\langle F \rangle = 595.77x^6 - 1566x^5 + 1603x^4 - 803.37x^3 + 213.18x^2 - 36.044x + 15.033 \qquad (3.7)$$

The linear relation between $\langle E \rangle$ and $l_{CUT} / \langle l \rangle$ can be best-fitted by:

$$\langle E \rangle = -23.168 l_{CUT} / \langle l \rangle + 39.64 \quad (3.8)$$

One can indeed obtain the right numbers of faces or edges if appropriate cut-offs are used. This finding points out that we may need to include these cut-offs in our CVT or IMC simulation in order to obtain the correct numbers of phases and edges in order to make the microstructure confirm to those found in experiments [96]. In fact, the experimental measurements also have some "natural" cutoffs depending on the experimental techniques with different resolutions such as the minimal pixel size. For example, the grain-finding algorithm used in image-segmentation procedure [96] is unable to detect the presence of crystalline volume less than the minimum-size virtual sphere.

3.2.5.5 Application of the CVT in microstructure modeling

Voronoi tessellation using the PVT method has been used widely to represent the microstructures of polycrystalline materials, ranging from the coarse-grained to nanocrystalline polycrystals [100]. However, except for some limited modifications made to include certain microstructure properties commonly encountered in experiments, such as the Johnson-Mehl weighted VT [103], few quantitative and systematic method has been developed to improve the PVT for representing/approximating the real microstructures. From the study shown in this work, we see that large deviations of the topological properties are expected for the PVT cells from those seen in experiments. The microstructures represented by PVT can in turn affect the physical properties of the materials obtained based on this model, which includes both the continuum modeling and atomistic modeling as well. Indeed, our recent atomistic simulation using the CVT method shows that as large as 15-30% change in mechanical properties, i.e., the yield strength, elastic modulus, and plasticity, can be achieved in nanocrystalline materials (Chapter 5), and even larger changes are expected in transport properties such as

diffusion in those materials if only the variance of the grain size distribution is considered. Some of our preliminary results show the same order of magnitude of changes can be expected in magnetic properties in nanomagnetic materials [131]. With the newly developed CVT, we plan to make more systematic studies to relate the microstructure-property relations in various polycrystalline materials.

3.2.5.6 Summary

We have developed a systematic space partition method to approximate the statistical and topological properties in cellular structures such as polycrystals and nanocrystals. The main feature of this method is the inclusion of some of the topological properties such as the cell/grain size distributions as the constraints for the PVT. The input constraints can be obtained either from experiments or from theoretical models. We used an inverse Monte Carlo method to implement the constraints. The constrained VT method is shown to have the capacity to produce cellular cells with specific topological and statistical properties.

Specifically, we found that as the standard deviation of lognormal cell volume distributions increases, the mean number of faces, edges, vertices per cell increase along with the mean value of bond angle in the entire sample. The mean value of the dihedral angle, however, decreases with the increasing standard deviation in the cell volume. The variances of the distribution in the number of faces and edges per cell also increase with increasing standard deviation of cell volume, along with that of cell surface area, cell perimeter, bond angle, and dihedral angle distributions. For the bimodal cell volume distributions, the mean numbers of faces, edges and vertices per cell do not shown systematic change as compared with those of the PVT, which might be partially attributed to the average taken from the two-mode distributions. The same applies to the mean values of bond angle and dihedral angles and the number of faces and edges per cell distributions, face area and edge length distributions. However, the distributions of

cell surface area and cell perimeter per cell exhibit large changes in the bimodal cases. In addition, we found that in general, Lewis's rule does not hold for lognormal cases studied; the most obvious violation is found for the PV cells; the linear relation is only obeyed when the range in the number of faces is small such as in the lognormal case with small standard deviation in the cell volume and in the randomly displaced fcc lattice. However, the Aboav-Weaire law holds for all cases. Moreover, we showed that as the standard deviation in the lognormal cell volume distributions decreases, or the two modes in bimodal distributions moves closer to each other, the Voronoi cells become more isotropic. The cell shape anisotropy is found to contribute to the changes in various topological properties.

The CVT method, although only tested in limited cases, is a general approach for producing cellular cells or grains with complex topological/microstructural properties. In our testing, we showed that the changes in the topological and statistical property are closely related to the changes in the VT cells that one produced, which in turn can lead to changes in physical properties in some of the widely used or modeled polycrystalline materials.

Chapter 4

Sample preparation

Once the grain cells, or grain boundary networks, are built, we still need another piece of information before filling atoms into the Voronoi structure, which is the crystallographic orientation or misorientation distribution of these Voronoi cells. Since the crystallographic orientation is closely related to specific crystal structure, we shall describe the procedure here for FCC crystals in section 4.1. The general procedure remains the same as long as the specific structure is known. Next, a random ray-crossing algorithm is described in section 4.2 to determine whether a lattice point is located inside or outside of a Voronoi grain cell. Finally, we will explain how to relax the rigid nc-Cu samples using MD relaxation in section 4.3.

4.1 Crystallographic orientation and misorientation distribution

Each Voronoi cell represents a grain with a specific crystal structure, like fcc, its orientation is determined by Euler angles, $(\alpha_i \quad \beta_i \quad \gamma_i)$ where i stands for the i_{th} grain. If the grain cell contains fcc lattice points, we can assign the orientation of the lattice points as follows: A reference single-crystal lattice is generated first with the [100], [010] and [001] directions coinciding with the Cartesian coordinates. The center of the reference lattice coincides with the origin of the Cartesian coordinates for the convenience of rotating the reference lattice. The specific orientation of the crystalline lattice points in the grain is therefore determined by the rotation matrix corresponding to the Euler angle,

$$\begin{bmatrix} \cos\alpha_i \cos\beta_i \cos\gamma_i - \sin\alpha_i \sin\gamma_i & -\sin\alpha_i \cos\beta_i \cos\gamma_i & \sin\beta_i \cos\gamma_i \\ \sin\alpha_i \cos\gamma_i + \cos\alpha_i \cos\beta_i \sin\gamma_i & -\sin\alpha_i \cos\beta_i \sin\gamma_i + \cos\alpha_i \cos\gamma_i & \sin\beta_i \sin\gamma_i \\ -\cos\alpha_i \sin\beta_i & \sin\alpha_i \sin\beta_i & \cos\beta_i \end{bmatrix}$$

(4.1)

Specific orientations as in texture can be produced if the distribution of certain crystallographic orientation is known. For random orientation, we can simply assign an orientation to each Voronoi cell by generating $3N$ random numbers, every three for a grain, that eventually give Euler angles for all grains, $(\alpha_i \quad \beta_i \quad \gamma_i)$, $i = 1 \cdots N$, where N is the total number of grain cells.

More elaborate efforts, however, are needed in building misorientations for polycrystalline samples. Since the orientation of each grain can be expressed as a 3×3 matrix shown in Eqn. (4.1), O_i, a misorientation of two adjacent grains forming a grain boundary is described by the misorientation matrix $M_{ij} = O_i O_j^{-1}$ [132], where O_i and O_j are the orientation matrixes of two adjacent grains *i* and *j*. Defined as the minimum rotation angle between two neighboring lattices, the misorientation angle can be expressed by the following equations based on the *angle:axis* format,

$$\theta = \cos^{-1}\left(\left[trace(M) - 1\right]/2\right) \tag{4.2}$$

and the axis is determined by

$$u : v : w = (M_{32} - M_{23}) : (M_{13} - M_{31}) : (M_{21} - M_{12}) \tag{4.3}$$

Due to the crystal symmetry in fcc materials, the maximum misorientation angle between any two grains is 62.8°. For fcc metals, there are 24 crystal symmetry operators in the space group of O_{432}. By applying the symmetry operators to the misorientation matrix, M_{ij}, we can determine the misorientation angle of each grain boundary as the minimum required rotation angle according to the following relation, $\theta = \min\left|\cos^{-1}\left\{tr\left(O_{432} M_{ij} - 1\right)/2\right\}\right|$. Consequently, the misorientation *angle:axis* pair can

be calculated for each boundary as well as the misorientation distribution function $P(\theta, \Delta\theta)$ that defines the probability of finding a grain boundary with a misorientation angle between θ and $\theta + \Delta\theta$.

In real polycrystalline materials, the misorientation angles take different distributions among which the simplest one follows the random distribution, or the MacKenzie distribution [133]. The mean misorientation angle, $\overline{\theta}$, for MacKenzie distribution is 40.831°. In order to obtain a misorientation distribution different from MacKenzie distribution, a Monte Carlo optimization procedure similar to the one applied to the polycrystalline grains in a Potts model [132] is developed. The MC optimization is performed on the grain cells obtained from the constrained Voronoi tessellation method discussed in Chapter 3. Initially, each grain cell is assigned a random orientation. Through the MC minimization, we can obtain a minimized misorientation distribution with a majority of low-angle grain boundaries. The MC procedure to obtain a minimized misorientation distribution is summarized below:

(1) Construct a Voronoi structure of N cells obtained from the constrained Voronoi tessellation and identify all interfaces presented in the structure;

(2) Assign each cell a random orientation (Eqn. 4.1) and calculate the misorientation angle of each interface and the mean misorientation angle, $\overline{\theta} = \sum_{i=1}^{N} \overline{\theta}_i / N$, where $\overline{\theta}_i = \sum_{j=1}^{M_i} \theta_j / M_i$ is the mean misorientation angle of each cell and M_i is the number of interfaces in that cell.

(3) Sort all cells in descending order of $\overline{\theta}_i$ and select cells in the top 5% on the list. The orientations of the selected cells are changed randomly and the new mean misorientation angle, $\overline{\theta}'$, is calculated.

(4) If $\overline{\theta}'$ is smaller than $\overline{\theta}$, then accept the change; if $\overline{\theta}'$ is larger than $\overline{\theta}$, but still satisfies $\exp(-\Delta\theta / kT) \geq \xi$, where ξ is another random number between 0 and 1, then keep the move; otherwise, reject the move.

(5) Go to step (3) until a preset limit is reached or convergence is slow.

Using the algorithm, we produce a minimized misorientation distribution with a mean misorientation angle, $\overline{\theta}$, of 10.496° (Figure 4.1). Using the same algorithm, except that we reverse the order in selecting the misorientation angles in step 4 above, we can obtain a maximized misorientation distribution on Voronoi cells that contains a majority of high-angle grain boundaries with a mean misorientation angle of 46.705° (Figure 4.1). Any misorientation distributions with a mean misorientation angle between 10.496° and 40.831° can also be extracted during the MC simulation. This can be done by simply stopping the MC optimization process when a desired intermediate misorientation distribution is reached.

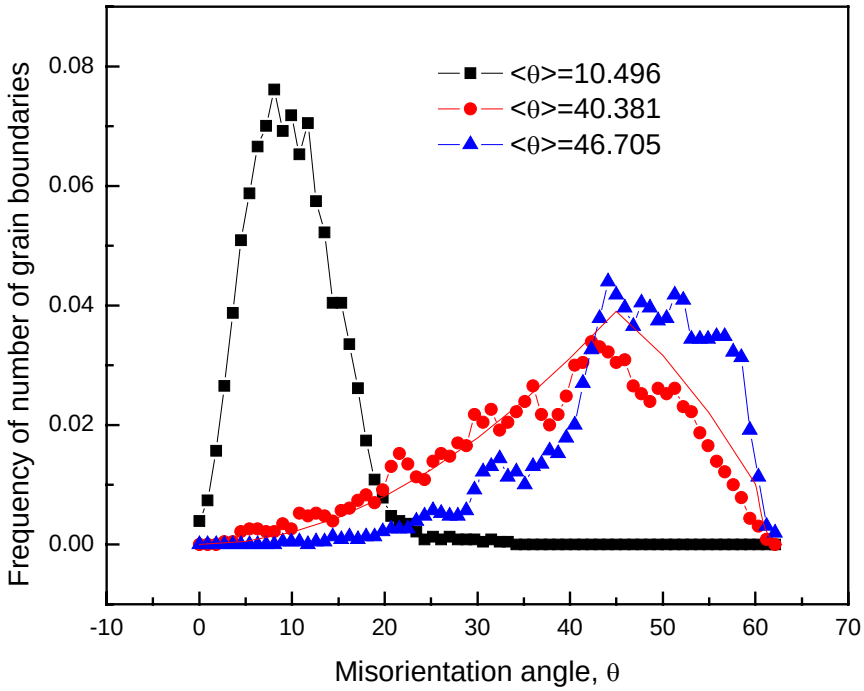

Figure 4.1. The distributions of misorientation angles for a sample with 50 grains. The black square represents the distribution with a minimized misorientation with the mean misorientation angle at 10.496°, the filled green triangle represents the distribution with a maximized misorientation with the mean misorientation angle at 46.705°, and the filled red circles represents an intermediate distribution.

4.2 Atomic structure of grains

Once the grain cell topological structure, orientation and misorientation are constructed, we are ready to fill each empty grain cell with atoms of our choice that have a specific atomic structure, specific size, shape, number of neighbor grains, crystallographic orientation and misorientation. Each grain cell is given a grain index (GI) and all the atoms inside each grain are specified with the coordinates within the sample. The information is needed for carrying out atomistic calculations later.

There are several ways to "fill" the empty dimension-less grain cells with atoms of specific lattice structure. A commonly used on is to select *N* single crystals with

random orientations, each for a grain. The atoms that are supposed to belong to, say the i_{th} grain cell would have no overlapping with atoms in any other $N-1$ grains. In another word, the atoms that overlap with the atoms in other grains would be discarded. So at the end, only the atoms without overlapping with others are kept. The "overlapping" is therefore used as a criterion to decide which atom should belong to each grain cell. In this work, we shall adopt more precise approach that is free of ambiguities when the overlapping is not that obvious and the desired grain boundary locations are affected by the overlapping.

A random ray-crossing algorithm [134, 135] is used to determine whether a lattice point is inside or outside of a Voronoi grain cell. First, we select N single crystal lattices that the specific lattice structure, e.g. *fcc*; and the coordinates of the lattices would have a common origin with the sample of the Voronoi cells. We then rotate each single crystal lattice according to the orientation information prescribed in section 4.1 that also gives the desired misorientation distribution. The next step is to examine the lattice points in each single crystal lattice to see which one belongs to the grain cell. To do so, we use the ray-crossing method: from each lattice point, randomly orientation rays of infinite length are generated and the number of intersections between each random ray and the interfaces of the grain cell is counted. If the number of crossing made by the ray for a lattice point is odd, then it is inside the Voronoi grain cells or polyhedron; If the number of crossing is even, then that lattice pint is located outside of the cell. Further geometrical tests can reveal whether a lattice point is located on the surface, triple junction or vertex of a grain cell.

Specifically, in order to use the ray-crossing algorithm to determine if a lattice point belongs to a grain cell, we need the solutions of a ray that crosses a grain boundary face. Since the faces are polygons, triangulation needs to be performed on all faces of the grain cell. We can then solve linear equations for the coordinates of the possible intersections between a random ray and a non-overlapping triangle on a face, so the

number of "crossing" can be determined. The detailed algorithm can be found in Appendix A.

For each grain cell, only the lattice points located inside the polyhedron are kept. The same procedure is applied for every cell and the Cartesian coordinates of those selected lattice points form the atomic structure of a polycrystalline sample. It is worth to mention in passing that in doing so, one must use the same unit for both the lattice and the polycrystalline sample or Voronoi grain cells: If one uses the reduced unit between [-0.5, 0.5], for the sample with a actual physical length L of a cube box, one must the lattice parameter of the crystal lattice for the grain cells scaled by the box length, or $\alpha = a_0 / L$, where α is the reduced lattice parameter and a_0 is the actual lattice parameter. For *fcc* copper, the lattice constant is 3.615Å. Of course, one would obtain the actual positions and lengths for the atoms later by multiplying the coordinates by a_0 / α. Besides, one should also take caution to deal with the atoms in adjacent grains that might have overlapped during the process. Since the ray-crossing method deals with (lattice) points while atoms have a physical size, it is inevitable to have some atoms near certain grain boundary that are closer than the equilibrium interatomic distance, or they may overlap with each other. Atoms that are too close, say less than 85% of the nearest neighbor distance, must be removed to avoid unphysical high repulsive potential energy during molecular dynamics simulation to be carried out later. Another critical condition that must be satisfied is that the reference single crystal lattice must be large enough to cover the 3D Voronoi structure during rotation operations. In this case, we chose a cubic shape for the reference lattice with a box length of L_{ref} and the following condition must be followed: $L_{ref} \geq (a_0 / \alpha)\sqrt{3}$. A schematic drawing can be found in Figure 4.2 that shows the relative size and position of the reference lattice with respect to the actual sample with a physical box size. By modifying the reduced lattice constant, atomic structures of different mean grain sizes can be easily achieved.

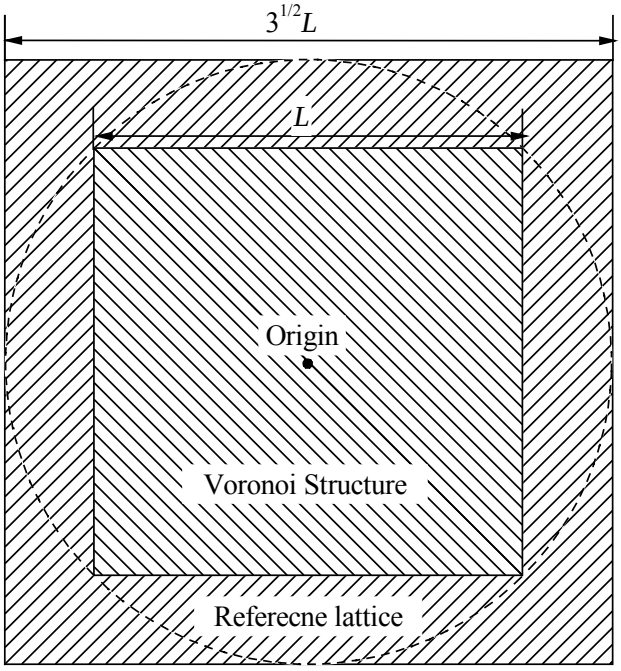

Figure 4.2. Projection of 3D Voronoi structure and reference lattice onto a 2D plane. The box length of reference lattice must be larger than $\sqrt{3}L$ to cover the domain of Voronoi structure during rotation around the origin.

4.3 Relaxation of thermal stability test of the atomic structures

The atomic structure established using the method described previously is not in equilibrium and must be relaxed; and sometimes additional "heat treatment" is also needed in order to get rid of the more persistent meta-stable configurations. The relaxation is performed using MD simulations. Since most polycrystalline materials are isotropic, we use the Gibbs ensemble, or constant pressure and temperature MD. The typical MD simulation is performed at various temperatures and zero external pressure, so not only can the sample volume but also individual atom changes position freely from the initial "rigid" values to the equilibrium ones. The criterion to judge if a sample reaches the steady state is to check the change of the total configuration energy and volume versus the simulation time; we terminate the run if the energy and volume are

leveled off and approach steady values. The fully relaxed samples will then be kept for various uses later, including probing mechanical behaviors, phase transitions, and transport properties.

In this section, we will describe the molecular dynamic simulation method used to relax the rigid *nc*-Cu samples. In section 4.3.1, we will give a brief introduction of MD method. In section 4.3.2, we discuss the atomic potential selected for simulating *nc*-Cu samples, which is embedded atom method (EAM). In section 4.3.3, we will present the procedure to perform MD relaxation and test the stability of the potential chosen for simulating *nc*-Cu samples.

4.3.1 Molecular dynamics method

During the past few decades, molecular dynamics simulation has been successfully applied to study the properties of a variety of physical systems under different physical conditions [136, 137], which is a method for studying classical statistical mechanics of well-defined systems through a numerical solution of Newton's equations. In MD simulations, atoms interact with each other through an atomic potential and the motion of each atom is determined by Newton's second law. By solving the equation of motion of all atoms in the physical system, the velocity and position of each atom at different time can be obtained. As the system evolves in time, it eventually reaches an equilibrium state. The statistical averages of physical properties are calculated as temporal averages over the trajectory of the system in its phase space. To simulate the property of a bulk material, periodic boundary conditions are usually applied by repeating a unit cell of volume V containing N particles.

To simulate a physical system at different physical conditions, several ensembles can be applied. For example, the number of particles N, system volume V and the total energy E are kept constant during MD relaxation in a NVE ensemble. NVE ensemble is

suitable to study the physical system in equilibrium conditions. The lagrangian of the system of *N* particles is

$$L = \sum_{i=1}^{N} \frac{1}{2} m_i \dot{\vec{r}}_i^{\,T} \dot{\vec{r}}_i - \sum_{i=1}^{N} \sum_{j>i}^{N} \phi\left(r_{ij}\right) \tag{4.4}$$

where *i* represents the *i*th particle, m_i represents the atomic mass of the *i*th particle, $\dot{\vec{r}}_i$ represents the velocity of a particle, $\dot{\vec{r}}_i^{\,T}$ is the transpose of $\dot{\vec{r}}_i$, r_{ij} represents the distance between a pair of particles and $\phi\left(r_{ij}\right)$ is the interatomic potential. The equation of motion for each particle can be derived from equation (4.4) using the relation,

$$d\left(\partial L / \partial \dot{\vec{r}}\right) / dt = \partial L / \partial r_{ij}, \tag{4.5}$$

$$\text{as } \ddot{\vec{r}}_i = -\frac{1}{m_i} \sum_{j \neq i} \frac{\phi'\left(r_{ij}\right)}{r_{ij}} \left(\vec{r}_i - \vec{r}_j\right) \tag{4.6}$$

where $\phi'\left(r_{ij}\right)$ is the first derivative of the interatomic potential.

In order to accommodate different physical conditions, Parrinello and Rahman proposed a method to allow both volume and shape of the simulation box to change during the simulation. This method is also known as the Parrinello-Rahman molecular dynamics (PRMD) during which the number of atoms, pressure and enthalpy of the system are kept constant (namely, the NPH ensemble). A 3×3 shape matrix, $h = \left(\vec{a}, \vec{b}, \vec{c}\right)$, is introduced to provide the extra degree of flexibility where the simulation box can have arbitrary shape and volume described the three vectors $\vec{a}$, $\vec{b}$ and $\vec{c}$. The position vector $\vec{r}_i$ of a particle *i* is scaled with the shape matrix, *h* as $\vec{r}_i = h\vec{s}_i$. The lagrangian of the system when only hydrostatic pressure is applied is

$$L = 1/2 \sum_{i=1}^{N} m_i \dot{\vec{s}}_i' G \dot{\vec{s}}_i - \sum_{i=1}^{N} \sum_{j>i}^{N} \phi\left(r_{ij}\right) + 1/2 Tr\left(\dot{h}^T \dot{h}\right) W - PV, \tag{4.7}$$

where $G = h^T h$ is the metric tensor, W is the mass of a fictitious "piston" that controls the pressure, Tr is an operator calculating the trace of a matrix and P is the hydrostatic pressure. The equation of motion can be easily found from Eqn. (4.7),

$$\dot{\vec{s}}_i = -\sum_{j \neq i} \frac{m_i^{-1} \phi'(r_{ij})(\vec{s}_i - \vec{s}_j)}{r_{ij}} - G^{-1}\dot{G}\dot{\vec{s}}_i \tag{4.8}$$

$$\text{and } W\ddot{h} = (\pi - P)A, \tag{4.9}$$

where $A = Vh^{-T}$ is an area tensor, $V = \det h$ is the volume of the simulation box and π is the microscopic stress tensor

$$\pi V = \sum_i m_i \vec{v}_i \vec{v}_i - \sum_i \sum_{j>i} \phi'(r_{ij}) \vec{r}_{ij} \vec{r}_{ij} / r_{ij} \tag{4.10}$$

where $\vec{v}_i = h\vec{s}_i$ is the velocity vector.

However, Eqn. (4.8) is not valid when an external stress σ is applied to the system. A strain tensor induced by the external stress can be defined as

$$\vec{\varepsilon} = 1/2(h_0^T G h_0^{-1} - 1). \tag{4.11}$$

where h_0 is the reference matrix before the box shape change under external stress. By introducing a symmetric tensor Γ, Eqn. (4.8) can be replaced by

$$\ddot{h} = \frac{1}{W}(\pi - P)A - h\Gamma, \tag{4.12}$$

$$\text{and } \Gamma = h_0^{-1}(\sigma - P)h_0^T V_0. \tag{4.13}$$

Using NPH ensemble, the box shape and volume can respond to the external pressure or stress, however the temperature of the system cannot be controlled.

The above two ensemble obviously are not suitable for relaxing the *nc*-Cu sample generated earlier because the temperature are not controlled. If not controlled properly, the grain boundary network presented in the sample may be damaged by thermal fluctuation. In our case, we must find a way to control the system temperature and

pressure at desired values and use the NPT ensemble. One commonly used method to keep the temperature constant during MD simulation is the Noses method [136, 137]. A scaling variable q is introduced in this method and the velocity of i_{th} particle can be written as $\dot{\vec{r}}_i = h\dot{\vec{s}}_i q$. The Lagrangain of the system becomes

$$L = 1/2\sum_{i=1}^{N} m_i q^2 \dot{\vec{s}}_i^T G\vec{s}_i - \sum_{i}^{N}\sum_{j>i}^{N}\phi(r_{ij}) + 1/2W \cdot Tr(\dot{h}^T \dot{h}) - PV$$

$$+ 1/2Q\dot{q}^2 - (3N+1)k_B T_{eq} \ln q\,, \qquad (4.14)$$

where Q is a fictitious mass coupling the scaling variable q to the system. The new equation of motion in NPT ensemble is

$$\ddot{\vec{s}} = -\frac{1}{m_i q^2}\sum_{j\neq i}\frac{\phi'(r_{ij})(\vec{s}_i - \vec{s}_j)}{r_{ij}} - G^{-1}\dot{G}\dot{\vec{s}}_i - 2\dot{q}\dot{\vec{s}}_i / q\,. \qquad (4.15)$$

NPT ensemble is often used when full periodic boundary condition are applied. In the section 4.3.3, we will relax the nc-Cu sample using the NPT ensemble in order to keep the grain boundary network in the sample stable. NVT ensemble is another type of ensemble used in MD simulation in which the Nose variable is introduced into the NVE ensemble to control the temperature. NVT ensemble is especially useful to simulate a system without full periodic boundary condition.

4.3.2 Interatomic potential for copper

Atomistic simulations are becoming an increasingly powerful tool for studying the structure and properties of materials. Interatomic potential is the key for carrying out successful molecular dynamics simulations. An accurate and efficient potential will lead to reliable and quick results. Most experimental and simulations works so far are concentrating on pure nanocrystalline materials such as Cu, Ni, Al, Pd, etc. Potentials for *fcc* metals have been extensively studied and reliable potentials are produced and tested,

especially for copper. We shall focus on the *nc*-Cu samples since our purpose is to compare the effects of microstructure.

Simulation methods generally fall into two classes, the *ab initio* or first-principle methods, and the semi-empirical methods. The *ab initio* methods involve solving the Schrödinger's equation with various degrees of approximation; these techniques are generally limited to very small systems due to the limitation of computing power. The semi-empirical methods are capable of treating much larger systems (thousands to millions of atoms), but their success is limited by the reliability of their potentials. Pair potentials have previously been popular for metals, but they suffer from two major errors: the vacancy-formation energy and C12=C44. To overcome the limitations of pair potentials, Daw and Baskes [138, 139] developed a model of metallic cohesion known as the embedded-atom method (EAM). It is more general than pair potentials, in that it involves many-body interactions. The EAM is based on density-functional theory, which asserts that the energy of a material can be written as a unique functional of the electron density. In the EAM, the important aspect of the electron density is assumed to be the local electron density at each atomic site, as provided by the surrounding atoms. The total energy is divided into an electrostatic interaction plus an embedding energy, which is the energy required to place an atom in a uniform electron gas.

Thus, the total energy of an arbitrary arrangement of atoms is given by

$$E_{total} = \sum_i F_i\left(\rho_{h,i}\right) + \frac{1}{2}\sum_{i,j(i\neq j)} \phi_{ij}\left(R_{ij}\right) \tag{4.16}$$

$$\rho_{h,i} = \sum_{j(\neq i)} f_j\left(R_{ij}\right) \tag{4.17}$$

where $F_i(\rho)$ is the embedding energy of i_{th} atom, $\rho_{h,i}$ is the host electron density at atom i due to the surrounding atoms, $\phi_{ij}\left(R_{ij}\right)$ is a short-ranged electrostatic interaction between atom i and atom j, R_{ij} is the distance between atoms, and the sums are over all

atoms. f_i is the electron density of atom *j* as a function of distance from its center. The host electron density is approximated by the superposition of atomic electron densities. The embedding energy is assumed to be independent of the electron distribution or gradients.

These equations are identical in form to those proposed by Finnis and Sinclair [140], for an atomistic model for metals. The interpretation is quite different from EAM where the FS derivation is based on tight-binding theory, with $F_i(\alpha_i)$ proportional to the square root of α_i and α_i being the linear superposition of squares of overlap integrals. EAM potential has been successfully applied on *fcc* metals including Ni, Cu, Fe, Pd, Au and Ag.

4.3.3 MD Relaxation and Thermal stability of EAM copper potential

The energetic and mechanical stability of non-equilibrium structure using EAM potential is essential to study the grain boundary structure. Y. Mishin [141] *et al* evaluated the ability of the EAM potential to predict reliable energies and stabilities of non-equilibrium structures by taking copper as a model material. They reported that excellent agreement is observed between *ab initio*, tight-binding and EAM results for energies and stability of several non-equilibrium structures of copper, as well as for energies along deformation paths between different structures. EAM copper potential is suitable for simulations in which correct energies and stability of different atomic configurations are essential. To test the thermal stability of EAM copper potential, a *nc*-Cu sample is generated by filling atoms into 200 Voronoi cells. The total number of atoms is 1396178 and the box length is 25.83 nm. The mean grain size is 5.478 nm. EAM potential developed by Foiles [139] is used for the simulation. NPT Molecular dynamic relaxation is then performed at 300K for 100,000 time steps to fully relax the nc-Cu sample using the Large-scale Atomic/Molecular Massively Parallel Simulator

(LAMMPS) package developed by the Sandia National Laboratories. The time step is 0.005 ps.

Figure 4.3 shows the atomic positions of the smallest grain before and after the MD relaxation. The red atoms represent atoms before relaxation and the blue atoms represent atoms after relaxation projected in <111> direction. We can clearly see that most atoms inside the grain vibrate around their initial positions. Only a few grain boundaries atoms migrate to a distance larger than one lattice constant. It is clear that even the smallest grain in the nc-Cu sample is stable enough to vibrate around its original lattice position after relaxation.

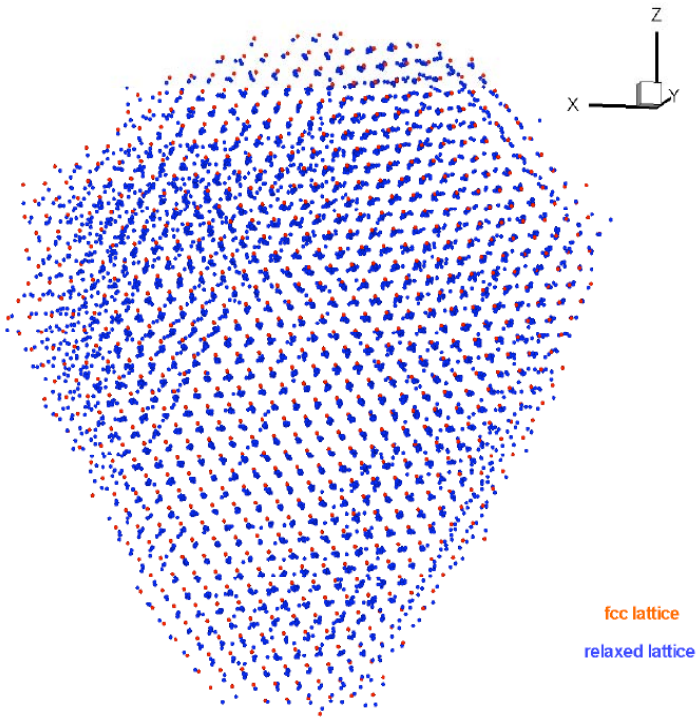

Figure 4.3. The projections of smallest grain in <111> before and after relaxation. The red atoms represent the initial atomic positions and the blue atoms represent the atomic positions after relaxation.

4.4 Summary

In this chapter, we present a procedure to generate a *nc*-Cu sample. Both Monte Carlo and MD methods are applied during the procedure. The dimensionless Voronoi structure and the corresponding misorientation distribution are generated using the MC method. After atoms are filled into the Voronoi structure using the random ray-crossing technique, MD simulation using EAM potential are performed in NPT ensemble to relax the rigid grain structure. Finally we obtain an equilibrated *nc*-Cu sample with a stable grain boundary structure. In the following study, *nc*-Cu samples of different mean grain sizes, number of grains and misorientation distributions are generated, which enable us to study the effects on the topological and thermodynamic properties of *nc*-Cu samples by various parameters such as mean grain sizes, temperature, misorientation distributions, etc.

Chapter 5

Atomistic grain boundary characterization

5.1 Introduction

Polycrystalline materials are made of aggregates of single crystallites or grains with the mean grain size ranging from nanometer to microns. They constitute the largest fraction of all materials used today. When assembled, the grains come into contact with each other, forming the so-called microstructure. As compared with single crystals and homogeneous phases such as glass and liquid, polycrystalline materials have complex microstructures composed of an array of *topological entities* with multi-dimensions, including vertices (zero dimension) formed at a contact point with four or more grains, triple junction lines (one dimension) formed by three intercepting grain boundary planes, interfaces or grain boundaries (two dimensions) formed between two adjacent grains, and grain volumes (three dimensions). The collection of these microstructure attributes forms the *statistical ensembles* from which the distributions and some of the means, variances and higher moments can be measured experimentally. For example, mean grain size often measured by grain diameter can be obtained from variety of techniques [101, 142] whereas the triple junction length and interface area are hard to measure directly, not to mention the vertices which are much smaller in volume fraction and lack of long-range atomic order. The material properties of polycrystalline materials are therefore a collective response from all these microstructure attributes. The well-known case is the so-called Hall-Petch relation that relates the onset yield stress of a polycrystalline metal to its mean grain size [1, 2]. Besides the topological entities, *crystallographic properties* of each individual grain also play important roles in polycrystalline materials. They include the crystallographic orientation of each grain and grain boundary misorientation

[143] which is measured by the relative orientation angle(s) of two adjacent grains. A preferred crystallographic orientation, for instance, can lead to texture and strong anisotropy in physical properties. The misorientation, on the other hand, is intimately related to the nature and structure of grain boundaries formed by the neighboring grains [101, 142-144]. Different types of grain boundaries respond differently to mechanical and thermal as well as other external stimuli [145]. The disordered boundaries are more susceptive to applied stresses, such as in fracture and creep, and thermal agitation, as compared with the more ordered ones [145, 146]. The last attribute that determines the microstructure-property relations of a polycrystalline material is *atomic structures and chemistry* of the topological attributes. Detailed atomic structure and chemical composition of both the grains and grain boundaries, for example, can impart dramatic changes to the material properties as evidenced in impurity segregation induced embrittlement [147] and intergranular fracture [148]. Therefore, the microstructure properties in polycrystalline materials can be classified as being composed of the four types of attributes: *topological*, *crystallographic*, *atomic structures*, and their *statistical properties*. These attributes are also known to relate to and influence each other. For example, as mentioned above, the misorientation correlates closely to the structure of grain boundaries; a moving grain boundary enriched with segregating atoms could alter the grain growth kinetics, leading to different final grain size and shape; and the change of the mean grain size can lead to changes in the relative volume fraction of vertices, triple junction lines and grain volumes, which is the major cause for many outstanding properties in the recently developed nanocrystalline materials which are simply a polycrystalline material with just smaller mean grain sizes [63, 149, 150].

These microstructure attributes have long been the subject of scientific research and industrial development. But the complexity and intricate interplay among the microstructure attributes still impose a formidable challenge. As compared with single crystals and those with dilute defects and imperfections, characterizing these

microstructure properties quantitatively proves to be much tedious and difficult. As a result, different probes must be used for the variety of microstructures with different resolutions. For example, misorientation and texture can be determined using backscattering or orientation image microscopy (OIM); grain boundary and triple junction structures can be determined using Mössbauer spectrometry in conjunction with x-ray diffractometry, transmission electron microscopy (TEM) or small angle neutron scattering [142]. (Although Mössbauer spectrometry can provide information about the grain boundary network as whole, it is still impossible to give detailed atomic information about each grain boundary interface and grain boundary triple junction.) Grain size and shape can be measured using various scattering and stereological methods, provided that the mean grain size is comparable in length scale with that used in the probes, say, the wavelength of light for optical microscopy. The difficulty becomes more acute for nanocrystalline materials, which have the mean grain size typically in the range between a few to a hundred nanometers. The small size and increasing volume fraction of the low dimensional microstructure attributes such as grain boundaries (GBs), triple junctions (TJs), and vertex points (VPs) render most of the traditional characterization methods ineffective and less accurate [63, 149, 150].

These difficulties form the motivation for developing alternative approaches to acquire the microstructure-property relations using *numerical modeling* such as finite element method (FEM) and atomistic simulation. For continuum modeling of polycrystalline materials using FEM, one can import microstructures from digitized micrographs taken from real samples [151]. In conjunction with other inputs, such as texture or misorientation obtained separately, one could start the calculation with reasonable expectation of obtaining a quantitative microstructure-property relation. In doing so, however, one obviously ignores other microstructure properties such as the atomic structure, thickness and chemistry of grain boundary and triple junctions. Besides, this approach is often limited to two-dimensions since acquiring a full three-dimensional

microstructure requires considerable amount of efforts [101]. For nanocrystalline materials, this approach is out of the question due simply to the small grain sizes and large number of grains involved. An alternative approach involves creating the so-called digital microstructure (DM) based on some geometric constructions such as Poisson-Voronoi construction (PVC) [9, 152]. The PVC partitions a space into individual cells made of convex polyhedron that *visually* resemble the polycrystalline grains typically observed in many materials, such as steels and cast irons [153]. This method has been used extensively in both continuum and atomistic simulations, especially in molecular dynamics (MD) simulation of nanocrystalline materials recently [9, 152]. However, it has not been evaluated systematically and quantitatively for the microstructure attributes mentioned above and compared with experimental ones. As we pointed out recently [14], the microstructures created from the default PVC have many differences from real microstructures, which could lead to significant changes in the properties. On the other side, real polycrystalline materials, especially nanocrystals, contain many imperfections and flaws introduced during synthesis. These extrinsic structural entities contribute to property change that often obscure the observation of intrinsic properties that, as the first order of any theoretical work, should be acquired. Therefore, it is highly desirable to have a systematic and reliable approach to render microstructures that can be used for the numerical calculations of the relations between the microstructure and the intrinsic property of polycrystalline materials. Without an accurate description of grain boundaries presented in *nc* materials, it is impossible to determine the most dominant factors that control the evolution of microstructures during plastic deformation or thermal activities.

In this chapter, we will first try several commonly used methods to analyze the grain structure in the relaxed *nc*-Cu sample. We then propose a new and accurate method to identify multi-dimensional grain boundary features presented in the relaxed *nc*-Cu sample. Using this method, we can identify atoms in each GB entity including GB interfaces, triple junctions and vertices. Furthermore, we are able to determine the

surface normal of GB interface and obtain the potential energy, atomic Voronoi volume and atomic stress profile across each grain boundary interface. Finally, we study the influence on the grain structures temperature, grain size and misorientation distributions.

5.2 Structure analysis

Using the procedure described in Chapter 4, *nc*-Cu samples of stable grain structures are generated. However, a dramatic change in the structure of the nc-Cu sample from the Voronoi structure should be expected due to the transition from a dimensionless structure to the atomic structure with an actual size, especially after MD relaxation. Therefore, we need to find a reliable and accurate way to determine the grain structure before additional mechanical tests can be performed on the relaxed *nc*-Cu samples. In this section, we will test several commonly used methods in an attempt to characterize the structure of the *nc*-Cu samples.

5.2.1 Radial distribution function

Radial distribution function (RDF), also called the pair correlation function, $g(r_{ij})$, has been widely used to characterize the structure of materials [136]. This function gives the probability of finding a pair of atoms a distance r_{ij} apart, relative to the probability expected for a completely random distribution at the same density. Because of the large number of atoms in a typical *nc*-Cu sample, the computation time required to calculate the distance between every pairs of atoms is extremely time-consuming. A cutoff distance R_C is normally selected to reduce the amount of calculation. For each atom, only distances to neighbor atoms within the cutoff distance are recorded. The calculated pair distances are then converted to the RDF. Let us assume there are N atoms in a *nc*-Cu sample with a volume of V. The average number of atom pairs with a distance between r and $r + dr$, $\langle \Delta N_i(r) \rangle$, is

$$\left\langle \Delta N_i(r) \right\rangle = \sum_{i=1}^{N} \Delta N_i(r) / N \,, \qquad (5.1)$$

where $\Delta N_i(r)$ is the number of atoms in the shell between r and $r + dr$ for the ith atoms. Dividing the volume of the spherical shell between r and $r + dr$ give us the density in the shell

$$\rho(r) = \sum_{i=1}^{N} \Delta N_i(r) / 4\pi N r^2 dr \,. \qquad (5.2)$$

The radial distribution function can be obtained by dividing Eqn. (5.2) by the average density of the sample, $\overline{\rho} = N/V$,

$$g(r) = \rho(r) / \overline{\rho} = V \sum_{i=1}^{N} \Delta N_i(r) / 4N^2 \pi r^2 dr \,. \qquad (5.3)$$

Figure 5.1 shows the RDFs of a *nc*-Cu sample of 200 grains at different temperature from 350K to 900K. Although this method can clearly detect the increasing degree of disorder in the whole sample with increasing temperatures, it does not offer the flexibility to identify each GB entity presented in the sample.

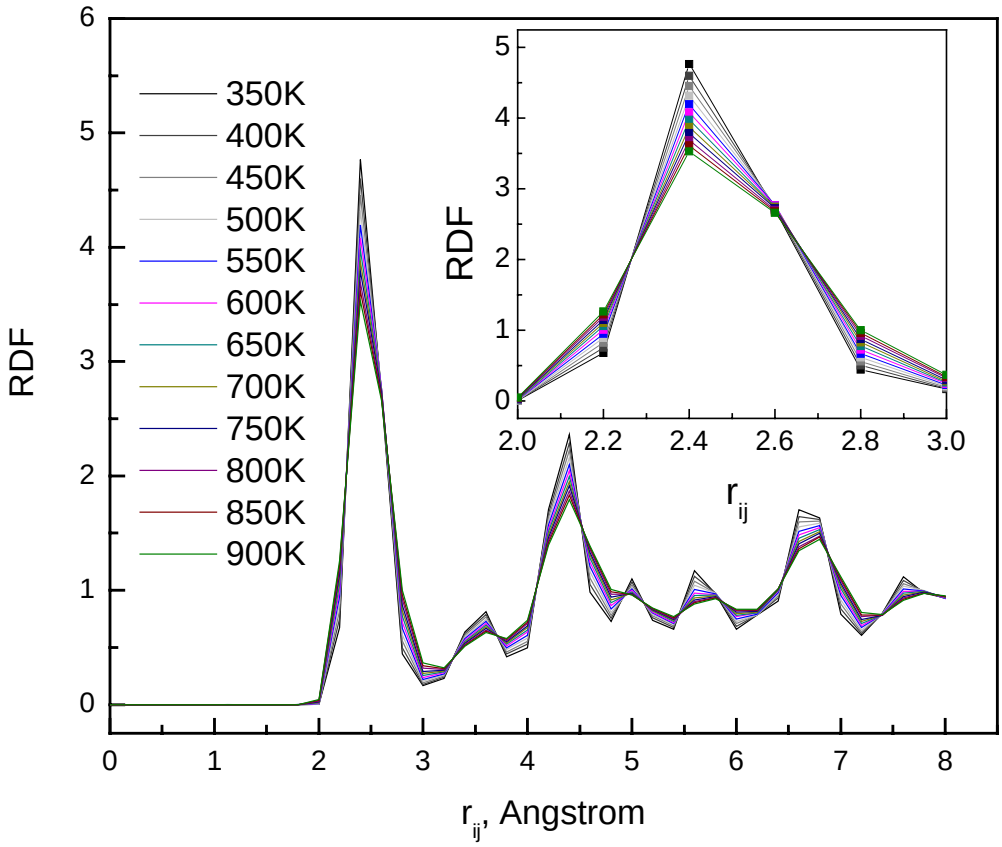

Figure 5.1. Temperature effects on radial distribution function of *nc*-Cu sample relaxed at different temperatures from 350K to 900K.

5.2.2 Central-symmetry parameter

The central symmetry parameter, $\{c_i\}$, $i=1\ldots N$, is a method to characterize the degree of inversion symmetry breaking in each atom's local environment. This method is especially useful to identify planar faults in FCC and BCC crystals [154]. The central symmetry parameter should be less than 0.01 even at finite temperature and the c_i of atoms on a stacking fault in *fcc* lattice is about 0.0416. The detailed algorithm can be found in Ref. [155] and is also included in Appendix B for convenience.

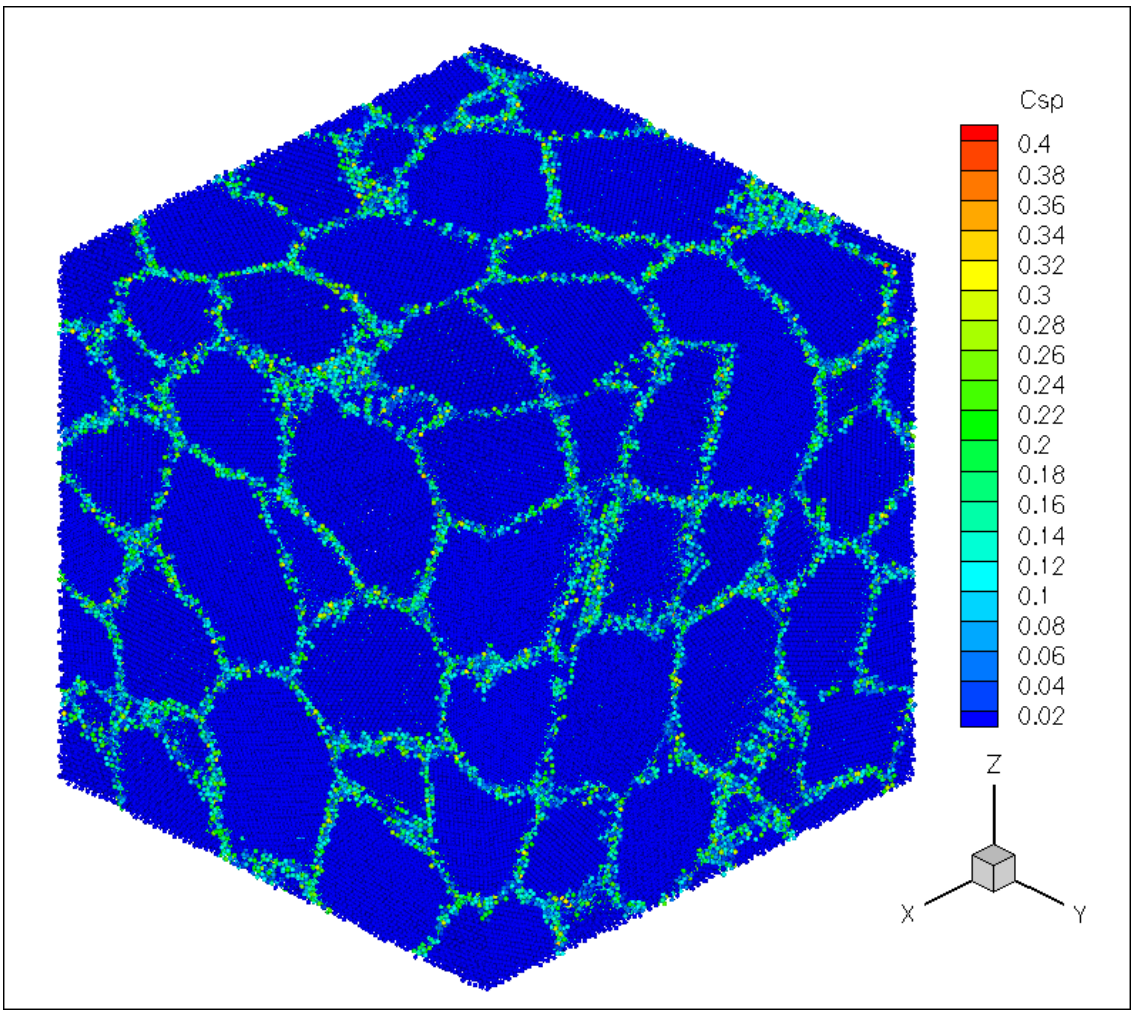

Figure 5.2. A *nc*-Cu sample of 50 grains is characterized by the CSP after MD relaxation at 300K.

Figure 5.2 shows an atomic configuration of a *nc*-Cu sample with 50 grains and atoms are colored by the CSP method. Atoms located inside a grain have the lowest value of CSP and are colored blue. As the value of CSP increases, the degree of disorder surrounding an atom increases and atoms are colored according to the contour shown in Figure 5.2. The grain structure is clearly visualized using CSP method, however CSP alone is not enough to identify the grain boundary entities.

5.2.3 Common neighbor analysis

The common neighbor analysis (CNA) developed by Honeycutt and Anderson [156] has been used to identify *grain boundary* atoms and thus grain boundary networks [152]. CNA is very useful to identify *fcc* and *hcp* types of atoms by looking at the common neighbors of a pair of atoms within the second nearest neighbor distance. Each atom has a unique crystalline signature and is assigned a label including four indexes based on the topological structure of common neighbors. Using this method, the atoms which do not have *fcc* structure are labeled as the atoms on the grain boundary network.

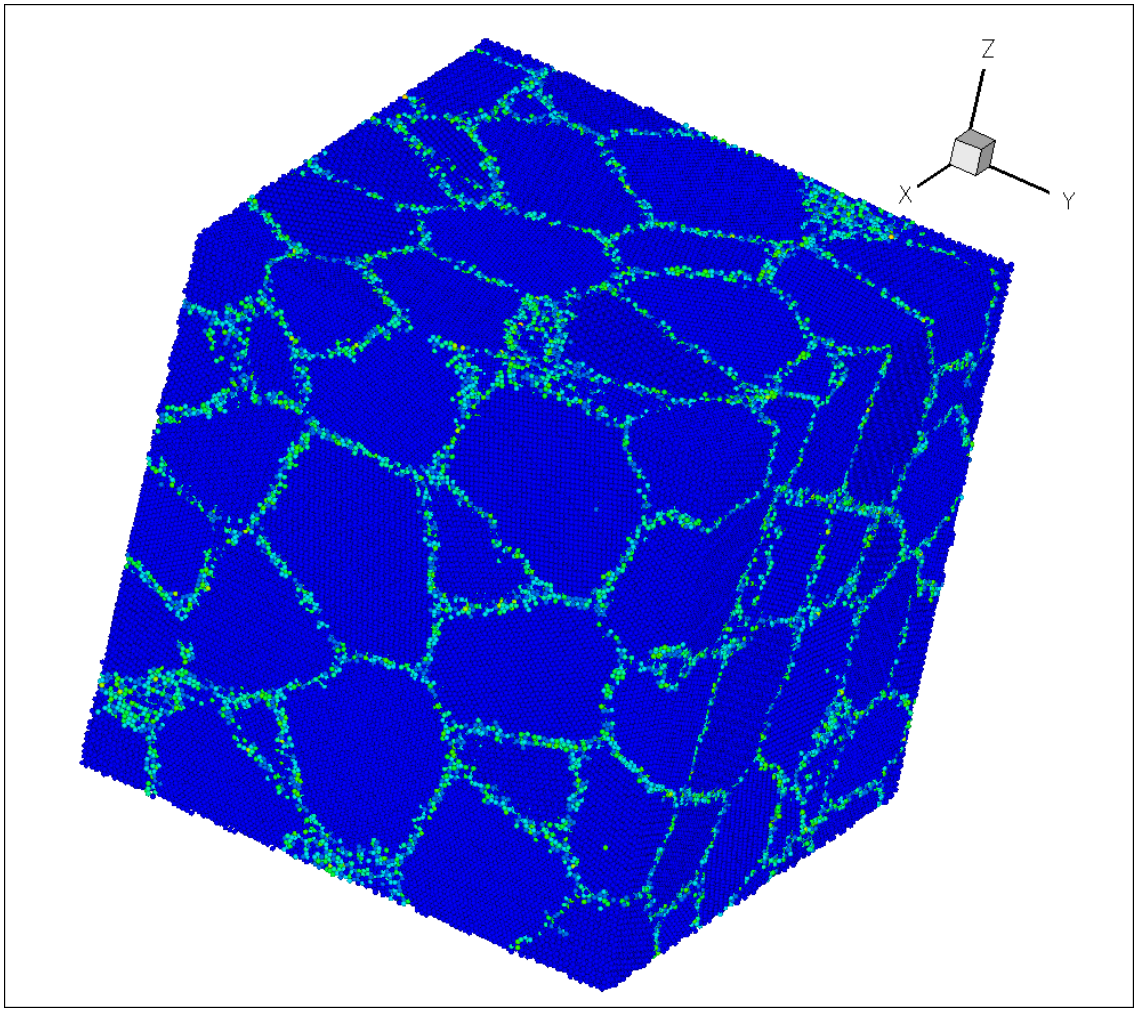

Figure 5.3. The *nc*-Cu sample of 50 grains after MD relaxation is characterized by common neighbor analysis. The blue atoms are *fcc* atoms. Green atoms are *hcp* atoms and yellow atoms represent the rest.

Figure 5.3 shows a *nc*-Cu sample characterized by the CNA method. The *fcc* atoms inside the grains are colored in green; *hcp* atoms are colored in blue; non-*fcc* and non-*hcp* atoms at the grain boundaries are in red. It is obvious that the grain boundaries after relaxation are clearly visualized. However, further classification of the atoms into triple junction or vertex atoms is still not possible using this method.

5.2.4 Potential Energy

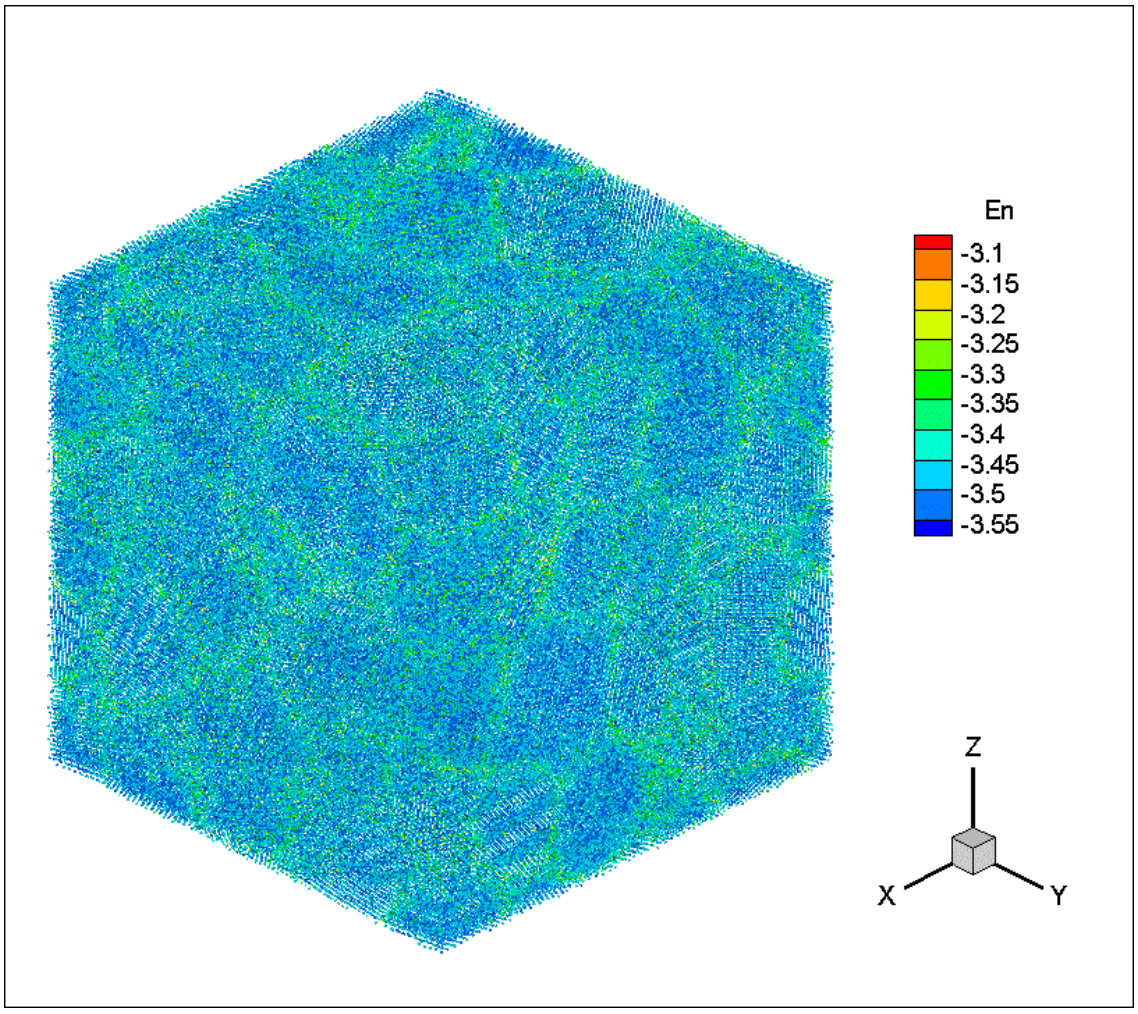

Figure 5.4. A *nc*-Cu sample characterized by the potential energy.

The potential energy of each atom can be evaluated using Eqn. (4.16). However, the potential energy of an atom is strongly affected by its local environment. Due to thermal fluctuation during MD simulation, potential energies of atoms located inside a grain sometimes are close to those on the grain boundaries. Once again, potential energy alone is not sufficient to identify individual grain boundary entities. Figure 5.4 shows a *nc*-Cu sample characterized by the potential energy of each atom. The potential energies vary from -3.55eV to -3.1eV and atoms are colored using the contour shown in Figure 5.4. The grain structure characterized by potential energy method is not as clear as methods mentioned above.

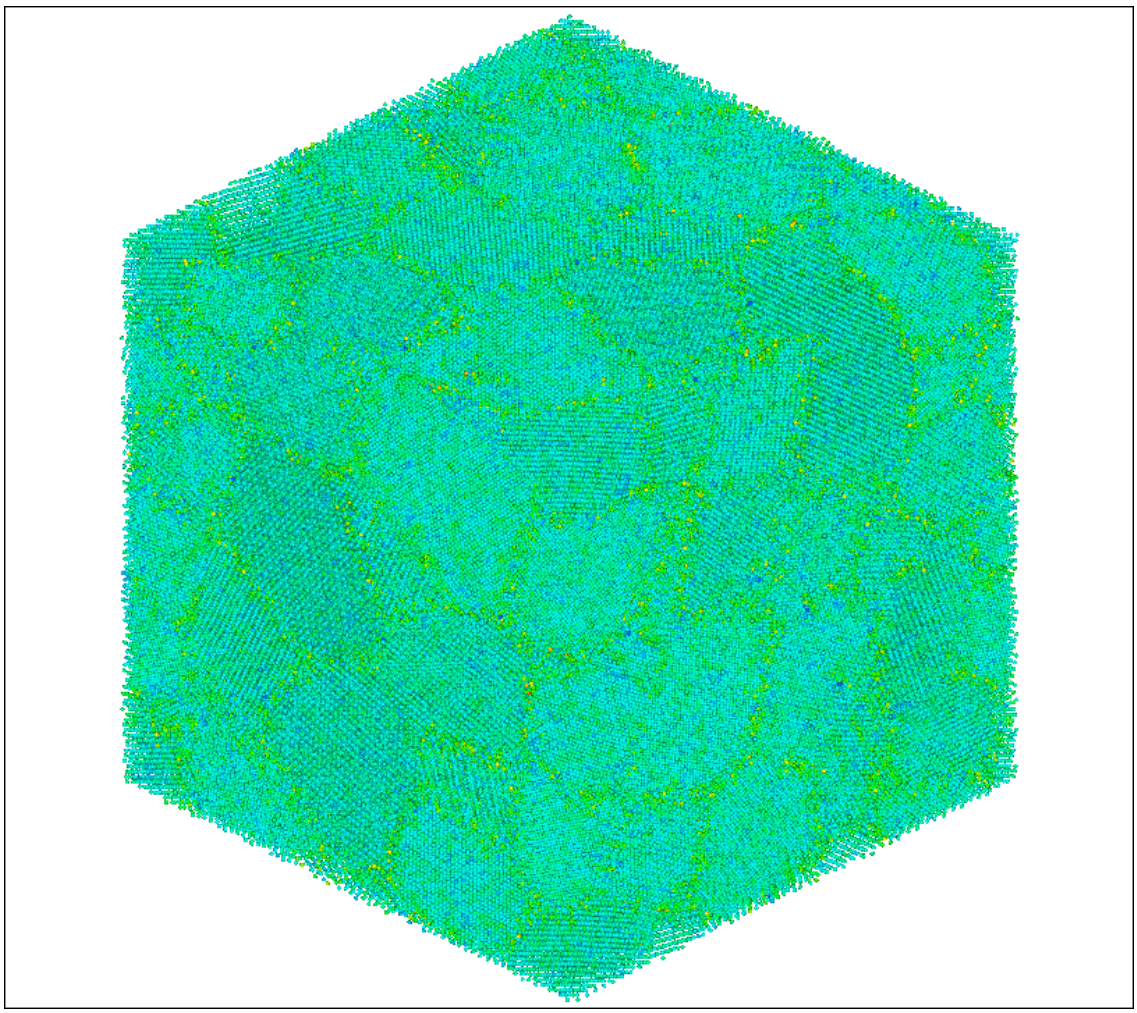

Figure 5.5. A *nc*-Cu sample of 50 grains characterized by the atomic Voronoi volume.

5.2.5 Atomic Voronoi Volume

Atomic Voronoi volume is another parameter that has been used to characterize the structure of materials, e.g. shear band in metallic glass [157]. The method is similar to the Voronoi tessellation mentioned in section 3.2.2 except that the Voronoi cells are constructed around atoms with a physical size. Similar to the potential energy method, the grain structure characterized by AVV method is not very clear and cannot be used to identify GB entities presented in the nc-Cu samples as shown in Figure 5.5.

5.3 Atomic Scale Characterization of Grain Boundaries of Nanocrystalline Materials

Obviously, none of the methods (section 5.2) alone is able to provide the characterization needed to identify grain boundary entities. A critical piece of information is absent that is giving each atom an accurate grain index (GI) so that atoms can be further classified into four different types of atoms including grain atoms (atoms located inside a grain), GB interface atoms (atoms located between two adjacent grains), TJ atoms (atoms located between three neighboring grains) and vertex atoms (atoms located at the junction of four neighboring grains). Fortunately, we already have each atom's original GI before MD relaxation. When atoms are filled into each Voronoi grain cell, a grain index is associated with each atom naturally that is the initial Voronoi index. However, atoms near grain boundaries tend to move further away from their as-filled position during MD relaxation. The initial GI is no longer accurately especially for atoms on grain boundaries. In this section, we will first propose a new method to update each atom's GI and then identify atoms in each GB entity based on the updated GI.

5.3.1 Method to give each atom an accurate GI

The method we proposed here is called the "peeling-onion method". After MD relaxation, atoms located deep inside each grain only vibrate around their equilibrium positions as we have seen in Figure 4.3. Atoms located in the core of any grain retain their initial grain index. Thus, we will first identify all atoms located inside grain cores by giving a definition for core atoms and then associate the rest of atoms layer by layer to the nearest grain core until all atoms in the sample are assigned an updated grain index. The method we developed is based on two quantities: one is the grain indexing that is inherited from the Voronoi construction and the other one is the common neighbor analysis. After performing CN analysis, atoms are classified into three different types: FCC atoms, HCP atoms and others. The method includes three steps:

1) Identify the atoms, or "core" atoms deep inside a grain labeled as *i*: The core atoms are defined as those with at least 8 first nearest neighbors that are fcc atoms as determined by CNA. Atoms in the same grain core are labeled by the same grain index GI(*i*) assigned before MD relaxation. The grain cores of all grains are identified during this step (Figure 5.6(a)).
2) Label another layer of atoms within the first nearest neighbor distance of the previous indexed atoms: For each atom in a grain core, or a layer indexed previously, all atoms that are within its first nearest neighbor distance are found and labeled with the same grain index as the core atom (even they may not satisfy the condition for being a grain core atom, see Figure 5.6(b).
3) Keep repeating step 2) for all grains until all atoms in the relaxed sample are assigned an updated grain index. (Our experience shows that one only needs to include 3-4 layers of atoms outside of the originally indexed grain core atoms in order to index all the atoms.)

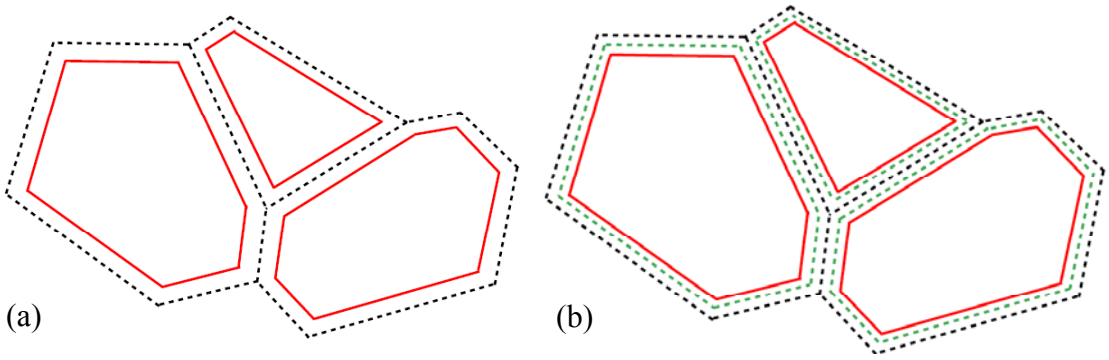

Figure 5.6. a) Step 1 in the peeling-onion method during which the grain cores (red polygon) are identified. The dotted black line shows the positions of the grain boundaries from the constrained Voronoi construction; b) Step 2 during which additional layers of atoms are associated with the identified grain cores;

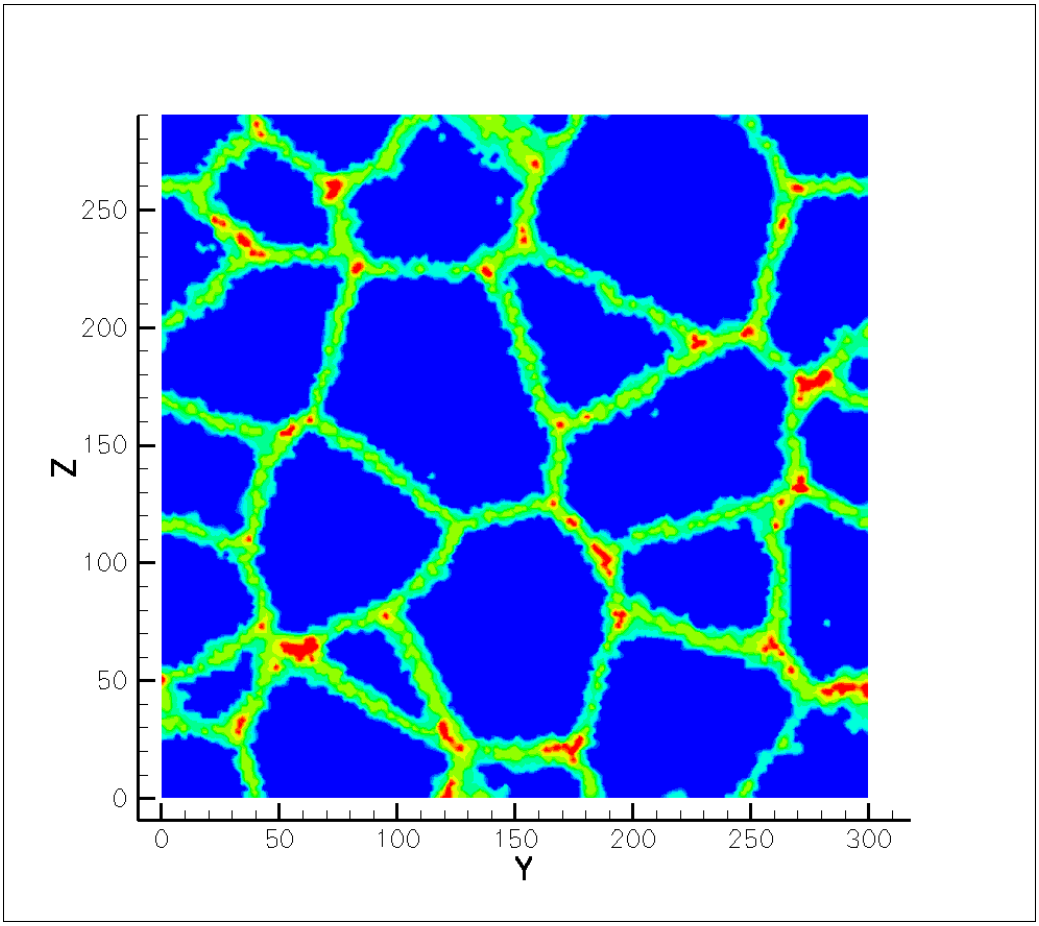

Figure 5.7. 2D section of the relaxed *nc*-Cu sample showing the layered structure identified by the peeling-onion method. The blue area is occupied by atoms in grain core. The green area is occupied by atoms in layer 1. The dark yellow area is occupied by atoms in layer 2. The yellow are is occupied by atoms in layer 3. The red area is occupied by atoms in layer 4.

To illustrate how this method works, we first cut a thin slice in a relaxed 50-grain copper sample and obtain a 2D contour plot in Figure 5.7. The first two layers outside of the "grain core" identified in step 1 usually are located along the GB interfaces and the last two layers usually are close to the triple junction or vertices. Table 1 lists the geometrical properties of atoms in different layer, such as the number fraction of atoms, the percentage of *fcc* atoms (*fcc*%), the average central-symmetry parameter (CSP) and the average root mean square displacement (RMSD) of atoms in each specific layer. The fcc percentage drops rapidly as the layers move away from the grain core indicating that atoms in outer layers are more disordered and closer to grain boundary.

Table 5.1. The properties of atoms in different layers in a procedure using the *peeling-onion* method: the number fraction of atoms in each layer, *fcc* percentage (*fcc*%) of the atoms, mean central symmetry parameter <CSP>, mean square displacement <MSD>, in the layers.

	Number fraction	*fcc*%	<CSP>	<MSD>
Grain core	0.5206	98.835	0.00382	0.249845
Layer 1	0.2234	36.110	0.05606	0.249862
Layer 2	0.1969	3.1825	0.10425	0.250245
Layer 3	0.0555	3.0732	0.10543	0.250429
Layer 4	0.0035	4.0261	0.09985	0.246667

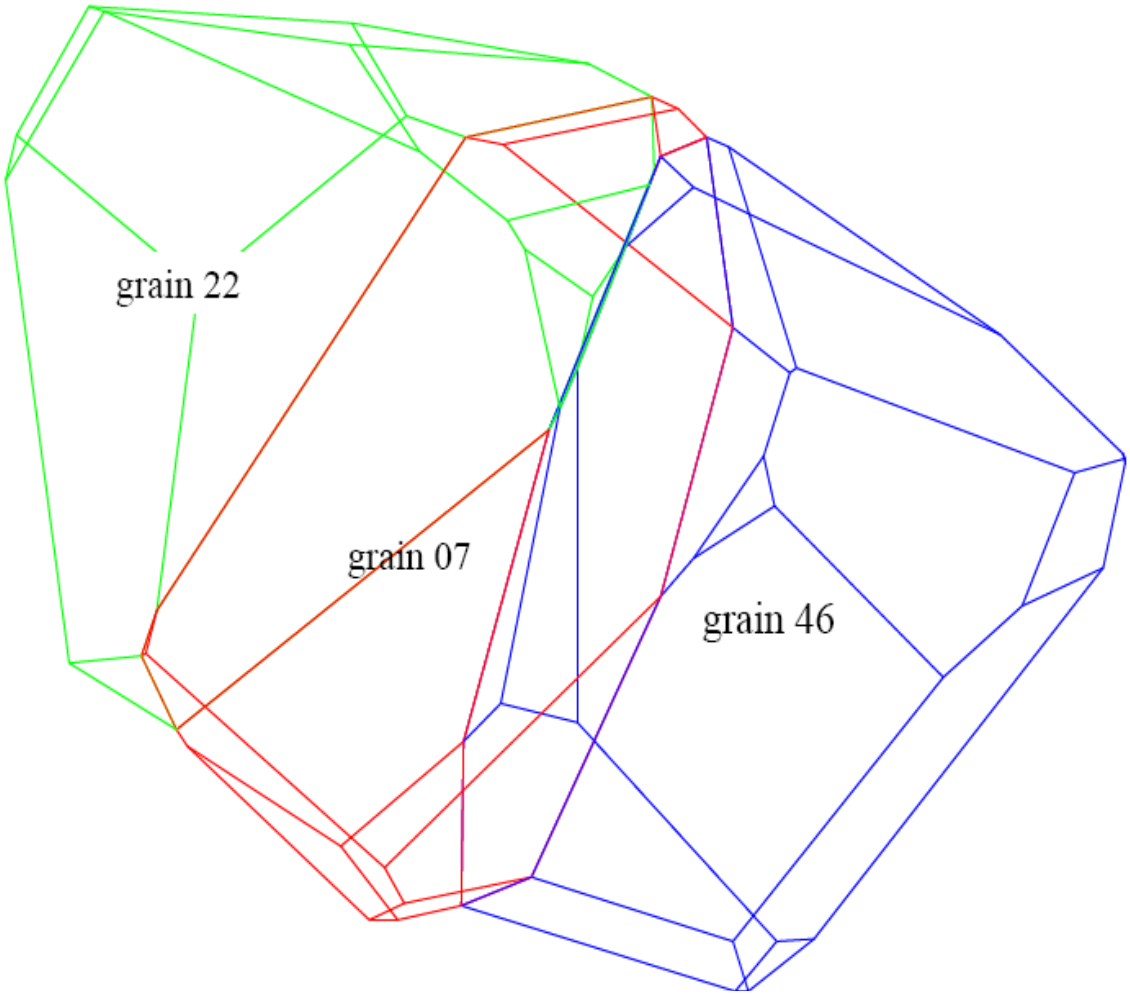

Figure 5.8. The initial Voronoi cells for grain 07, 22 and 46. Red cell represents grain 07, green cell represents grain 22 and blue cell represents grain 46

Next, we concentrate on three neighboring grains with GIs, 7, 22 and 46. The initial Voronoi cells of these three grains are shown in Figure 5.8. The atomic configuration of three grains in the relaxed 50-grain sample is plotted in Figure 5.9. Atoms in grain cores are omitted for better visualization of the layered structure identified by the peeling-onion method in Figure 5.10.

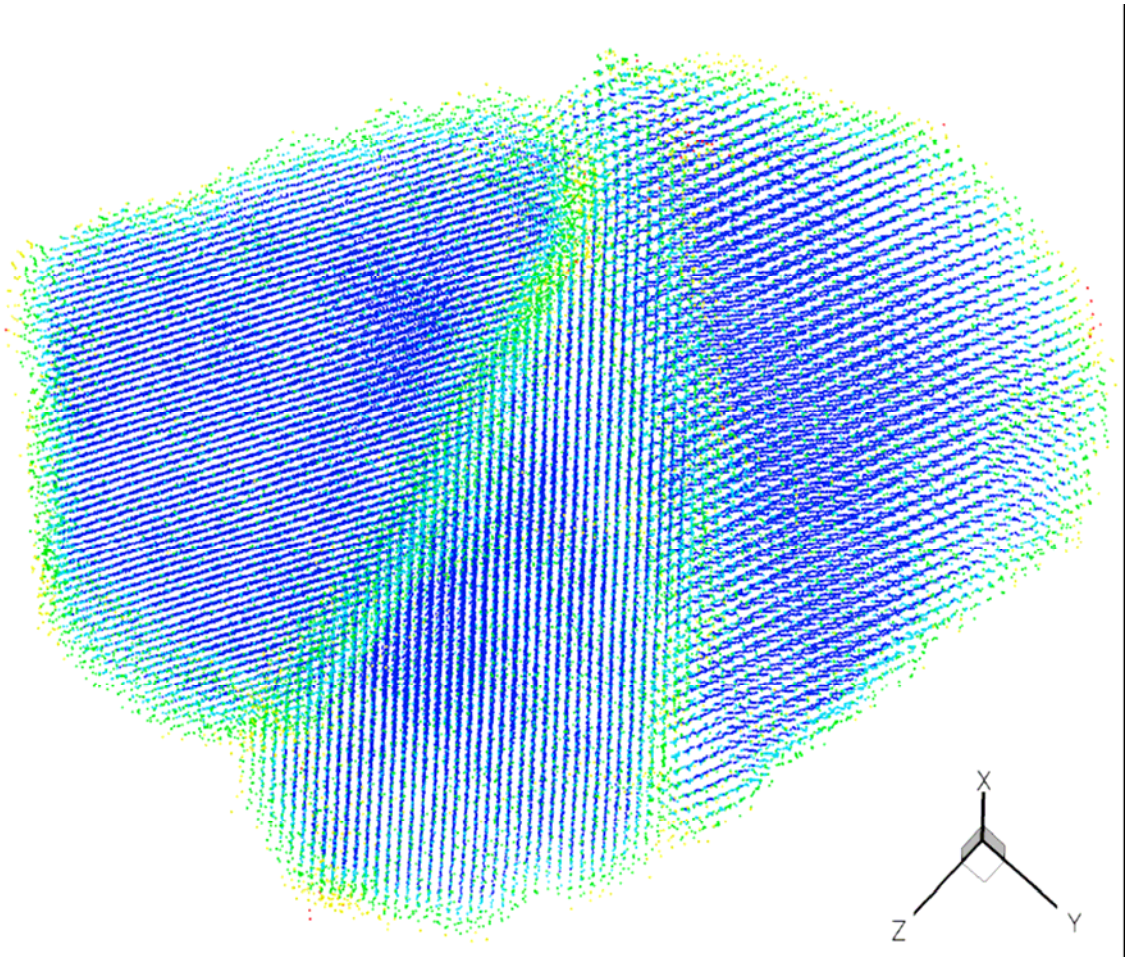

Figure 5.9. Three neighboring grains 07, 22 and 46 are characterized by the peeling-onion method. Blue atoms represent atoms in grain core. Green atoms are atoms in shell 1. Dark yellow atoms are in shell 2. Yellow atoms are in shell 3. Red atoms are in shell 4.

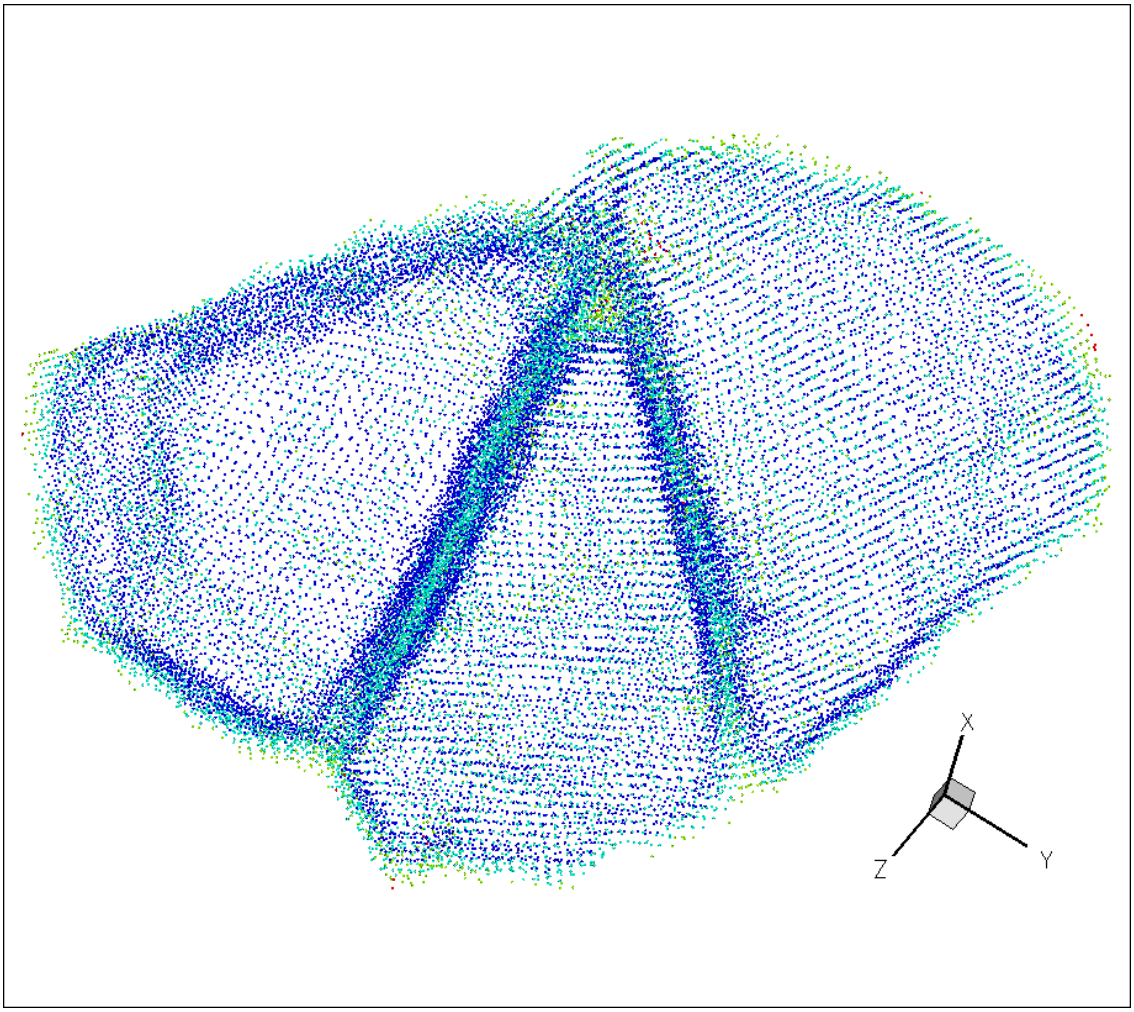

Figure 5.10. Three neighboring grains (07, 22, 46) without atoms in grain core. Blue atoms are in shell 1. Dark yellow atoms are in shell 2. Yellow atoms are in shell 3 and red atoms are in shell 4.

Figures 5.6-5.10 show that the proposed "*peeling-onion*" method can indeed cut the grain structure layer by layer and successfully give each atom a updated GI after MD relaxation. With the accurate GI for each atom, we can perform further grain boundary characterization.

5.3.2 Grain Boundary Characterization

The definition of grain boundary atoms is another critical issue to study the grain boundary structures in nanocrystalline materials. Derlet and Van Swygenhoven [152] identified grain boundary atoms by defining "positionally disordered atoms" as atoms that cannot be attached to at least one nearby *fcc* lattice. However "positionally disordered atom" gives a rigid definition of grain boundary atoms. In fact, some of the neighboring atoms of a "positionally disordered atoms" may also participate the grain boundary activities. Although this definition of grain boundary atom can locate the grain boundary network visually, it is difficult to identify each individual grain boundary interface or triple junction without a more detailed definition. The thickness of grain boundary characterized by this kind of structural analysis usually is fixed and may not be necessarily identical to real grain boundary thickness. A more accurate method is needed, which can not only identify each grain boundary interface and triple junction presented in the grain boundary structure, but also provide the flexibility to control the thickness of the grain boundary.

Once the indexing is done using the "*peeling-onion*" method, we can use the GIs assigned to each atom to further sort and index the atoms that are at grain boundaries, triple junctions, or vertex points. This is done by using the geometric properties that if an atom's neighbors have the same GI, then it is a atom located inside that grain, the so-called "grain atom"; If an atom's neighbors have two different GIs, then it is a grain boundary atom; If an atom's neighbors have three different GIs, then it is a grain boundary triple junction atom; If an atom's neighbors have four or more different GIs, then it is a vertex atom. Following this classification scheme, we start another round of search for the neighbors of each atom at the outer layers and check their GIs. This process is relatively swift since as our experience shows, typically only atoms belonging to the last three layers outside of each grain core are considered as the candidates for GB atoms. The algorithm is described below:

First, atoms located in the last three layers identified by the "*peeling-onion*" method are selected as candidate for grain boundary atoms. For each candidate atom, its neighbors within a cutoff distance are selected and the number of different grain indexes of these neighbor atoms is recorded. The cutoff distance is set as one and half first nearest neighbor distance. Using the geometric criterion mentioned above, we can classify atoms into the four groups by counting the number of different GIs that each atom's neighbors have. We could repeat this procedure for all atoms until they are all characterized into four groups.

There are three parameters in this method that can affect the results, although the effect is relatively small: (1) the definition of core atoms in the *peeling-onion* method, (2) the number of layers considered as candidate atoms for further indexing as grain boundaries, triple junctions, and vertices, 3) the cutoff distance for selecting a candidate atom's neighbors. These parameters can be adjusted by comparing with other calculations such as the potential energies and the experimentally known results such as grain boundary thickness.

5.3.3 Results

5.3.3.1 Classification of atoms into grain, grain boundary, triple junction, and vertex point

One of the unique capabilities of the method developed in this work is to sort, or classify atoms in polycrystalline materials into different topological entities that they belong to: grain, grain boundary interface, grain boundary triple junction, and vertex atoms using the *peeling-onion* method. This capability allows us to calculate a range of physical, thermal, mechanical, and structural properties associated with each type of these atoms.

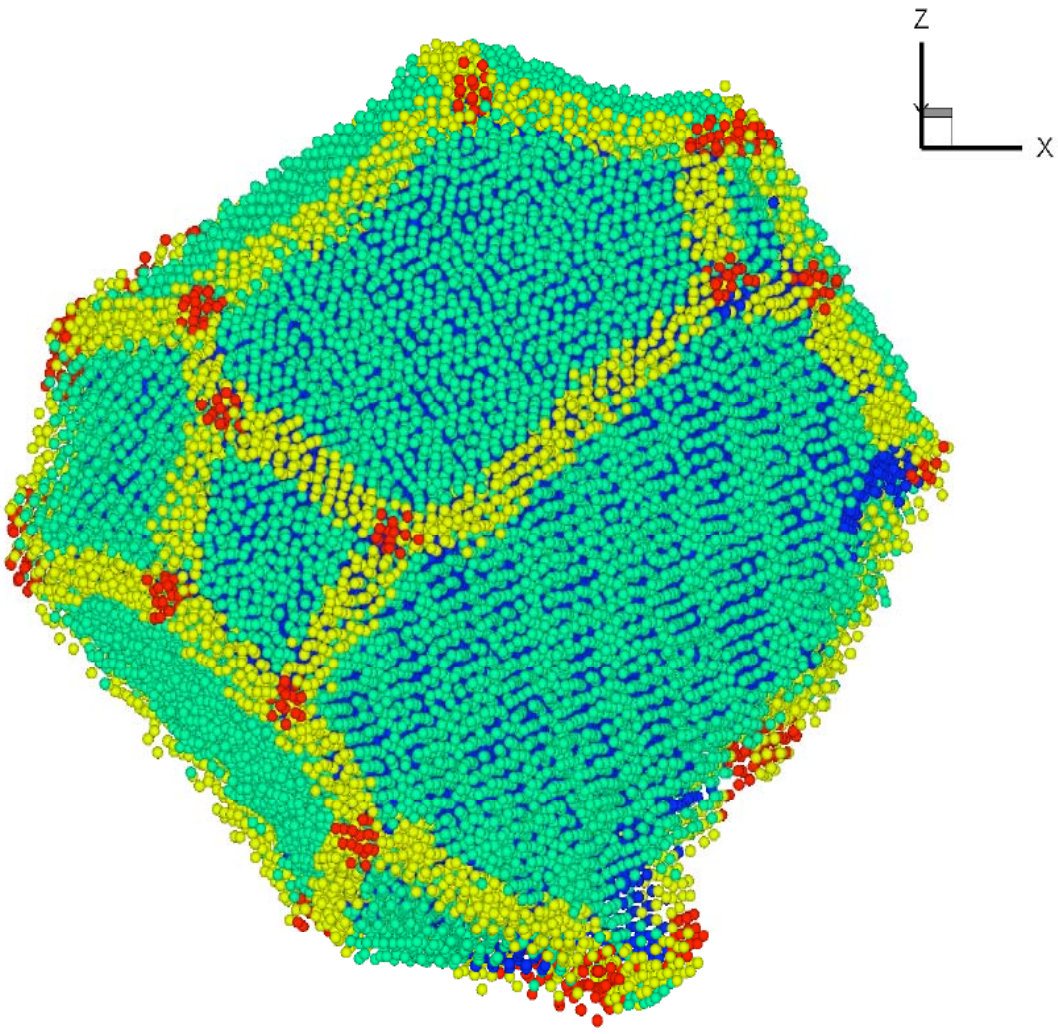

Figure 5.11. The characterized grain 7. Blue atoms represent atoms inside the grain. Green atoms represent grain boundary interface. Yellow atoms are triple junction atoms and red atoms are vertex atoms.

Figure 5.11 shows an individual grain isolated from the relaxed polycrystalline nc-Cu sample. The atoms that belong to different topological structures are colored differently. The detailed atomic configurations associated with the grain atoms, GB interface atoms, and triple junction atoms and vertex atoms are shown. For the sample with random misorientation, the fractions of atoms in grains, grain boundary, triple junction and vertex points are plotted in Figure 5.12. As seen, about 66% of the atoms belong to grain, 21% are grain boundary, 8% for triple junction, and 5% for vertex points.

The effects of rising temperature, mean grain size, and misorientation on the number of atoms in the grains, grain boundaries, triple junctions and vertex points will be presented in section 5.3.3.3.-5.3.3.5.

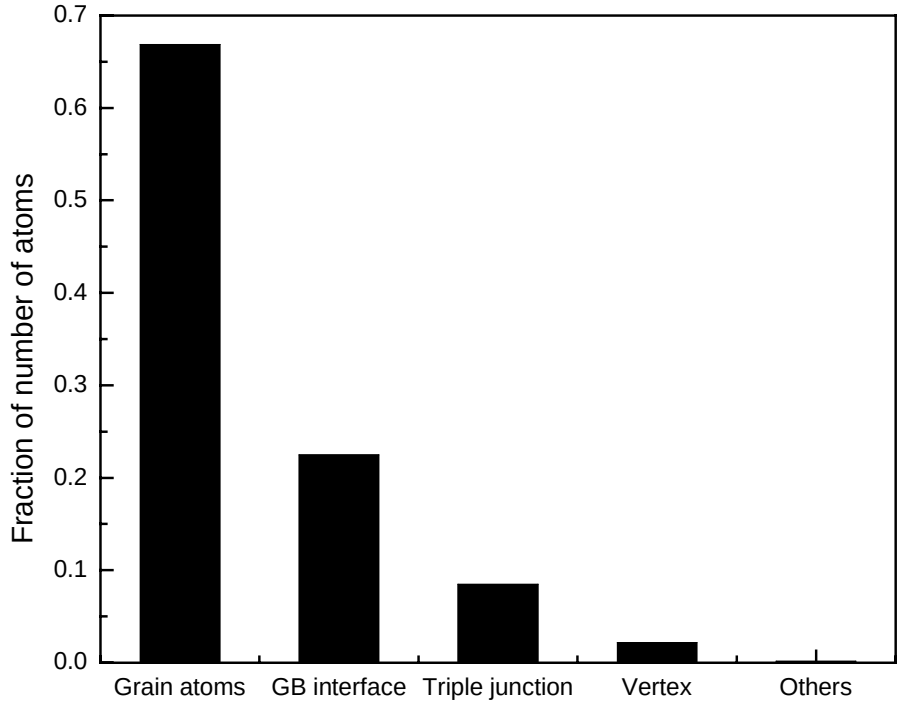

Figure 5.12. The fraction of the different types of atoms in the sample that is associated with different microstructure entities.

5.3.3.2 Grain boundary profile

The successfully classification of atoms into four different groups and identify atoms in each microstructure entity allows us to acquire more detailed information about these entities, such as grain boundary thickness and degrees of disorder, triple junction length, etc. On the other hand, the results produced also allow us to cross-check how well this method works in identifying these entities as compared with other criteria and available experimental results. Here, we present such a case for grain boundaries.

A grain boundary is a transition zone bordering two grains adjacent to each other. On atomic scale, the boundary should exhibit gradual change in atomic structure or physical properties from one side to another, no matter how narrow it is. This transition can be captured in configuration energy, atomic structure, and other physical properties. The profile of a grain boundary is characterized by these quantities across the boundary, from which we can obtain information about its thickness and degrees of disorder.

In order to calculate the grain boundary profile of each grain boundary interface, we first identify the interface normal vector of each interface and then measure the configuration energy and other physical or structural properties along the normal direction perpendicular to the grain boundary interface. Figures 5.13(a) and 5.13(b) show the interface between two adjacent grains in two different directions. The algorithm to determine the surface normal of each GB interface is presented in Appendix C and D. Next we calculate the potential energy of the atoms along a sampling unit taken as a cylinder in the normal direction of the boundary from the grain atom on one side to another, crossing the grain boundary (Figure 5.13(d)). We take the mean value within each thin slice (2Å) perpendicular to the normal (or parallel to the grain boundary) along the cylinder; the distribution, or profile of the potential energy of the boundary can then be obtained (Figure 5.13(e)).

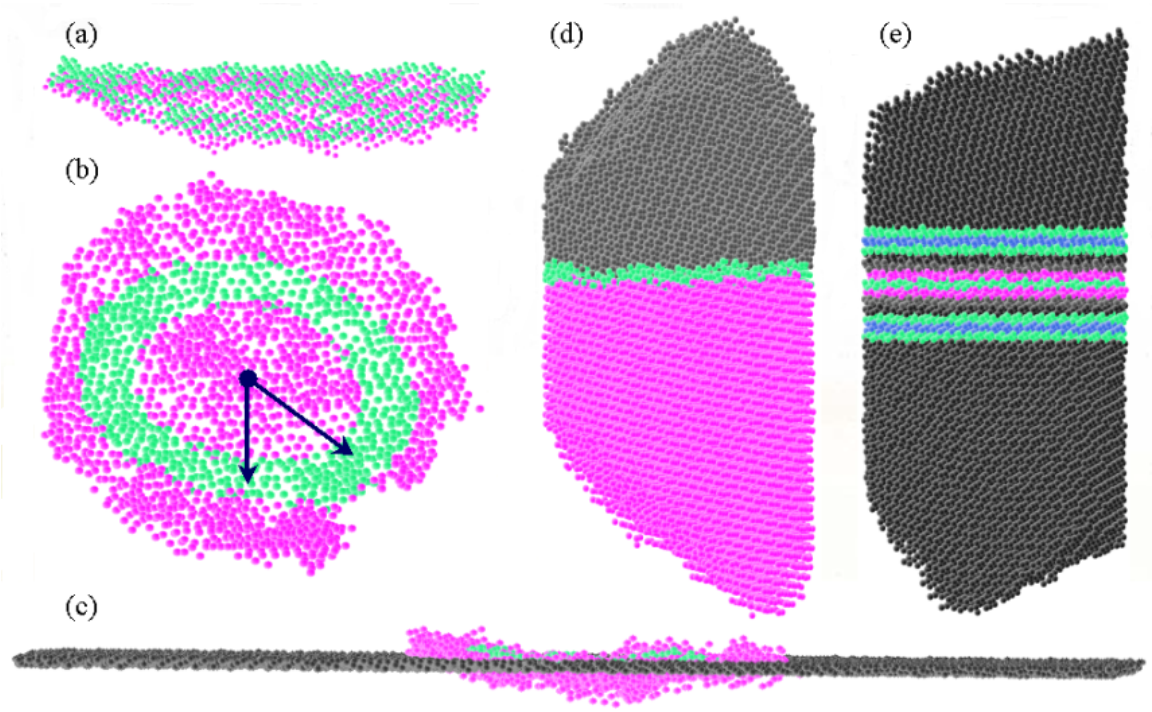

Figure 5.13. The projection of interface between two grains in two different directions, one parallel to the GB (a) and other perpendicular to it (b); (c) the grain boundary on a reference plane from the crystal structure inside the grain which is perpendicular to the surface normal; (d) the cylinder cut along the direction of GB interface normal; (e) thin slices within the cylinder (2Å) cut parallel to the GB.

Figure 5.14 shows the potential energy profile of the grain boundary interface between the two grains in a sample of 50 grains with a mean grain size of 8.696 nm. The profile looks symmetric with the peak position located in the middle. From the profiles, we can estimate the grain boundary thickness for each GB; and from all GBs calculated, we obtain the mean GB thickness in the sample: The area (S_{pot}) under the potential energy profile, for example, can be obtained by integration across the boundary. The height of each profile is known as H_{pot}. The width of each grain boundary, W_{pot}, can be determined by $W_{pot} = S_{pot} / H_{pot}$. Using the same technique, we obtained the CSP profile for the same grain boundary to represent the degree of grain boundary disorder (Figure 5.14). The CSP profile looks similar to the potential energy profile. Similarly, we can

also obtain the thickness of each GB interface using the CSP profile. In this case, the width is determined by $W_{CSP} = S_{CSP} / H_{CSP}$. The distributions of H_{pot} and H_{CSP} of a 50-grain nc-Cu sample are illustrated in Figure 5.15. The results obtained from the profiles using potential energy and CSP are fairly close to each other indicating that there exists a strong correlation between CSP and potential energy.

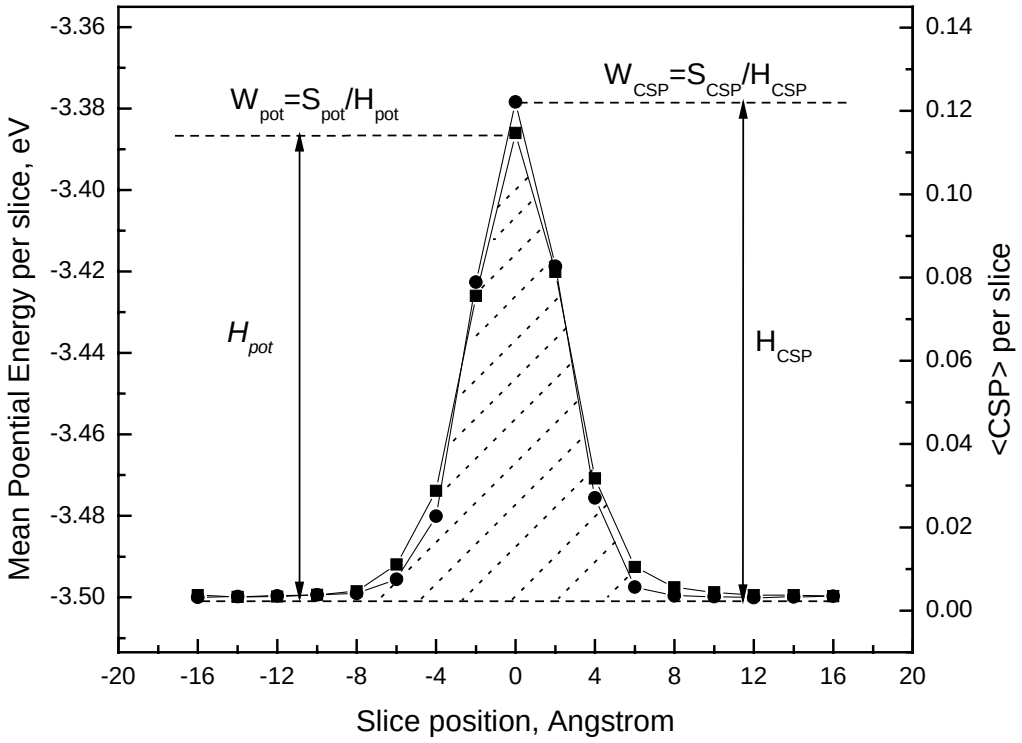

Figure 5.14. The potential energy and central symmetry parameter profiles across a grain boundary interface between two neighboring grains and definition of grain boundary width.

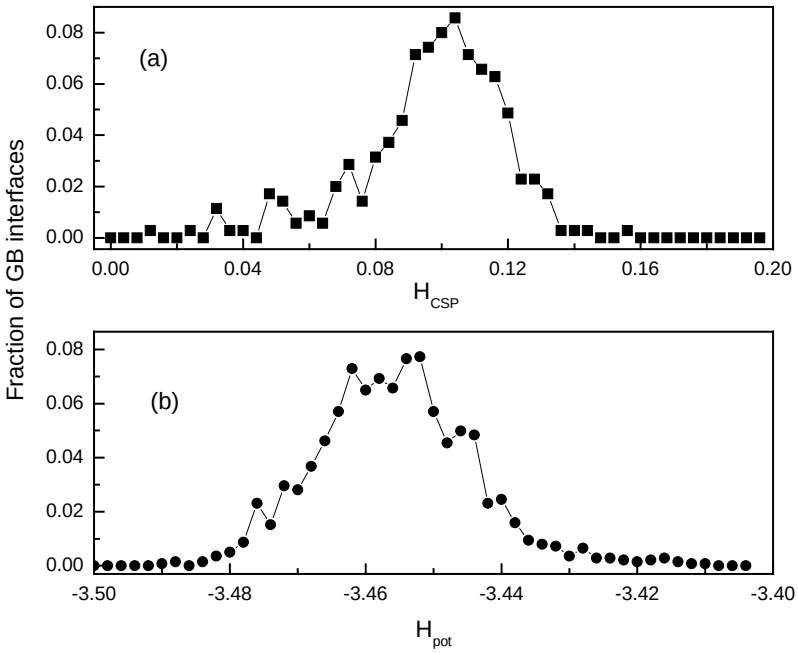

Figure 5.15. The distributions of H_{CSP} (a) and H_{pot} (b) with a mean grain size of $\langle D \rangle = 8.696nm$.

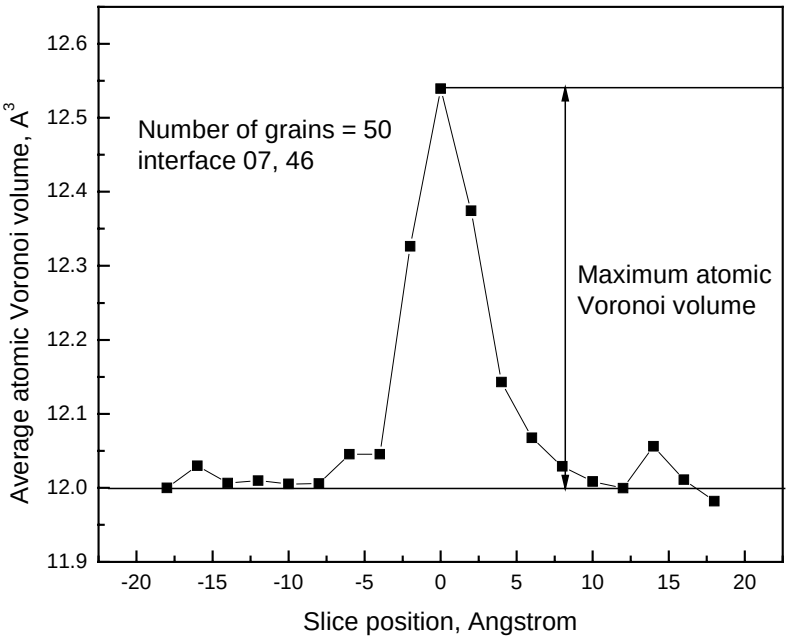

Figure 5.16. The average Voronoi volume profile for GB interface between grain 07 and 46.

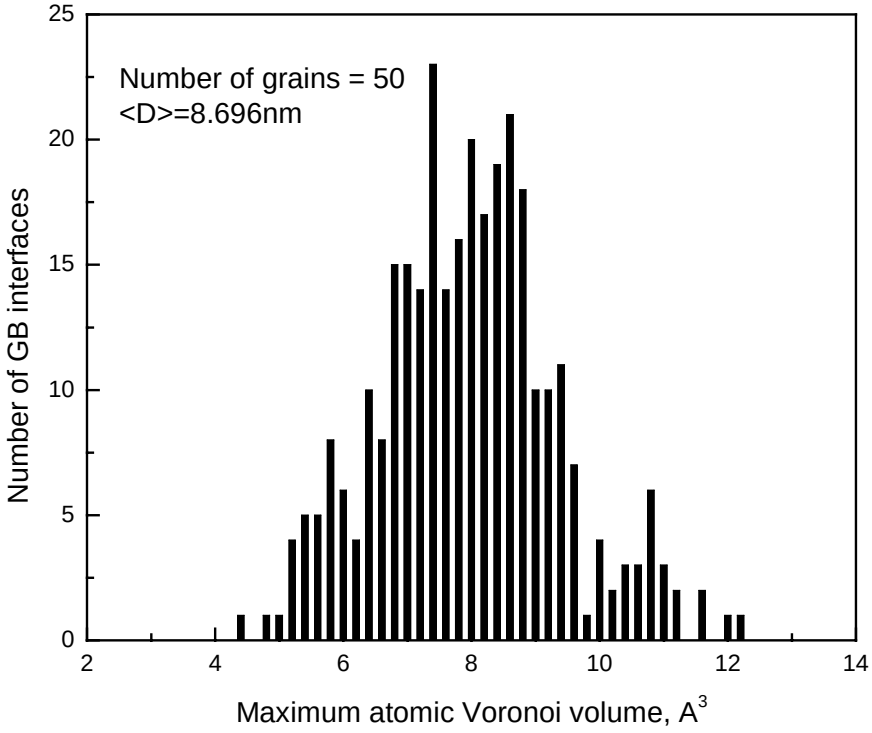

Figure 5.17. The distribution of maximum Voronoi volume from the average Voronoi volume profile for each GB interface in *nc*-Cu sample of 50 grains. $\langle D \rangle = 8.696nm$.

5.3.3.3 Effects of misorientation

As mentioned earlier, the nature and structure of grain boundaries in polycrystalline materials are closely related to the misorientations of the grains. The higher the misorientation angle, more disordered the grain boundaries are; and vise versa. But so far, the majority of the nanocrystalline samples used in numerical modeling are those with random misorientations. Armed with the new methods and grain boundary characterization procedure described above, we are able to establish the relation between the complicated grain boundary network structure and the misorientation distributions. To demonstrate this capability, we generated two very different misorientation distributions in two samples that have the same grain cell topology and the total number of 50 grains: one has minimized misorientation distribution with a mean misorientation

angle at 10.496 and the other has a random distribution with a mean misorientation angle of 40.381. After relaxation, following the characterization procedure introduced in section 5.3.2 and 5.3.3.2, we obtain the information about the difference in the grain boundary thickness and disorder in the two samples.

Figure 5.18 shows the distribution of the structural order in the grain boundaries widths as measured by the CSP for the two samples with different misorientations. Close observation shows that the difference in misorientation greatly affects the order of the grain boundary structures as shown by the mean CSP per face (Figure 5.18). The mean CSP value for the sample with minimum misorientation distribution moves to smaller values as compared with that of the sample with the MacKenzie distribution, indicating that more order is present in the sample with the minimum misorientation. Figure 5.19 shows the GB CSP width distributions for the two samples calculated from the GB CSP profiles. The mean GB CSP width of the minimized misorientation sample apparently has a higher value and narrower width than that of the random misorientation sample. These results show that the changes in misorientation distributions not only affect the geometries of the grain boundaries, but also their width, or volume, or density.

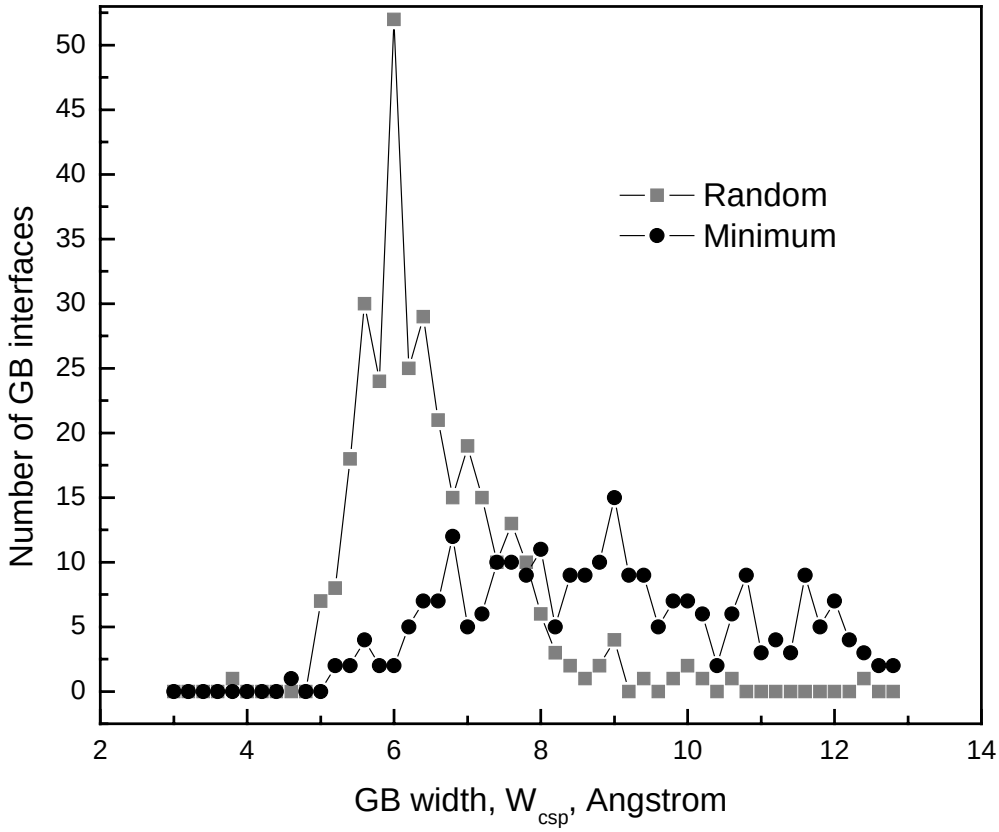

Figure 5.18. GB width distributions for two samples with random and minimized misorientation distributions

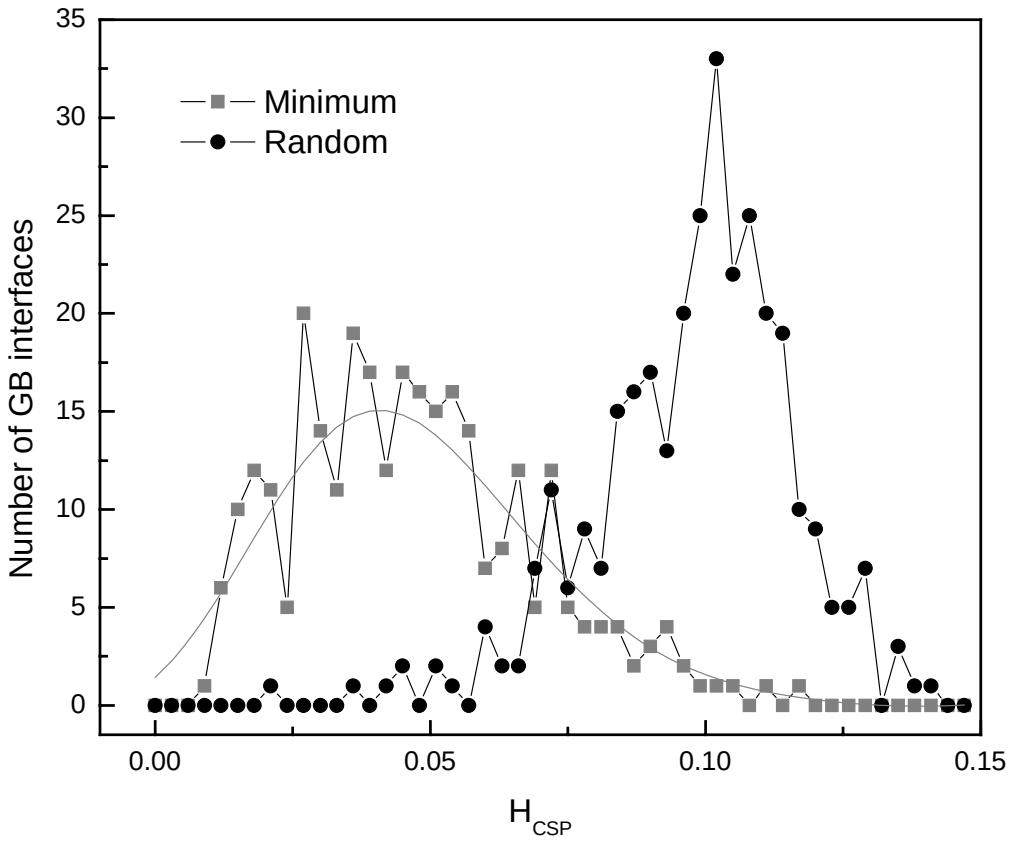

Figure 5.19. The distributions of H_{CSP} for two samples with random and minimized misorientation distributions.

5.3.3.4 Effects of grain size

As the grain size becomes smaller, it is observed that the distortion on the grain boundaries becomes more severe, which does not follow Gibbs' description of the interfaces that are considered as the interfaces without thickness [158]. Part of the reason is that the effect of the stress field mediated from the disorder in the boundaries becomes more effective in small grains. As shown in previous section, the degree of disorder is reflected by the thickness of the grain boundaries.

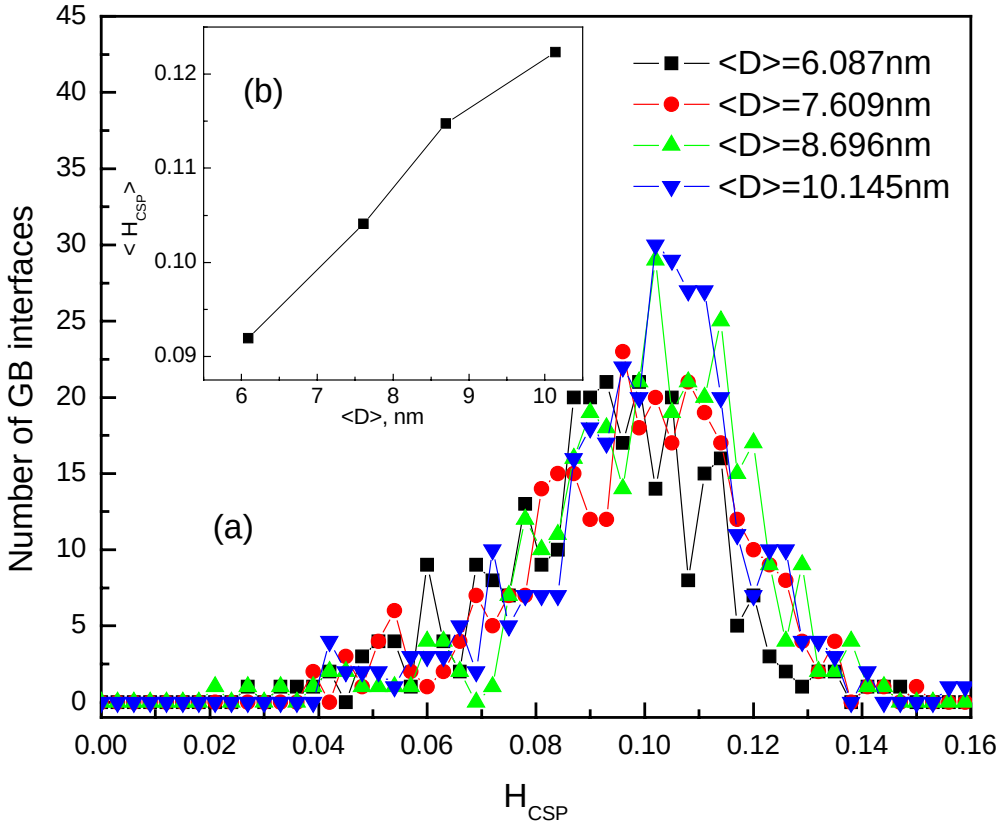

Figure 5.20. a) The grain size effects on the distribution of H_{CSP} obtained from GB CSP profiles; b) $\langle H_{CSP} \rangle$ increases with mean grain size.

Four nc-Cu samples of different mean grain sizes are generated by filling different number of atoms into the same 50-grain Voronoi structure. The mean grain sizes are 6.087, 7.609, 8.696 and 10.145nm. After MD relaxation at 300K, we calculate the distributions of H_{CSP} (Figure 5.20(a)) and W_{CSP} (Figure 5.21(a)) from these four samples. As the mean grain size increases, the average H_{CSP} increases (Figure 5.20(b)) while the average GB width measured from CSP profiles decreases (Figure 5.21(b)). At smaller grain size, the grain boundary width is larger indicating that the volume fraction of grain boundary region is also larger. Similarly, we obtain the distributions of H_{AVV} in samples

of different mean grain sizes (Figure 5.22(a)). However, the average H_{AVV} fluctuates as mean grain size increases (Figure 5.22(b)) indicating that the density at the center of grain boundaries does not change much while the volume fraction of grain boundaries decreases with mean grain size.

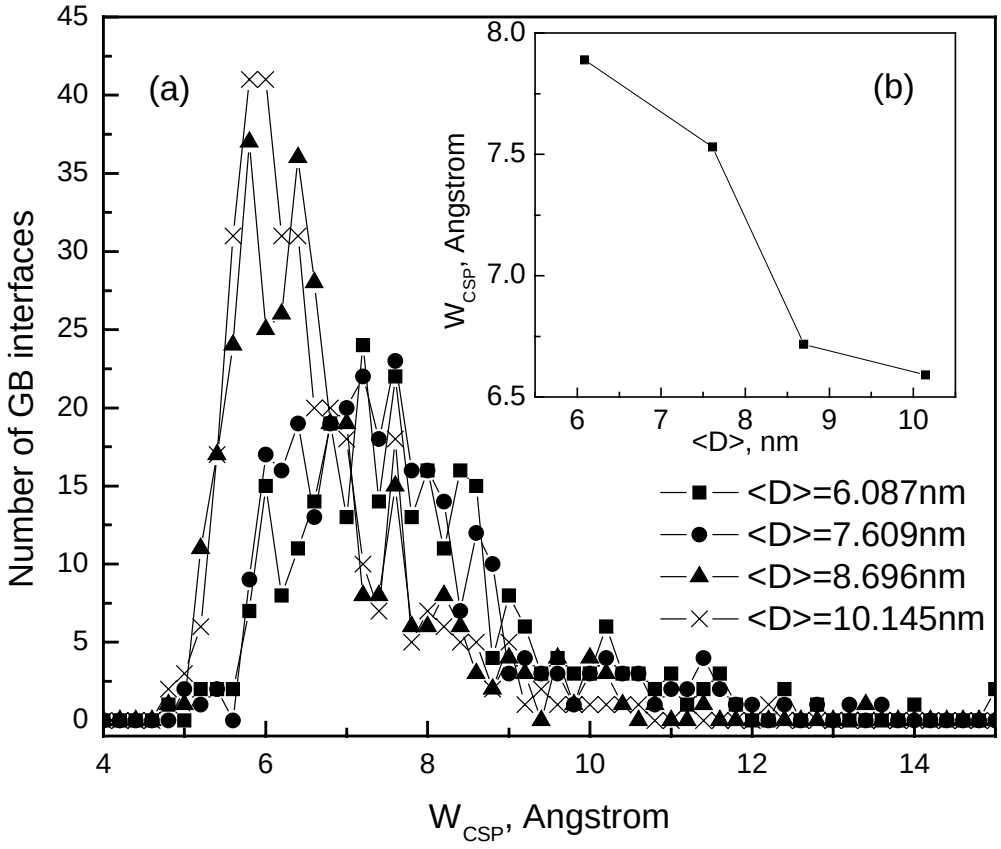

Figure 5.21. a) Grain size effects on the distribution of GB width obtained from GB CSP profiles; b) The average GB width decreases as mean grain size increases.

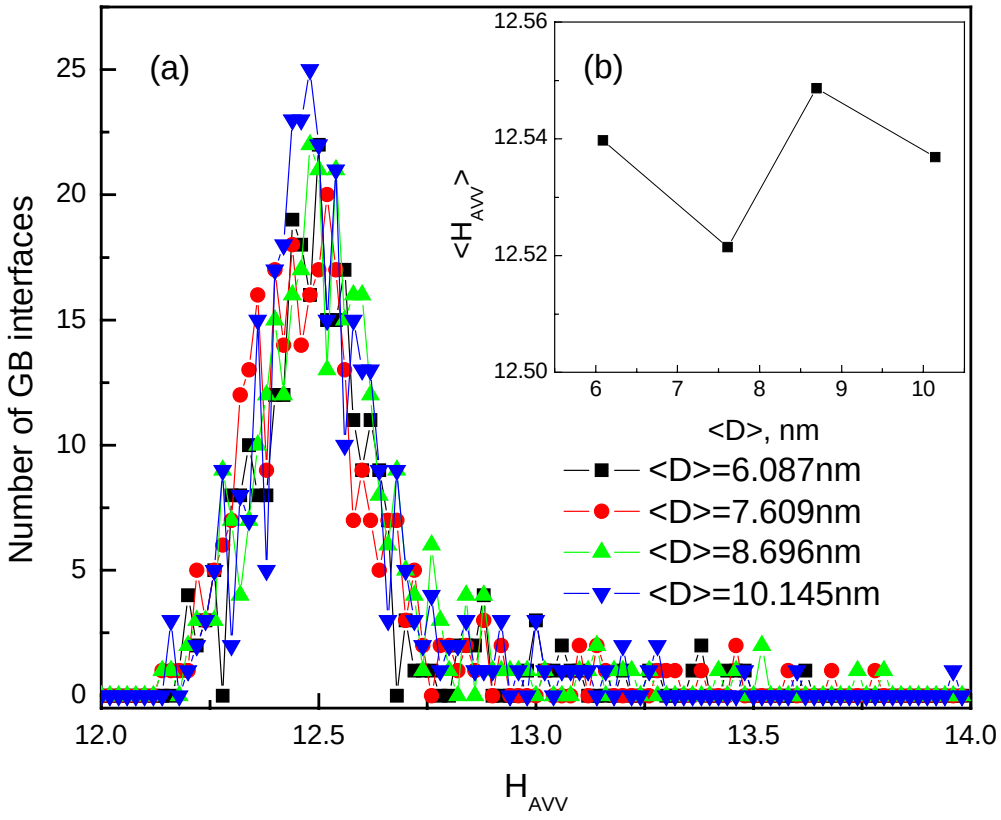

Figure 5.22. a) The grain size effects on the distribution of H_{AVV} obtained from GB atomic Voronoi volume profiles; b) H_{AVV} fluctuates as $\langle D \rangle$ increase.

To further test the grain size effect, we took two samples; one is made of 50 grains with a mean grain size of 8.696 nm and another 20 grains with the mean grain size of 16.52nm. Due to the limitation of computing resource, there exists a limit in the simulation box. In order to increase the mean grain size, the number of grains has to be reduced to 20. Figure 5.23 shows the distribution of the grain boundary width measured using the CSP for two samples with different mean grain sizes. Clearly, the mean grain boundary width for the sample with smaller grain size has larger or wider grain boundaries as compared with the sample with larger mean grain size. As the average grain size increases, the average GB thickness decreases. The average GB thickness,

$\langle W_{CSP} \rangle$, of all interfaces for the sample with the mean grain size of 8.696 nm is 0.666 nm, whereas the sample with the mean grain size at 16.52 nm has the mean grain size of 0.574 nm. As the mean grain size increases, the average boundary CSP thickness approaches the value determined for fcc alloys by Mössbauer spectrometry (~0.5 nm) [159].

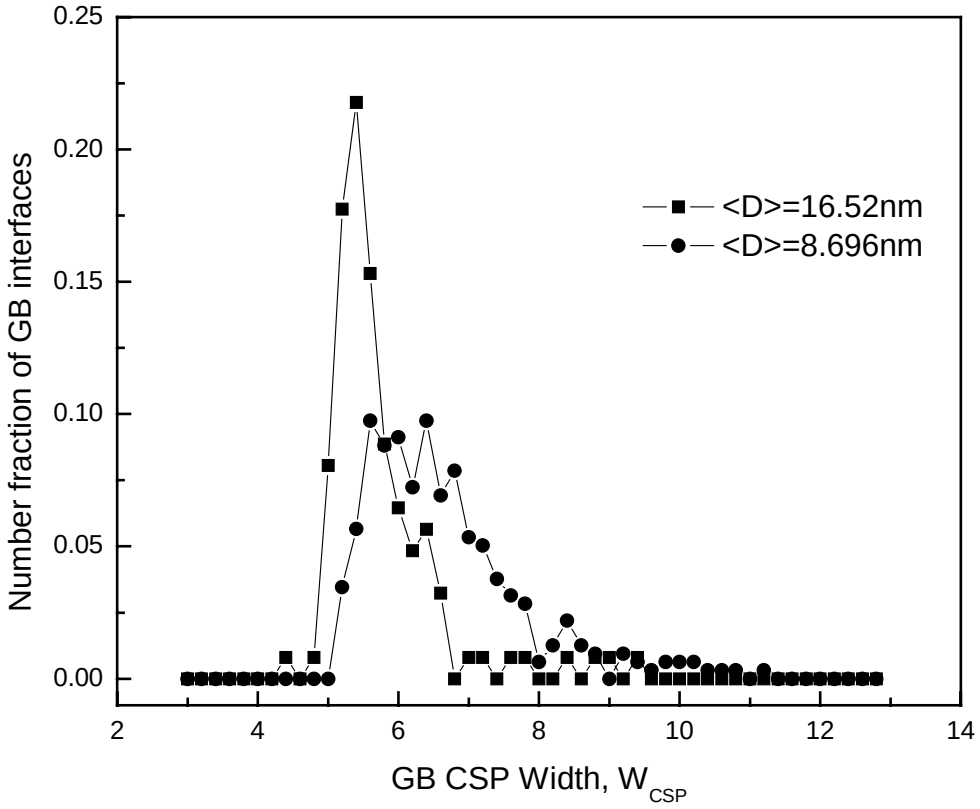

Figure 5.23. The normalized GB width distributions of two nc-Cu samples of $\langle D \rangle = 8.696nm$ (50 grains) and $\langle D \rangle = 16.52nm$ (20 grains). Both have the same topological structure.

Figure 5.24 and 5.25 shows the internal stress distributions across a grain boundary and in the two adjacent grains. Note that we used two samples with the same topological grain cell structures but different mean grain sizes. After MD relaxation, the

stress profiles of the same interface between two grains are shown. The residual stresses increase as the mean grain size decreases. The stress profile for the large sample, Figure 24, is more homogeneous. A big change in the stresses is seen for the small sample with a mean grain size of 7.61 nm (Figure 5.25), which indicates that there exists a large amount of residual stress in nc-Cu sample with a mean grain size less than 10 nm.

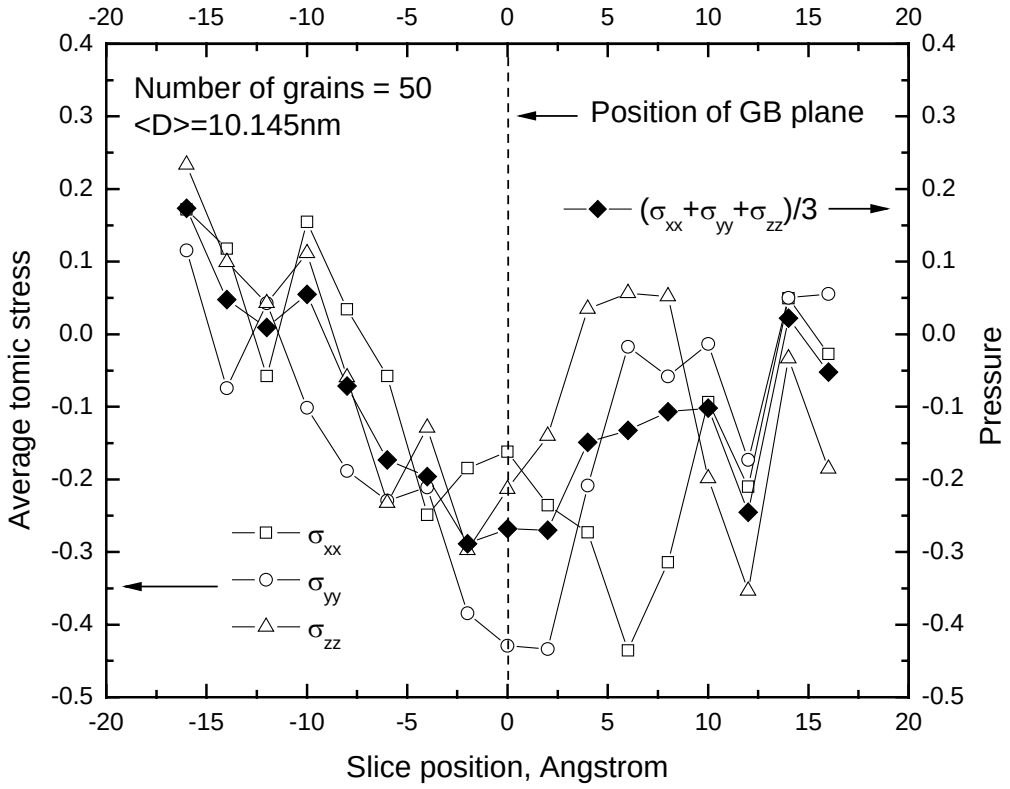

Figure 5.24. Stress profile of the interface between two grains in the sample with the largest mean grain size ($\langle D \rangle = 10.145nm$)

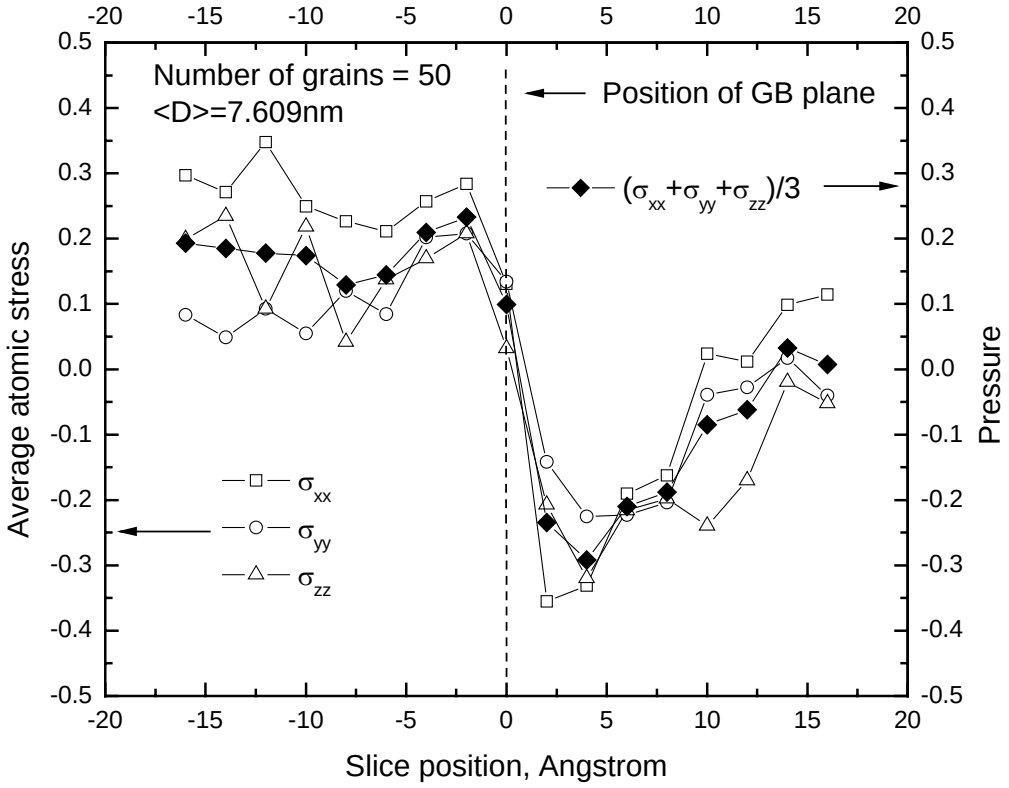

Figure 5.25. Stress profile of the interface between two grains in the sample with the smallest mean grain size ($\langle D \rangle = 7.609nm$)

5.3.3.5 Effects of temperature

As compared with the internal stress, temperature exerts a different type of agitation to grain boundary structures through increasing lattice vibration, anharmonicity, and maybe enhanced grain boundary diffusion. We tested a sample with 200 grains for a series test at 100K, 170K, 230K and 300K. The same grain boundary characterization is applied on relaxed samples at different temperatures. We first explored the change of the mean potential energies of grain atoms, GB interface atoms, triple junction atoms and vertex atoms with increasing temperature. As shown in Figure 5.26, as temperature increases, the four curves representing the four types of atoms increase linearly.

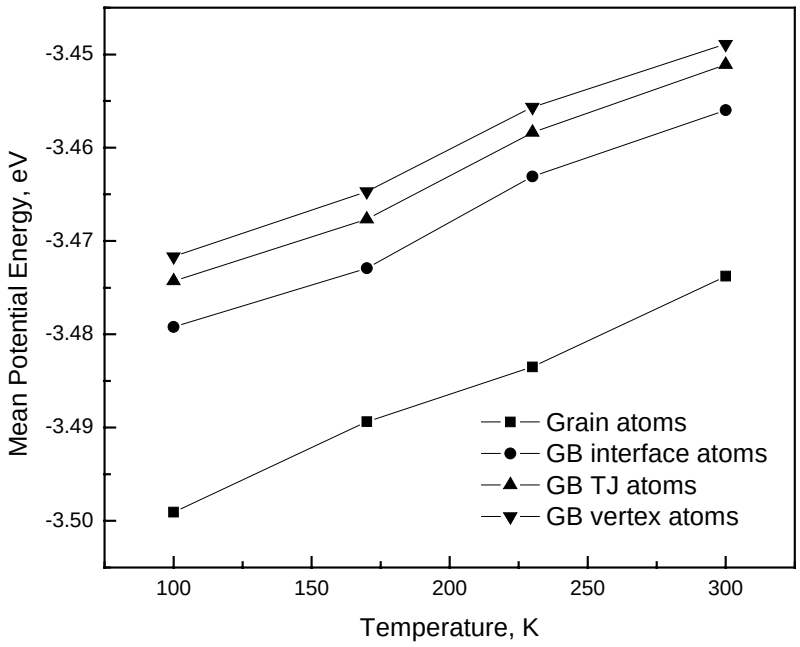

Figure 5.26. The effects of rising temperature on the mean potential energies of all grain atoms in the sample as well as that of grain boundary interface atoms, triple junction atoms and vertices atoms.

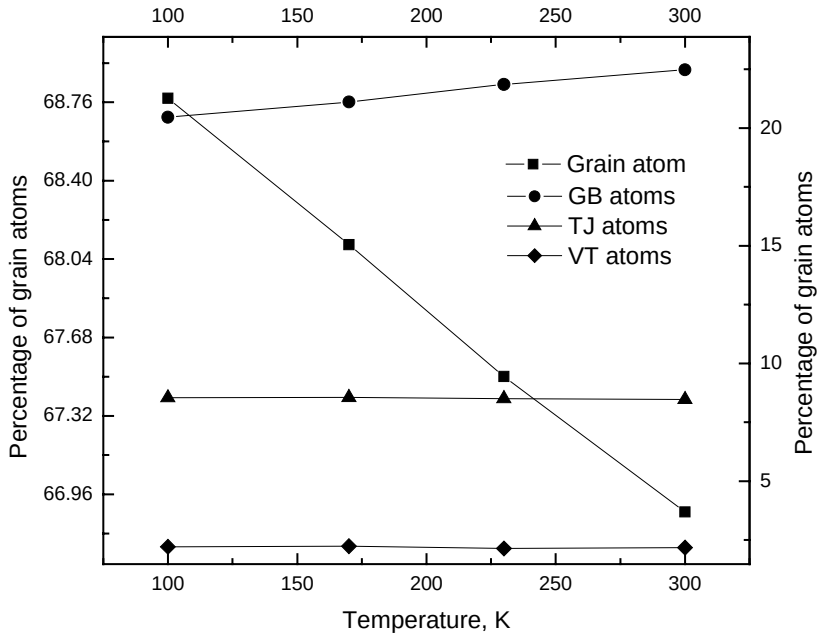

Figure 5.27. The effects of rising temperature on the number of atoms in the grains, grain boundaries, triple junctions and vertex points.

In contrast, the number of grain atoms in the sample decreases as the temperature increases (Figure 5.27). Figure 5.28 shows the temperature effects on the mean potential energy distributions of atoms in each boundary interface. As the temperature increases, the mean potential energy distribution moves toward a higher potential energy value.

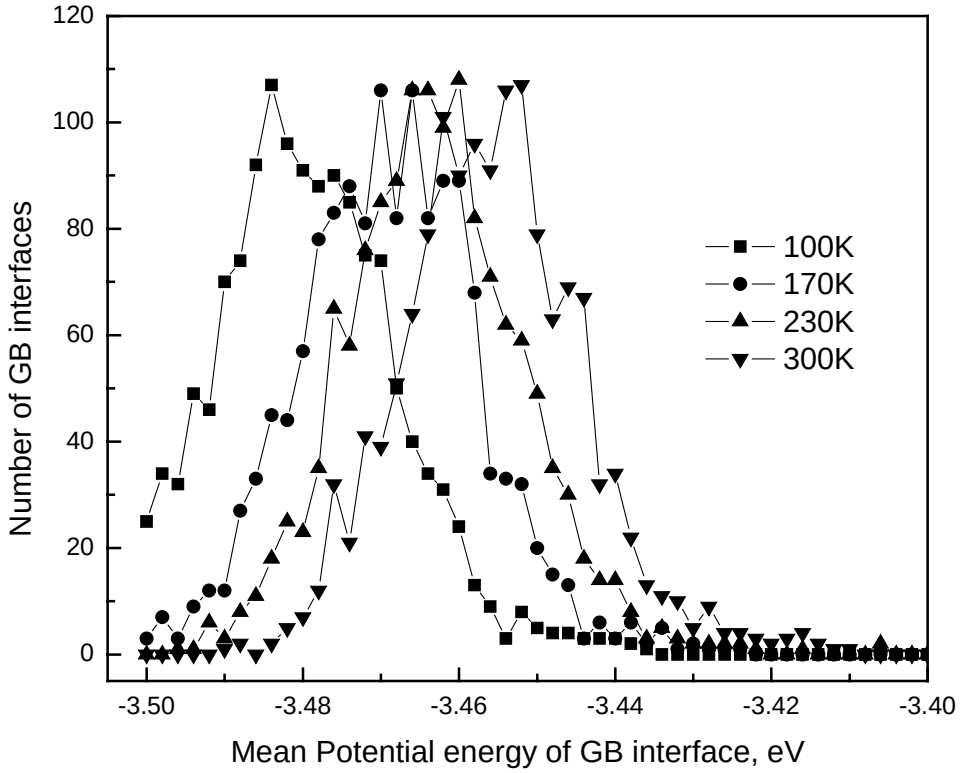

Figure 5.28. The effects of rising temperature on the distribution of mean potential energies of atoms on the same grain boundary interface.

Similar tests are applied on a 50-grain *nc*-Cu sample at five temperatures, 100, 150, 200, 250 and 300K. Figure 5.29 shows the grain boundary thickness distribution in the sample at these temperatures. The inset shows the mean grain boundary thickness. As seen clearly, the thickness increases with the increase temperature. The average CSP also increases as the temperature increases.

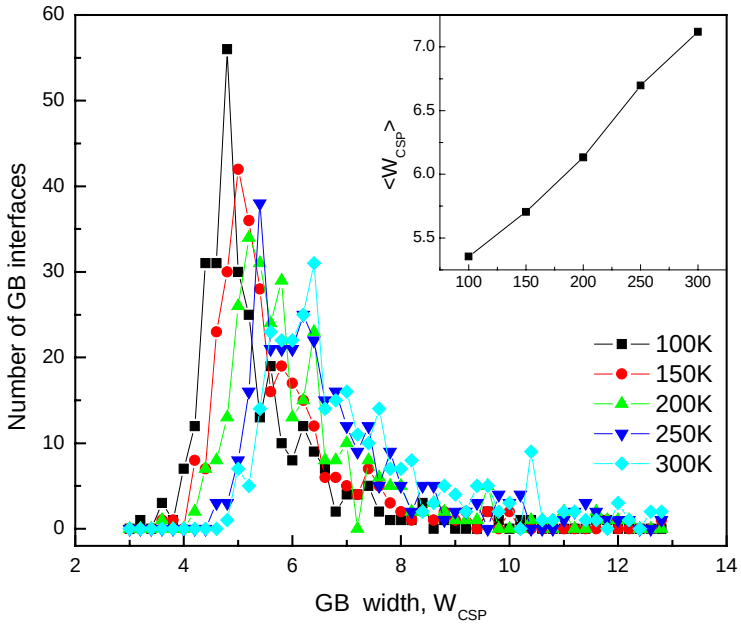

Figure 5.29. The effects of rising temperature on the distribution of GB width.

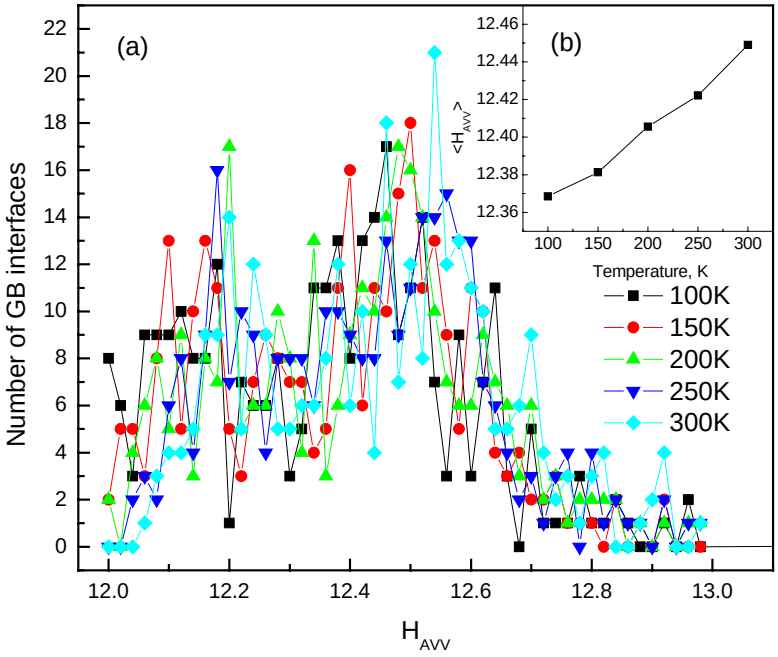

Figure 5.30. The temperature effects on the distribution of maximum atomic Voronoi volumes.

5.3.3.6 Pair Correlation Function of Grain Boundary Atoms

Radial distribution function or pair correlation function has been used widely to determine the degree of disorder presented in the structure of a material. The method is described in section 5.2.1 where we studied the temperature effect on RDF. While calculating the RDF of a 3D *nc*-Cu sample, a cutoff distance is usually selected. For each atom, pair distances are only calculated between the center atom and its neighboring atoms located within the cutoff distance. This technique is useful to calculate RDF in a sample of large number of atoms.

Technically, pair correlation function shall also be able to detect the degree of disorder in regions across the GB interfaces. Due to the absence of a detailed grain boundary characterization method, pair correlation function has not been calculated successfully on nanocrystalline materials. In this section, we will first describe the procedure to calculate pair correlation functions of GB atoms and TJ atoms and then compare them with pair correlation functions of nc-Cu sample at 300K and liquid copper at 1200K.

In a section 5.3.3.2, we have successfully obtained the GB profiles using potential energy, hydrostatic stress and central-symmetry parameter. We shall give a brief description of the procedure. Using the grain boundary characterization method, atoms in each GB interfaces are identified and the normal vector of each GB interface is determined using the method described in Appendix C and D. For each GB interface, we first cut a cylinder perpendicular to the interface. The radius of the cylinder is 25Å and the length of the cylinder is 36 Å. In case, the interface area has a radius less than 25 Å, only atoms identified on that boundary are selected. The total number of atoms in the slices will increase as the distances to the boundaries increase. Next, we cut the cylinder into thin slices with a thickness of 2Å that are parallel to the GB interface and calculate the statistical averages of geometrical or thermal properties of atoms in each slices. The statistical averages include average central-symmetry parameter, potential energy, atomic

stresses, atomic Voronoi volume, etc. In this study, we shall focus on the GB profiles of CSP and atomic Voronoi volumes. The grain sizes effect and temperature effect are studied in section 5.4.4.

Utilizing the method for calculating GB profiles, we are able to identify atoms in each slice parallel to the GB interfaces. For atoms in each slice, pair distance between every atom pair, r_{ij}, is calculated and we can accumulate all pair distances in slices with the same distance between each slice and the corresponding GB interface, denoted by d. The pair distances between atoms located on different GBs are not counted. All pair distances are only between atoms on the same GB. The accumulated pair distances are plotted in Figure 5.31.

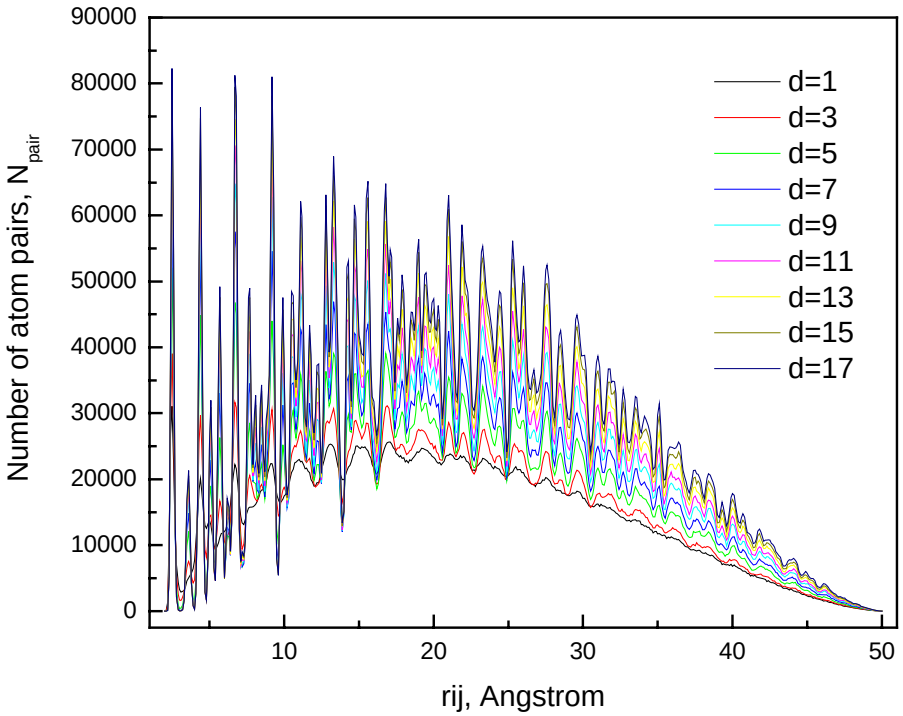

Figure 5.31. The number of atom pairs increases as the distance to GB increases.

The total number of atom pairs increases as the distance to GB, *d*, increases. There are two primary reasons for the increase in the total number of atom pairs: 1) The radius of the cylinder is selected as 25Å and the areas of many small GB interfaces are smaller than the area of the cylinder parallel to the GB; 2) The number of atoms in slices with the same distance to GB increases as d increases. There exists a maxima in each curve around pair distance of 20 Å after which the number of atom pairs starts decreasing. This behavior is caused by the shape of each slice, which is a disk with a fixed thickness. The number of atom pairs decreases when the pair distance is larger than 20 Å because only atoms sitting near the edge of each disk is possible to form a pair with atoms on the other side of disk. The accumulated number of atom pairs must be normalized by the density in each slice. Here we propose the definition of grain boundary pair correlation function.

The grain boundary pair correlation function for atoms in the same slice position, pcf_d, is defined as follows:

$$pcf_d(r) = \frac{\left[n_d(r+\delta r) - n_d(r)\right]}{m(d)\pi\Delta\left[(r+\delta r)^2 - r^2\right]} \tag{5.4}$$

where V_s is the volume of each slice, $m(d)$ is the total number of atom pairs accumulated from all slices with the same distance to GB interface, d and $n_d(r)$ is the number of atom pairs with a distance less than r. Because of the complex shape of grain structures, it is difficult to accurately estimate the total volume of slices with the same distance to interfaces. The pair correlation function for atoms in the same slice position is normalized by the product of the volume of a shell between $r+dr$ and r, V_{shell}, and the total number of atom pairs in slices with the same distance to GB, $m(d)$. The thickness of each slice is 2Å, denoted by Δ. The volume of a shell is area of a shell projected onto

the plane of each slice multiplied by the thickness of each slice, that is $V_{shell} = \Delta \times \pi\left((r+dr)^2 - r^2\right)$.

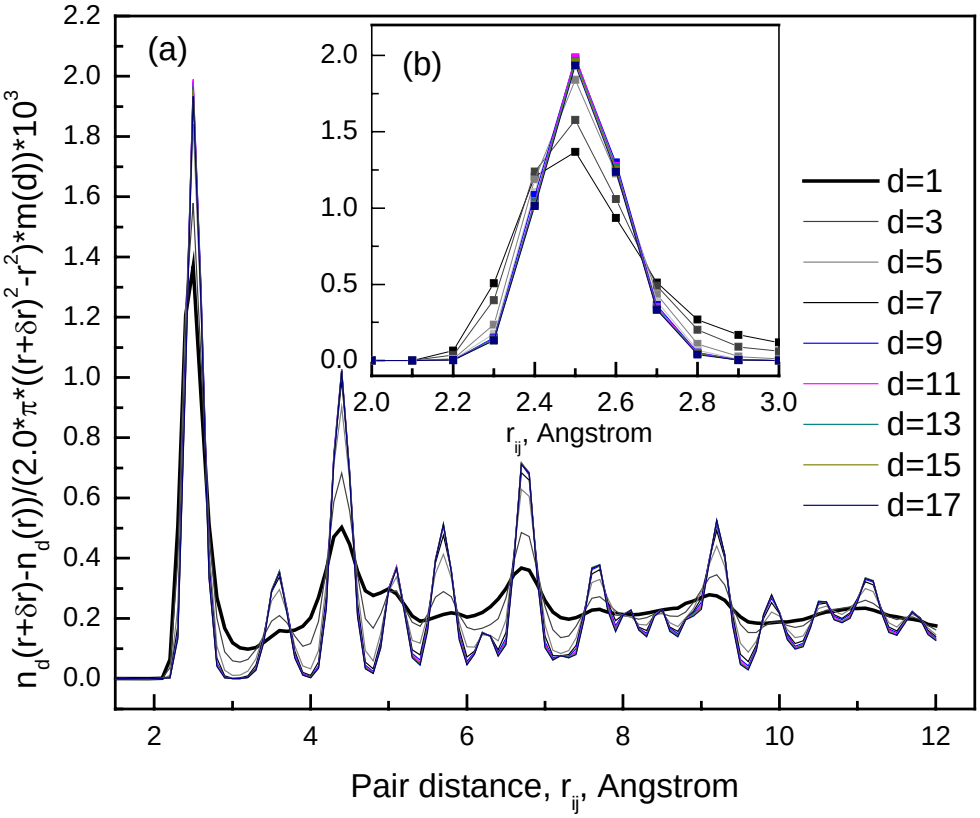

Figure 5.32. Pair correlation function (PCF) of atoms in slices with the same distance to the grain boundary interfaces. The PCF becomes more acute as the distance to GB interfaces decrease indicating that atoms are more ordered.

Using the method described above, we are able to calculate the grain boundary PCF profile for the first time. The PCFs of atoms in the slices with the same distance to the GB interfaces, d, are shown in Figure 5.32. As the slice position moves closer to the center of grain boundary region, the degree of disorder increases. However, a close look at the first peak in Figure 5.32(b) reveals that the PCFs with $d \geq 9$ overlap with each other. Most small peaks disappear from PCF as d decreases. On the other hand, the

degree of disorder revealed by GB PCF profiles confirms once again that the recently proposed grain boundary characterization method is accurate.

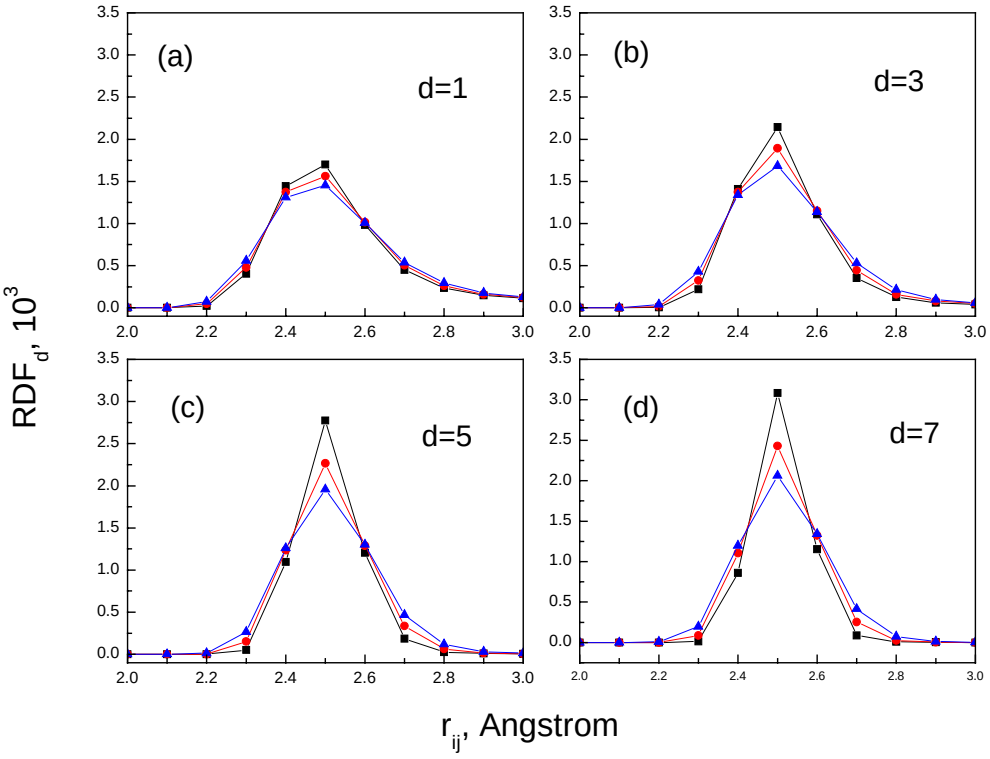

Figure 5.33. The temperature effects on the GB PCF profiles at different slice positions: a) d=1; b) d=3; c) d=5; d) d=7 angstroms. Only the first peaks are shown.

Grain boundary PCF profiles shown in Figure 5.32 are calculated from a nc-Cu sample after MD relaxation at 300K. The same calculation was performed on the same sample after relaxation at three different temperatures: 100K, 200K and 300K. The response to temperature change in GB PCF profiles (Figure 5.33) is similar to that of conventional RDF (observed in Figure 5.1). Only the first peaks in GB PCFs are shown since the trend stays the same for peaks at a longer pair distance. The heights of these first peaks drops as temperature increases and the distance to GB interface, *d*, decreases. A drawback of this definition is that the GB PCF is not properly normalized without a

accurate estimation of the density of atoms in each slice. We will make an attempt to solve this problem later in this section.

Next, the pair correlation function of TJ atoms can be evaluated since we already know the atomic positions of atoms in each TJ. The pair distances between atoms in the same TJ are calculated and accumulated for all characterized TJs. The accumulated pair distances are plotted in Figure 5.34(a). Topologically, TJ is a one-dimensional object and initially a straight line during Voronoi tessellation. However, triple junction is a 3D object with both a finite length and thickness. Based on our observation during grain boundary characterization, TJ lines are often distorted during MD relaxation and no longer have a simple cylinder shape. Unlike the grain boundary interfaces, we cannot overcome this problem by calculating a TJ profile because of the physical sizes and shapes of TJs. To solve this problem, we propose a normalization method that can be applied on most pair correlation function calculations including both PCFs of grain boundary atoms and triple junction atoms. First, we fit the relation between pair distance, r_{ij}, and the number of pairs using a 3rd-order polynomial in the range from 2.0 to 50.0 Å and the divide the function, $N_{pair}\left(r_{ij}\right)$, by the fitted polynomial function, which gives us the normalized pair correlation function of TJ atoms with a tail fluctuating around 1.0 in Figure 5.34(b). For the sample of mean grain size of 8.696nm, the best-fitted polynomial obeys the Eqn. 5.5. For the sample of mean grain size of 10.145nm, the best-fitted polynomial obeys Eqn. 5.6.

$$N_{pair}\left(r_{ij}\right) = 0.0894 r_{ij}^3 - 1.3511 r_{ij}^2 - 419.8 r_{ij} + 14146, \tag{5.5}$$

$$N_{pair}\left(r_{ij}\right) = -0.0259 r_{ij}^3 + 8.1948 r_{ij}^2 - 846.21 r_{ij} + 28864, \tag{5.6}$$

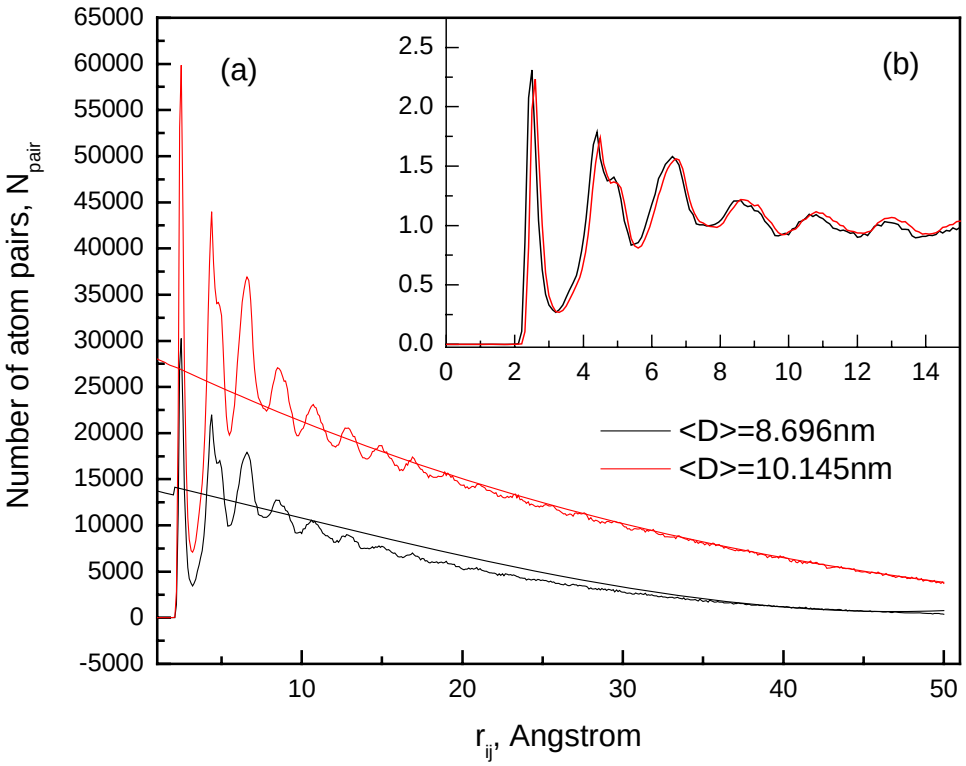

Figure 5.34. a) The accumulated pair distances for two *nc*-Cu samples of mean grain sizes of 8.696 (black) and 10.145nm (red); b) The normalized pair correlation functions of two samples by the fitting third-order polynomials.

To verify this normalization method, we will apply it on two cases: the pair correlation functions of both 1) all atoms in the *nc*-Cu sample and 2) GB atoms. First, we calculated the relation between number of *pairs* and pair distance, $N_{pair}(r_{ij})$, in a *nc*-Cu samples at two temperatures: 300K and 1200K in Figure 5.35 using the method described in section 5.2.1. The same *nc*-Cu sample is relaxed using MD simulations at two different temperatures. At 1200K, the *nc*-Cu sample is in liquid state. Because of the large number of atoms in a sample of 50-grains and mean grain size of 8.696nm, a cutoff distance of 15Å is selected to speedup the calculation. The best-fitted 3rd-order

polynomials at two temperatures are also plotted in Figure 5.35 and the normalized pair correlation functions are shown in Figure 5.36.

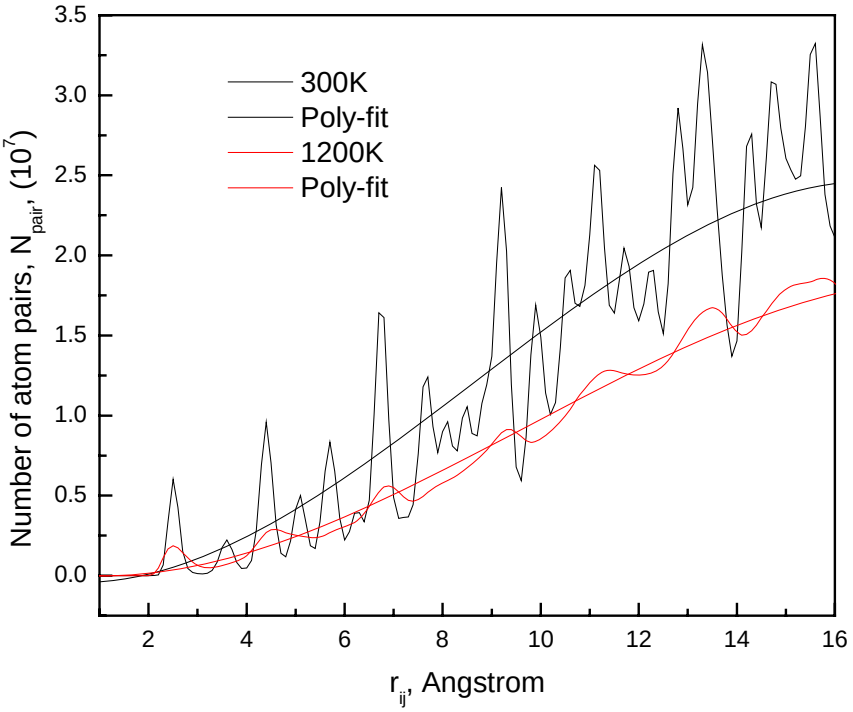

Figure 5.35. The relations between N_{pair} and pair distance r_{ij} of a *nc*-Cu sample at 300K (black lines) and 1200K (red lines) are fitted by a 3rd-order polynomial.

The best-fitted polynomial for the *nc*-Cu sample at 300K obeys is

$$N_{pair}(r_{ij}) = -7264.1r_{ij}^3 + 210638r_{ij}^2 - 423740r_{ij} + 201537, \qquad (5.6)$$

and the best-fitted polynomial for the *nc*-Cu sample at 1200K obeys is

$$N_{pair}(r_{ij}) = -7555r_{ij}^3 + 210447r_{ij}^2 - 279185r_{ij} - 63881. \qquad (5.7)$$

The normalized pair correlation functions are plotted in Figure 5.36 where two functions clearly fluctuate around 1.0 when pair distance, r_{ij}, is larger than 5.0 Å. The normalized PCF at 300K clearly shows the peaks corresponding to a FCC structure while the PCF at 1200K indicates a liquid structure. Most peaks presented at 300K disappear in

PCF at 1200K except three peaks at the small pair distance. The results verify that our proposed normalization method is working at least in relative scale.

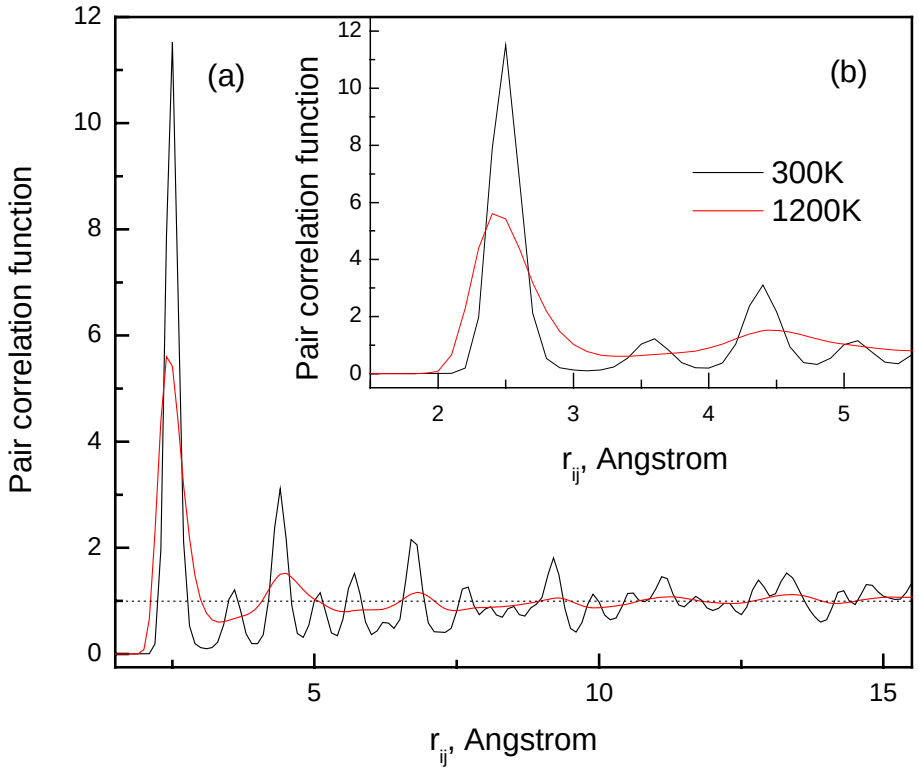

Figure 5.36. The normalized pair correlation functions at two temperatures for the same 50-grain *nc*-Cu sample with a mean grain size of 8.696nm. A dotted line is plotted at $PCF(r)=1.0$.

Next, we test the proposed method on the pair correlation functions for atoms in different slice positions. The relations between the number of atom pairs and pair distances (Figure 5.37), $N_{pair}(r)$, are fitted again using the 3rd-order polynomials. The fitted parameters are listed in Table 5.2. From Figure 5.31, we know that the GB pair correlation functions overlap each other when the distance to GB is larger than 9Å. Thus, we only show five curves in Figure 5.37, e.g. *d*=1, 3, 5, 7 and 17 Å. The normalized pair correlation functions are plotted in Figure 5.38.

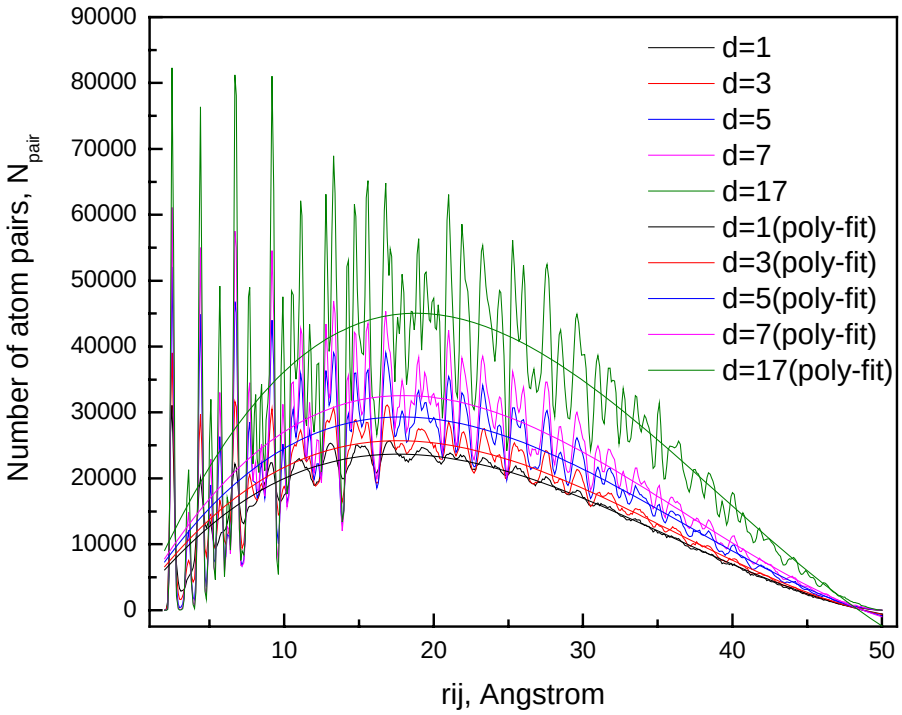

Figure 5.37. The relations between the number of atom pairs and pair distances are fitted by a 3rd-order polynomial for atoms in slices with a different distance, *d*, to grain boundaries (*d*=1, 3, 5, 7 and 17 Å).

Table 5.2. The fitted parameters of the 3rd-order polynomials to $N_{pair}(r)$ for atoms in different slice position, *d*, where $N_{pair}(r) = a_0 + a_1 r + a_2 r^2 + a_3 r^3$.

d (Å)	a_3	a_2	a_1	a_0
1	1.0246	-110.40	2934.0	647.08
3	1.1100	-119.79	3188.2	654.77
5	1.2208	-133.78	3607.3	607.05
7	1.3395	-147.92	4020.4	316.48
9	1.4244	-159.69	4396.1	86.155
11	1.5339	-172.73	4778.9	-376.76
13	1.5795	-180.54	5055.9	-684.37
15	1.6378	-189.18	5342.9	-1022.6
17	1.6405	-192.48	5499.3	-1204.5

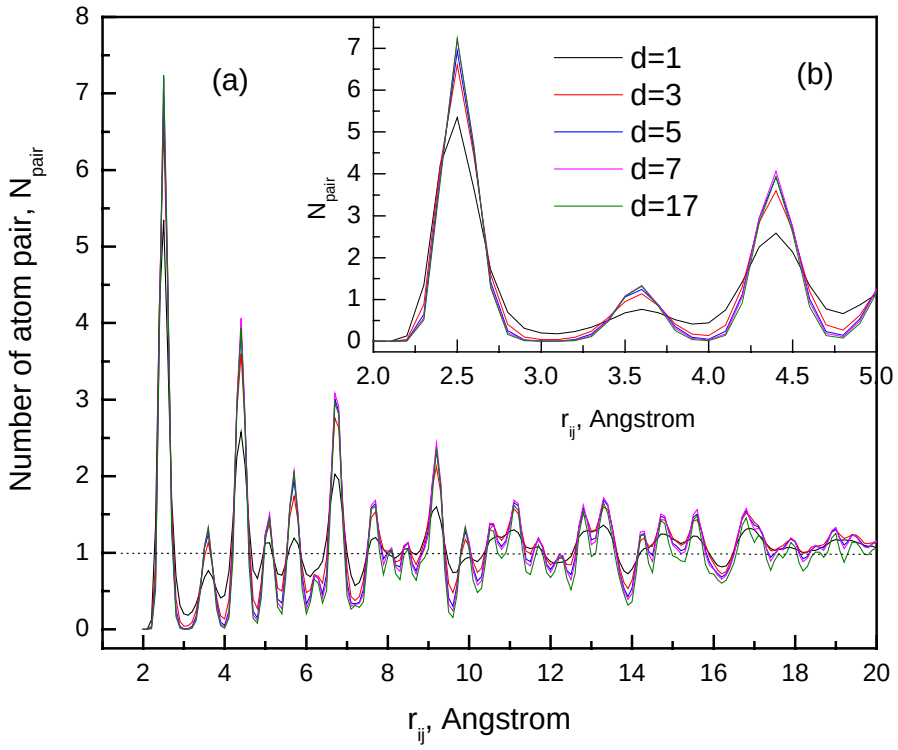

Figure 5.38. The normalized pair correlation functions for atoms in slices with a distance, *d*, to the grain boundaries (*d*=1, 3, 5, 7 and 17Å).

Finally, we are able to apply the same normalization method to obtain PCFs for three types of atoms, namely the grain atoms (*d*=17Å), grain boundary atoms (*d*=1Å) and triple junction atoms in Figure 5.39. Figure 5.40 shows the normalized PCFs where grain atoms have the highest first peak followed by grain boundary atoms and triple junction atoms in descending order. From the normalized PCFs for three cases, we see that the relative scales in PCFs are correct using the proposed normalization method. From the potential energy calculation (Figure 5.26), we know that the average potential energy increases as the dimensionality of GB entity decreases. Grain atoms associated with grain volume have the highest dimensionality (3D) are in the most stable and ordered state and thus have the highest peaks in PCFs. GB atoms (2D) have a higher first peak than TJ atoms (1D).

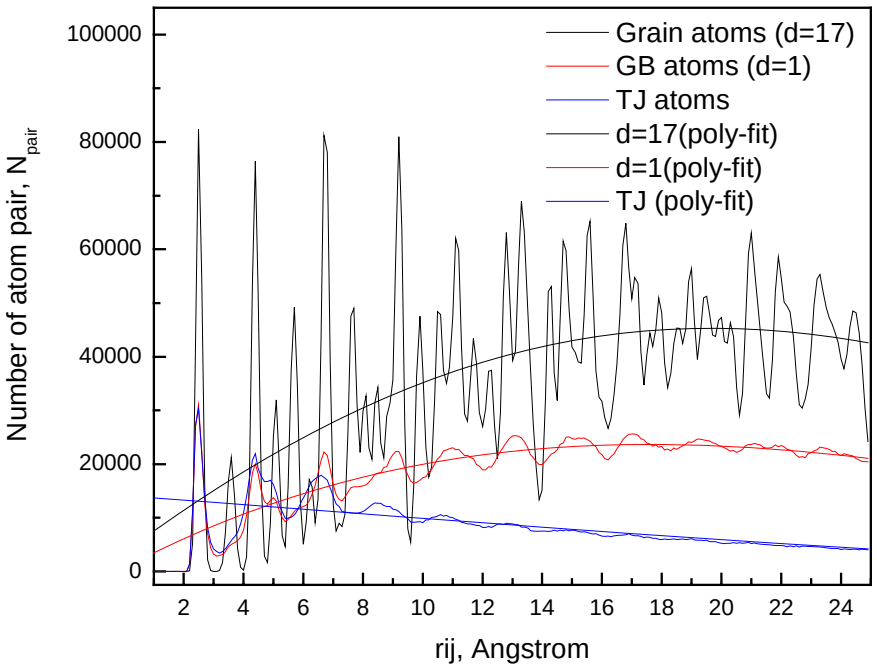

Figure 5.39. The relations between the number of atom pairs and pair distances for three types of atoms are fitted using a 3rd-order polynomial: 1) Grain atoms (*d*=17Å, black lines); 2) GB atoms (*d*=1Å, red lines); and 3) TJ atoms (blue lines).

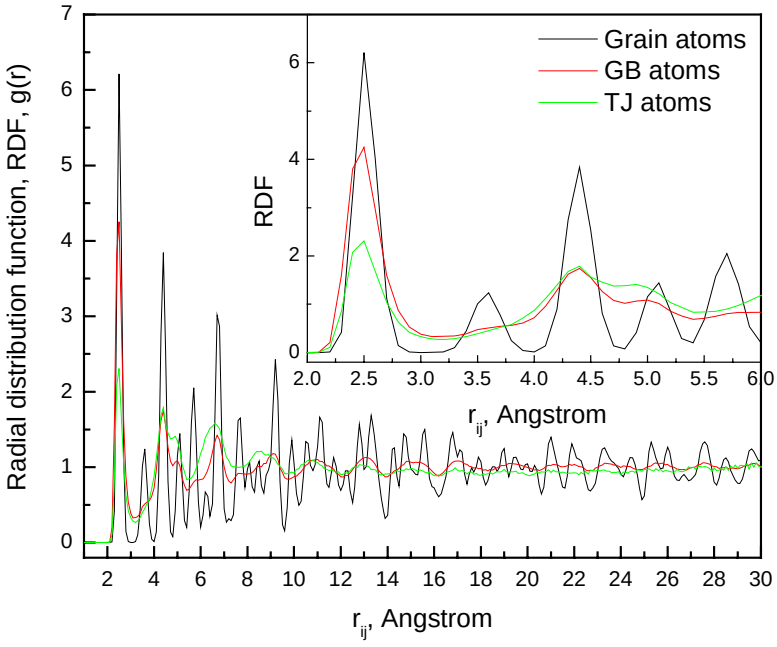

Figure 5.40. Normalized PCFs for three types of atoms: 1) Grain atoms; 2) GB atoms; 3) TJ atoms.

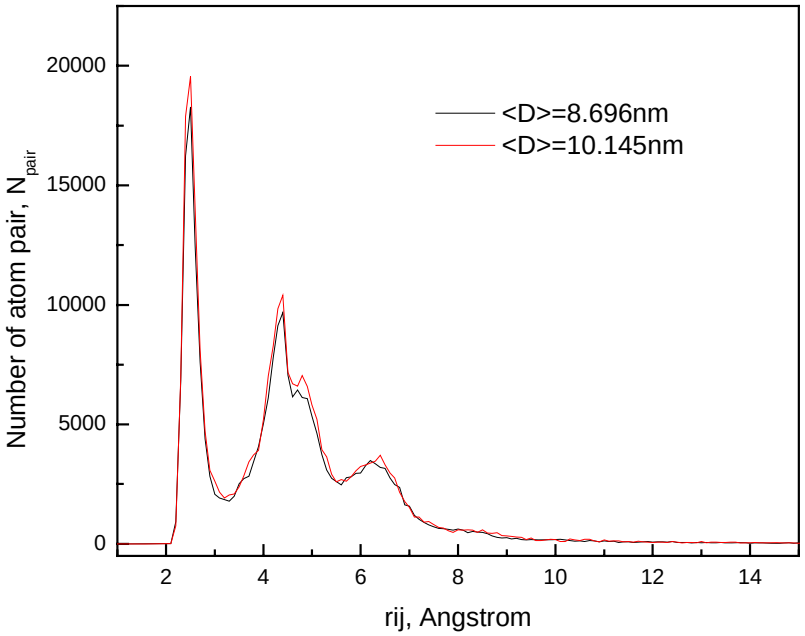

Figure 5.41. The relation between the number of atom pairs and the pair distance for vertex atoms in *nc*-Cu samples of different mean grain sizes: 1) 8.696nm (black line) and 2) 10.145nm (red line).

However, we are not able to apply the same method on PCF of vertex atoms because of the lack of statistics and small number of pairs between vertex atoms. Since we only calculate pair distance between atoms on the same vertex, the total number of pairs between vertex atoms is limited even after all pair distances are accumulated for every characterized vertex. As shown in Figure 5.41, the total number of pairs between vertex atoms doesn't change much when the average grain size increases from 8.696nm to 10.145nm. Both samples have the same initial Voronoi structure except that different number of atoms are filled into it using different reduced lattice parameters, $\alpha = a_0 / L$. The detailed procedure can be found in Chapter 5.

5.4 Conclusions

In this chapter, we present a systematic approach to rebuild microstructures in nanocrystalline materials. A constrained Voronoi tessellation method in conjunction with an inverse Monte Carlo method is applied to build grain cells, or grain boundary networks, that bear resemblance to the real microstructures in quantitative fashion. The crystallographic orientations of the microstructures are selected through an optimization method described in Chapter 4. After filling atoms into the Voronoi structure, we obtain the *nc*-Cu sample with different misorientation distributions and the lattice of each grain is FCC. Finally, we are able to apply the new method, the peeling-onion algorithm, to the relaxed *nc*-Cu after MD simulations and characterize atoms in nanocrystalline samples as grain, grain boundary interface, triple junction and vertex atoms. This method allows us, for the first time, to characterize measure and correlate the detailed microstructure attributes to the properties in nanocrystalline or polycrystalline materials.

Chapter 6

Topological properties of grain boundaries of nc-Cu materials

The characterization of grain boundary (GB) entities remains a big obstacle to understand the structure-property relation in polycrystalline materials especially at nano-scale. It is still challenging both experimentally and theoretically to determine the topological properties of polycrystalline materials, such as the GB interface area and triple junction length, due to the complex and disordered grain boundary network presented in the nanocrystalline materials. In this chapter, defect free nanocrystalline Copper (*nc*-Cu) samples are first generated by filling atoms into the Voronoi structure and then relaxed by molecular dynamics simulations. Atoms in the relaxed nc-Cu samples are then characterized into grain atoms, GB interface atoms, GB triple junction atoms and vertex atoms using a recently proposed method. Atoms in each GB entity can also be identified. Next, the topological properties of *nc*-Cu samples before and after relaxation are calculated and compared, which indicate there exists a physical limit in the number of atoms to form a stable grain boundary interface and triple junction in nanocrystalline materials. In addition, we are able to obtain the statistical averages of geometrical and thermal properties of atoms across each GB interfaces, the so-called GB profiles, and study the grain size and temperature effects on the microstructures in nanocrystalline materials.

6.1 Introduction

Nanocrystalline materials possess the same set of microstructure attributes as those typically seen in conventional polycrystals [93, 159]. The presence of large volume faction of grain boundaries not only induces many novel properties in nanocrystalline

materials but also introduces a large degree of disorder especially near grain boundaries. The complexity and disorder in grain boundary region provide the biggest obstacle to the microstructure of nanocrystalline materials. The microstructure properties include topological properties of grain boundary network such as the grain volume or diameter, boundary area, triple junction length, and vertex point, as well as their statistical properties such as the distributions and various moments (means and variances, for example). These topological and statistical attributes contribute collectively to the mechanical responses of the nanoscale polycrystals. Experimentally, it is difficult to obtain the topological properties of nanocrystals. For example, TEM could handle only a limited number of grains, while a reliable answer should be drawn from the ensemble average of a large number of grains and measurements. In addition, the lack of detailed account of microstructures and calibration of sample conditions can influence the outcome significantly. Although Mössbauer spectroscopy [160] has been utilized to study the grain boundary region in nanocrystalline materials through hyperfine field, it is still challenging to study individual grain boundary entities. The presence of defects and voids in experimentally produced nanocrystalline materials also make it difficult to study the intrinsic topological properties of microstructures. On the other hand, atomistic simulation provides an alternative way to generate defect free nanocrystalline samples using digital microstructure generated by Voronoi tessellation. Atomistic simulations have been performed to study the contribution of grain boundary entities, such as interfaces [161-163] and triple junctions [164, 165], to the properties of nanocrystalline materials. However, most computer simulations focus on individual grain boundary entities with special orientations or spatial arrangement. One of the important elements of nanocrystalline materials has not been presented properly, that is the topological properties of the complex grain boundary network presented in the nanocrystalline materials.

It is crucial to obtain topological properties of nanocrystalline materials, especially from the equilibrated grain structure after molecular dynamics simulations. Many commonly used characterization methods cannot give a clear classification of atoms located on different GB entities. For example, pair correlation function or radial distribution function (RDF) can only reveal the structure of the whole sample, while geometrical methods such as centro-symmetry parameter (CSP) [155] and atomic Voronoi volume (AVV) are strongly affected by the thermal fluctuation during MD simulations. For the same reason, thermal properties like potential energy and atomic stresses are not efficient for grain boundary characterization at atomistic level. The common neighbor analysis (CNA) [156] has been used to identify *fcc*, *hcp* or other types of atoms presented in nanocrystalline materials. The grain structure is clearly visible since most grain boundary atoms are non-*fcc* and non-*hcp* atoms. However, this information alone is not enough to identify atoms in every GB entity. Another detailed grain boundary characterization technique is still absent that is essential to understand the structure of nanocrystalline materials.

In this chapter, we will apply a grain boundary characterization technique called the "peeling-onion" method to determine the number of unique grain boundary entity, such as interface, triple junction and vertex and also the number of atoms in each grain boundary entity. The topological properties such as the interface area and triple junction length are then calculated using the positions of vertices as well as their statistical distributions. In section 6.2, we will describe how an equilibrated nanocrystalline copper sample is generated based on Voronoi tessellation technique. In section 6.3, we present the method to calculate the topological properties of *nc*-Cu sample before and after MD relaxation and describe a procedure to detect the degree of disorder presented in the grain structure. In section 6.4, we compare the topological properties of *nc*-Cu samples and study the grain size and temperature effects on the structure of *nc*-Cu samples.

6.2 Sample Preparation

Voronoi tessellation has been used widely to represent the grain cell structures in metallurgy [89, 93, 101] and computer simulations [95, 152]. Voronoi tessellation mimics the homogeneous nucleation and grain growth during microstructure formation when a space of dimension d is partitioned into space-filling, convex polyhedron, or cells [83]. The Poisson-Voronoi polyhedron are constructed by first placing N random points in the space and then partitioning the space into N numbers of polyhedron formed by the planes bisecting the bonds connecting each point and its nearest neighbors. Another set of information is needed before atoms with a specific crystal structures (e.g. *fcc*, *hcp*, etc.) can be filled into the grain structure generated from Voronoi tessellation, which is the crystallographic orientation of each grain.

Each Voronoi cell represents a *nc*-Cu grain and a randomly selected orientation is selected for each grain. The misorientation angle of each grain boundary interface can be calculated [132, 166] and the misorientation distribution follows the Mackenzie distribution [133]. The detailed atom filling procedure is described in Chapter 4. Due to the physical size of each atom located at each lattice point, it is inevitable to have some atoms near the grain boundary that are closer than the equilibrium lattice constant. Atoms that are too close (less than 80% of the nearest neighbor distance a) must be removed to avoid unphysical high repulsive potential energy during molecular dynamics simulation. After deleting the overlapped atoms, the atomic density near grain boundaries will vary around the equilibrium atomic density. Next, molecular dynamic simulations are performed to relax the non-equilibrium grain structures in the *nc*-Cu sample.

The number of grains in the sample is 50 and kept constant in this study. The total number of atoms is 1396178 and the box length is 25.83 nm with a mean grain size of 8.696 nm. The same grain structure can be used to generate samples of different mean grain sizes later. EAM potential developed by Foiles [167] is used for the

simulation. Y. Mishin *et al* [141] evaluated the ability of the EAM potential to predict reliable energies and stabilities of non-equilibrium structures by taking copper as a model material. NPT Molecular dynamic relaxation is then performed at 300K for 100,000 time steps to fully relax the nc-Cu sample using the Large-scale Atomic/Molecular Massively Parallel Simulator (LAMMPS) package developed by the Sandia National Laboratories. The time step is 0.005 ps. The atomic configuration of relaxed nc-Cu sample is shown in Figure 6.1 using common neighbor analysis [[156]] (CNA).

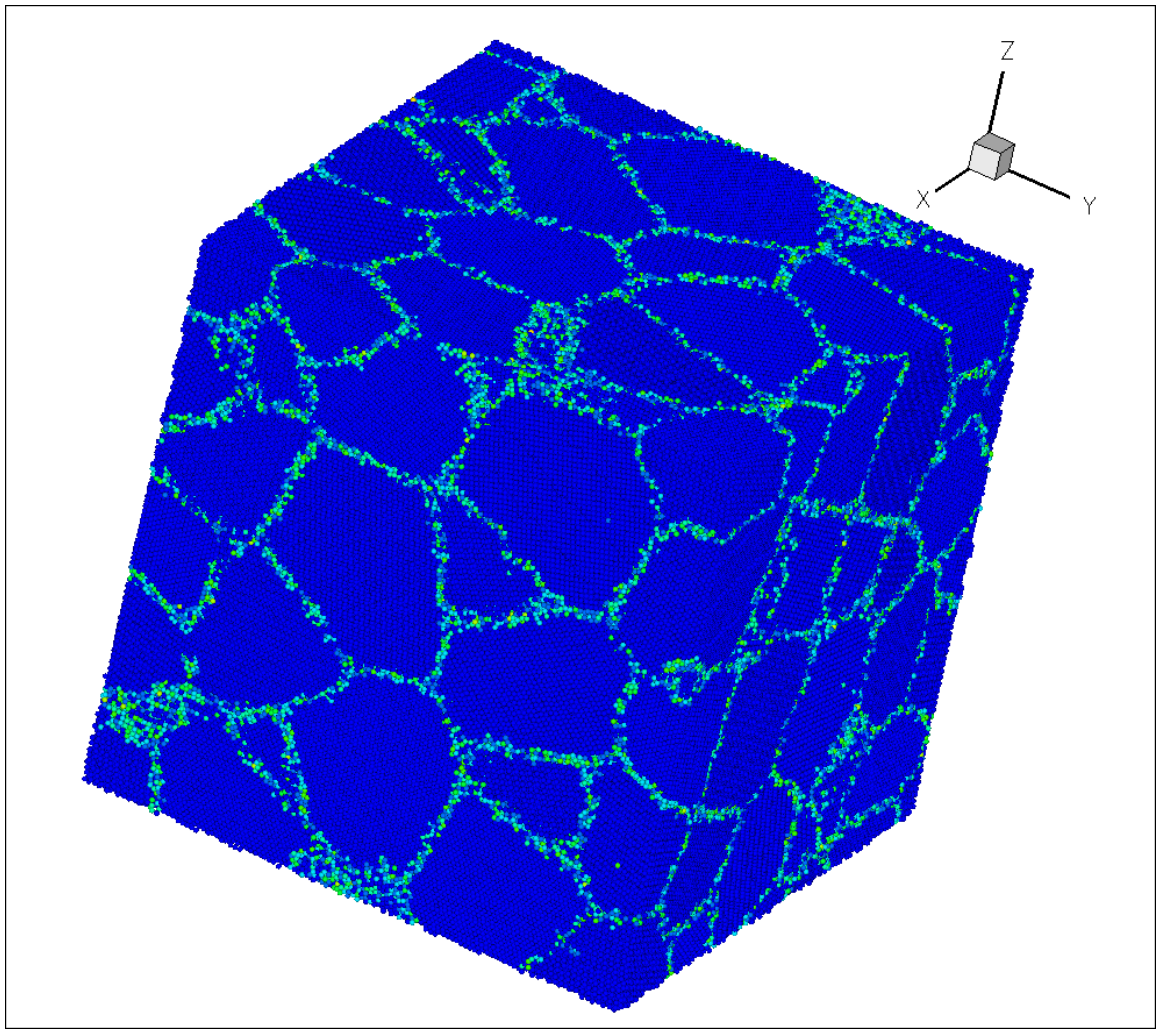

Figure 6.1. The *nc*-Cu sample of 50 grains after MD relaxation is characterized by common neighbor analysis. The blue atoms are *fcc* atoms. Green atoms are *hcp* atoms and yellow atoms represent the rest.

6.3 Methods

6.3.1 Calculate the number of atoms in each GB entity

In order to characterize the grain boundary entities in the relaxed sample, we need to update each atom's grain index since some atoms on the grain boundary will move closer to a different grain. Here, we apply the *peeling-onion* method proposed in section 5.3 to update all atoms' grain index (GI). Using the *peeling-onion* method, we first identify the core atoms of each grain and then associate the rest of atoms one layer at a time to the closest grain core. The core atoms are defined as *fcc* atoms with at least eight *fcc* neighbor atoms. All core atoms' grain indexes are kept the same as their initial GIs before MD relaxation. The thickness of each layer is the first nearest neighbor distance of *fcc* copper atom. After all atoms are associated with a grain core, atoms belonging to the same grain core are given an updated grain index (GI). Next, atoms in the relaxed sample are further characterized into four groups: grain atoms, grain boundary interface atoms, triple junction atoms and vertex atoms. For each atom, we first find its neighbor atoms within a cutoff distance and the number of different grain indexes of these neighbor atoms is counted. The cutoff distance is set as one and half first nearest neighbor distance. If an atom's neighbors have the same GI, then it is a grain atom. If an atom's neighbors have two different GIs, then it is a grain boundary interface atom. If an atom's neighbors have three different GIs, then it is a grain boundary triple junction atom. If an atom's neighbors have four different GIs, then it is a vertex atom.

Similarly, we can characterize the unrelaxed *nc*-Cu sample using the above procedure where each atom's initial GI in the Voronoi tessellation is used instead of the updated GI. Next, atoms in each GB entity can be easily identified. For example, atoms in the same grain boundary interface have the same two different GIs. Atoms in the same triple junction have the same three different GIs and atoms in the same vertex have the same four different GIs. We can then calculate the number of atoms in each GB entity

and obtain their distributions before and after relaxation. The results will be discussed in section 6.4.1.

6.3.2 Calculate the interface area and triple junction length

Grain boundary characterization using the peeling-onion method provides the detailed atomic configuration of each grain boundary entity such as GB interface, triple junction and vertices. In the previous section, we use the atomic configuration of atoms on the same grain boundary to determine the normal vector and calculate the grain boundary profiles. On the other hand, atomic positions of vertices can reveal the topological properties of the structure such as interface area and triple junction length. The procedure to calculate the GB interface area and triple junction length includes four steps:

1. For each grain with grain index, i, we obtain the list of its neighbor's grain index, $neibGI\left[numNeib[i]\right]$, where $numNeib[i]$ is the number of neighbors of grain, i. The number of neighbors of a grain is the same as the number of GB interfaces of that grain. Atoms on the same GB interface will have the same two GIs in the array $diffGIs[numDiffGIs[i]]$.

2. For each GB interface, we obtain the list of vertices located on the interface, $validVertices[numVerticesOnGBInterface]$ but discards small vertices (e.g. vertices with less than 13 atoms). Vertices that have more than 13 atoms are called valid vertices. Each vertex has four GIs in the array $diffGIs[numDiffGIs[i]]$. Vertices on the same GB interface should have at least two common GIs. One is current grain's GI, i, and the other is on the list $neibGI\left[numNeib[i]\right]$.

3. For each GB interface, search for a closed loop that connects all valid vertices. The two common GIs are sorted into the first two slots in the array $diffGIs[numDiffGIs[i]]$. When searching for the loop, we only need to look at the last two GIs, namely, $gid1$ and $gid2$. Figure 6.2 shows the interface between grain 06 and 07. Each vertex is labeled by the two GIs excluding two common GIs. Two vertices are connected by a triple junction line if they have a common GIs in either $gid1$ or $gid2$. For example, vertex (18,37) is connected to vertex (35,37) because they have a common GI, 37.

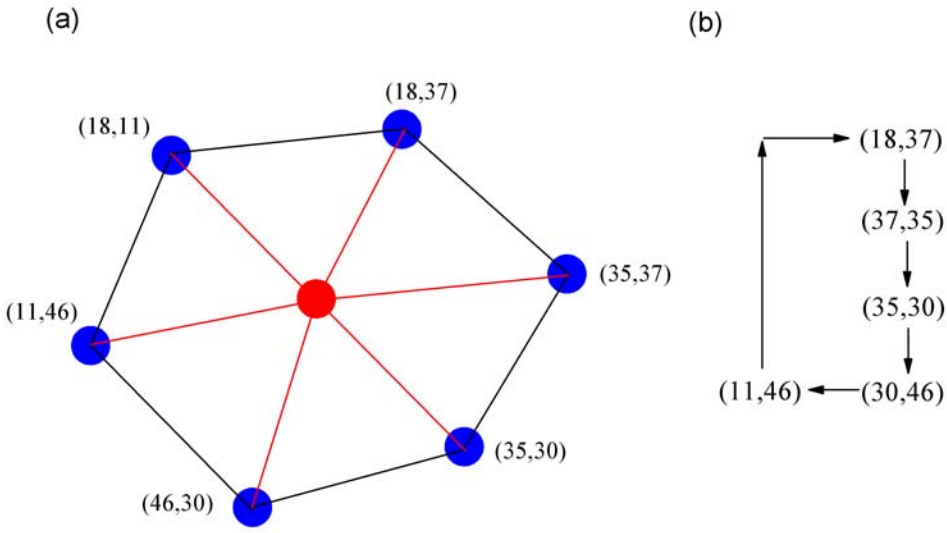

Figure 6.2. a) Schematic diagram of GB interface between Grain 06 and 07. b) The perfect closed loop linked by a common grain index, either $gid1$ or $gid2$.

4. Determine the center of mass of atoms on the interface (the red circle on Figure 6.2) and then calculate the area of the triangles formed between the

face center and two vertices connected by a triple junction line. The area of the interface is obtained by taking the summation of areas of triangles. The calculation of triple junction length is straightforward once each pair of connected vertices is identified.

The GB interface described by Figure 6.2 represents the majority of GB interfaces presented in the relaxed nc-Cu sample and their interface areas can be calculated using the above procedure. However, there are two cases where a perfectly closed loop cannot form.

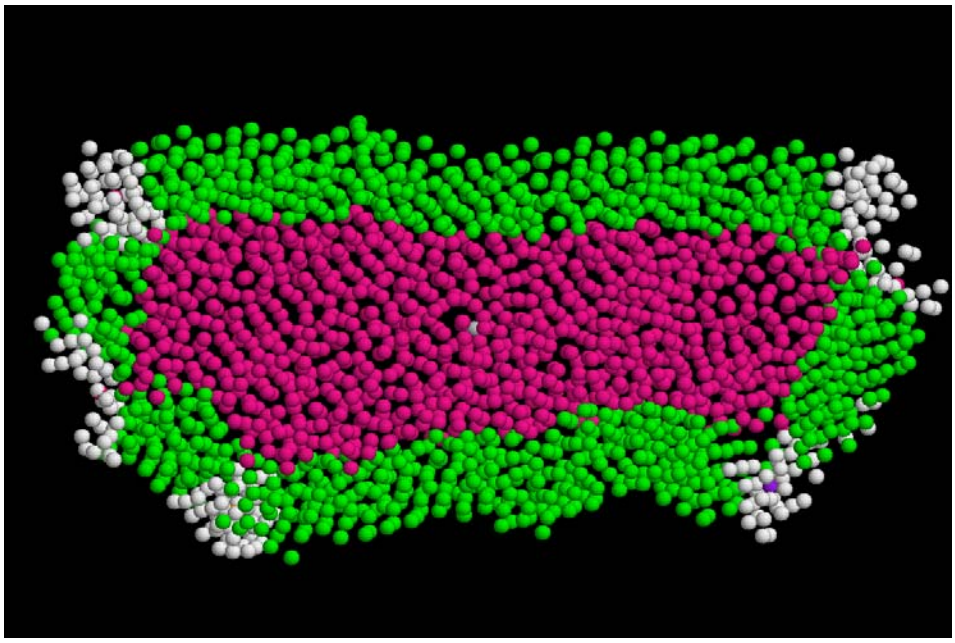

Figure 6.3. Atomic configuration of the GB interface between 06 and 34.

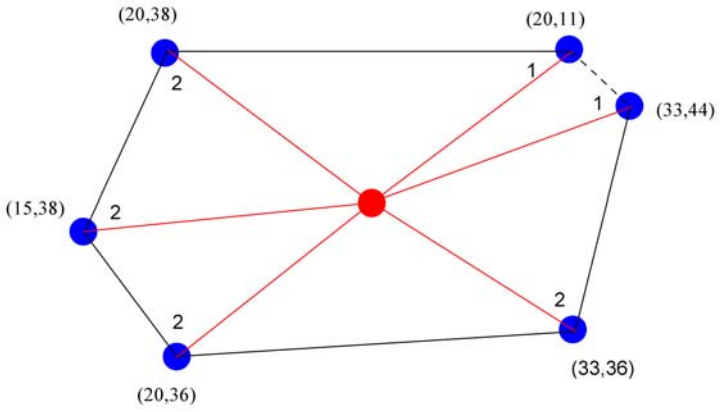

Figure 6.4. The missing link identified in the open loop.

Case 1. Figure 6.3 shows the atomic configuration of GB interface between grain 06 and 34. The positions of vertices on the GB interface are plotted in Figure 6.4 along with the last two GIs in the array *diffGIs*[*numDiffGIs*[*i*]]. There is a missing triple junction line between two merging vertices (20,11) and (33,44). The missing link can be easily identified by counting the number of times that each vertex is used to form a triple junction line. In a perfect loop (Figure 6.2(b)), each vertex should be connected to two neighboring vertices. The missing link is found between two vertices that are used only once. The total area of the GB interface should be increased by the area of triangle formed by the center of mass and vertices (20,11) and (33,44).

Case 2. Figure 6.5 shows the interface between grain 06 and 46. The position and GIs of vertices is drawn in Figure 6.6 where an additional vertex (30, 35) is introduced by a neighboring grain 35 (Figure 6.7). Because of vertex (30,35), the area of the GB interface is overestimated and needs to be adjusted. Similarly, the problem can be solved by counting the number of times that each vertex is used to form a triangle. Vertices

(7,30) and (30,31) are both counted 3 times. The area of the triangle between these two vertices and the face center should be subtracted to obtain the correct interface area.

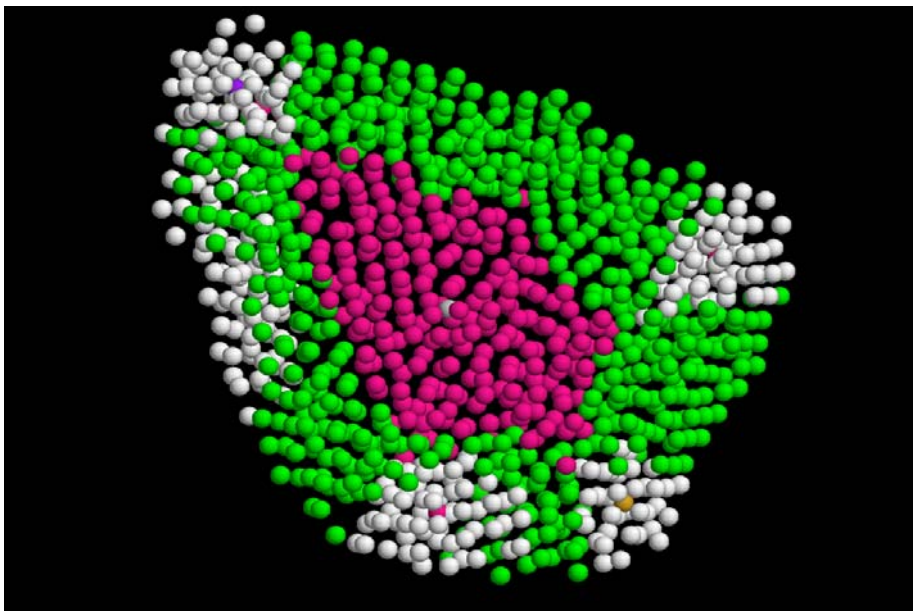

Figure 6.5. Atomic configuration of the GB interface between 06 and 46. The mass center of grain boundary atoms (pink atoms) is plotted as a gray atom. The mass centers of all vertices are plotted as atoms of different colors.

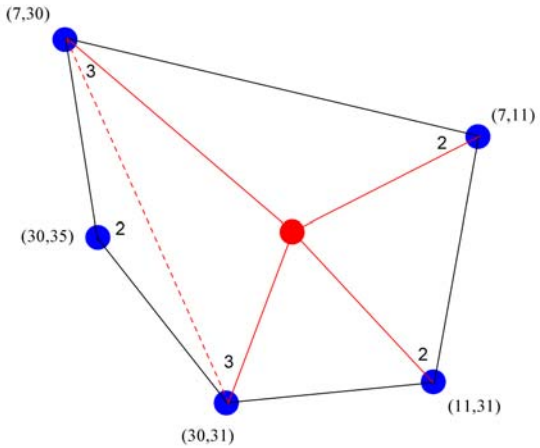

Figure 6.6. An additional vertex identified as (30,35).

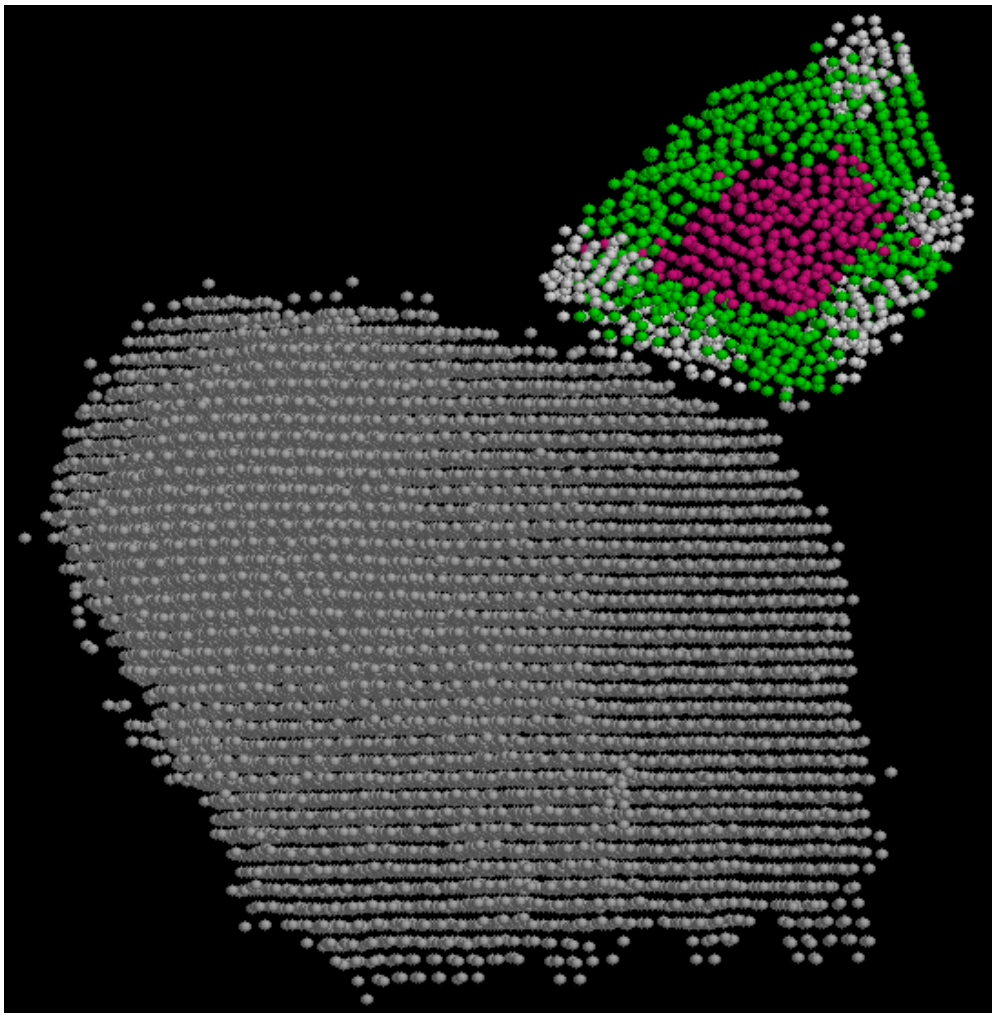

Figure 6.7. GB interface (6, 46) and grain 35. The additional vertex is introduced by the neighboring grain 35.

6.4 Results

6.4.1 Number of atoms in each GB entity

From the initial Voronoi structure of 50 grains, we can obtain topological properties such as the cell volume distribution, face area distribution and triple junction length distribution, shown in Figure 6.8-6.10. Figure 6.8(a) shows the distribution of volumes of 100 grains. Figure 6.9(a) shows a large amount of small interfaces existing in the unrelaxed nc-Cu sample. A large amount of short triple junction is also present in the unrelaxed sample as shown in Figure 6.10(a). Those extremely small interfaces and short

triple junctions are not stable and will disappear after relaxation. Moreover, large grain boundary interfaces are often distorted to resolve the initial artificial stresses near grain boundaries during MD relaxation.

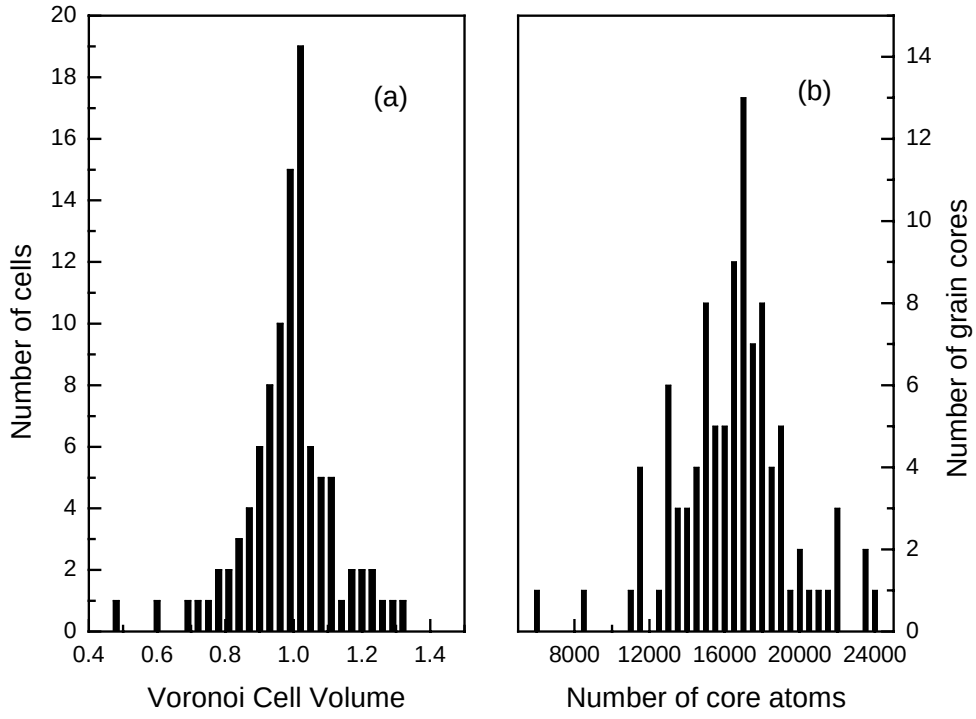

Figure 6.8. a) Cell volume distribution of nc-Cu sample with $\langle D \rangle = 8.05nm$, number of grains is 100; b) the distribution of number of atoms in each grain core.

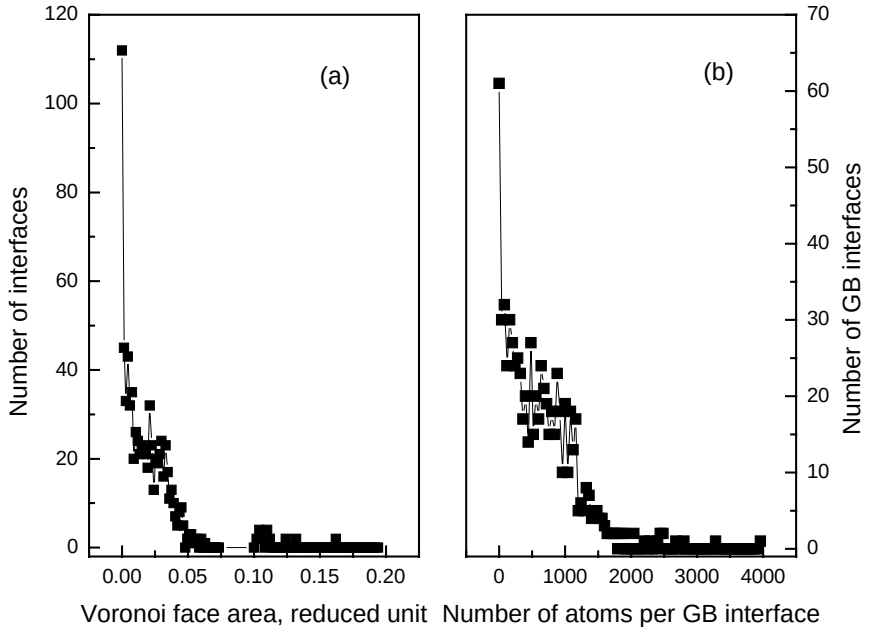

Figure 6.9. a) Face area distribution of Voronoi structure with 100 cells; b) The distribution of the number of atoms per GB interface.

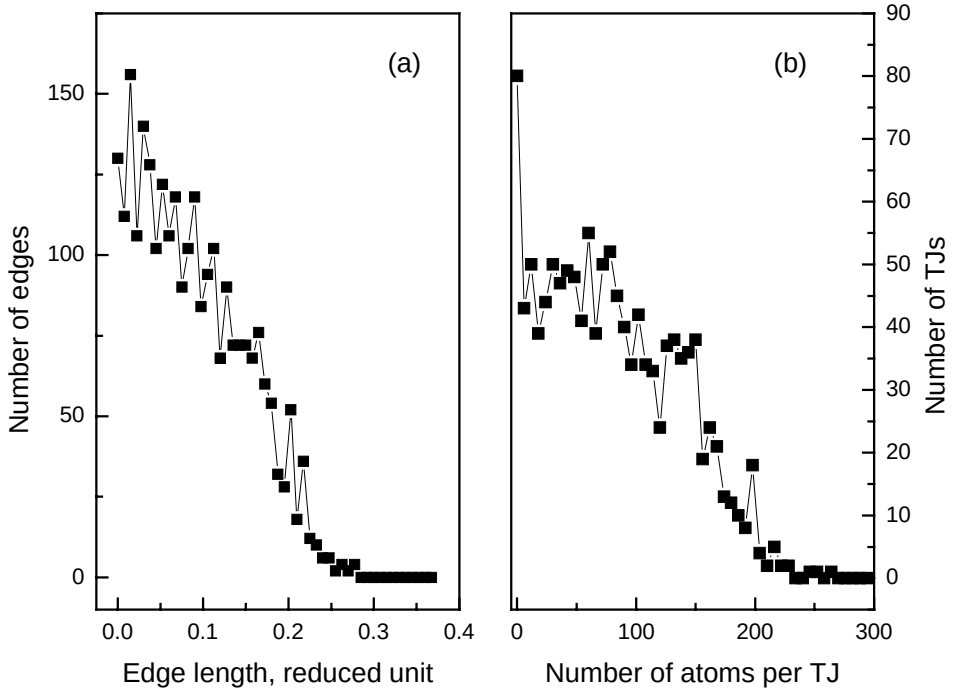

Figure 6.10. a) Triple junction length distribution of Voronoi structure with 100 cells; b) The distribution of number of atoms per triple junction.

Using the GB characterization technique described earlier, we can obtain the distributions of the number of atoms in grain cores (Figure 6.8(b)), GB interfaces (Figure 6.9(b)) and TJs (Figure 6.10(b)) presented in the relaxed nc-Cu sample. Both distributions of number of atoms closely resemble the face area and triple junction length distributions of the initial Voronoi structure. However, physical dimension of GB interfaces with less than 100 atoms are close to that of vertices. These small GB interfaces are discarded and are not accounted during interface area calculation. The same applies for small TJs.

6.4.2 Interface area and triple junction length

The accuracy of grain boundary area calculation can be determined by linear relation between the number of atoms in each grain boundary interface and the calculated area using the above-mentioned procedure. Figure 6.11 plots the number of atoms in each grain boundary interface, n_f, against the calculated area, a, and a linear relation, $a = 1.9957 n_f - 382.37$, is clearly. Each point represents a GB interface. Due to the nature of GB interface after relaxation and the large number of GB interfaces presented in a nc-Cu sample of 50 grains, it is difficult and time consuming to calibrate for each GB interface. The mean grain size is 12.17nm. While determining the number of atoms on each GB interface, we must include the atoms in the TJ and vertices surrounding the same GB interface. The number of atoms in TJs is multiplied by $2/3$ since the same TJ on a GB interface is shared by two neighboring grains. The number of atoms in vertices is divided by two for a similar reason. The GB interface area approaches zero at a finite number of atoms (~100 atoms). This indicates that there exists a physical limit in the number of atoms to form a GB interface. From the GB CSP profiles, we calculated the average GB width for the same nc-Cu sample as 6.194Å. From the slope in Figure 6.11,

we can estimate the average atomic volume of grain boundary atoms by $V_{at} = a \cdot \langle W_{CSP} \rangle / n_f$, which is 12.363Å^3.

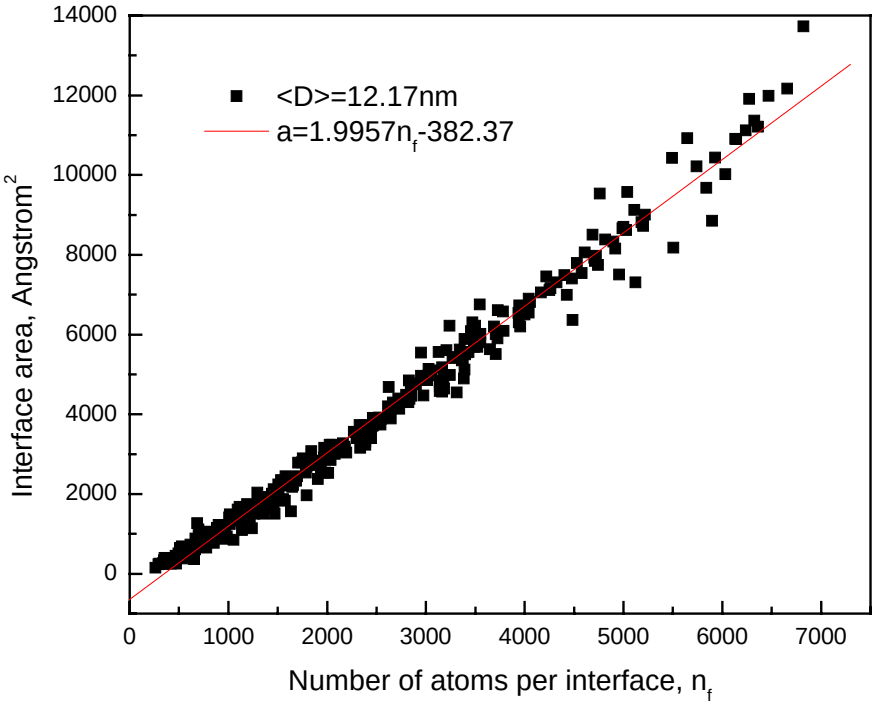

Figure 6.11. The linear relation between the number of atoms per interface, n_f, and the calculated GB interface area is best fitted by $a = 1.9957 n_f - 382.37$, for a 50-grain sample of mean grain size of 12.17nm.

Similarly we plot the number of atoms in each triple junction, n_{tj}, against the calculated triple junction length, l, in Figure 6.12. A linear relation between n_{tj} and l, $l = 0.27416 n_{tj} + 1.01826$, is clearly present. While determining the number of atoms on each TJ, we also include atoms in vertices connected by the same triple junction. The minimum number of atoms in each TJ is around 18, which indicates the physical limit in the number of atoms to form a triple junction.

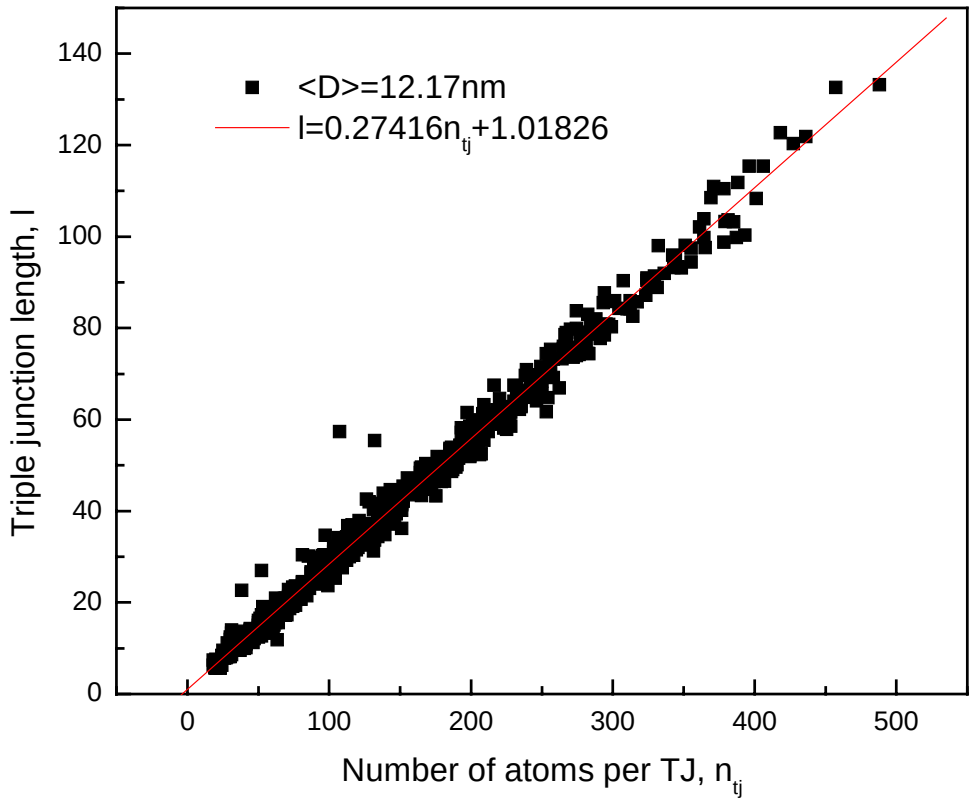

Figure 6.12. The linear relation between the number of atoms per TJ, n_{tj}, and the calculated TJ length is best fitted by $l = 0.27416 n_{tj} + 1.01826$. Number of grains is 50 and average grain size is 12.17nm. The minimum number of atoms on a TJ is 18.

To test this technique on samples of different mean grain sizes, a 50-grain *nc*-Cu sample of mean grain size of 10.15nm is generated using the same Voronoi structure. Another 100-grain *nc*-Cu sample of mean grain size of 8.7nm is also generated. After MD relaxation at 300K, the same procedure is performed on two samples. The linear relation is clearly shown in Figure 6.13 for three samples with different grain sizes after a simply least square fitting. Once again, the GB interface area approaches zero at a finite number of atoms. However, we did not observe any systematic changes in the slope between interface area and number of atoms per interface. Similarly, we obtain the linear relation between the TJ lengths and the number of atoms in each TJ for three samples,

shown in Figure 6.14. The ratio between calculated TJ length, l, and the number of atoms per TJ, n_{tj}, is not affected by the mean grain sizes.

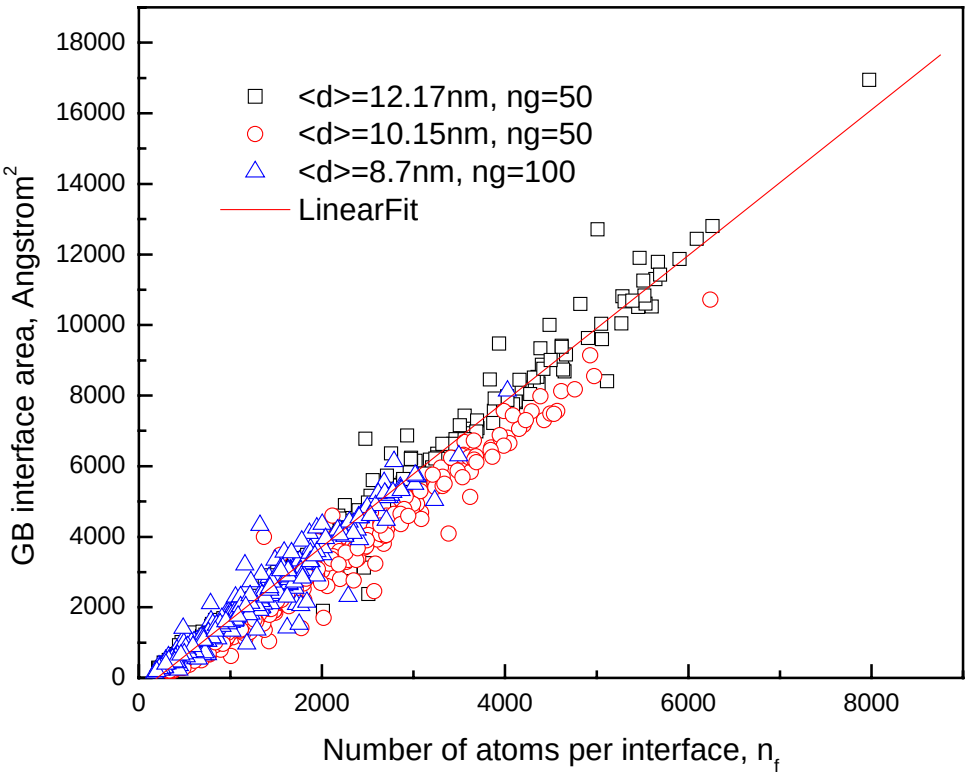

Figure 6.13. The calculated GB interface areas for three samples with different mean grain sizes and grain numbers: a) <*D*>=12.17nm, number of grains is 50; b) <*D*>=10.15nm, number of grains is 50; and c) <*D*>=8.05nm, number of grains is 100.

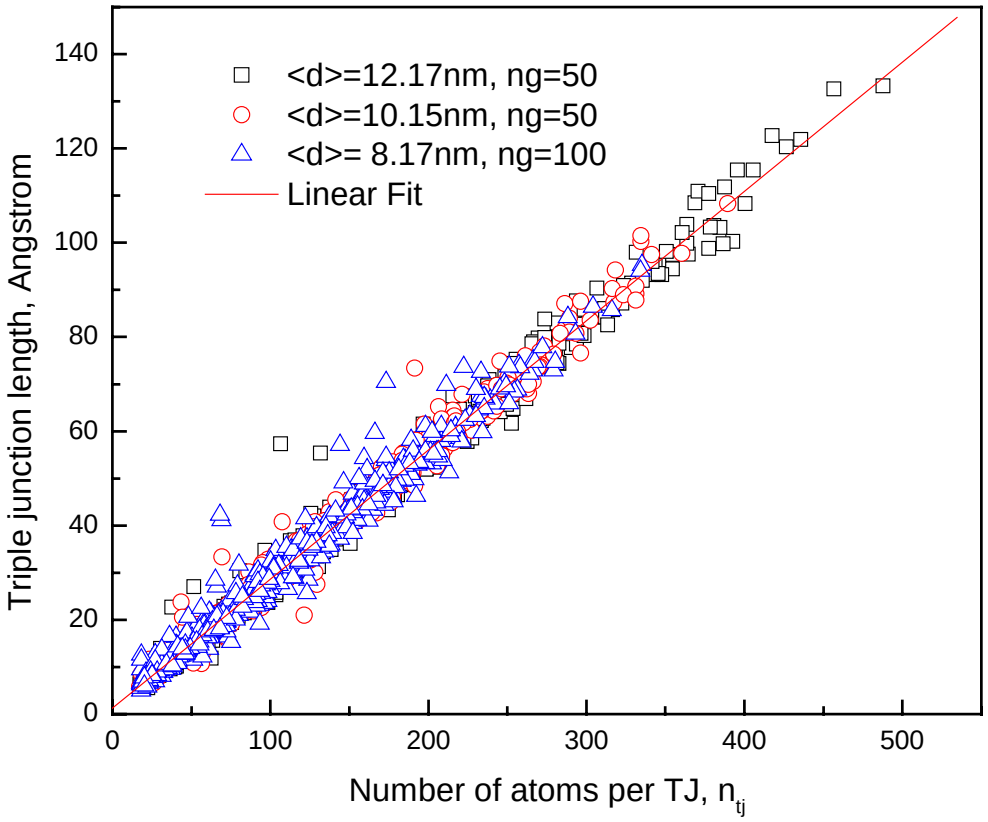

Figure 6.14. The calculated TJ lengths for three samples with different mean grain sizes and grain numbers: a) <*D*>=12.17nm, number of grains is 50; b) <*D*>=10.15nm, number of grains is 50; and c) <*D*>=8.05nm, number of grain is 100.

Up to now, all calculations are performed on nc-Cu samples relaxed at 300K. Next, we will test the applicability of our method on nc-Cu samples relaxed at different temperatures from 100K to 500K. The same 50-grain nc-Cu sample with a mean grain size of 12.17nm is relaxed at different temperature using molecular dynamics simulations. The same procedure is applied on the relaxed sample to calculate the GB interface area and triple junction lengths. Figure 6.15 shows the linear relation between the calculated interface area, a, and the number of atoms per interfaces, n_f, at five different temperatures. The slope, a/n_f, decreases as the temperature increases indicating that the GB density decreases with rising temperatures. Figure 6.16 shows the linear relation

between the calculated TJ length, l, and the number of atoms per TJ, n_{tj}, at different temperatures. However, the slope between l and n_{tj} is not affected by the temperatures.

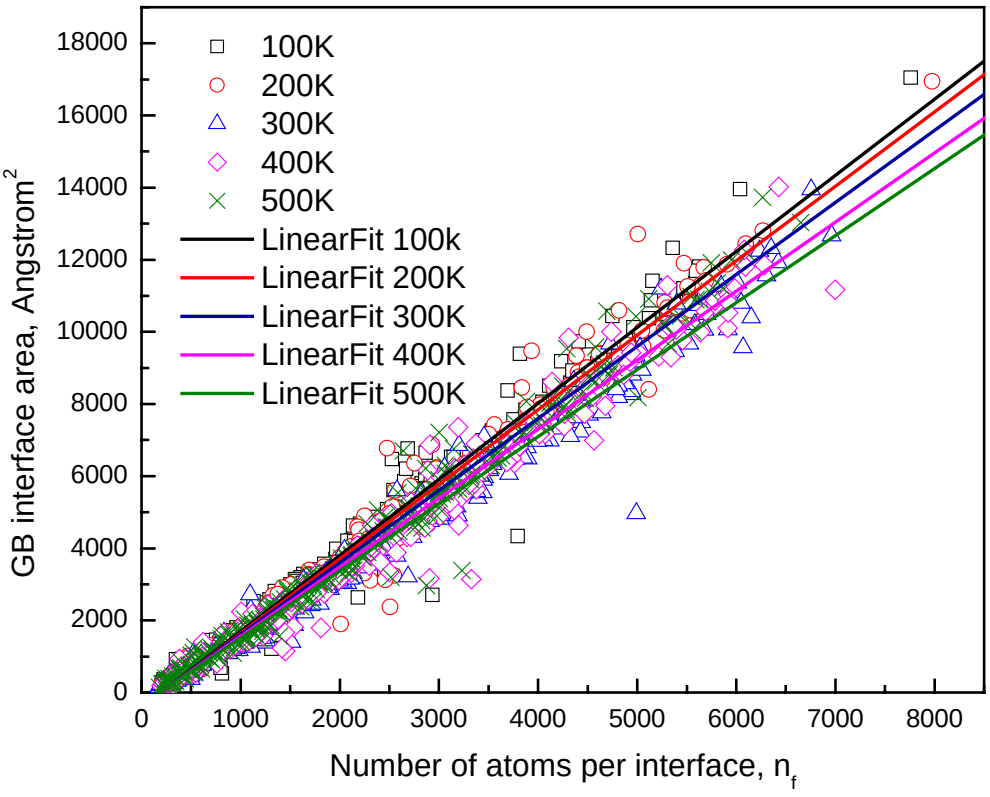

Figure 6.15. The temperature effects on the linear relation between interface area, a, and the number of atoms per interface, n_f, for the same 50-grain nc-Cu sample with a mean grain size of 12.17nm. The slope, a/n_f, decreases as the temperature increases from 100K to 500K.

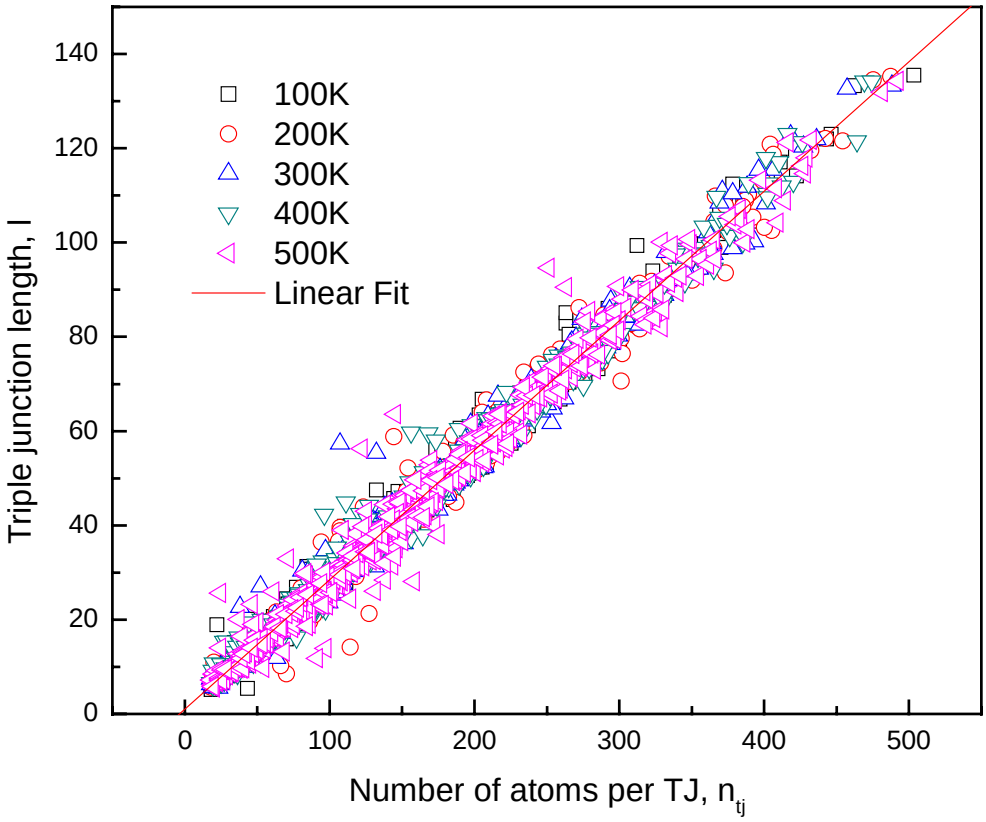

Figure 6.16. The temperature effects on the linear relation between TJ length, l, and the number of atoms per TJ, n_{tj}, for the same 50-grain *nc*-Cu sample with a mean grain size of 12.17nm. The slope, l/n_{tj}, does not change much as the temperature increases from 100K to 500K.

6.4.3 Advantages and Limitations

The biggest advantage of the proposed method is that atoms in each stable GB entity can be identified. Using the position of identified vertices, the 3D grain structure can be reconstructed and the corresponding topological properties are calculated including the interface area and triple junction length. Using the atomic configuration of atoms on each GB interface, the GB profiles can be extracted after determining the normal vector of the GB interface. For the first time, we are able to calculate the topological properties of a nanocrystalline material from the atomic configuration after

MD relaxation. A stable grain boundary structure is a prerequisite to the applicability of method proposed in this study. Most molecular dynamic simulations performed in this study is kept below room temperature to produce *nc*-Cu samples of stable grain boundary networks. A critical grain size exists when the volume fraction of grain boundary region increases over 50% and the transition between crystalline materials and glass happens.

6.5 Summary

In this study, the topological properties of nanocrystalline copper materials are calculated based on a recently proposed grain boundary characterization technique. The digital samples are prepared by filling atoms into a Voronoi structure of 50 cells. The samples are then relaxed using NPT MD relaxation at different temperatures. Using the proposed *peeling-onion* method, each atom in the relaxed sample is given a new grain index. Atoms are further characterized into four groups: grain atoms, GB interface atoms, triple junction atoms and vertex atoms. All grain boundary interfaces and triple junctions are identified as well as atoms in each GB interface and TJ. Next, the interface area and lengths of all triple junctions on the interfaces are calculated using primarily the positions of identified vertices. The linear relation between the number of atoms in each interface and the calculated GB interface area shows that our area calculation is accurate. The same can be said for the TJ length calculation. Comparing the distribution of calculated GB interface area in the relaxed sample and that of initial Voronoi structure, we see that there exists a physical limit in the number of atoms to form a stable grain boundary interface in nanocrystalline materials. Similarly, there also exists a physical limit in the number of atoms to form a stable triple junction in nanocrystalline materials.

To quantify the degree of disorder presented in nanocrystalline copper materials, we measured the distributions of GB width, the peak heights of CSP and AVV profiles at different grain sizes and temperature. As mean grain size decreases, the average GB width increases and the volume fraction of grain boundaries increases. Similar effects are

found when temperature increases. The average AVV does not increase with mean grain size indicating that the density in the center of grain boundary region remains the same. However, the average AVV does increases with temperatures. Finally, we are able to calculate the GB RDF profile based on the proposed method and successfully detect the increasing degree of disorder when approaching the center of grain boundary region.

Chapter 7

Grain boundary misorientation effects on mechanical properties of nanocrystalline copper

In this chapter, we present a systematic study of misorientation and its effects on mechanical properties of nanocrystalline cooper with a particular attention paid to yielding and plastic deformation. To have realistic microstructures, we employ a recently developed constrained Poisson-Voronoi tessellation and inverse Monte Carlo methods to obtain the polycrystalline structure with lognormal grain size distribution and a wide range of misorientation distributions from the most populated small misorientation angles to maximum angles. We show from extensive molecular dynamics simulation that the strength of the nanocrystalline cooper increases with the decreasing misorientation angle, or more fractions of small angle grain boundaries for a wide range of mean grain sizes from a few nanometers to 20 nm. The maximum difference of the strengths could reach 40% for the samples with minimum misorientation distribution and those with maximum distribution. Although dislocation activity is initiated at the small strains for small angle boundaries, it is the overall amount of grain boundary disorder that dominates the onset of yielding and plasticity subsequently.

7.1 Introduction

Over the past two decades, the mechanical behavior of nanocrystalline (*nc*) metals and alloys has been a subject of considerable interest, owing largely to the tremendous increase of the strength found in the materials at nanometer scales. Several explanations have been proposed to rationalize this finding, most of which are based on dislocation

activities known previously in polycrystalline materials. For example, the Hall-Petch (H-P) relation [1, 2] based on dislocation pile-up at grain boundaries has been invoked to describe the strength dependence on grain sizes, that is, $\sigma_y = \sigma_0 + kd^{-1/2}$, where σ_y is the yield strength, d is the average grain size[3, 5, 6, 9, 168], σ_0 and $k(>0)$ are material constants. However, It is found that the strength does not always increase monotonically with the decreasing grain size. Softening, or the so-called inverse Hall-Patch relation ($k<0$) were also observed at smaller grain sizes. Besides the causes from sample conditions (pores, impurities, etc.), to rationalize this "abnormality", many non-dislocation-centric explanations were proposed, including grain boundary (GB) sliding and grain rotation, Cobb creep or grain boundary diffusion [11], grain boundary thickness change [12, 13], and so on. Despite intensive research performed in the past two decades, a definitive and quantitative answer to the mechanical response in nanocrystalline materials is still not fully comprehended. The difficulty lies in the fact that both experimental characterization and atomistic modeling of microscopic mechanisms are severely limited by the fact of the small dimensions and a large number of grains that are present in the *nc*-materials. For example, TEM could handle only a limited number of grains, while a reliable answer should be drawn from the ensemble average of a large number of grains and measurements. What is fundamentally short-handed in particular in this endeavor comes from the lack of detailed account of *microstructures* that are as equally prevalent in the nanocrystalline materials as those in coarse-grained, or polycrystalline materials since, after all, the former is also a kind of polycrystalline materials only with grain sizes in nanometer scales. The microstructure attributes include the geometric and structure properties: (a) grain size, (b) grain shape, (c) grain boundary type, or misorientation, (c) crystallographic orientation, or texture of the grains, (d) grain boundary disorder, or thickness, (e) triple junctions, and (f) vertices. Of course, there are also the statistical properties of these geometric attributes, including

their means, variance, and higher order moments. These properties are known to contribute collectively to the physical and mechanical properties of polycrystalline materials. Therefore, one should expect to see the same, if not larger, influence on the properties from the microstructures on the nanoscales.

In this chapter, we focus on one particular set of microstructure attributes, that is, the *grain boundary misorientation*, and study its effects on the strength and plasticity in nanocrystalline materials. Misorientation is defined as a relative orientation of two adjacent grains along an axis; it is closely related to the nature and properties of the grain boundaries. For small angle boundaries with the misorientation angle less than 15°, the boundaries can be considered as composed as arrays of dislocations and thus have lower energy, while the high angle boundaries with the misorientation angle larger than 15° are in general much disordered and have higher energy. We expect these properties, known to play important roles in mechanical properties in polycrystalline materials, to contribute similarly to nanocrystalline materials. Due to difficulties in synthesis and characterization in nanocrystalline metals and alloys, the structure-property relations specific for the misorientation effect are not easy to obtain. An earlier atomistic simulation shows large dislocation activities occurring in the samples with low angle boundaries [74]. Caturla *et al.* [169] studied the effects of high-angle and low-angle grain boundaries on the strength of nanocrystalline nickel by using atomistic simulations. They found that the sample of low-angle grain boundaries (<17°) has a higher strength when the average grain size is small (4 nm) than the sample of high-angle grain boundaries (≥17°). The trend is reversed when the average grain size is at 12 nm. They also reported that the low-angle grain boundaries have more hcp atoms than the high-angle grain boundaries at smaller strain, indicating a more active dislocation activity. However, the number of grains in their simulation is only 20. There are two critical issues that have been often overlooked in atomistic simulation and continuum modeling as well of nanocrystalline materials. One is the *anisotropy induced by small number of grains* in the simulation and the other

is the difference in volume fraction of grain boundaries induced by different misorientation distributions. When the number of grains is small, two neighboring grains may form more than one grain boundary interfaces with the same misorientation angle but different *grain boundary plane orientation*. Both the grain boundary misorientation distribution and their spatial distribution in the relation to the loading direction may affect plastic deformation in nanocrystalline materials. Another is the *loading mode*. Most of the modeling performed to date has used uniaxial loading with either tension or compression. The simple loading mode may be the choice for experiment but not for theoretical study, as we know that they introduce complex stress or strain states. For instance, normal stress or strain is induced in uniaxial loading that may make it difficult to analyze the intrinsic activation volume and dislocation process.

As shown in this work, by using large samples and simple shear, we can indeed probe some intrinsic responses of a nanocrystalline sample in atomistic modeling. By focusing exclusively on the misorientation effect, we observe that the mechanical properties of the nanocrystalline material are dominated primarily by the grain boundary properties and structure. We show that as in polycrystalline materials, the small angle boundaries in the nanocrystals are more ordered, relatively thin and thus have small excess atomic volumes; as a comparison, the high angle boundaries are more disordered, thicker and with larger excess atomic volume. Under applied shear load, the small angle boundaries are prone to dislocation activities, beginning at small strains while the high angle boundaries only do so at larger strains after some local boundary motions at small strains. We also shed some light on the grain size effect through systematically varying the misorientation. We found that mechanical responses at small grain size (<10 nm) remains the same as those at larger grain sizes, which disagrees with Caturla *et al* [169]. One salient feature is that the grain boundaries become more disordered and thicker at smaller grain sizes, which is more so for samples with high angle boundaries. We should note that the size-induced-grain boundary-disorder is not in the relative sense as has been

argued in the field, rather it is in a absolute sense in terms of grain boundary thickness and local atomic excess volume, for instance.

This chapter is organized as follows. In next section, we shall go over the methodologies used in this work for sample preparation, atomistic simulation, and defect characterization. In particular, we shall present the methods to build specific grain boundary orientation and misorientation. In section 7.3, we shall presents the results obtained using atomistic simulation. In section 7.4, we go over discussions on several issues pertinent to deformation mechanism of nanocrystalline Cu materials. Finally in section 7.5, we make some conclusions from the results drawn from this work.

7.2 Methods

7.2.1 Sample preparation

In this work, we use cooper as our model material. Since Cu is the most widely used model metal [33] among the large number of *nc*-materials investigated, we can find references in both experiments and simulations performed earlier. A large number of nanocrystalline copper is produced experimentally through severe plastic deformation (mechanical attrition, rolling, equal channel angular extrusion, etc.). As the result, they contain different degrees of disorder in grain boundaries. An increasing fraction of the grain boundaries are small angle boundaries, along with texture, in rolling and equal channel angular extrusion; as a comparison, high angle boundaries with more disorder are found in mechanical attrition. In addition, there are various flaws such a pores, voids, and impurities [33], which are known to contribute to softening effects.

The *nc*-Cu samples used in our simulation are obtained from a recent developed constrained Voronoi Tessellation (CVT) method (described in Chapter 3). In this approach, to obtain the microstructure, i.e., grains with convex shape and specific grain sizes, we use the known grain size and misorientation distribution functions as the

constraints in obtaining the optimal topological properties for the polycrystalline materials. The distribution functions come from either experiments or theoretical models. By employing inverse Monte Carlo method we can construct the polycrystalline grains as represented by the Voronoi cells with the desired microstructural distribution functions. In this work, we used the lognormal grain size distribution with the mean and variance, $\sigma = 0.108$ and $\mu = 0.972$. This method allows us to generate polycrystalline samples with different means and variances. It is worth noting that the polycrystalline samples used extensively in various simulations do far are generated from the default Poisson-Voronoi method which has a fixed grain size distribution close to the lognormal distribution with the mean $\sigma = 0.4454$ and $\mu = 1.0$ [14]. In next step, we fill copper atoms with fcc lattice into each of the Voronoi cells obtained from the CVT method. The *nc*-Cu samples with different mean grain sizes can be achieved by filling different numbers of atoms into the same Voronoi cells since the original Voronoi cells have no natural scales. As the default, the poly-crystallites have random orientations (the adjacent grains with nearly the same orientation are not permitted though) or high angle grain boundaries. As shown later, we can use the inverse Monte Carlo method to change the misorientation distribution to any desired one.

The atoms in the samples prepared using the CVT method are rigid and further relaxation is needed. To do so, we used parallelized molecular dynamics (both in-house developed Rahman-Parrinello MD programs and the LAMMPS package by the Sandia National Laboratories) to relax the initial atomic configurations. All systems are kept with the periodic boundary condition (PBC) at 300 K and zero pressure by using the Nose-Hoover thermostat and barostat [170, 171]. Typically, the samples are relaxed for 100,000 time steps, or until the structure of the samples reaches a steady state with no drifting in energy and sample size. The embedded atom method (EAM) potential is used for Cu atoms [167]. Figure 7.1 shows a *nc*-Cu sample before MD relaxation. The relaxed

nc-Cu sample is characterized using CNA in Figure 7.2. The fully relaxed samples are used subsequently in deformation simulation.

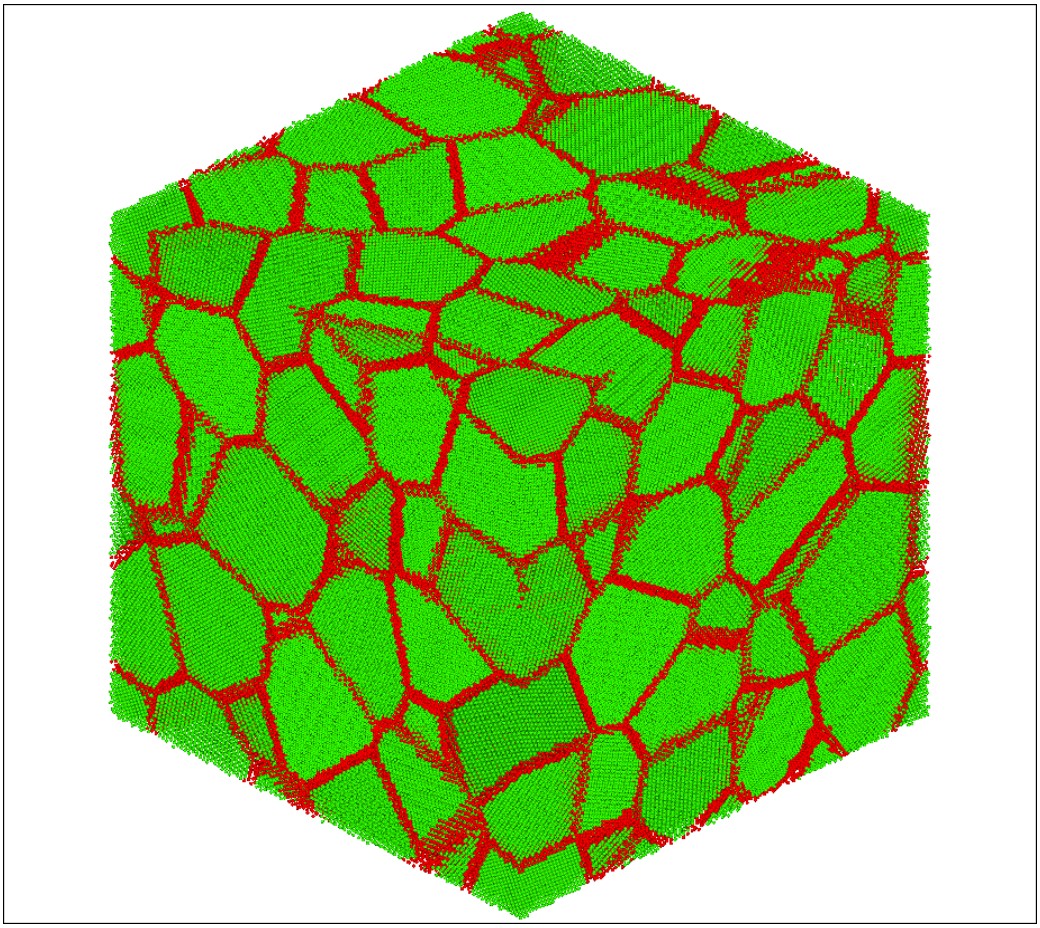

Figure 7.1. Common neighbor analysis of *nc*-Cu sample before relaxation. Green atoms are *fcc* atoms, blue atoms are *hcp* atoms and red atoms are the rest of atoms.

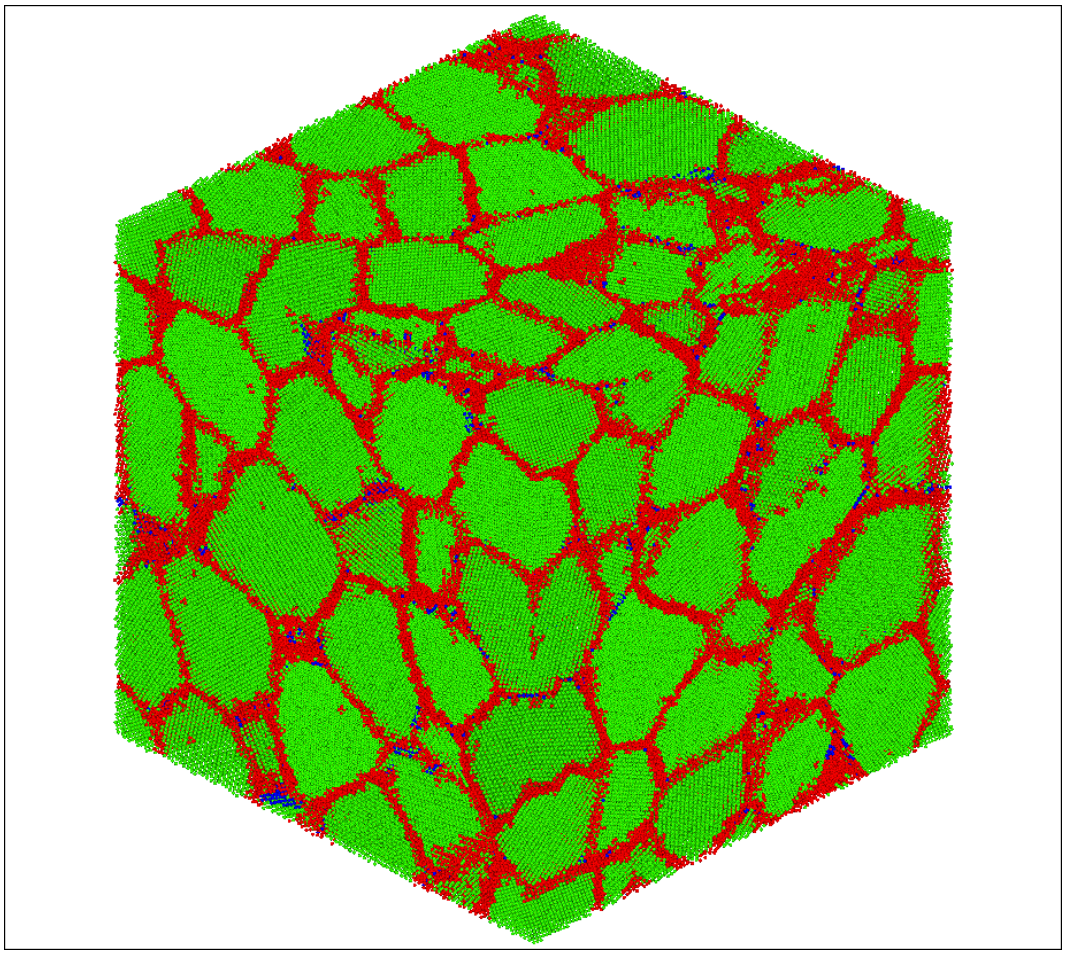

Figure 7.2. Common neighbor analysis of *nc*-Cu sample after relaxation. Green atoms are *fcc* atoms, blue atoms are *hcp* atoms and red atoms are the rest of atoms.

7.2.2 Deformation simulation

Most atomistic simulation of nanocrystalline materials so far are performed using uniaxial loading, i.e., tension or compression. However, careful analysis points to some complications associated with this loading mode: (a) it is not always straightforward to implement uniaxial deformation; as a result, biaxial loading is actually used. Depending on how one handles the lateral contraction and expansion during unaxial loading, the final results may be different from a true uniaxial deformation. (b) There are resolved normal stresses along with shear stresses in uniaxial loading. The former may cause some extra complications in the stress state in analyzing dislocation activities (see below). (c)

Uniaxial loading with the PBC is known prevent heterogeneous deformation. As a result, we will not use uniaxial loading in work, although it is certainly a convenient choice in experiment. Instead, we shall use simple shear.

The deformation is performed using two different methods by displacing atoms according to simple shear in the sample with the PBC along the two directions in the shear plane but non-PBC perpendicular to the plane. One method is to subject the atoms with a constant velocity gradient in the direction perpendicular to the shear plane that is commensurate to the desired strain rate [16]. The second method is by subjecting each atom with an increment or displacement per time step, $R_i = r_i(1+\varepsilon)$, where R_i is the new position for the *i*th atom, r_i the previous position before shear, and ε is the shear strain parameter. Following each displacement per MD step, we also take 100 MD steps to let the atoms to relax. In Lammps, the MD step is about 0.005 picoseconds. The strain rate is kept at 3.873×10^{9} per second.

7.2.3 Grain boundary orientation and anisotropy

The polycrystalline samples in atomistic simulations contain certain number of grain boundaries, which is limited directly by the number of grains, or atoms that can be handled in the simulation. The grain boundaries, distributed as *planes* in three-dimensional space, are oriented differently. It becomes immediately obvious if the number of grains are not large enough, the grain boundaries will likely oriented in such way that certain preferred responses will arise, giving rise to, for example, anisotropy in stress-strain relations. In simple shear, there are three different shear planes that one can implement shear deformation, each of which should give the same result if the sample is isotropic. To test the anisotropy effect, Voronoi cells of different number of grains are generated and the distribution of angles between surface normal vector of the GB plane and three shear planes are accumulated. Three shear planes are *xy*-, *zx*-, *zy*-planes and

their normal vectors are $\vec{v}$, or (1, 0, 0), (0, 1, 0) and (0, 0, 1). Let the unit normal vector of each GB plane be $\vec{n} = (n_x, n_y, n_z)$ and $\sqrt{n_x^2 + n_y^2 + n_z^2} = 1$. The angle between any GB plane and three shear planes are determined by the unit normal vector of the GB and the normal vectors of three shear planes, or

$$\theta_{xy} = \cos^{-1}(n_z), \tag{7.1a}$$

$$\theta_{zx} = \cos^{-1}(n_y), \tag{7.1b}$$

$$\theta_{zy} = \cos^{-1}(n_x). \tag{7.1c}$$

Operationally, we can use spherical projection of the normal vectors of the GBs on to a unit sphere and measure their distribution within certain angles (see Figure 7.3 for illustration). The end points of the unit normal vectors with the same angle between GB plane and the shear plane will project onto the sphere. Let the angle interval be $\Delta\theta$. The ideal probability of angles between θ_i and $\theta_i + \Delta\theta$, $P_{ideal}(\theta_i)$, are the number of the GB normal vectors projected in this range, which is proportional to the area on the sphere between the rings corresponding to angles θ_i and $\theta_i + \Delta\theta$,

$$2\pi[\cos(\theta_i + \Delta\theta) - \cos(\theta_i)], \tag{7.2}$$

which is illustrated in Figure 7.3.

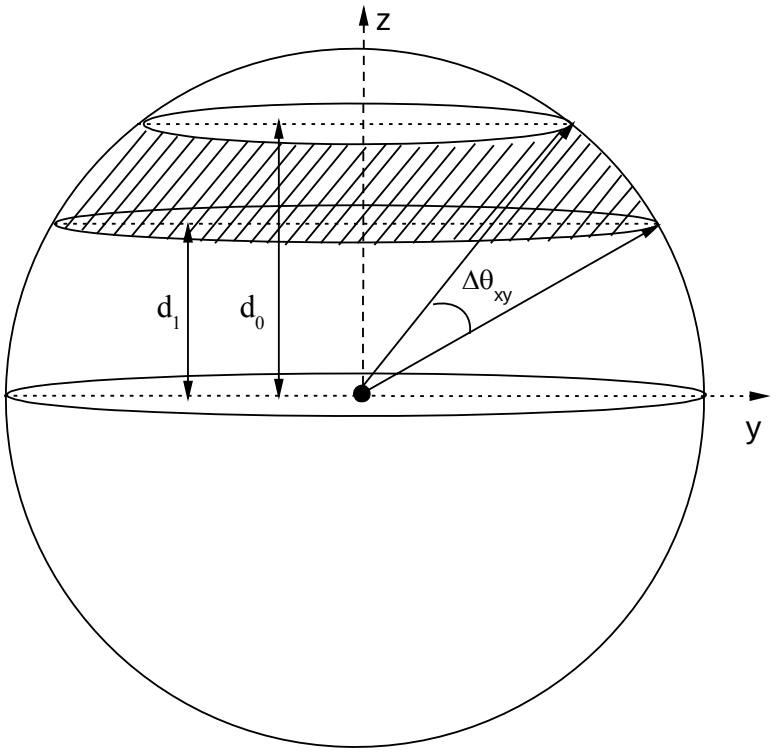

Figure 7.3. Probability GB interfaces whose unit normal vectors are located in the range from θ_{xy} to $\theta_{xy}+\Delta\theta_{xy}$ is equivalent to the area of surface on the sphere between two planes normal to the z-axis, where $d_0=\cos\theta_{xy}$ and $d_1=\cos\left(\theta_{xy}+\Delta\theta_{xy}\right)$.

There are three distributions for the three shear planes. The distribution for the isotropic case with an infinite number of randomly oriented GB interfaces present is shown in Figure 7.4. As a comparison, the distributions of θ_{xy}, θ_{zx}, θ_{zy} for the grain boundaries in a Voronoi cells of N_C =5,000 grains are also shown in Figure 7.4 that follows closely the isotropic case of infinite number of grains. As the number of grains N_C decreases from 5,000 to 20 (Figure 7.4-7.7), the deviation from the ideal case becomes more obvious.

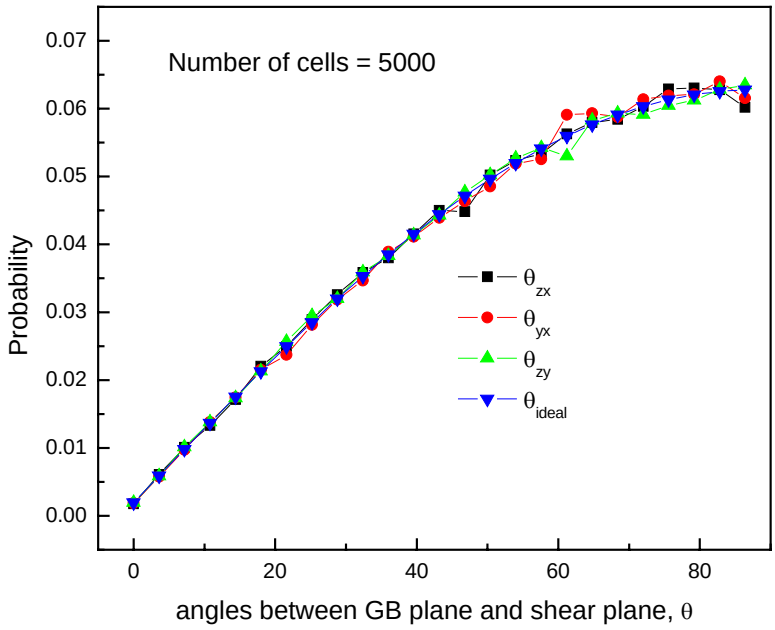

Figure 7.4. The distributions of θ_{xy}, θ_{zx} and θ_{zy} *w.r.t* the probability of the ideal isotropic case calculated from 5,000 Voronoi cells. The total number of interfaces is 38494.

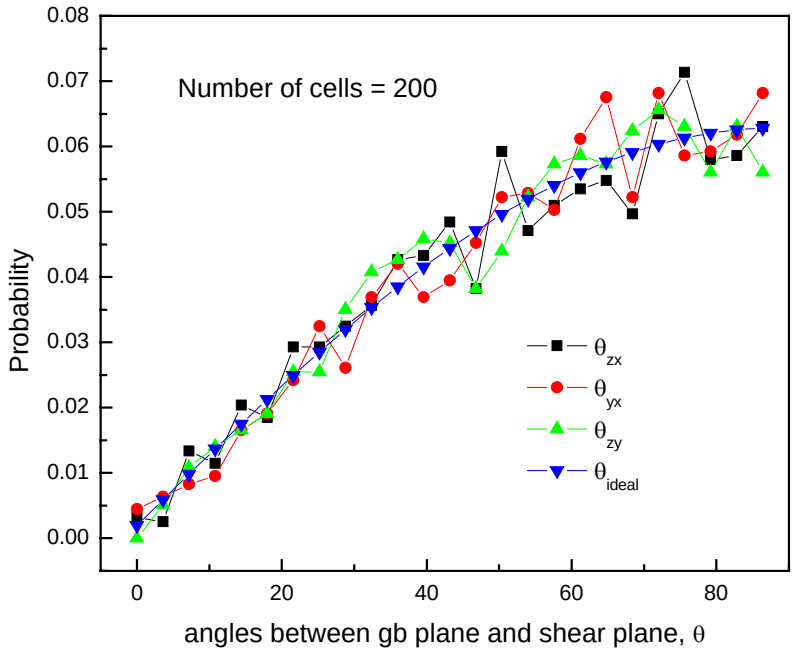

Figure 7.5. The distributions of θ_{xy}, θ_{zx} and θ_{zy} w.r.t the probability of the ideal isotropic case calculated from 200 Voronoi cells. The total number of interfaces is 1570.

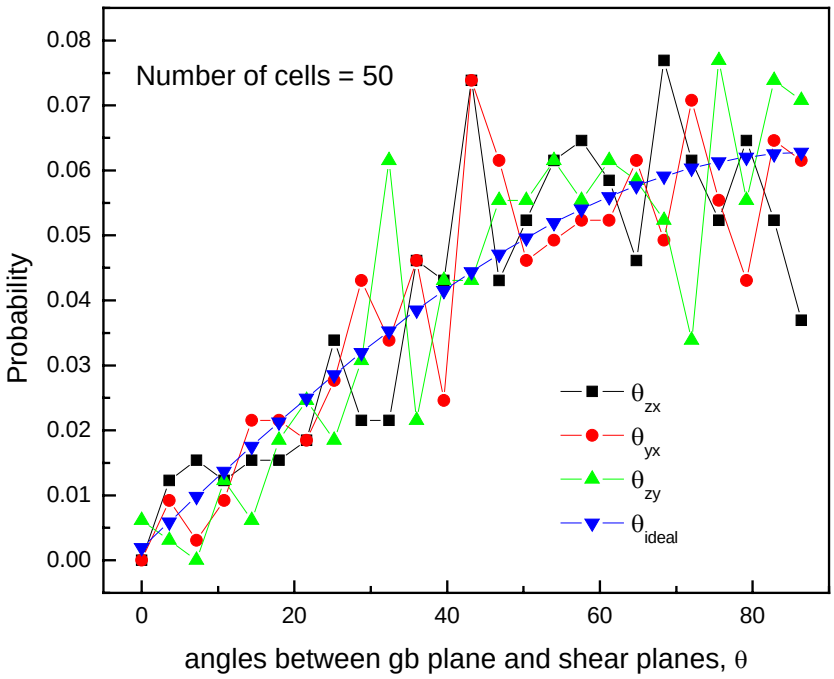

Figure 7.6. The distributions of θ_{xy}, θ_{zx} and θ_{zy} w.r.t the probability of the ideal isotropic case calculated from 50 Voronoi cells. The total number of interfaces is 325.

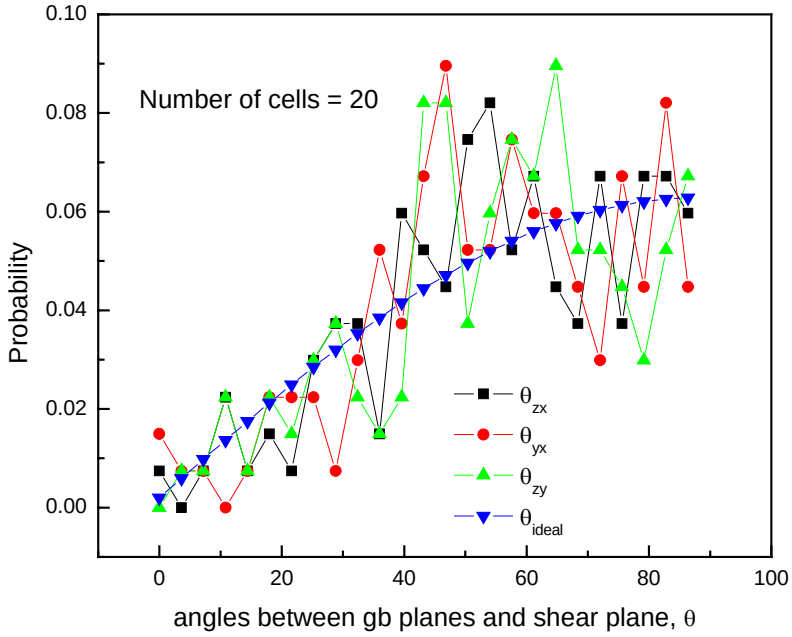

Figure 7.7. The distributions of θ_{xy}, θ_{zx} and θ_{zy} with respect to the probability of the ideal isotropic case calculated from 20 Voronoi cells. The total number of interfaces is 134.

Using the perfect isotropic case as the reference, we can calculate the variances for θ_{xy}, θ_{zx}, θ_{zy} in the sample with different number of grains and plot the average of three variances against the logarithm of number of cells shown in Figure 7.8. Apparently, there exists two linear relation separated by the interception at $N_C = 141.82$. As the number of grains decreases from 5,000 to 200, the variance increases linearly according to the linear relation: $\sigma = -0.0025\log(N_C) + 0.0102$. When the number of grains decreases further below 141.82, the variance increases more rapidly according to the linear relation $\sigma = -0.0127\log(N_C) + 0.032$.

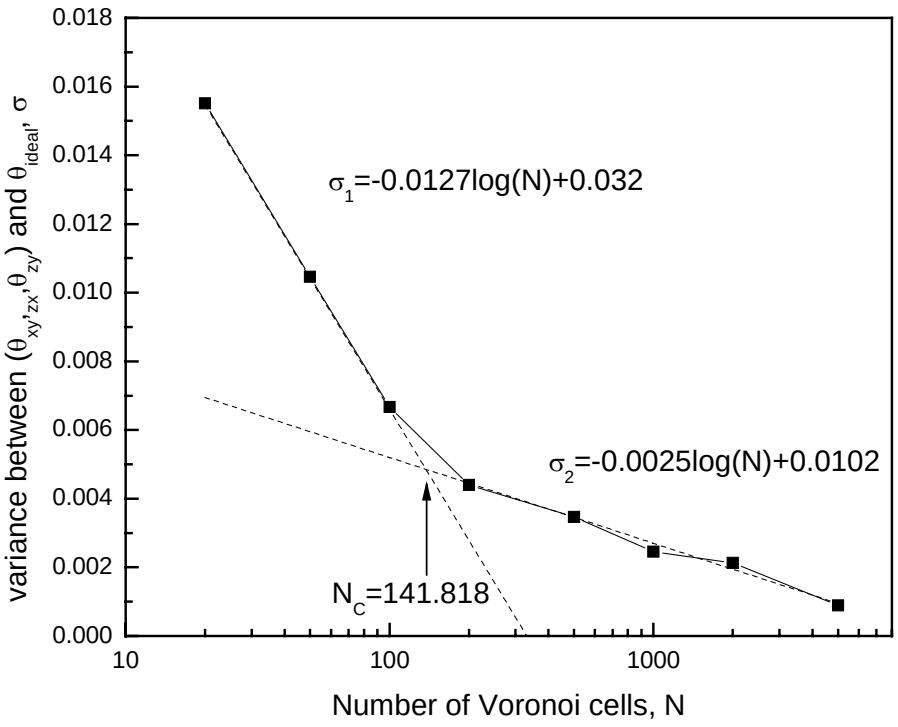

Figure 7.8. The deviation from ideal probability of angles between GB and shear planes increases as the number of Voronoi cells decreases.

The anisotropy of the GB orientation is measured by the differences among $P(\theta_{xy})$, $P(\theta_{zx})$, $P(\theta_{zy})$ for different shear planes. From Fig. 7.8, we can see that the

anisotropy increases as the variance between $P(\theta_{xy})$, $P(\theta_{zx})$, $P(\theta_{zy})$ and the $P_{ideal}(\theta_i)$ increases. The maximum difference between $P(\theta_{xy})$, $P(\theta_{zx})$, and $P(\theta_{zy})$ is also measured for Voronoi structures of different number of cells and the results are plotted in Figure 7.9. The maximum difference also increases as the number of cells decreases. Therefore, to avoid the strong anisotropy effect, the number of grains or cells in the *nc*-Cu sample should be larger than $N_C = 142$. In this study, the number of grains in *nc*-Cu samples varies from 20 to 200 while studying the misorientation effects and the results are discussed in later section.

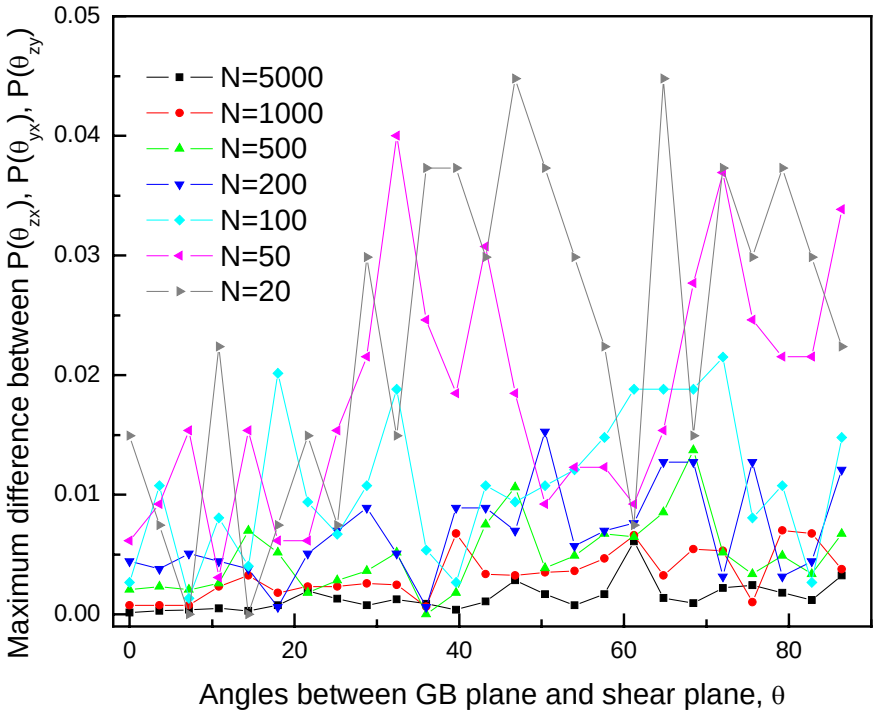

Figure 7.9. The maximum difference among $P(\theta_{zx})$, $P(\theta_{yx})$ and $P(\theta_{zy})$ increases as the number of cells decreases.

7.2.4 Misorientation

The majority of grain boundaries in most *nc*-materials synthesized in the laboratory and simulations so far are high-angle grain boundaries. In order to generate

certain specific misorientation, we firstly obtain the random misorientation distribution by randomly assigning a crystallographic cubic orientation to each grain in the Voronoi cells with a lognormal grain volume distribution [14]. Using the procedure described in Chapter 4, we can obtain both a minimized misorientation distribution and a maximized misorientation distribution through a MC optimization procedure. The mean misorientation angles $\overline{\theta}$ for minimum, random, and maximum distributions are 10.496°, 39.673° and 46.705°, respectively. Five more intermediate configurations are also selected using the IMC method and their mean misorientation angles are 15.389°, 20.222°, 25.085°, 29.948° and 34.810° as shown in Figure 7.10. The atoms in these samples with the desired misorientation distributions are relaxed using MD and then subject to shear deformation simulation at 300K.

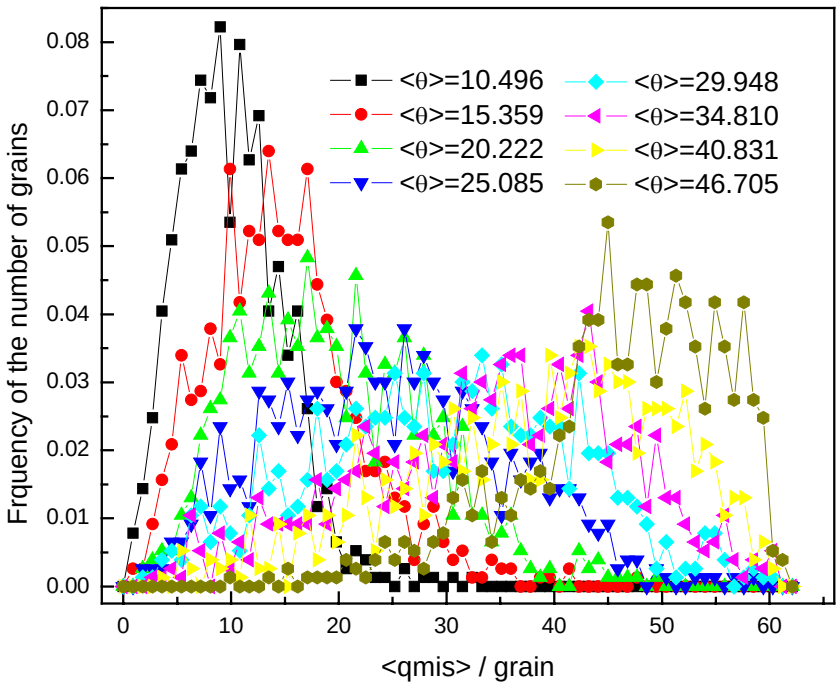

Figure 7.10. Distributions of misorientation angle obtained through minimization and maximization using Monte Carlo technique.

7.2.5 Structure and defect characterization

To characterize changes of grain boundary structure, dislocation activities, stacking faults and twins during severe plastic deformation during deformation, we employed several methods, including common neighbor analysis (CNA) [156], central-symmetry parameter (CSP) [154, 155], local hydrostatic pressure [172], the number of first nearest neighbors [82], etc. Common neighbor analysis (CNA) is very useful to identify *fcc*, *hcp* types of atoms by looking at the common neighbors of a pair of atoms within the second nearest neighbor distance. Each atom has a unique crystalline signature and is assigned a label including four indexes based on the topological structure of the common neighbors. This method has been used extensively to study the grain boundary and dislocations in nanocrystalline materials [75, 95, 173]. Central symmetry parameter is another method for identifying dislocation, partial dislocations, stacking faults. In this study, we will use primarily CNA and CSP to characterize the *nc*-Cu samples.

Another very useful property characterizing GB and defect process is the local atomic volume (LAV). The LAV is defined as the Voronoi volume of the atoms. Using this technique, we can identify the LAVs for those atoms in various microstructures, GBs, triple junctions, and inside the crystallites of course.

7.3 Results

Misorientation between two adjacent grain is tightly connected to not only the nature of the grain boundaries but also other microstructure attributes that are and play equally important roles in understanding the mechanical properties on *nc*-Cu, which include grain size, grain boundary disorder, and sample conditions such as the number of grains and sample size. Using the approaches developed in this work, we have the freedom to focus on misorientation while still able to vary other attributes. For sample,

we can use the same grain topology (i.e., the same Voronoi cells with the fixed grain boundary structure) while vary the mean grain size or misorientation. By doing so, we could obtain some quantitative comparative results for the microstructure properties. In the following, we shall present our results in terms of these variables.

7.3.1 Stress-strain relation and shear modulus

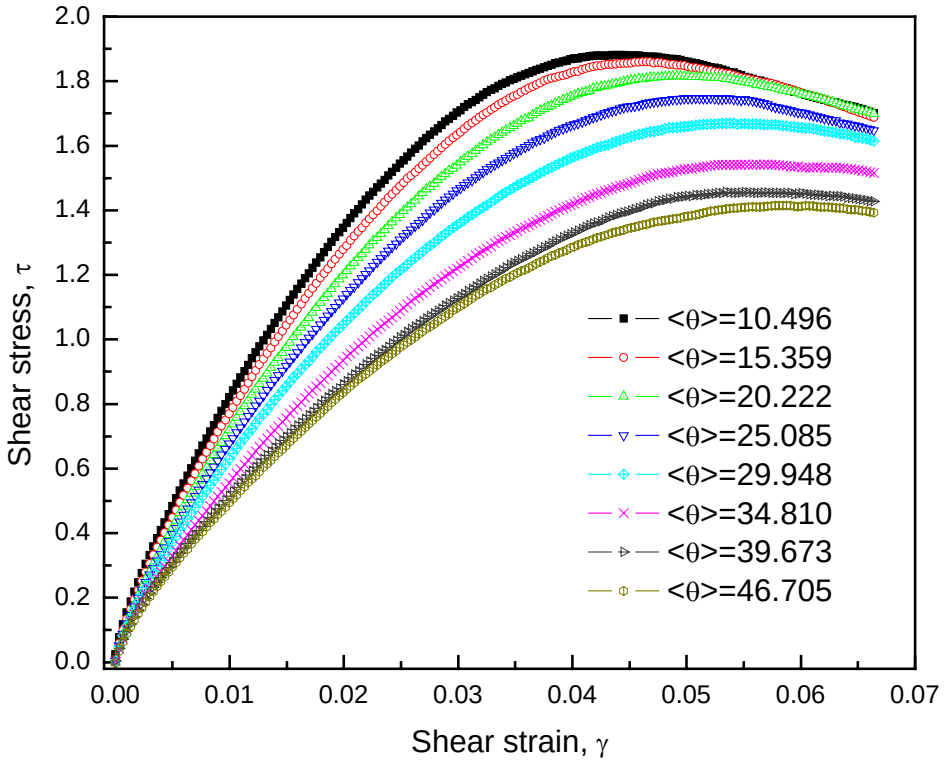

Figure 7.11. Shear stress-strain curves show misorientation effects on the mechanical properties of *nc*-Cu. Number of grains is 100, L=30.125nm, $\langle D \rangle$=8.05nm.

Figure 7.11 shows the shear stress-strain relations for the samples with the mean grain size of 8.05 nm and different misorientation distributions where the mean misorientation angles $\overline{\theta}$ are used to identify each simulation. In general, the stress-strain curves show a linear elastic region (although a perfect linear relation is still hard to get as that in experiment) followed by a maximum stress or peak stress. An overshot at the

maximum stress is observed. This is an artifacts caused partly by the periodic boundary conditions along the shear plane, which is equivalent to having an infinitely large dimension in the shear direction. For a finite sample, upon reaching the peak stress, failure or shearing off would be anticipated eminently.

Table 7.1. The average misorientation angle per grain, $\langle\theta\rangle$, Maximum shear stresses, $\tau_{\max}$, the shear strains at maximum shear stress, $\gamma_{\max}$, yield stress at 2% strain, and the shear modulus μ.

$\langle\theta\rangle$	$\tau_{\max}$ (GPa)	$\gamma_{\max}$	μ ($\gamma = 0.02$, GPa)
10.496	1.88095	0.04415	67.18667
15.359	1.86017	0.04614	63.75358
20.222	1.81553	0.05012	59.87556
25.084	1.74795	0.05079	56.32642
29.948	1.66996	0.05344	52.21877
34.810	1.54224	0.05676	46.8079
39.673	1.45570	0.05344	42.99951
46.705	1.41516	0.05776	41.73383

From the relations, we observe a systematic change of the stress-strain response with the mean misorientation angle, $\overline{\theta}$, in both the peak shear stress and shear modulus. As shown in Table 7.1, as the mean misorientation angle increases, both the maximum shear stress and yield stress decrease. The yield stress is defined as the stress corresponding to 2% of strain and the maximum stress the peak stress or flow stress. The corresponding strain at the peak stress also increases with increasing $\overline{\theta}$. The shear modulus μ is obtained from the slope of the line connecting the stress-strain relation at 2% strain and the origin. In other words, μ obtained this way is the so-called scant shear modulus, which gives a good measure of the modulus in the samples with not so-well defined linear stress-strain region.

The results indicate that for the *nc*-Cu with small $\overline{\theta}$ or more small angle boundaries are in general stronger than those with the maximum $\overline{\theta}$ which is close to the

samples with the random, or Mackenzie distribution. As we show below, the same trend holds for the samples with grain sizes ranging from a few nanometers to over 20 nm. This result disagrees with that from Caturla *et al.* [169] who predicted the opposite effect when the grain size is larger (12 nm) in *nc*-Ni under tension; at small grain size (4 nm) they reported the same result as what we see in our *nc*-Cu. As we show below, the root cause for the misorientation effect can be traced back to the amount of disorder present in the grain boundaries.

Under the same sample condition (i.e., the number of grains, the grain boundary topology, the sample size), for samples of 8.05 nm mean grain size, the difference between the maximum stresses for the samples with the minimum misorientation and the random misorientation distribution where high angle boundaries are prevalent is about 37.88%. As the mean grain size decreases, the gap of the maximum stresses between the samples with the minimum and maximum misorientation becomes smaller. For samples with mean grain size of 6.9 nm, the difference is about 26.32%.

The above results follow pretty much what we have known in coarse-grained polycrystalline materials, that is, the samples with large fraction of high angle grain boundaries, excluding the special high angle boundaries, are mechanically weak as compared with those with small angle boundaries.

7.3.2 Defect process

The detailed defect process involving dislocations, partial dislocations, stacking faults, and other disorders can be measured in the simulation. Using the CNA technique, we are able to identify defect *fcc* and *hcp* atoms in *nc*-Cu samples and keep track of the percentage change during shear deformation as shown in Figure 7.12. CNA are performed on twenty atomic configurations for each misorientation during shear deformation for the *nc*-Cu sample containing 100 grains.

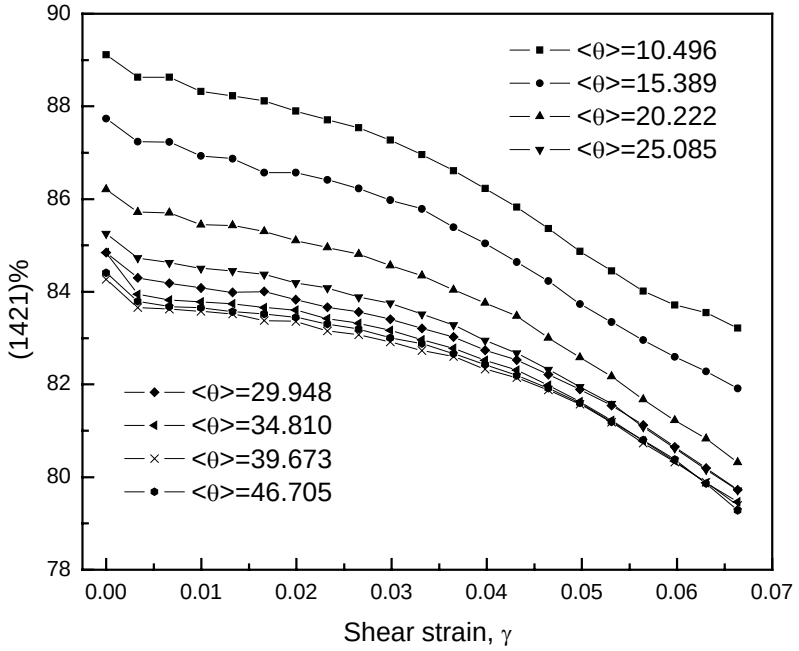

Figure 7.12. The change in percentage of (1421) type with different misorientation distributions.

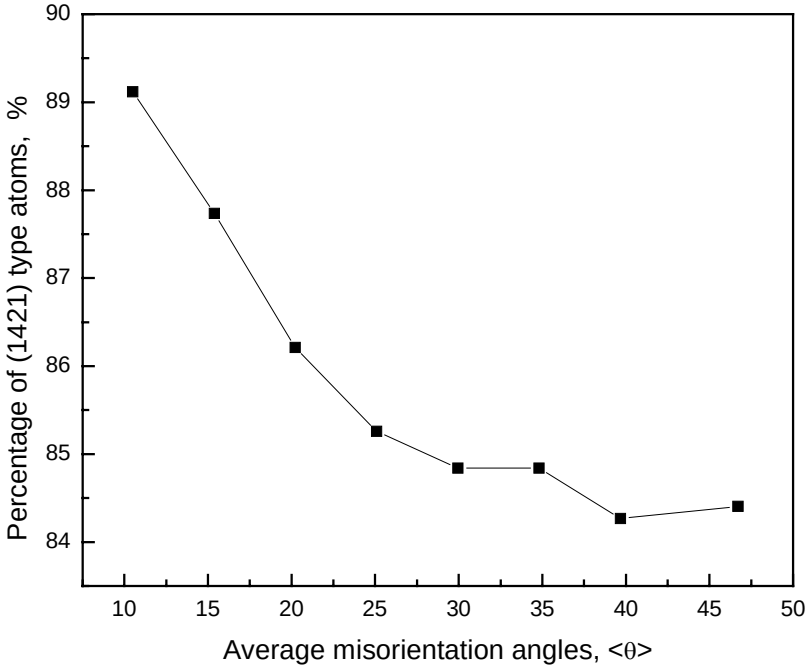

Figure 7.13. The relation between average misorientation angles, $\langle\theta\rangle$ and the percentage of (1421) type atoms.

Fig. 7.12-7.15 shows the percentage of (1421), (1422) and other types of atoms not included in the above two categories in the samples before deformation starts. As shown in Figure 7.13, we can see that the initial percentage of (1421) type of atoms in the samples decreases with increasing misorientation and becomes leveled when the misorientation reaches 25°, while the percentage of (1422) type of atoms are roughly the same. As the shear deformation applied to the sample, the percentage of the (1421) type of atoms keeps decreasing during the shear for all samples with different misorientation distributions, while the (1422) type atoms keep increasing (Figure 7.14). However, the percentage changes in (1421) and (1422) types of atoms alone are not sufficient to account for the changes in grain boundaries during deformation. Another type of atoms needs to be taken into consideration for studying the deformation mechanism, which is the (1311) type of atoms determined by the common neighbor analysis (Figure 7.15). Atoms of (1311) types are observed in grain boundaries regions as seen in the undeformed samples and show consistent increase with the average misorientation angles in *nc*-Cu sample from 10.496 to 46.705. During deformation, the (1311) type of atoms increases almost linearly with strain.

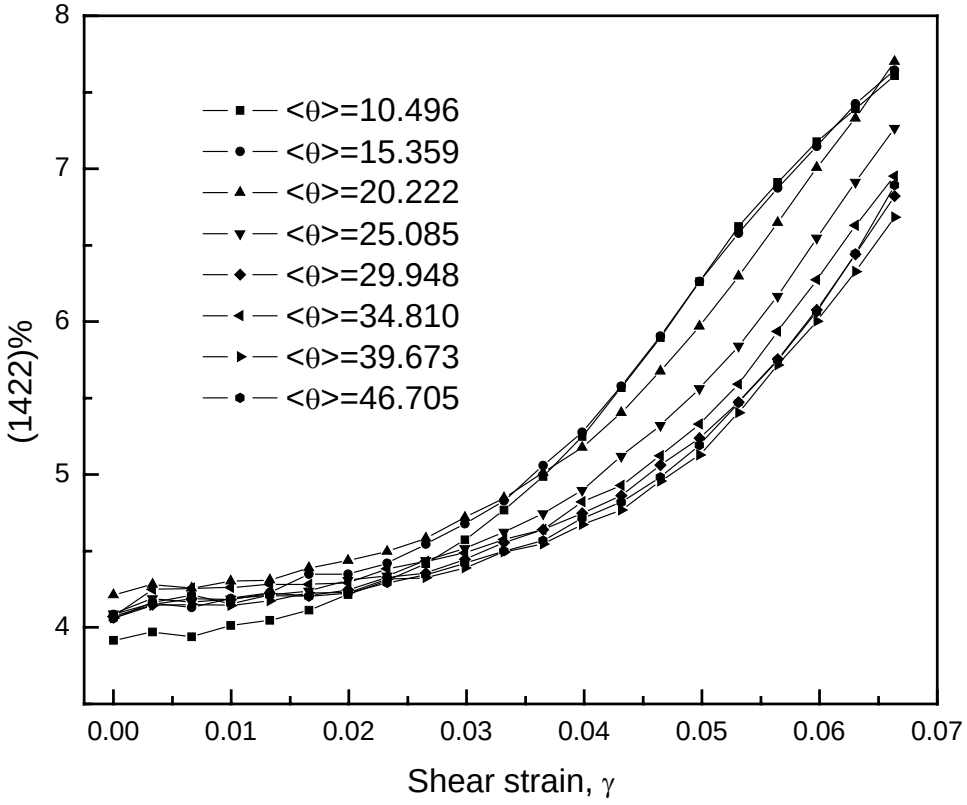

Figure 7.14. The change in percentage of (1422) type with different misorientation distributions.

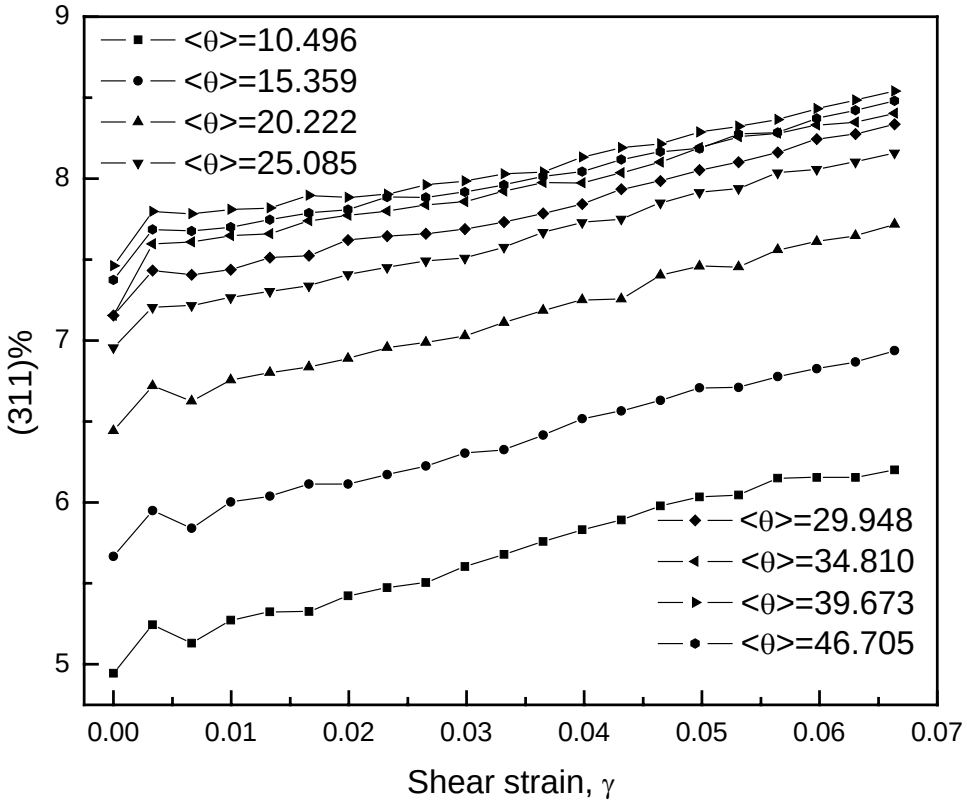

Figure 7.15. The change in percentage of (1311) type of atoms with different mirorientation distributions.

To further characterize the evolution of grain boundary networks with different misorientation distributions, we further categorize the grain boundary atoms as grain boundary atoms, triple junction atoms and vertex atoms according to the unique topological structures where these atoms are located using the method mentioned in Chapter 5. A typical characterization of a grain with different types of atoms is shown in Figure 5.11 where blue atoms represent atoms inside the grain, green the grain boundary interface atoms, yellow the triple junction atoms and red the vertex atoms. The number fraction of the atoms inside the grain, on grain boundary, triple junction and vertices for eight misorientation samples is plotted in Figure 7.16. As the mean misorientation angle

increases, the volume fraction of the atoms inside the grains decreases dramatically and then reaches a plateau while those of grain boundaries, triple junctions and vertices show a reverse trend, among which the GB atoms increases the most. It is clear that the misorientation distributions indeed affect the volume fractions of grain boundaries, which, in turn, dictate the mechanical properties of the nanocrystalline samples during deformation. There is a strong correlation between the volume fraction of grain boundaries and the maximum shear stress of *nc*-Cu samples with different misorientation distributions.

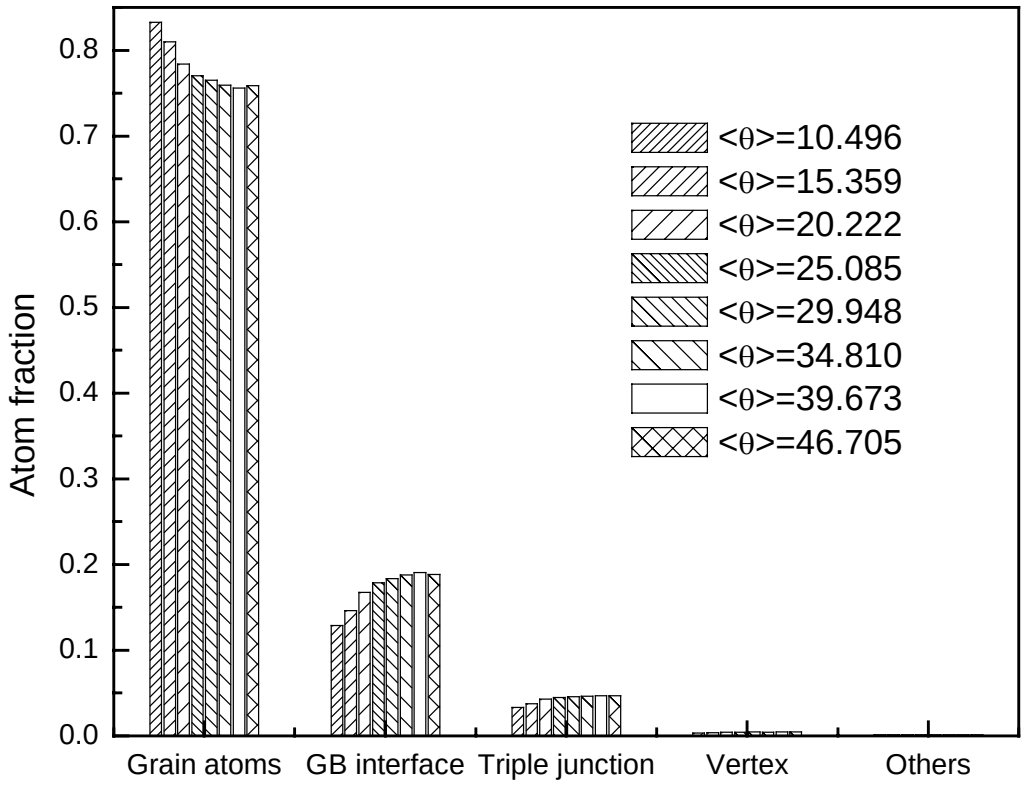

Figure 7.16. Characterization of grain boundary atoms in nc-Cu samples of different misorientation distributions. Number of grains is 100, L=30.125nm, $\langle D \rangle$=8.05nm.

In addition to common neighbor analysis, we also calculated the central-symmetry parameter and atomic LAV of each atom in *nc*-Cu samples. For each grain

boundary interface, we are able to obtain the average CSP and atomic volume by taking the average value from all atoms belonging to the same grain boundary interface. The distribution of CSP and volume of all GB interfaces in *nc*-Cu samples of different misorientation distributions are then accumulated and shown in Figure 7.17 and 7.18. Grain boundaries in the samples of minimized misorientation distribution have smaller values of CSP and volume compared to those in sample of random misorientation distribution. These findings are consistent with the common belief that low-angle grain boundaries are more ordered and have low mobility than the general high angle grain boundaries.

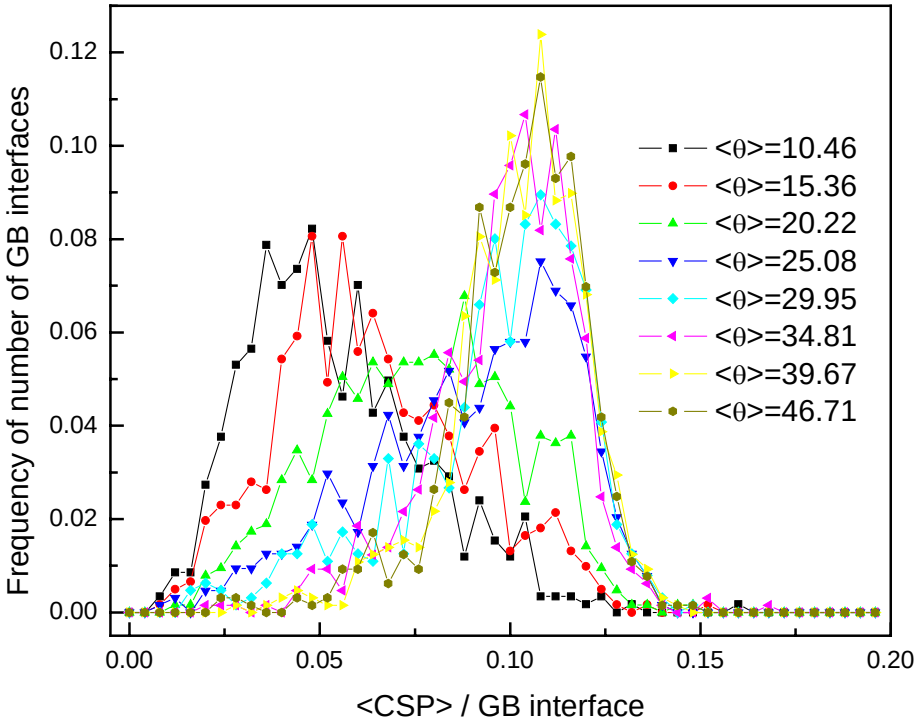

Figure 7.17. The distributions of average Central symmetry parameter of atoms on the each grain boundary are accumulated from all GB interfaces presented in eight misorientation samples: $\langle\theta\rangle = 10.46$, 15.36, 20.22, 25.08, 29.95, 34.81, 39.67, 46.71.

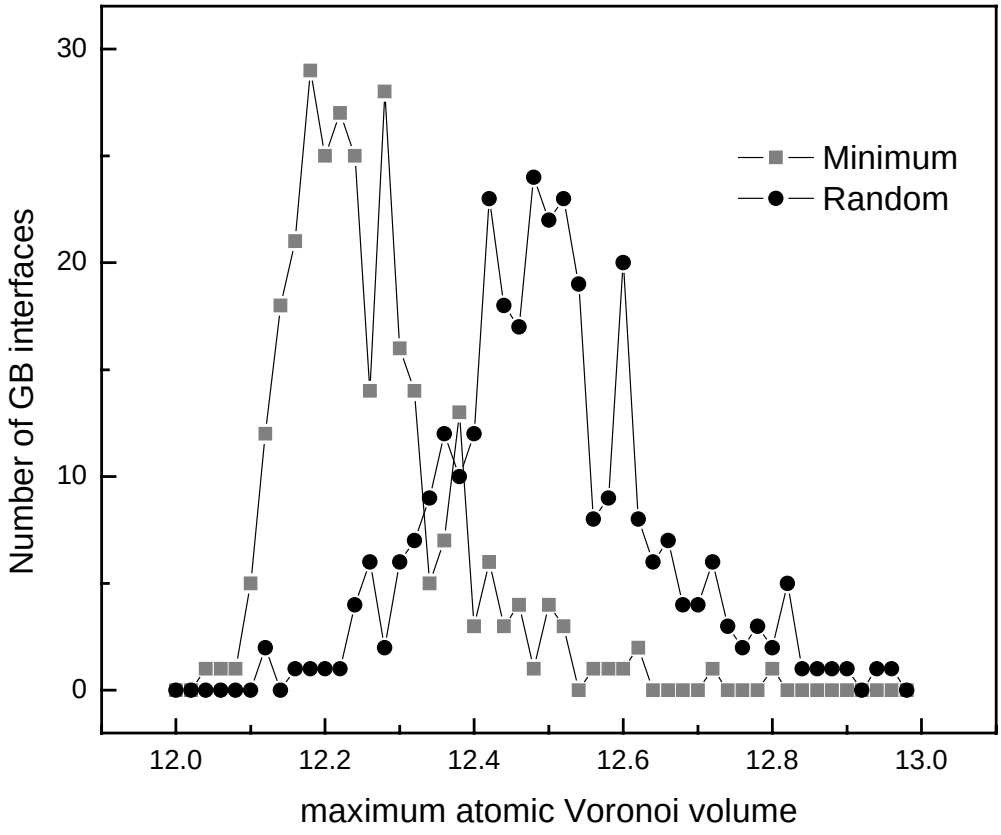

Figure 7.18. The distributions of average atomic Voronoi volume of atoms on the each grain boundary are accumulated from all GB interfaces presented in two misorientation samples: random and minimized misorientation distributions.

When it comes to the explain the deformation mechanism of *nc*-Cu sample, the information about *fcc* and *hcp* atoms alone are not enough. The large volume fraction of grain boundaries presented in most nanocrystalline materials plays a critical role. It is true that low-angle grain boundaries have more dislocation activities than high-angle grain boundaries, however we believe the softening induced by grain boundaries are far more significant than softening induced by dislocation activities. The presence of grain boundary will accommodate the shear strain at the beginning of shear deformation and reduce the amount of stresses asserted on grain boundary atoms, which, in turn, will

delay the nucleation and propagation of dislocations. To illustrate this point, we performed CN analysis on four misorientation samples at four shear strains: 0% (Fig. 7.19-7.22), 3.3% (Fig. 7.23-7.26), 4.98% (Fig. 7.27-7.30) and 6.6% (Fig. 7.31-7.34). The average misorientation angles of the four samples are 10.496 (sample 1), 20.222 (sample 2), 29.948 (sample 3) and 39.673 (sample 4). At zero shear strain, stacking fault (represented by green *hcp* atoms) already starts to form in sample 1, while *hcp* atoms are mostly concentrated on grain boundaries in the other three samples. At 3.3% strain, a large amount of stacking faults appears in sample 1. Due to low mobility and strong shear resistance of low-angle grain boundaries, grain boundaries in sample 1 can no longer accommodate the strain. At 4.98% strain, large amount of stacking faults appears in both sample 1 and 2 while a small number of stacking faults start to nucleate and propagate from grain boundaries in sample 3 and 4. At 6.6% strain, large amount of stacking faults appears in all four samples. However, the amount of stacking faults in sample 1 is the largest. The grain boundary network in sample 4 (maximized misorientation sample) is the most stable and clearly present at 6.6% strain. Figures 7.19-7.34 show that the amount of grain boundaries present in the sample before shear deformation is the most important parameter that dictates the softening during shear while dislocations nucleation and propagation are secondary mechanism that only happens when the grain boundary networks can no longer accommodate shear strain and the atomic stress reaches the critical point for nucleation of dislocations from grain boundaries.

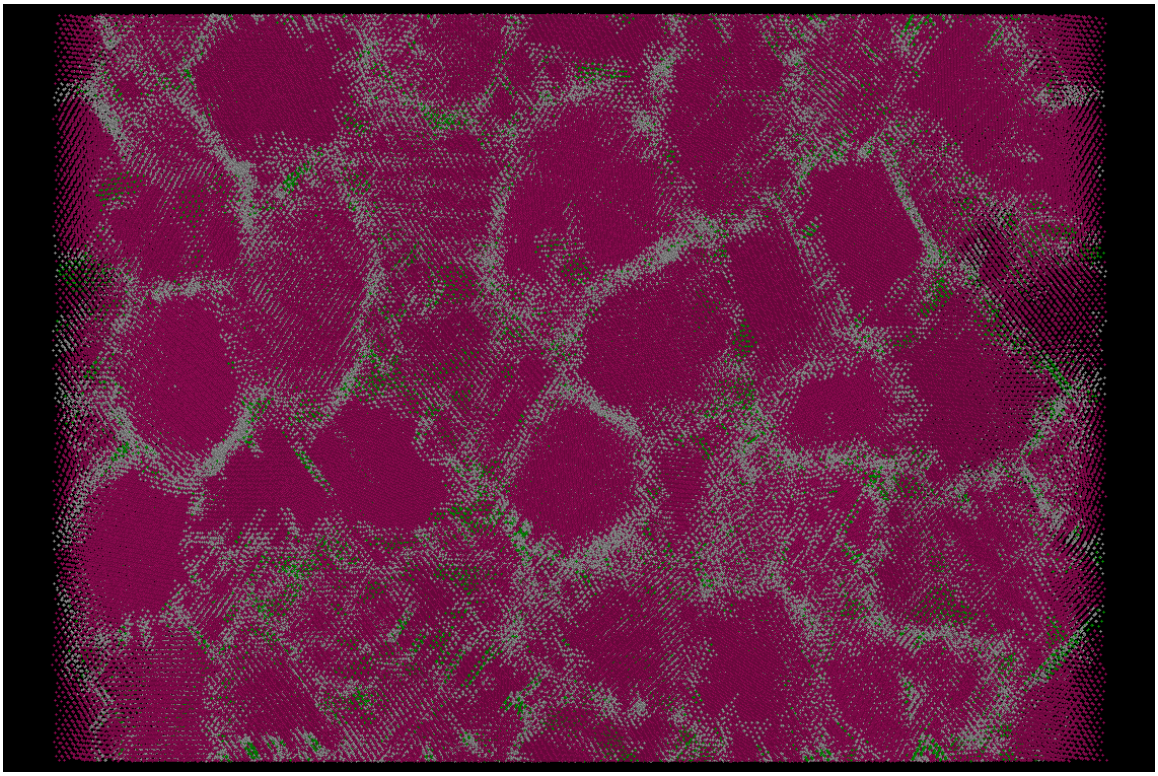

Figure 7.19. CN analysis of *nc*-Cu with $<\theta>$=10.496 at 0% shear strain. Pink atoms are *fcc* atoms, green atoms are *hcp* atoms and silver atoms are the rest.

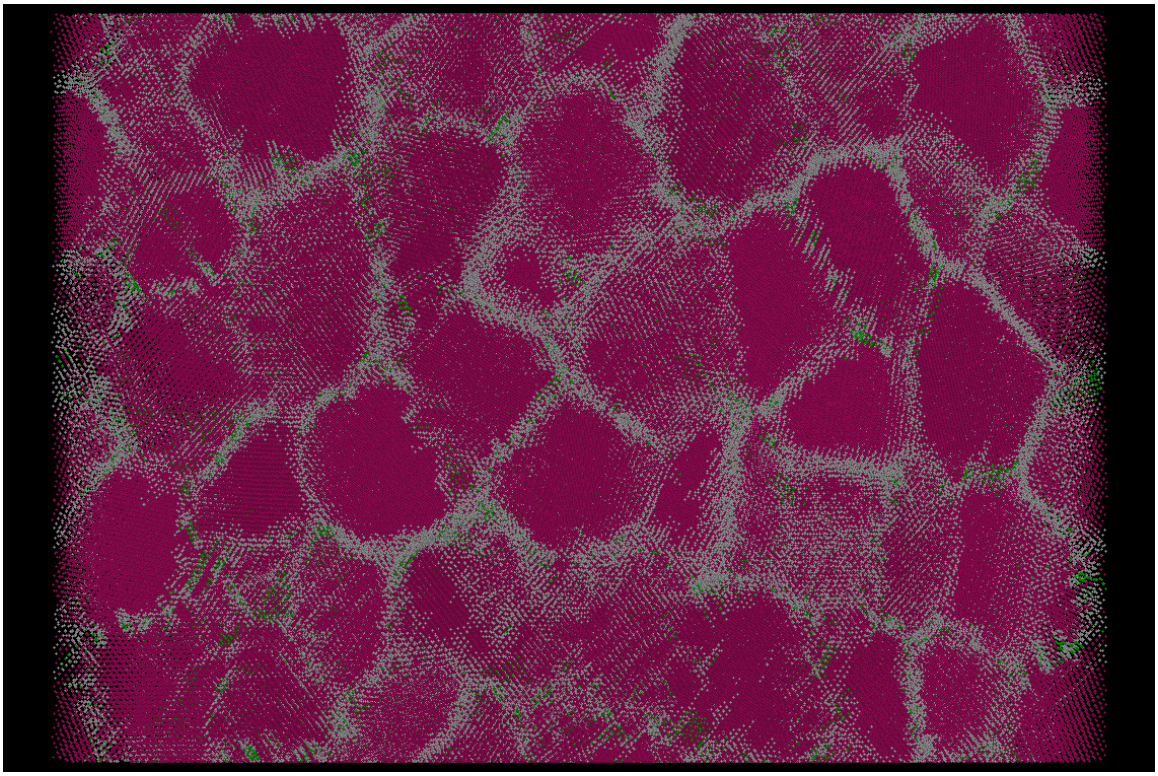

Figure 7.20. CN analysis of *nc*-Cu with $<\theta>$=20.222 at 0% shear strain.

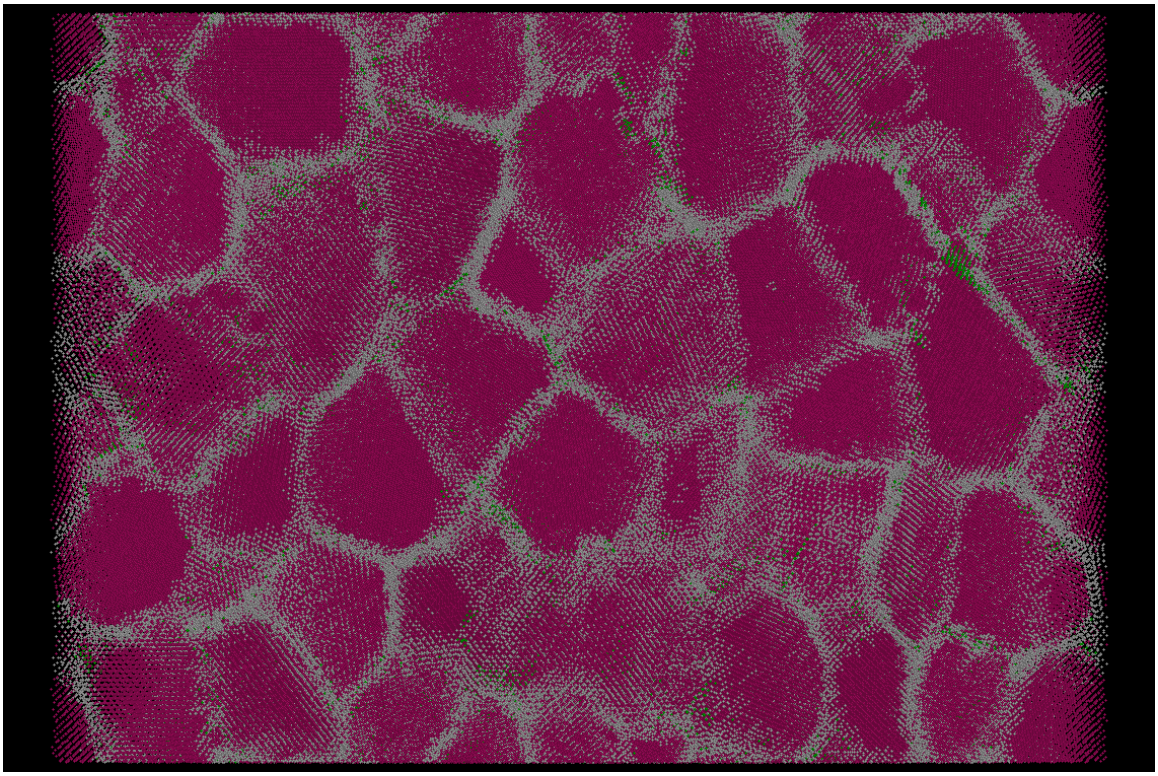

Figure 7.21. CN analysis of *nc*-Cu with <θ>=29.948 at 0% shear strain.

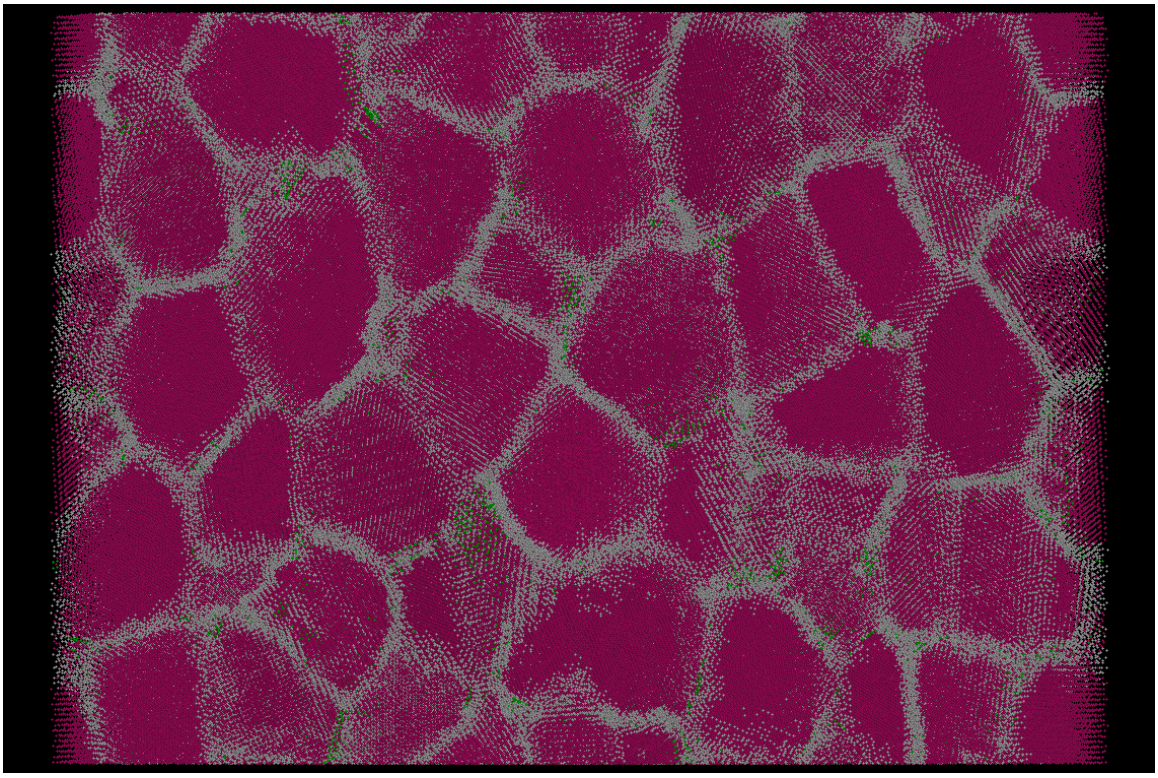

Figure 7.22. CN analysis of *nc*-Cu with <θ>=39.673 at 0% shear strain.

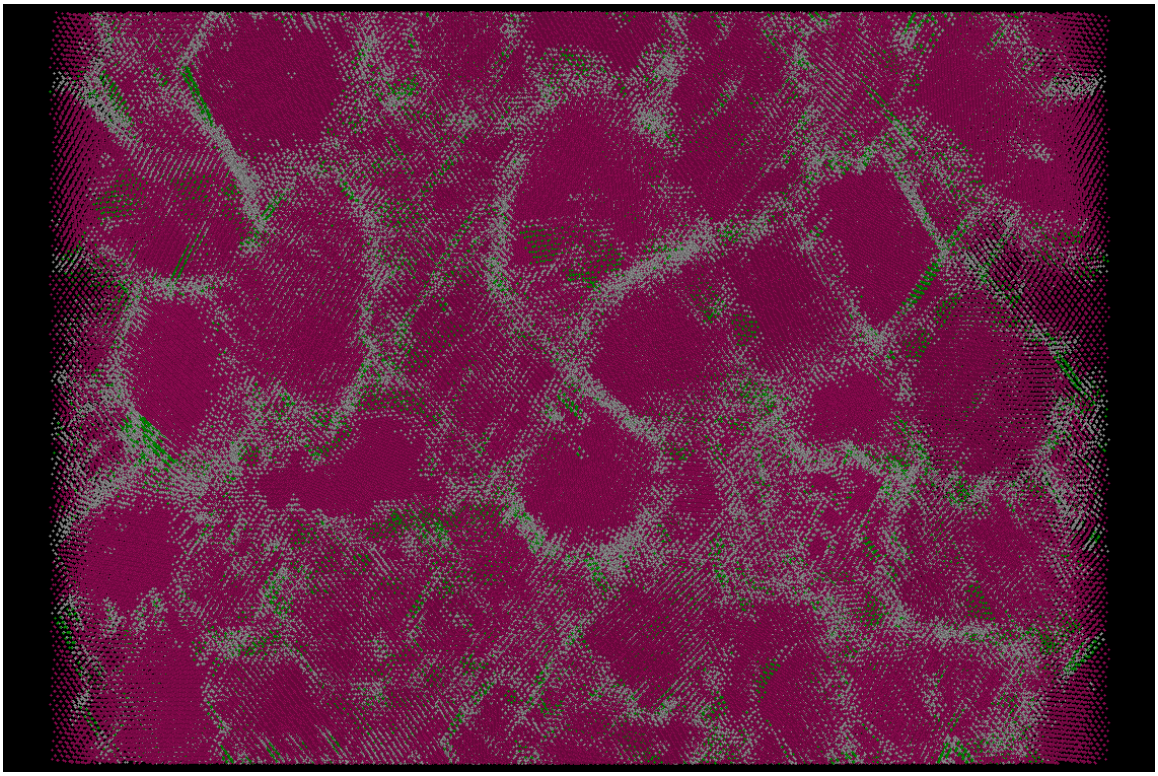

Figure 7.23. CN analysis of *nc*-Cu with $<\theta>$=10.496 at 3.3% shear strain.

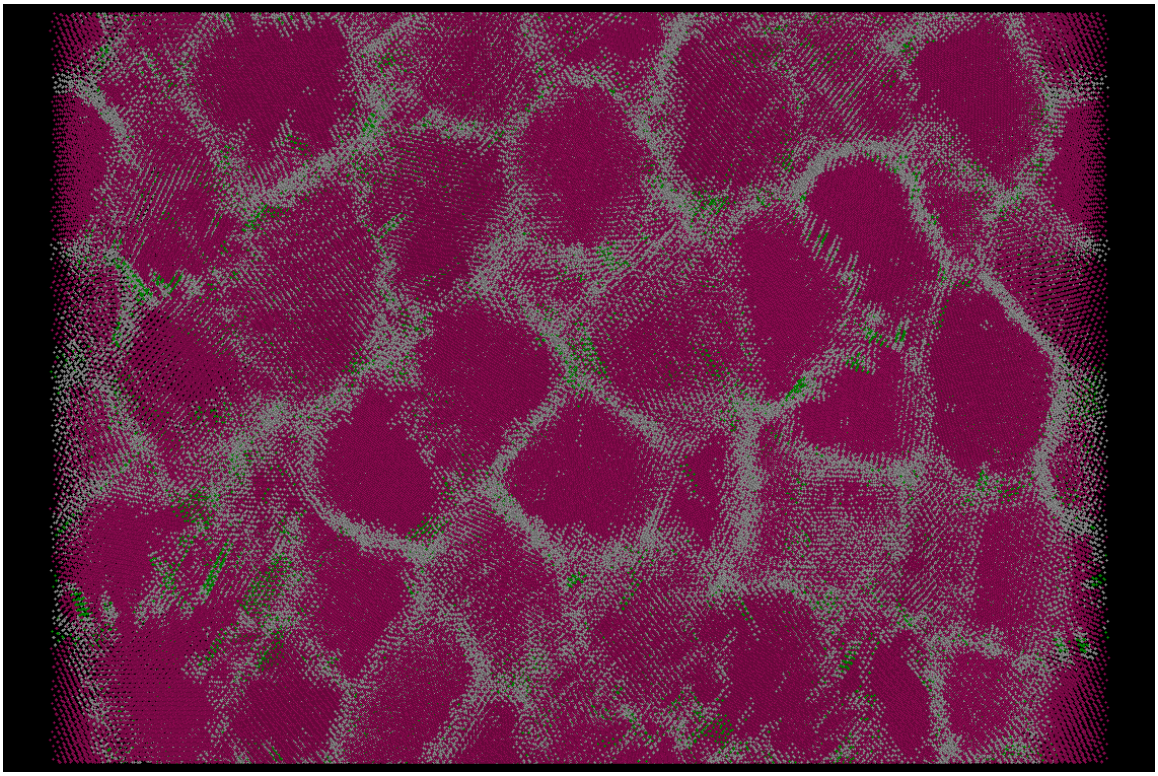

Figure 7.24. CN analysis of *nc*-Cu with $<\theta>$=20.222 at 3.3% shear strain.

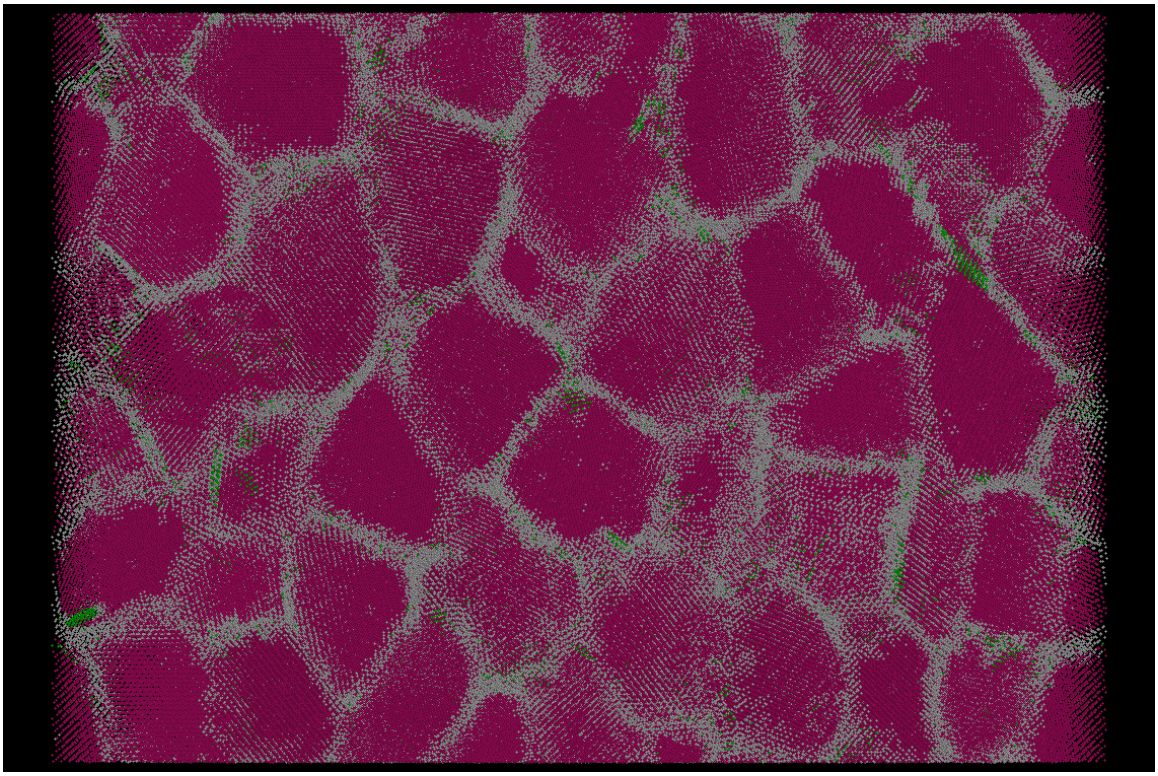

Figure 7.25. CN analysis of *nc*-Cu with $<\theta>$=29.948 at 3.3% shear strain.

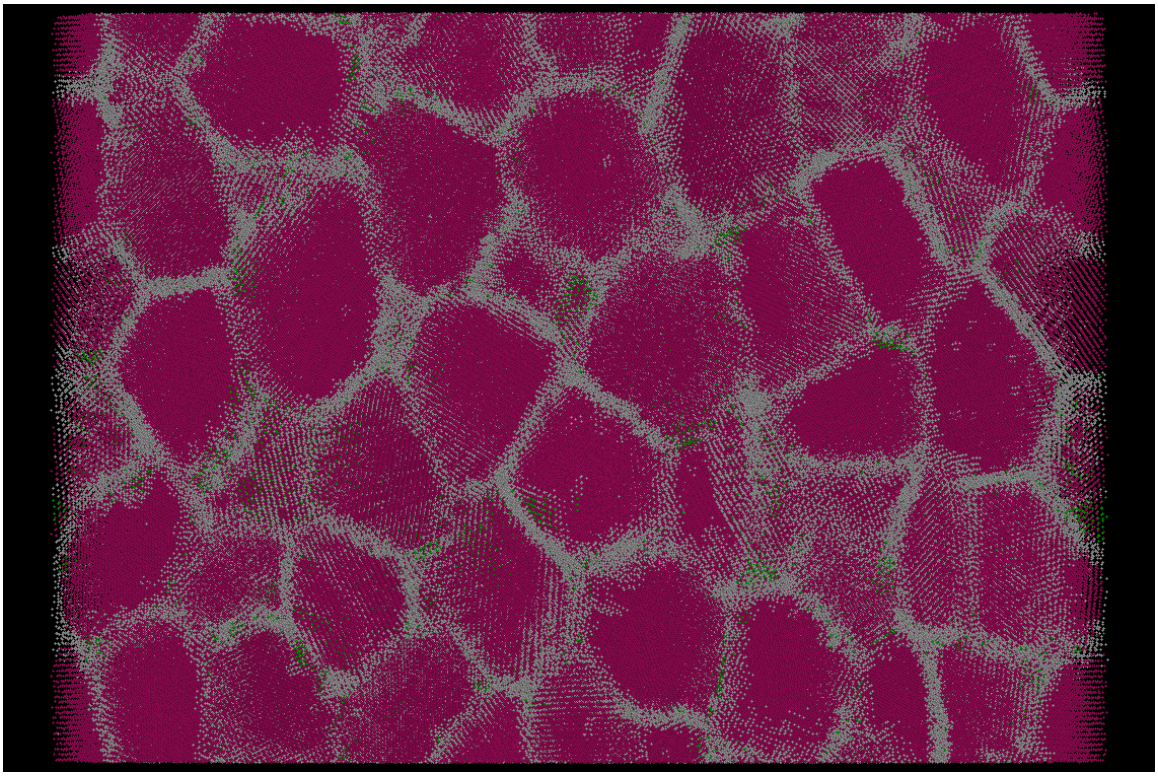

Figure 7.26. CN analysis of *nc*-Cu with $<\theta>$=39.673 at 3.3% shear strain.

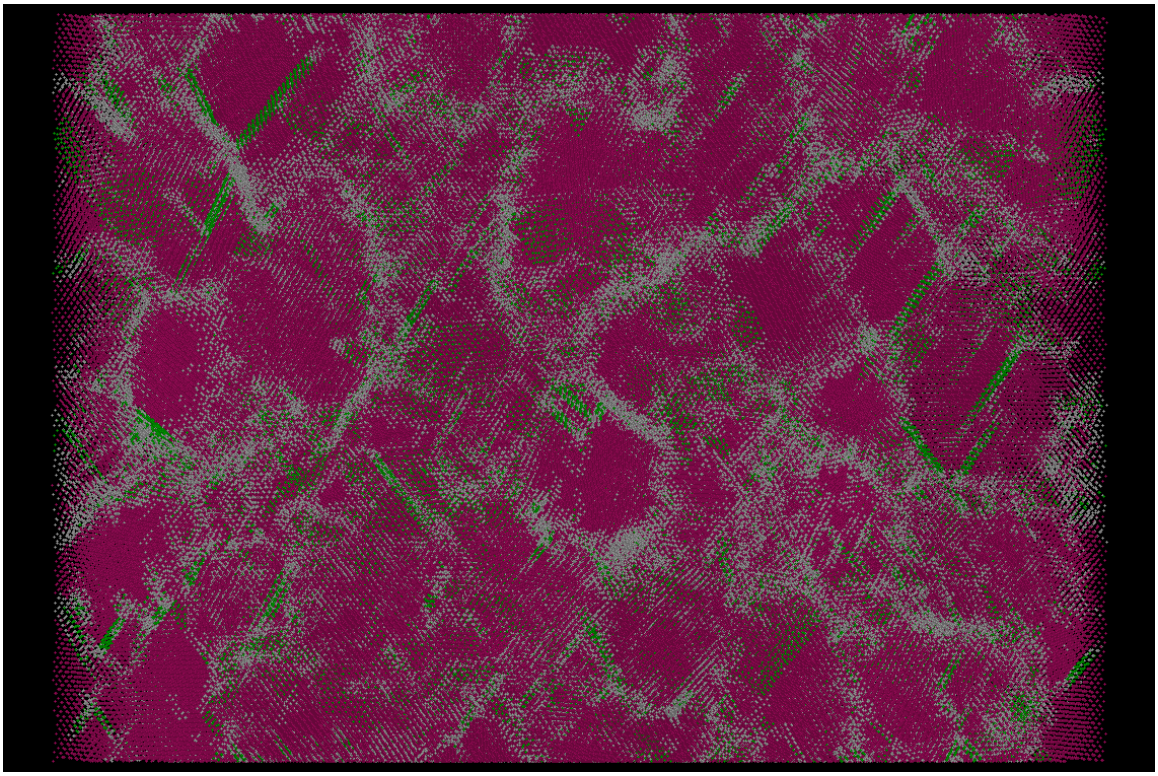

Figure 7.27. CN analysis of *nc*-Cu with $<\theta>$=10.496 at 4.98% shear strain.

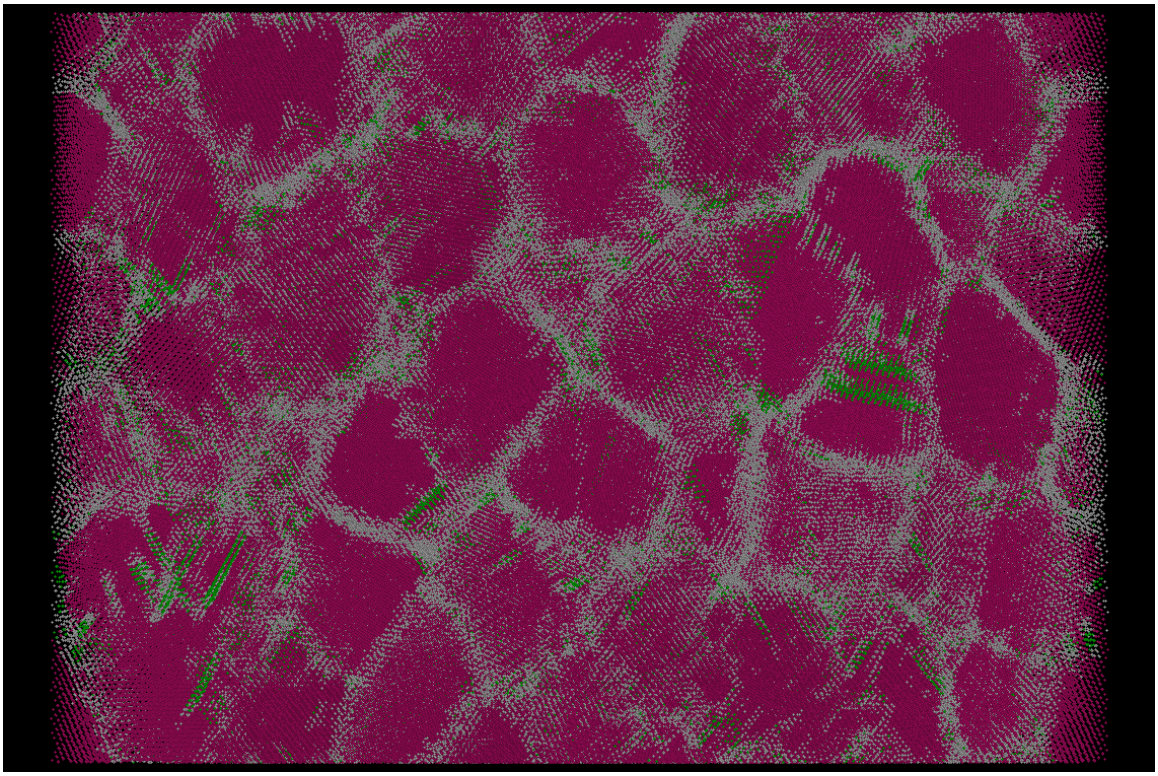

Figure 7.28. CN analysis of *nc*-Cu with $<\theta>$=20.222 at 4.98% shear strain.

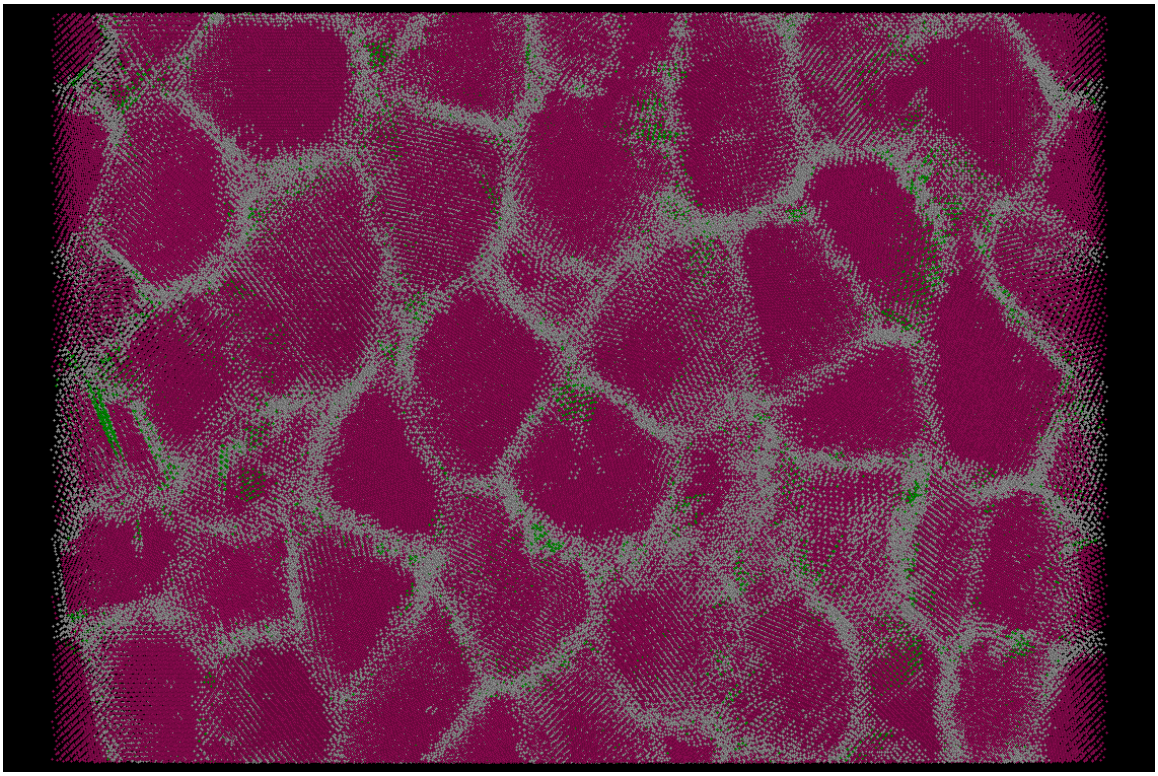

Figure 7.29. CN analysis of *nc*-Cu with <θ>=29.948 at 4.98% shear strain.

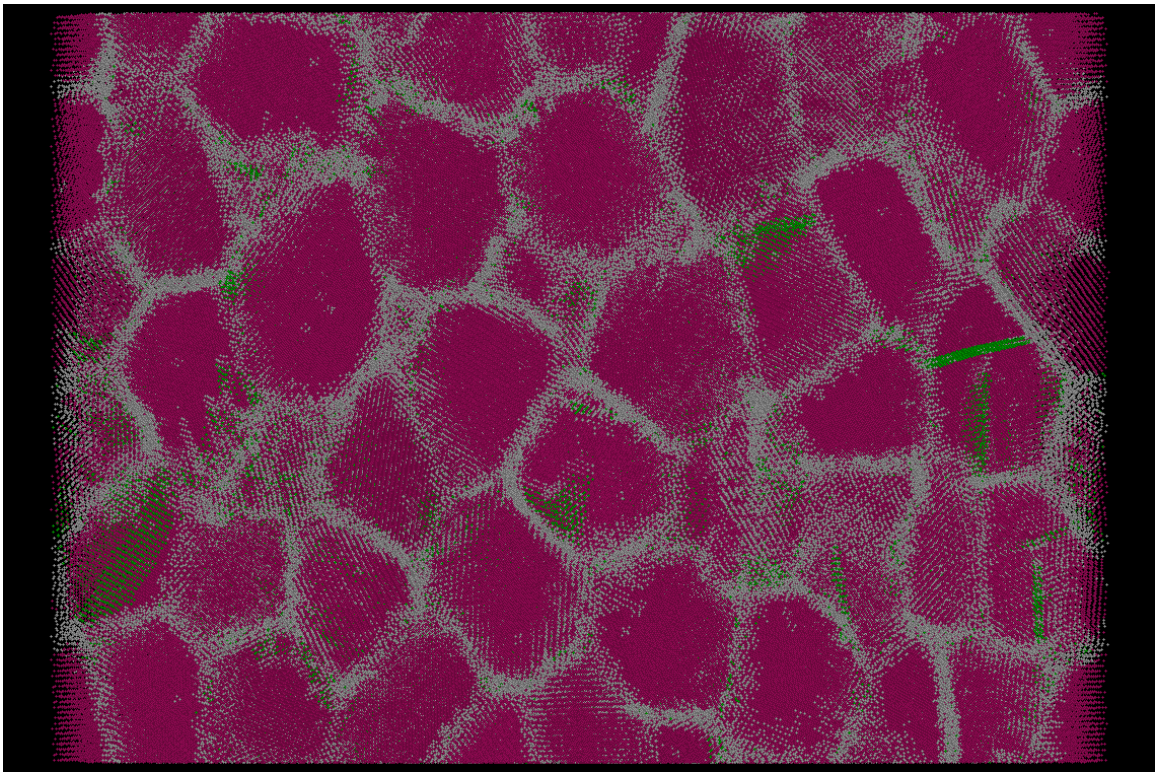

Figure 7.30. CN analysis of *nc*-Cu with <θ>=39.673 at 4.98% shear strain.

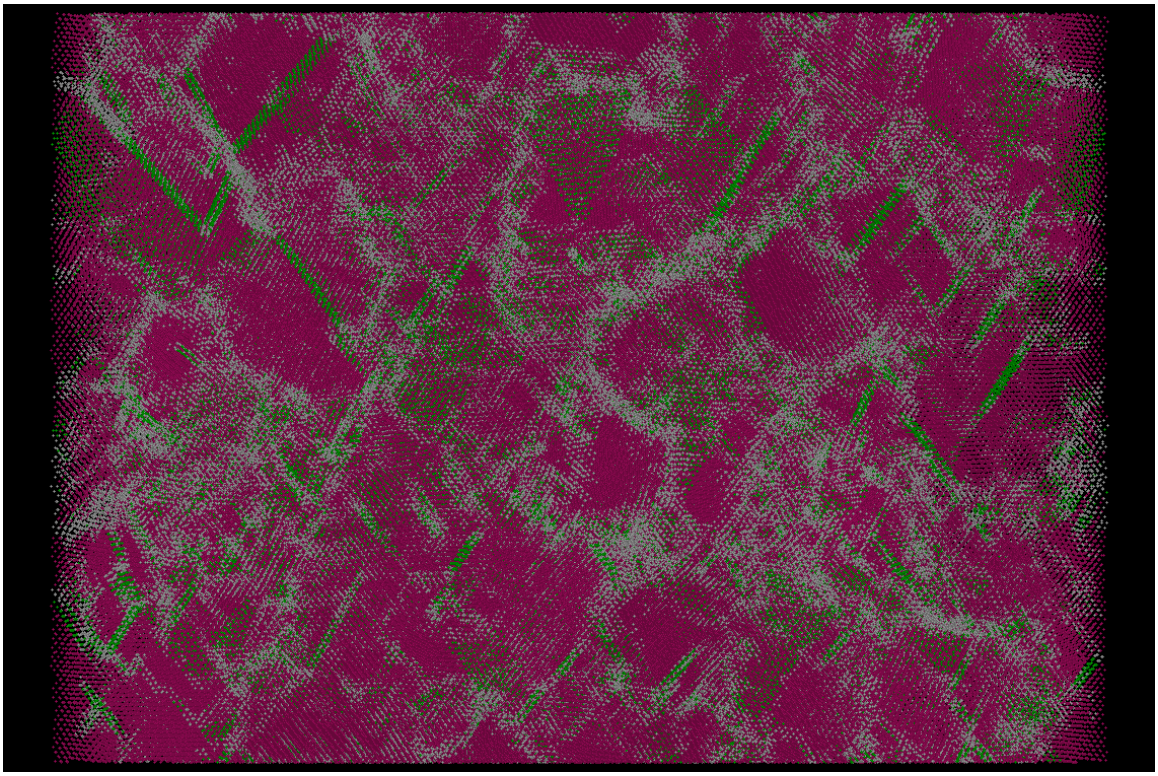

Figure 70.31. CN analysis of *nc*-Cu with $<\theta>$=10.496 at 6.6% shear strain.

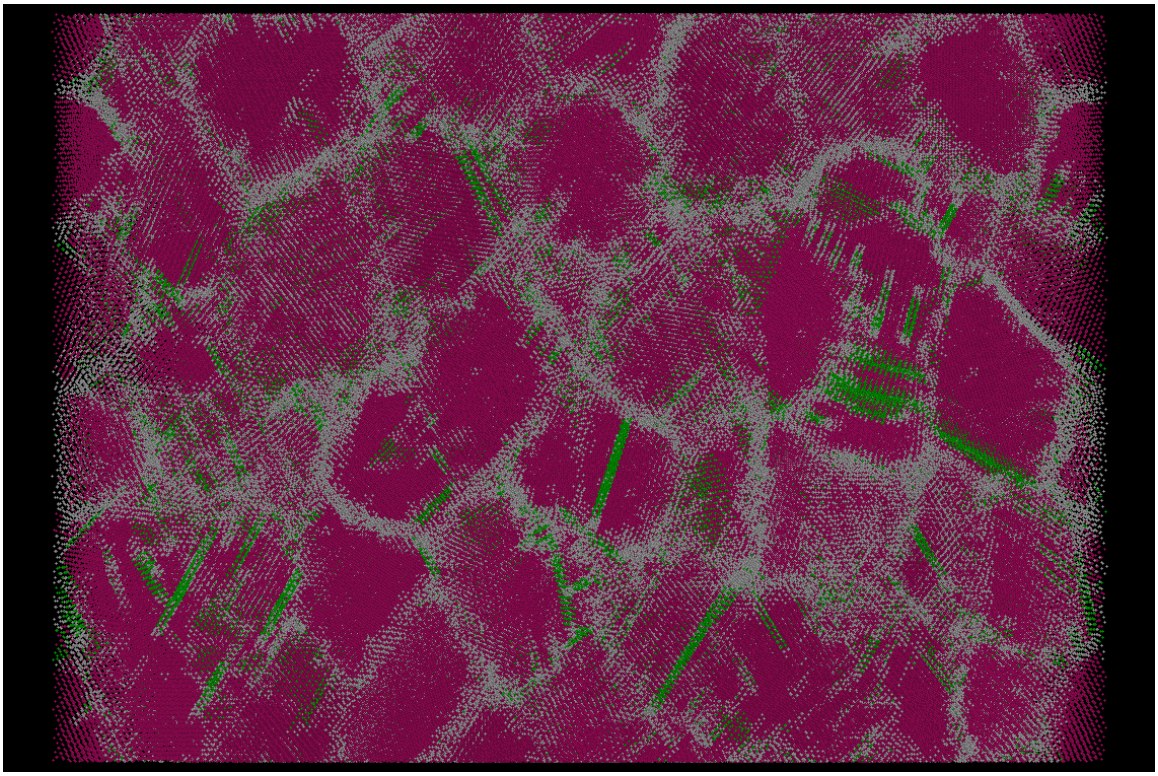

Figure 7.32. CN analysis of *nc*-Cu with $<\theta>$=20.222 at 6.6% shear strain.

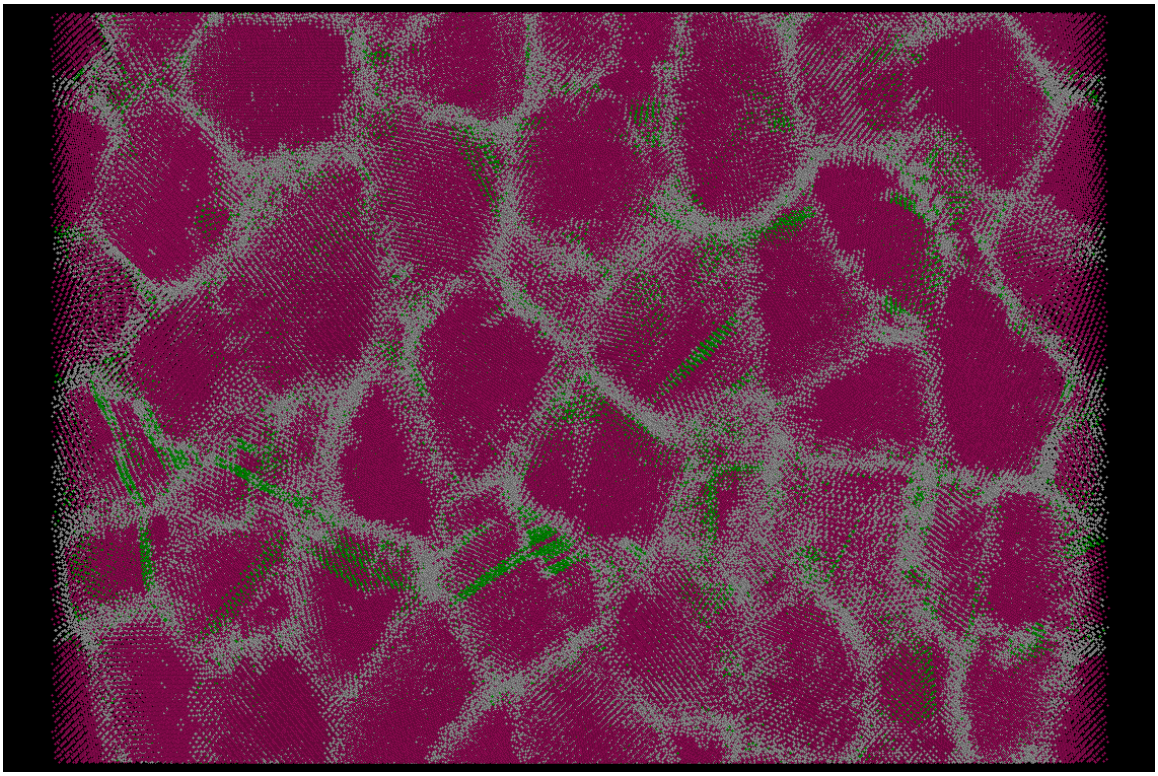

Figure 7.33. CN analysis of *nc*-Cu with $<\theta>$=29.948 at 6.6% shear strain.

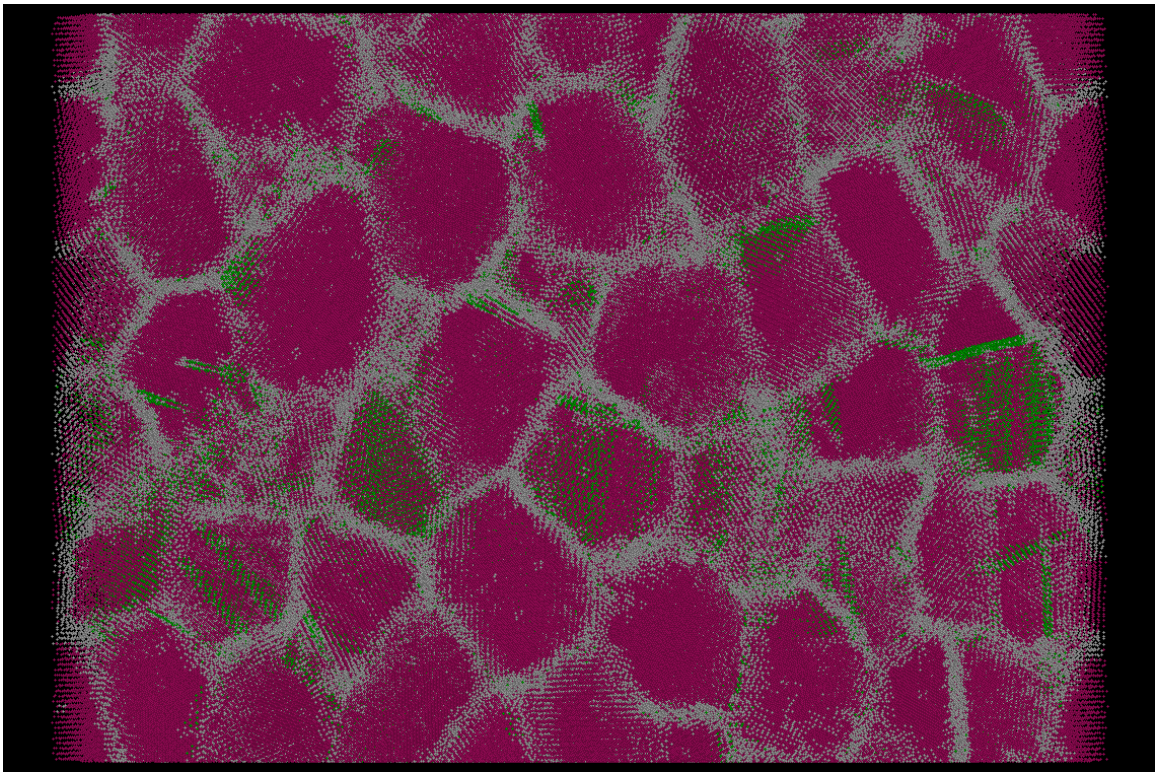

Figure 7.34. CN analysis of *nc*-Cu with $<\theta>$=39.673 at 6.6% shear strain.

7.3.3 Grain rotation

From previous section, we know that the misorientation distribution has a strong effect on the mechanical response of nc-Cu samples. Based on our observation, the grain boundary sliding and rotation are secondary mechanism during shear deformation. Nc-Cu sample with random misorientation distribution are softer than that of minimized misorientation distribution because of the ability to accommodate shear strain through grain boundaries at the beginning of the deformation. Nc-Cu sample of minimized misorientation distribution has a majority of low-angle grain boundaries. Low-angle grain boundaries are more ordered and have less ability to accommodate shear strain. Partial dislocations are observed in an early stage during shear of low-angle samples. To further prove that the grain sliding and rotation are not the primary mechanism, we calculate the rotation of each grain during the shear deformation.

Let us take the simple shear in *–yx* direction for example. During deformation, grains should rotate around *z*-axis. Using the grain boundary characterization technique described in chapter 5, we can identify the core atoms of each grain. We know the initial positions of these core atoms. The positions of these core atoms can also be tracked during deformation (Figure 7.35). At different shear strain, the rotation angle of each grain core can be estimated by finding the rotation matrix determined by three Euler angles, $(\varphi \quad \phi \quad \psi)$,

$$\begin{bmatrix} x' \\ y' \\ z' \end{bmatrix} = \begin{bmatrix} x \\ y \\ z \end{bmatrix}$$

$$\begin{bmatrix} \cos(\varphi)\cos(\psi) - \cos(\phi)\sin(\varphi)\sin(\psi) & -\cos(\psi)\sin(\varphi) - \cos(\varphi)c_2\sin(\psi) & \sin(\phi)\sin(\psi) \\ \cos(\varphi)\sin(\psi) + \cos(\phi)\cos(\psi)\sin(\varphi) & \cos(\varphi)\cos(\phi)\cos(\psi) - \sin(\varphi)\sin(\psi) & -\cos(\psi)\sin(\phi) \\ \sin(\varphi)\sin(\phi) & \cos(\varphi)\sin(\phi) & \cos(\phi) \end{bmatrix} \tag{7.3}$$

where (x y z) are the initial position of core atoms and (x', y', z') are their position at certain shear strain. The rotation matrix can be estimated by simply taking average of all core atoms for a specific grain. The rotation angle is defined as:

$$\alpha = \varphi + \psi - 2\pi \qquad (7.4)$$

because φ and ψ are rotation angle around z-axis using the -zxz convention.

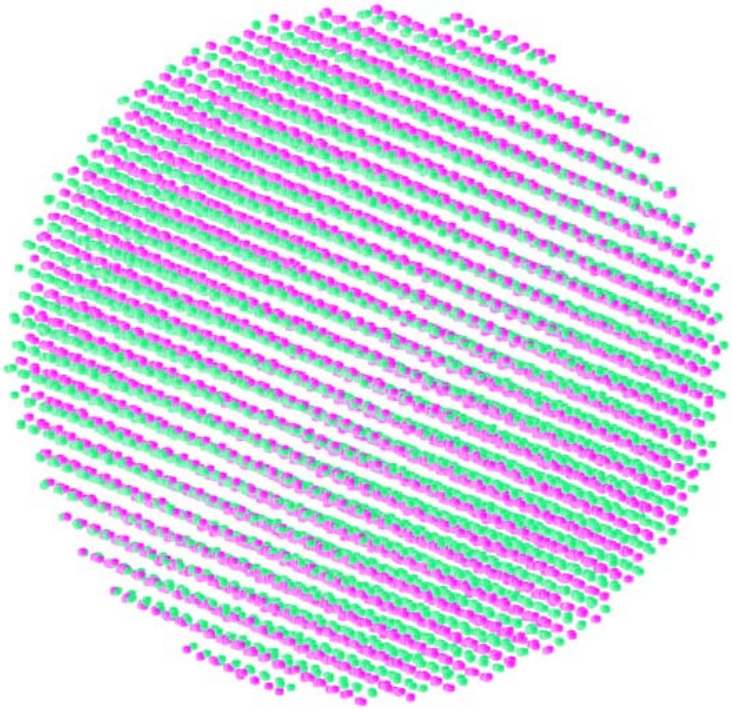

Figure 7.35. The core atoms of a grain in a 20-grain *nc*-Cu samples at zero shear strain and a finite shear strain. The rotation angle can be evaluated by Eqn. 7.4.

Next, we measure the rotation angle of every grain in three 20-grain *nc*-Cu samples with different misorientation distributions. The average misorientation angle of the minimized misorientation distribution is close to 10 and that of random misorientation distribution is close to 40. Another misorientation distribution is selected with an average misorientation angle around 25. The grain rotation angles in three samples are recorded at different shear strain and are shown in Figure 7.36, 7.37 and 7.38, respectively. In

each figure, only seventeen curves are plotted because the broken periodic boundary condition in y-direction in grain number 05, 10 and 11.

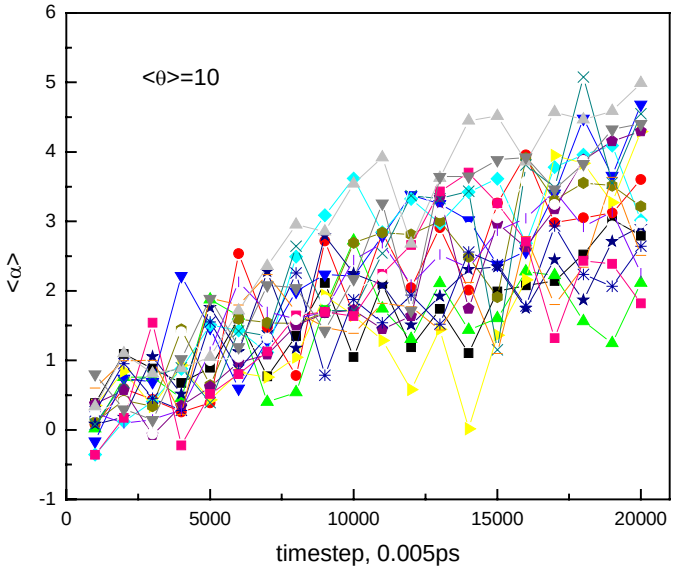

Figure 7.36. The rotation angles of grains in a 20-grain *nc*-Cu sample with an average misorientation angle of 10° at different timestep during shear deformation.

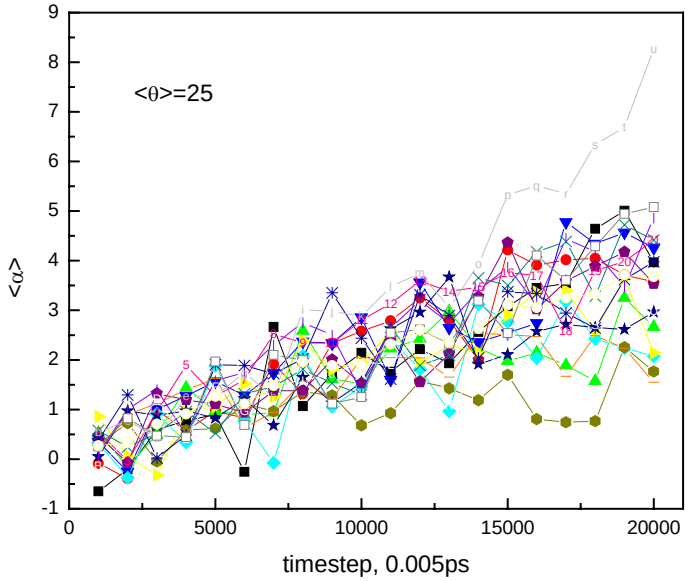

Figure 7.37. The rotation angles of grains in a 20-grain *nc*-Cu sample with an average misorientation angle of 25° at different timestep during shear deformation.

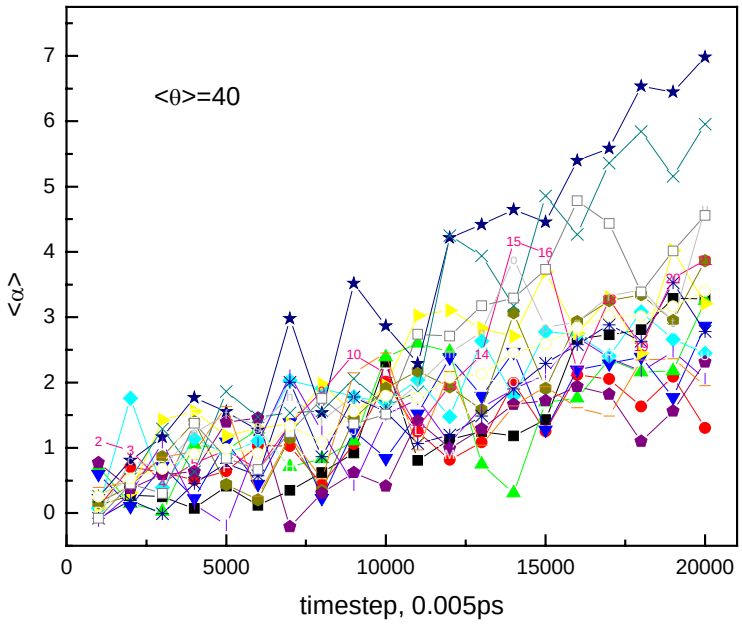

Figure 7.38. The rotation angles of grains in a 20-grain *nc*-Cu sample with an average misorientation angle of 40° at different timestep during shear deformation.

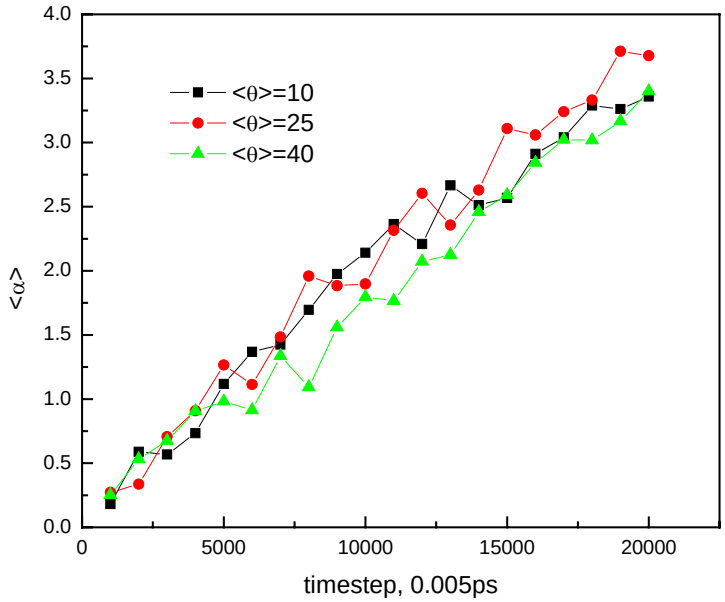

Figure 7.39. The average rotation angles of three 20-grain *nc*-Cu samples at different timestep during shear deformation.

Figure 3.39 shows the average rotation angles of three 20-grain *nc*-Cu samples at different timestep during shear deformation. Significant different between them are not observed indicating that grain rotation are not the primary mechanism that control the onset of the deformation for *nc*-Cu samples.

7.3.4 Grain size effects

As mentioned earlier, we can generate *nc*-Cu samples of different box sizes by filling different number of atoms into the same dimensionless Voronoi structure of 100 grains. Using the eight different misorientation distributions (Figure 7.10), we performed MD relaxation and shear deformation on *nc*-Cu samples of mean grains of 8.05 nm and 6.9nm, the same trend in maximum shear stress and volume fraction of grain boundaries is observed. The *nc*-Cu samples of random misorientation (or larger mean misorientation angle) always have a lower shear modulus than those of minimum misorientation distributions.

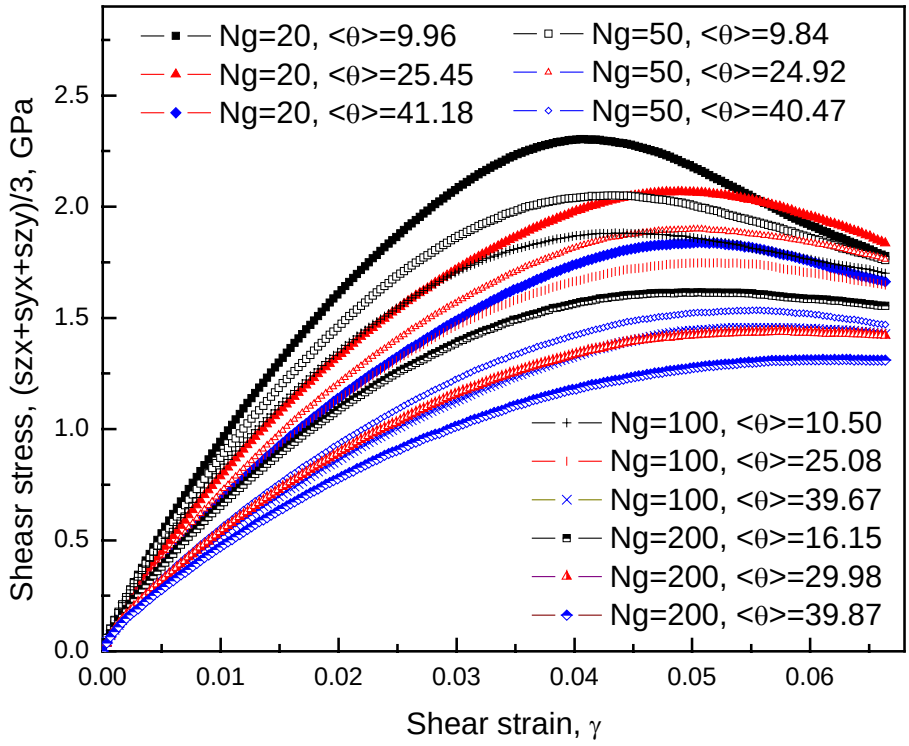

Figure 7.40. The shear stress-strain curves for *nc*-Cu samples of the same box size but different number of grains and misorientation distributions. The box size is 30.125nm. The average grain sizes are 13.77nm (Ng=20), 10.145nm (Ng=50), 8.05nm (Ng=100) and 6.39nm (Ng=200).

For further verification, *nc*-Cu samples of different number of grains (20, 50, 100, 200) are generated. The box sizes are kept at 30.125 nm. The average grain diameters are 13.77nm, 10.145nm, 8.05nm and 6.39 nm, respectively. For each grain number, a Voronoi structure is generated and two misorientation distributions (random and minimum) are obtained based on the same Voronoi structure using the MC technique described earlier. After relaxation and shear deformation, the stress-strain relations of eight *nc*-Cu samples are plotted in Figure 7.40. In the case of 20-grain, the sample of minimum misorientation distribution still has a higher maximum shear stress than that of random misorientation, which is opposite to what Caturla *et al.* [169] observed. We do not observe the inverse effects when the mean grain size is larger (12nm). A set of 50-

grain *nc*-Cu samples with mean grain size of 12.17nm is also tested and the results are consistent. Two 20-grrain *nc*-Cu samples of average grain size of 20.6nm of minimized and random misorientation distributions are also tested and similar results are found. For each *nc*-Cu sample, eight atomic configurations are selected during the shear deformations. The changes in percentage of (1422) type atoms are plotted in Figure 7.41 using the CNA. As the number of grains in *nc*-Cu samples decreases, the percentage of fcc atoms increases dramatically. Once again, the amount of grain boundaries presented in *nc*-Cu samples dominates the deformation process. *nc*-Cu sample of large grain number has strong softening during shear due to the large amount of grain boundaries compared to that of small number of grains.

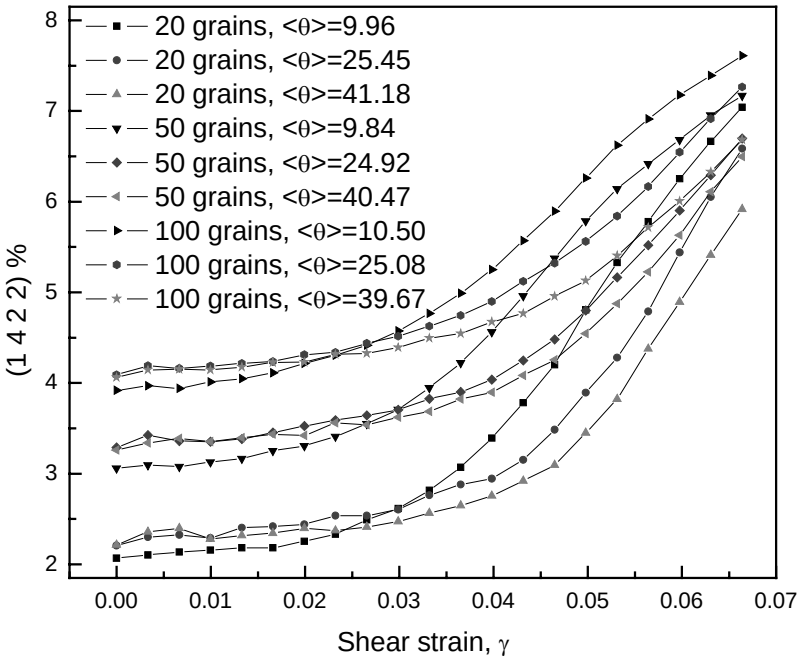

Figure 7.41. The percentage change of (1422) type of atoms during shear deformation for nc-Cu samples of different misorientation distributions and different number of grains. The box sizes are kept the same at 30.125nm as the number of grains varies from 20 to 100.

7.4 Discussion

The inverse Hall-Petch phenomena have been observed and studied in both experiments and atomistic simulations. Many theories have been proposed to explain the softening in the strength of nanocrystalline materials as grain sizes decreases into nanoscale. A lot of atomistic simulations on nanocrystalline materials have been focusing on the competing process between dislocation activities and grain boundary sliding. The large amount of grain boundaries presented in most nanocrystalline materials have not been studied systematically, especially the grain boundary misorientation and GB plane orientation. Our result shows that misorientation effect is similar to the inverse HP phenomena, where both average grain sizes and average misorientation angles affect the amount of grain boundaries presented in nanocrystalline materials. An advantage of studying the misorientation effects is that the same grain structure can be used to generate digital microstructures of different misorientation distributions.

Another critical issue has been overlooked in atomistic simulation of nanocrystalline materials, which is the anisotropy induced by the small number of grains. Due to the limit of computing, the maximum number of grains generated in this study is 200. A disadvantage of Voronoi tessellation is the large amount of small interfaces presented even in a structure of 20 grains. For a certain box size, only a limited number of grains can be generated in order to keep most of the interfaces and triple junction from disappearing upon molecular dynamic relaxation. Based on an earlier study, we know that grain structure of a narrow grain size distribution is more isotropic [14]. For each grain number, a narrow grain size distribution is obtained through the CVT method with a standard deviation close to 0.1. The experimentally produced nanocrystalline materials often have a large amount of small grains. Although the problem can be solved partially using the periodic boundary conditions, the author believes there still exists a lower limit in the number of grains when it comes to study the mechanical properties of

nanocrystalline materials. A large number of grains are also necessary to have a random misorientation distribution close to the Mackenzie distribution. When the number of grain boundaries is large enough, special high angle grain boundaries will naturally appear instead of being inserted manually in a sample of small number of grains.

It is true that the deformation mechanism in nanocrystalline materials is a competing process between dislocation activities and the grain boundary motion. The different volume fraction of grain boundaries induced by both grain sizes and misorientation distributions will greatly affect the onset of dislocation nucleation. Our misorientation results indicate that the grain boundary motion is the dominant factor during plastic deformations. *nc*-Cu sample of low angle grain boundaries has lower amount of grain boundaries and less ability to accommodate the resolved shear stresses on the boundaries than samples of high angle grain boundaries. In addition, the distribution of CSP and volume of all GB interfaces follows the misorientation distributions closely. These results confirm that low-angle GBs are denser and more ordered than high-angle GBs. As a result, low-angle GBs have a low mobility and high shear resistance as commonly observed in both experiments and simulations.

7.5 Conclusions

In this study, we observe that the misorientation distributions have a strong effect on the nanocrystalline copper materials. The same Voronoi structure of 100 cells is used while generating *nc*-Cu samples using eight misorientation distributions obtained using the Monte-Carlo minimization and maximization techniques. MD relaxation and deformation are then performed on these misorientation samples of 100 grains. A decrease in shear modulus is observed as the mean misorientation angles in the sample increases. Grain boundary characterization and Common neighbor analysis confirm that

the misorientation distributions indeed affect the volume fraction of grain boundary entities as well as the percentage of *fcc* and *hcp* atoms during shear deformation.

When the number of grains decreases, strong anisotropy effects may takes into place during shear deformation. In the case of Voronoi cells before filling atoms, the angles between interface and three shear planes deviate from the ideal isotropy case as the number of cells decreases. The deviation becomes larger than the number of cells is less than 141. Strong anisotropy effects are observed in *nc*-Cu samples of small grain numbers after MD relaxation and shear deformation. MD simulations are performed on *nc*-Cu samples of grain number varying from 20 to 200 and the largest grain diameter reaches 12nm. Two misorientation distributions are generated for each grain number and *nc*-Cu samples of minimized misorientation distributions always have higher yield stress and shear moduli than those of random misorientation distributions. However, we did not observe the inverse trend observed in Caturla's work [12] where a potential of high formation energy of stacking fault is used and a different model system (Ni) is study. A general deformation mechanism that emphasizes the influence of grain boundary is proposed and applied successfully to explain both misorientation effects and the inverse Hall-Petch phenomena in nanocrystalline copper materials.

Chapter 8

Conclusions

Nanocrystalline materials have been under extensive study in the past two decades. The reduction in grain size induces many abnormal behaviors in the properties of nanocrystalline materials that have been investigated systematically and quantitatively. As one of the most fundamental relations in materials science, the structure-property relation should still apply on materials of nano-scale grain sizes. The characterization of grain boundaries (GBs) and related entities remains a big obstacle to understanding the structure-property relation in nanocrystalline materials. It is challenging experimentally to determine the topological properties of polycrystalline materials due to the complex and disordered grain boundary network presented in the nanocrystalline materials. The constantly improving computing power enables us to study the structure-property relation in nanocrystalline materials via Monte Carlo and molecular dynamic simulations. In this study, we first developed a Monte Carlo technique to generate a digital microstructure that approximates the real or theoretical microstructures. Secondly, we proposed a new method, the "*peeling-onion method*", to characterize the grain boundary network in the relaxed *nc*-Cu sample using MD simulations. Equipped with these two techniques, we are able to characterize the atomic structure of each grain boundary entities in a relaxed *nc*-Cu sample and study the structure-property relation in nanocrystalline copper materials.

Firstly, we developed a systematic space partition method to approximate the statistical and topological properties in cellular structures such as polycrystals and nanocrystals. The main feature of this method is the inclusion of some of the topological properties such as the cell/grain size distributions as the constraints for the PVT. The

input constraints can be obtained either from experiments or from theoretical models. We used an inverse Monte Carlo method to implement the constraints. The constrained VT method is shown to have the capacity to produce cellular cells with specific topological and statistical properties. Using this technique, we successfully generated Voronoi structures with different cell volume distributions: 1) lognormal; 2) bimodal; 3) normal and found that the cell volume distribution strongly affects the grain shape and other topological properties. The validity of both Lewis rule and Aboav-Weaire Law is also examined. Another MC minimization procedure is developed to reduce the amount of small faces and edges in the Voronoi structure. The CVT method, although only tested in limited cases, is a general approach for producing cellular cells or grains with complex topological/microstructural properties. In our testing, we showed that the changes in the topological and statistical property are closely related to the changes in the VT cells that one produced, which in turn can lead to changes in physical properties in some of the widely used or modeled polycrystalline materials.

Secondly, we present a systematic approach to rebuild microstructures in nanocrystalline materials. A constrained Voronoi tessellation method in conjunction with an inverse Monte Carlo method is applied to build grain cells, or grain boundary networks, that bear resemblance to the real microstructures in quantitative fashion. The crystallographic orientations of the microstructures are selected through an optimization method described in Chapter 4. After filling atoms into the Voronoi structure, we obtain the *nc*-Cu sample with different misorientation distributions and the lattice of each grain is FCC. Finally, we are able to apply the new method, the *peeling-onion* algorithm, to the relaxed *nc*-Cu after MD simulations and characterize atoms in nanocrystalline samples as grain, grain boundary interface, triple junction and vertex atoms. This method allows us, for the first time, to characterize measure and correlate the detailed microstructure attributes to the properties in nanocrystalline or polycrystalline materials.

Using the proposed *peeling-onion* method, each atom in the relaxed sample is given a new grain index. Atoms are further characterized into four groups: grain atoms, GB interface atoms, triple junction atoms and vertex atoms. All grain boundary interfaces and triple junctions are identified as well as atoms in each GB interface and TJ. Using the atomic coordinates of grain boundary atoms on each interface, we are able to calculate the GB profiles (Potential energy, CSP, AVV, etc) for each interface and obtain their statistical distribution and averages. To quantify the degree of disorder presented in nanocrystalline copper materials, we measured the distributions of GB width, the peak heights of CSP and AVV profiles at different grain sizes and temperature. As mean grain size decreases, the average GB width increases and the volume fraction of grain boundaries increases. Similar effects are found when temperature increases. The average AVV does not increase with mean grain size indicating that the density in the center of grain boundary region remains the same. However, the average AVV does increases with temperatures. More importantly, we are able to calculate the GB RDF profile based on the proposed method and successfully detect the increasing degree of disorder when approaching the center of grain boundary region. On the other hand, the interface area and lengths of all triple junctions on the interfaces are calculated using primarily the positions of identified vertices. The linear relation between the number of atoms in each interface and the calculated GB interface area shows that our area calculation is accurate. The same can be said for the TJ length calculation. Comparing the distribution of calculated GB interface area in the relaxed sample and that of initial Voronoi structure, we see that there exists a physical limit in the number of atoms to form a stable grain boundary interface in nanocrystalline materials. Similarly, there also exists a physical limit in the number of atoms to form a stable triple junction in nanocrystalline materials.

Finally, we performed shear deformation on *nc*-Cu samples of different misorientation distributions and observed that the misorientation distributions have a strong effect on the mechanical properties of nanocrystalline copper materials. A

decrease in shear modulus is observed as the mean misorientation angles in the sample increases. Grain boundary characterization and Common neighbor analysis confirm that the misorientation distributions indeed affect the volume fraction of grain boundary entities as well as the percentage of *fcc* and *hcp* atoms during shear deformation. Our result shows that misorientation effect is similar to the inverse HP phenomena, where both average grain sizes and average misorientation angles affect the amount of grain boundaries presented in nanocrystalline materials. However, when the number of grains decreases, strong anisotropy effects may takes into place during shear deformation. In the case of Voronoi cells before filling atoms, the angles between interface and three shear planes deviate from the ideal isotropy case as the number of cells decreases. The deviation becomes larger than the number of cells is less than 141. Strong anisotropy effects are observed in *nc*-Cu samples of small grain numbers after MD relaxation and shear deformation. By keeping the number of grains and grain structure the same and changing the misorientation distribution, we are able to obtain the intrinsic properties of *nc*-Cu materials.

The deformation mechanism in nanocrystalline materials is a competing process between dislocation activities and the grain boundary motion. The different volume fraction of grain boundaries induced by both grain sizes and misorientation distributions will greatly affect the onset of dislocation nucleation. Our misorientation results indicate that the grain boundary motion is the dominant factor during plastic deformations. *nc*-Cu sample of low angle grain boundaries has lower amount of grain boundaries and less ability to accommodate the resolved shear stresses on the boundaries than samples of high angle grain boundaries. In addition, the distribution of CSP and volume of all GB interfaces follows the misorientation distributions closely. These results confirm that low-angle GBs are denser and more ordered than high-angle GBs. As a result, low-angle GBs have a low mobility and high shear resistance as commonly observed in both experiments and simulations.

Appendix A

Algorithm for Ray-crossing technique

Let q represent a lattice point and T represent a triangle on the face of Voronoi cell. The ray-crossing algorithm can be described as follows:

Algorithm: Point in Polyhedron

1) Compute bounding radius R;

2) loop forever

$r_0 =$ random ray of length R

$r = q + r_0$.

crossings = 0.

for each triangle T of polyhedron do

Call *SegTriInt*(T, q, r).

if degenerate intersection

then Go back to loop.

else increment *crossings* appropriately.

if *crossings* odd

then q is inside the polyhedron.

else q is outside the polyhedron.

Exit.

Appendix B

Procedure to calculate central symmetry parameter

Define an integer constant M to be the maximum number of neighbors for the computation of $\{c_i\}$. For FCC lattice, *M*=12. For BCC lattice, *M*=8. However, the computer does not know whether the lattice is FCC or BCC based, so by default M is defined as,

$$M_{default} = \lfloor N_{most} / 2 \rfloor \times 2, \tag{B.1}$$

where N_{most} is the most popular coordination number in the set $\{N_i\}$, *i*=1…*N* of the configuration. *M* must be an even number in any case as we are counting pairs of atoms.

Now for each atom $i \in 1 \cdots N$, define,

$$\tilde{m}_i \equiv \min(M, N_i), \tag{B.2}$$

If $\tilde{m}_i = 0$, c_i= 0 since an isolated atom should have perfect inversion symmetry. If $\tilde{m}_i$=1, c_i=1, since a coordination-1 atom has no inversion image to compare with, so in a sense its inversion symmetry is the most broken. For $\tilde{m}_i \geq 2$, define,

$$m_i \equiv \lfloor \tilde{m}_i / 2 \rfloor \times 2, \tag{B.3}$$

and we use the following procedure to determine c_i,

1. Sort the $j = 1 \cdots N_i$ neighbors of atoms *i* according to their distance $|d_j|$ to atom *i* in ascending order. Pick the smallest m_i-set.
2. Take the closest neighbor d_1. Search, among the other m_i-1 neighbors, the one that minimizes,

$$\tilde{D}_j \equiv \left| d_1 + d_j \right|^2, \tag{B.4}$$

And let us define,

$$j' \equiv \arg[\min_{j=2\cdots m_i}(\tilde{D}_j)], \text{ and } D_1 \equiv \tilde{D}_{j'}. \tag{B.5}$$

3. Throw atoms 1 and *j'* out of the set, and look for the closest neighbor in the remaining set. Then repeat Step 2 until the set is empty. We then have obtained D_1, D_2, ..., $D_{mi/2}$. Define,

$$c_i \equiv \frac{\sum_{k=1}^{m_i/2} D_k}{2\sum_{j=1}^{m_i/2} \left| d_j \right|^2}. \tag{B.6}$$

Equation (6) is dimensionless. In the case of m_i=2, suppose the two neighbors are independently randomly oriented, it is easy to show that the mathematical expectation,

$$E[c_i] = 1/2. \tag{B.7}$$

On the other hand, we can prove that,

$$\max_{\{d_j\}} c_i = 1, \tag{B.8}$$

so this matches with the definition of c_i=1 at m_i=1. But when m_i>>2,

$$E[c_i] < 1/2. \tag{B.9}$$

Because of the minimization process. For instance, at the intrinsic stacking fault in FCC lattice ABC|BCA, there is a loss of inversion symmetry in the two layers C|B, and c_i is,

$$c_i = \frac{3\times 0 + 3\times\left(d\sqrt{3}/2\times 1/3\times 2\right)^2}{2\times 12d^2} = \frac{1}{24} \approx 0.0416. \tag{B.10}$$

assuming perfect stacking.

Appendix C

Procedure to calculate the surface normal vectors

(1) Calculate the surface normal by taking the cross product of two vectors

$$\begin{aligned} N_x &= (U_y \cdot V_z) - (U_z \cdot V_y) \\ N_y &= (U_z \cdot V_x) - (U_x \cdot V_z) \\ N_z &= (U_x \cdot V_y) - (U_y \cdot V_x) \end{aligned} \qquad \text{(C.1)}$$

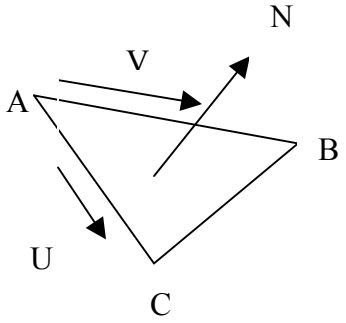

(2) The normal vector N(x,y,z) must be normalized:

$$l = \sqrt{x^2 + y^2 + z^2}\ ,\ x_2 = \frac{x_1}{l}, y_2 = \frac{y_1}{l}, z_2 = \frac{z_1}{l}. \qquad \text{(C.2)}$$

(3) The distance from the origin to the point the plane that is nearest to the origin can be determined by taking dot product:

$$d = N_x A_x + N_y A_y + N_z A_z . \qquad \text{(C.3)}$$

(4) The plane equation:

$$d = N_x \cdot x + N_y \cdot y + N_z \cdot z . \qquad \text{(C.4)}$$

(5) The square distance between a point X_2 on the line and a point X_0:

$$d = \frac{\left|(X_2 - X_1) \times (X_1 - X_0)\right|}{\left|X_2 - X_1\right|}, \qquad \text{(C.5)}$$

where X_1 is another point on the line.

Appendix D

Procedure to calculate surface normal vector of GB in *nc*-Cu

Method to determine the surface normal:

(1) Identify a shell of atoms located on the GB surface ($r_{min} < r < r_{max}$)

(2) Find all pair of atoms in the shell with separation larger than a cutoff distance($2*r_{max}$-1)

(3) For each pair of atoms, calculate the surface normal (N_x, N_y, N_z)

(4) Using each surface normal, calculate $\bar{d}$ and standard deviation $\chi = \sum_i \left(d_i - \bar{d}\right)^2$, by applying $d = N_x A_x + N_y A_y + N_z A_z$, where ($A_x$,$A_y$,$A_z$) is the position of an atom on the GB surface. Finally find the surface normal with the smallest X as the surface normal.

REFERENCES

[1] E. O. Hall, Proc. Phys. Soc. London Sect. B 64, 747 (1951).

[2] N. J. Petch, J. Iron Steel Inst. 174, 25 (1953).

[3] T. G. Nieh and J. Wadsworth, Scr. Metall. Mater. 25, 955 (1991).

[4] T. Volpp, E. Goring, W. M. Kuschke, et al., Nanostruct. Mater. 8, 855 (1997).

[5] P. G. Sanders, J. A. Eastman, and J. R. Weertman, Acta Mater. 45, 4019 (1997).

[6] K. Lu, H. Y. Zhang, Y. Zhong, et al., J. Mater. Res. 12, 923 (1997).

[7] L. Lu, X. Chen, X. Huang, et al., Science 323, 607 (2009).

[8] J. Schiotz, F. D. Di Tolla, and K. W. Jacobsen, Nature 391, 561 (1998).

[9] J. Schiotz and K. W. Jacobsen, Science 301, 1357 (2003).

[10] H. V. Swygenhoven and P. M. Derlet, Phys. Rev. B 64, 224105 (2001).

[11] R. A. Masumura, P. M. Hazzledine, et al., Acta Mater. 46, 4527 (1998).

[12] D. A. Konstantinidis and E. C. Aifantis, Nanostruct. Mater. 10, 1111 (1998).

[13] G. J. Fan, H. Choo, P. K. Liaw, et al., Mater. Sci. Eng. A 409, 243 (2005).

[14] T. Xu and M. Li, Phil. Mag. 89, 349 (2009).

[15] D. Gross and M. Li, Appl. Phys. Lett. 80, 746 (2002).

[16] D. Wolf, V. Yamakov, S. R. Phillpot, et al., Acta Mater. 53, 1 (2005).

[17] J. R. Ray and A. Rahman, J. Chem. Phys. 80, 4423 (1984).

[18] J. R. Ray, M. C. Moody, and A. Rahman, Phys. Rev. B 32, 733 (1985).

[19] H. Gleiter, in *Deformation of polycrystals : mechanisms and microstructures: proceedings of the 2nd Risø International Symposium on Metallurgy and Materials Science*, edited by N. Hansen, A. Horsewell, T. Leffers and H. Liltholt, Roskilde, Denmark, 1981), p. 15.

[20] R. W. Siegel, in *Processing of metals and alloys*, edited by R. W. Cahn (VCH, Weinheim, Germany, 1991), Vol. 15, p. 583.

[21] C. C. Koch, Nanostruct. Mater. 2, 109 (1993).

[22] B. H. Kear and L. E. McCandlish, Nanostruct. Mater. 3, 19 (1993).

[23] H. Chang, C. J. Altstetter, and R. S. Averback, J. Mater. Res. 7, 2962 (1992).

[24] R. L. Bickerdike, D. Clark, et al., Int. J. Rapid Solidi. 2, 1 (1986).

[25] W. Chang, G. Skandan, S. C. Danforth, et al., Nanostruct. Mater. 4, 507 (1994).

[26] C. Cheung, G. Palumbo, and U. Erb, Scr. Metall. Mater. 31, 735 (1994).

[27] C. H. Chou and J. Phillips, J. Mater. Res. 7, 2107 (1992).

[28] T. Yoshida, S. Takeyama, Y. Yamada, et al., Appl. Phys. Lett. 68, 1772 (1996).

[29] V. M. Segal, Mater. Sci. Eng. A 271, 322 (1999).

[30] E. M. Bringa, A. Caro, Y. M. Wang, et al., Science 309, 1838 (2005).

[31] X. McFadden, R. S. Mishra, R. Z. Valiev, et al., Nature 398, 684 (1999).

[32] J. E. Carsley, J. Ning, W. W. Milligan, et al., Nanostruct. Mater. 5, 441 (1995).

[33] J. R. Weertman, in *Nanostructured materials: processing, properties and applications*, edited by C. C. Koch (William Andrews Publishing, Norwich, NY, 2002), p. 397.

[34] S. R. Agnew, B. R. Elliott, C. J. Youngdahl, et al., Mater. Sci. Eng. A 285, 391 (2000).

[35] C. C. Koch, Scr. Mater. 49, 657 (2003).

[36] D. G. Morris and M. A. Morris, Mater. Sci. Forum 235, 861 (1997).

[37] M. Legros, B. R. Elliott, M. N. Rittner, et al., Phil. Mag. A 80, 1017 (2000).

[38] C. J. Youngdahl, P. G. Sanders, J. A. Eastman, et al., Scr. Mater. 37, 809 (1997).

[39] W. N. Sharpe, D. A. LaVan, and R. L. Edwards, in *the 1997 International Conference on Solid-State Sensors and Actuators*, Chicago, IL, 1997), p. 607.

[40] Y. Champion, C. Langlois, S. Guerin-Mailly, et al., Science 300, 310 (2003).

[41] H. S. Kim and Y. Estrin, Appl. Phys. Lett. 79, 4115 (2001).

[42] K. M. Youssef, R. O. Scattergood, K. L. Murty, et al., Appl. Phys. Lett. 87, 3 (2005).

[43] Y. Wang, M. Chen, F. Zhou, et al., Nature 419, 6910 (2002).

[44] H. Van Swygenhoven and P. M. Derlet, Phys. Rev. B 64, 224105 (2001).

[45] X. Z. Liao, Y. H. Zhao, Y. T. Zhu, et al., J. Appl. Phys. 96, 636 (2004).

[46] B. Zhu, R. J. Asaro, P. Krysl, et al., Acta Mater. 53, 4825 (2005).

[47] L. Margulies, G. Winther, and H. F. Poulsen, Science 291, 2392 (2001).

[48] X. Z. Liao, Y. H. Zhao, S. G. Srinivasan, et al., Appl. Phys. Lette. 84, 592 (2004).

[49] X. Z. Liao, J. Y. Huang, Y. T. Zhu, et al., Phil. Mag. 83, 3065 (2003).

[50] H. Van Swygenhoven, Science 296, 66 (2002).

[51] V. Yamakov, D. Wolf, S. R. Phillpot, et al., Nat. Mater. 1, 45 (2002).

[52] V. Yamakov, D. Wolf, S. R. Phillpot, et al., Acta Mater. 50, 5005 (2002).

[53] X. Z. Liao, F. Zhou, E. J. Lavernia, et al., Appl. Phys. Lett. 83, 632 (2003).

[54] X. Z. Liao, F. Zhou, E. J. Lavernia, et al., Appl. Phys. Lett. 83, 5062 (2003).

[55] H. Rosner, J. Markmann, and J. Weissmuller, Phil. Mag. Lett. 84, 321 (2004).

[56] J. Weissmuller and J. Markmann, Adv. Eng. Mater. 7, 202 (2005).

[57] V. Yamakov, D. Wolf, S. R. Phillpot, et al., Acta Mater. 51, 4135 (2003).

[58] V. Yamakov, D. Wolf, S. R. Phillpot, et al., Nat. Mater. 3, 43 (2004).

[59] M. B. Bush, Mater. Sci. Eng. A 161, 127 (1993).

[60] D. Chen, Mater. Sci. Eng. A 190, 193 (1995).

[61] D. Chen, Comput. Mater. Sci. 3, 327 (1995).

[62] H. L. Zhu and R. S. Averback, Mater. Sci. Eng.A 204, 96 (1995).

[63] H. Gleiter, Prog. Mater. Sci. 33, 223 (1989).

[64] A. C. Lund and C. A. Schuh, Acta Mater. 53, 3193 (2005).

[65] T. Shimokawa, A. Nakatani, and H. Kitagawa, Phys. Rev. B 71, 224110 (2005).

[66] J. Wang, D. Wolf, S. R. Phillpot, et al., Nanostruct. Mater. 6, 747 (1995).

[67] S. R. Phillpot, D. Wolf, and H. Gleiter, J. Appl. Phys. 78, 847 (1995).

[68] H. Van Swygenhoven and A. Caro, Nanostruct. Mater. 9, 669 (1997).

[69] H. Van Swygenhoven and A. Caro, Appl. Phys. Lett. 71, 1652 (1997).

[70] H. Van Swygenhoven, M. Spaczer, and A. Caro, Nanostruct. Mater. 10, 819 (1998).

[71] H. Van Swygenhoven and A. Caro, Phys. Rev. B 58, 11246 (1998).

[72] H. Van Swygenhoven, M. Spaczer, and A. Caro, Acta Mater. 47, 3117 (1999).

[73] H. Van Swygenhoven, M. Spaczer, and A. Caro, Nanostruct. Mater. 12, 629 (1999).

[74] H. Van Swygenhoven, M. Spaczer, D. Farkas, et al., Nanostruct. Mater. 12, 323 (1999).

[75] H. Van Swygenhoven, M. Spaczer, A. Caro, et al., Phys. Rev. B 60, 22 (1999).

[76] H. Van Swygenhoven, D. Farkas, and A. Caro, Phys. Rev. B 62, 831 (2000).

[77] V. Vitek and D. J. Srolovitz, *Atomistic Simulation of Materials: Beyond Pair Potentials* (Plenum Press, New York, N.Y., 1989).

[78] S. P. Marsh and C. S. Pande, *Modeling of Coarsening and Grain Growth* (Minerals Metals & Materials society, Warrendale, PA, 1993).

[79] M. P. Anderson, G. S. Grest, and D. J. Srolovitz, Phil. Mag. B 59, 293 (1989).

[80] S. Ling, M. P. Anderson, G. S. Grest, et al., Mater. Sci. Forum 94-96, 39 (1992).

[81] J. A. Glazier, Phys. Rev. Lett. 70, 2170 (1993).

[82] G. P. Zheng, Y. M. Wang, and M. Li, Acta Mater. 53, 3893 (2005).

[83] F. Aurenhammer, Comput Surv. 23, 345 (1991).

[84] S. Drysdale, *Voronoi Diagrams: Applications from Archeology to Zoology*, (Regional Geometry Institute, Smith Colledge, Northampton, MA, 1993).

[85] J. L. Finney, J. Mol. Biol. 119, 415 (1978).

[86] V. Icke, Astrophy. Space Sci. 244, 293 (1996).

[87] F. T. Lewis, Am. J. Bot. 30, 74 (1943).

[88] F. F. Mallory and B. N. Boots, Can. J. Zool. 61, 99 (1983).

[89] D. Weaire, J. P. Kermode, and J. Wejchert, Phil. Mag. B 53, L101 (1986).

[90] T. M. Barrett, Can. J. Forest Res. 27, 903 (1997).

[91] S. Li and S. Ghosh, Int. J. Numer. Methods Eng. 65, 1028 (2006).

[92] F. Baccelli, M. Klein, M. Lebourges, et al., Ann. Telecommun. 51, 158 (1996).

[93] J. L. Meijering, Philips Res. Rep. 8, 270 (1953).

[94] E. N. Gilbert, Ann. Math. Stat. 33, 958 (1962).

[95] A. G. Froseth, H. V. Swygenhoven, and P. M. Derlet, Acta Mater. 53, 4847 (2005).

[96] K. M. Dobrich, C. Rau, and C. E. Krill, Metall. Mater. Trans. A 35A, 1953 (2004).

[97] V. Y. Gertsman, M. Hoffmann, H. Gleiter, et al., Acta Metall. Mater. 42, 3539 (1994).

[98] M. F. Vaz and M. A. Fortes, Scr. Metall. 22, 35 (1988).

[99] S. Kumar, S. K. Kurtz, J. R. Banavar, et al., J. Stat. Phys. 67, 523 (1992).

[100] O. Watanabe, H. M. Zbib, and E. Takenouchi, Int. J. Plast. 14, 771 (1998).

[101] D. Rabbe, *Computer Simulations in Materials Science: The Simulation of Materials Microstructure and Properties* (Wiley-VCH Verlag GmbH & Co, KGaA, Weinheim, 2004).

[102] Z. G. Fan, Y. G. Wu, X. H. Zhao, et al., Comput. Mater. Sci. 29, 301 (2004).

[103] A. Okabe, B. N. Boots, K. Sugihara, et al., *Spatial Tessellations-Concepts and Applications of Voronoi Diagrams* (Wiley, New York, 2000).

[104] T. Ungar, J. Mater. Sci. 42, 1584 (2007).

[105] P. Jedlovszky and R. Vallauri, J. Chem. Phys. 105, 2391 (1996).

[106] D. C. Sterio, J. Microscopy-Oxford 134, 127 (1984).

[107] M. Evan, J. B. Peacock, and N. Hastings, *Statistical Distributions* (Wiley, John & Sons, New York, 2000).

[108] J. P. Troadec, A. Gervois, and L. Oger, Europhys. Lett. 42, 167 (1998).

[109] K. J. Kurzylowski, Scr. Metall. Mater. 24, 879 (1990).

[110] I. C. Dragomir, M. Gheorghe, N. Thadhani, et al., Mater. Sci. Eng. A 402, 158 (2005).

[111] R. Raj and A. K. Ghosh, Acta Metall. 29, 283 (1981).

[112] C. V. Thompson, *Solid State Physics* (Academic Press, New York, 2000).

[113] N. Rivier, Phil. Mag. B 52, 795 (1985).

[114] D. A. Aboav and T. G. Langdon, Metallography 1, 333 (1969).

[115] P. A. Beck, Adv. Phys. 3, 245 (1954).

[116] R. Y. Yang, R. P. Zou, and A. B. Yu, Phys. Rev. E 65, 041302 (2002).

[117] J. M. Drouffe and C. Itzykson, Nucl. Phys. B 235, 45 (1984).

[118] D. Weaire and N. Rivier, Contemp. Phys. 25, 59 (1984).

[119] M. A. Fortes, J. Phys. A 28, 1055 (1995).

[120] Y. Xun, M. J. Tan, and T. G. Nieh, Mater. Sci. Technol. 20, 173 (2004).

[121] A. H. Chokshi and A. K. Mukherjee, Metall. Trans. A 19, 1621 (1988).

[122] A. K. Deb, P. Chatterjee, and S. P. Sen Gupta, J. Appl. Crystallogr. 40, 33 (2007).

[123] B. Guillaume, F. Boschini, I. Garcia-Cano, et al., J. Eur. Ceram. Soc. 25, 3593 (2005).

[124] V. Y. Smorodin and P. K. Hopke, Atmos. Res. 82, 591 (2005).

[125] P. Richard, L. Oger, J. P. Troadec, et al., Physica A 259, 205 (1998).

[126] S. Hilgenfeldt, A. M. Kraynik, D. A. Reinelt, et al., Europhys. Lett. 67, 484 (2004).

[127] M. Li, W. L. Johnson, and W. A. Goddard, Phys. Rev. B 54, 12067 (1996).

[128] M. Li, Phys. Rev. B 62, 13979 (2000).

[129] L. Oger, A. Gervois, J. P. Troadec, et al., Phil. Mag. B 74, 177 (1996).

[130] K. Lochmann, L. Oger, and D. Stoyan, Solid State Sci. 8, 1397 (2006).

[131] G. P. Zheng, D. Gross, and M. Li, Physica A 355, 355 (2005).

[132] M. Miodownik, A. W. Godfrey, E. A. Holm, et al., Acta Mater. 47, 2661 (1999).

[133] J. K. Mackenzie, Biometrika 45, 229 (1958).

[134] M. Gombosi and B. Zalik, Comput. Geosci. 31, 1201 (2005).

[135] E. Haines, in *Graphic Gems IV*, edited by P. Heckbert (Academic Press, Boston, 1994), p. 24.

[136] M. P. Allen and D. J. Tildesley, *Computer simulation of liquids* (Oxford University Press, New York, 1987).

[137] M. Parrinello and A. Rahman, J. Appl. Phys. 52, 7182 (1981).

[138] M. S. Daw and M. I. Baskes, Phys. Rev. B 29, 6443 (1984).

[139] S. M. Foiles, M. I. Baskes, and M. S. Daw, Phys. Rev. B 33, 7983 (1986).

[140] M. W. Finnis and J. E. Sinclair, Phil. Mag. A 50, 45 (1984).

[141] Y. Mishin, M. J. Mehl, D. A. Papaconstantopoulos, et al., Phys. Rev. B 63, 16 (2001).

[142] D. G. Brandon and W. D. Kaplan, *Microstructural Characterization of Materials* (John Wiley, Chichester, England, 2004).

[143] V. Randle and O. Engler, *Introduction to Texture Analysis: Macrotexture, Microtexture And Orientation Mapping* (Gordon & Breach, Amsterdam, 2000).

[144] D. A. Porter and K. E. Easterling, *Phase Transformations in Metals and Alloys* (Van Nostrand Reinhold Co. Ltd., Berkshire, England, 1981).

[145] J. Hirth, Metall. Mater. Trans. B 3, 3047 (1972).

[146] T. Watanabe and S. Tsurekawa, Acta Mater. 47, 4171 (1999).

[147] R. P. Messmer and C. L. Briant, Acta Metall. 30, 457 (1982).

[148] T. L. Anderson, *Fracture Mechanics: Fundamentals and Applications* (Taylor & Francis, Boca Raton, FL, 2005).

[149] M. A. Meyers, A. Mishra, and D. J. Benson, Prog. Mater. Sci. 51, 427 (2006).

[150] C. C. Koch, I. A. Ovid'ko, S. Seal, et al., *Structural Nanocrystalline Materials: Fundamentals and Applications* (Cambridge University Press, Cambridge, 2007).

[151] K. Matous and A. M. Maniatty, Int. J. Numer. Methods Eng. 60, 2313 (2004).

[152] P. M. Derlet and H. V. Swygenhoven, Phys. Rev. B 67, 014202 (2003).

[153] *ASM Handbook: Metallography and Microstructures* (ASM International, Materials Park, Ohio, 2004).

[154] C. L. Kelchner, S. J. Plimpton, and J. C. Hamilton, Phys. Rev. B 58, 11085 (1998).

[155] J. Li, in *Handbook of Materials Modeling*, edited by S. Yip (Springer, Dordrecht, 2005), p. 1051.

[156] J. D. Honeycutt and H. C. Andersen, J. Phys. Chem. 91, 4950 (1987).

[157] Q. K. Li and M. Li, Appl. Phys. Lett. 88 (2006).

[158] J. W. Gibbs, *The Colleced Works of J. Willard Gibbs* (Longmans Green and Company, New York, 1928).

[159] B. Fultz and H. N. Frase, Hyperfine Interact. 130, 81 (2000).

[160] U. Herr, J. Jing, R. Birranger, et al., Appl. Phys. Lett. 50, 472 (1987).

[161] K. G. F. Janssens, D. Olmsted, E. A. Holm, et al., Nat. Mater. 5, 124 (2006).

[162] H. Zhang, N. Upmanyu, and D. J. Srolovitz, Acta Mater. 53, 79 (2005).

[163] J. M. Zhang, Y. H. Huang, X. J. Wu, et al., Appl. Surf. Sci. 252, 4936 (2006).

[164] G. Palumbo, S. J. Thorpe, and K. T. Aust, Scr. Metall. Mater. 24, 1347 (1990).

[165] M. Upmanyu, D. J. Srolovitz, et al., Acta Mater. 50, 1405 (2002).

[166] T. Xu and M. Li, Phil. Mag., Submitted (2009).

[167] S. M. Foiles, Phys. Rev. B 32, 3409 (1985).

[168] J. Eckert, J. C. Holzer, C. E. Krill, et al., J. Mater. Res. 7, 1980 (1992).

[169] M. J. Caturla, T. G. Nieh, and J. S. Stolken, Appl. Phys. Lett. 84, 598 (2004).

[170] S. Nose, Mol. Phys. 52, 255 (1984).

[171] W. G. Hoover, Phys. Rev. A 31, 1695 (1985).

[172] E. Bitzek, C. Brandl, P. M. Derlet, et al., Phys. Rev. Lett. 100 (2008).

[173] V. Yamakov, D. Wolf, S. R. Phillpot, et al., Phil. Mag. Lett. 83, 385 (2003).